BENDING AND SPRINGBACK OF DP780 AND DP980 STEEL SHEETS

EXPERIMENTAL, ANALYTICAL, AND FINITE ELEMENT STUDY OF THE BENDING AND SPRINGBACK BEHAVIOR OF DP780 AND DP90 STEEL SHEETS

By

TIMOTHY LIM

A Thesis

Submitted to the School of Graduate Studies

In Partial Fulfillment of the Requirements

For the Degree

Master of Applied Science

McMaster University

MASTER OF APPLIED SCIENCE (2008)
(Mechanical Engineering)

McMaster University
Hamilton, Ontario

TITLE

EXPERIMENTAL, ANALYTICAL, AND FINITE ELEMENT STUDY OF THE BENDING AND SPRINGBACK BEHAVIOR OF DP780 AND DP90 STEEL SHEETS

AUTHOR

Timothy Lim, B.Sc., B.A.Sc.,
(McMaster University, Hamilton, Ontario,
University of Toronto, Toronto, Ontario)

SUPERVISOR

Dr. Mukesh Jain, Associate Professor,
Department of Mechanical Engineering

NUMBER OF PAGES

xxxix, 325

ABSTRACT

The bending and springback behaviors of DP780 and DP980 were investigated using experiments, analytical models, and FEA. An FEA study using 3D shells was first performed of the work by Queener and DeAngelis (1968) and demonstrated that the 3D shell element behavior in bending and springback, is similar to that from simple bending theory.

Experimental and FE studies were then performed using DP780 and DP980 steels under simple and general bending conditions. Simple bending conditions were studied in V-die bending. General bending was studied for DP780 using a commercial bending machine. The FEA examined the effect of element formulation and material hardening assumptions on springback, bending stresses, and the residual stress distributions after springback. Corresponding simple and general bending analytical models were also compared. The simple bending model was from Queener and DeAngelis (1968), and the general bending model was from Tan et al. (1995), modified for Ludwig hardening.

Overall, the FEA predicted the springback magnitude in the order; 2D continuum >3D continuum > 3D shells, and kinematic hardening > mixed hardening> isotropic hardening.

In the V-die bending study the 3D shell FEA, using a calibrated mixed hardening assumption, produced the most accurate results. The FEA using pure isotropic hardening demonstrated that bending and springback behaviors for both

steels were consistent with that described by simple bending theory. The behaviors demonstrated by the FEA using mixed or pure kinematic hardening were not.

In the general bending study, the 3D continuum element FEA using pure kinematic hardening was the most accurate. The 3D continuum element FEA captured the bending stress interaction with the hardening assumption as well as thinning deformation, in agreement with the analytical model and thinning measured experimentally. 3D Shell elements could not capture these behaviors and significantly under-predicted springback under the pure isotropic hardening assumption.

ACKNOWLEDGMENTS

I would like to express my gratitude to supervisor Dr. M. Jain for his patience and guidance throughout this work.

I would also like to thank Dr. M. Bruhis for many fun hours spent in the lab, as well as R. Lemmon for the help in the experimental work. In addition I am grateful for the support of ArcelorMittal, specifically Masamichi Ichikawa, Bruce Farrand, Elliot Biro and Isadora van Riemsdijk for help in sourcing and materials characterization.

I would like to express my gratitude to my wife Diana, for enduring the isolation over the past few years, waiting for it all to end.

I would like to express my gratitude to my families both Lim's and Klancic's for their patience and support. Also I would like to dedicate this thesis to my father, Yong NGI Lim, and brother, Robert G.H Lim who inspired me to take this journey, and who I miss dearly. Also, to my faithful friend Arthur, who was always by my side. I wish we had more time together. And last, I'd like to make a dedication to my other lost friends, Sebastian, Binx, and Boots who are also sadly missed.

TABLE OF CONTENTS

CHAPTER 3 LITERATURE REVIEW

CHAPTER 4 NON-LINEAR FEA IN SHEET METAL FORMING

LIST OF FIGURES

LIST OF TABLES

LIST OF SYMBOLS

e_x, e_1	Engineering bending strain
$e_{max/\ min}$	In simple bending, the maximum/minimum engineering fiber strains
t	Thickness of blank
ε_x, ε_1	True bending strain where "x" or "1" is a principle direction perpendicular to the bending radius
$\varepsilon_{max/\ min}$	In simple bending, the maximum/minimum true fiber strains
σ_x, σ_1	Bending stress, where "x" or "1" is a principle direction perpendicular to the bending radius
R_p, R_i	Punch radius or inner bend radius
R_m	Bend radius at the mid-plane (in the thickness direction) of the blank.
R_m'	Bend radius at the mid-plane (in the thickness direction) of the blank after springback.
R_y	Radius at the outer surface (opposite the punch)
R_n	Radius of the neutral bending fiber which is the dividing line between tensile and compressive stresses
R_u	In general bending, the radius of the bending fiber at which the bending strain is zero.
R, r	In general bending, the radial position of a given bending fiber

$1/R_m^e$	Maximum bending curvature just prior to elastic-plastic deformation of the inner/outer surface bending fibers
$1/R_m^{bend}$	Bending curvature at the end of bending.
$1/R_m^{springback}$	Bending curvature after springback
$\overline{\sigma}$	Von Mises effective stress
$\bar{\varepsilon}$	Von Mises effective or equivalent strain
k	Strength coefficient from the Hollomon work hardening law
n	Work hardening parameter from the Hollomon work hardening law
M_p	Plastic bending moment
M_e	Elastic bending moment due to elastic bending stresses.
M_t, M	Total bending moment as the sum of elastic and plastic components
y	In simple bending, the coordinate in the thickness direction.
E	Young's Modulus
ν	Poisson's ratio
$\overline{\varepsilon_y}$	Effective yield strain in uni-axial tension
ε_{1y}, ε_{1yield}	Plane strain yield strain
θ	Bend angle
θ_i	Bend angle just prior to springback

θ_f	Bend angle after springback
$d\theta/\theta = (\theta_f-\theta_i)/(180°- \theta_i)$	Relative springback
k_s , $K_s = 1- d\theta/\theta$	Springback ratio
$\sigma_{residual}$	The principle bending stress, after springback
σ_θ	General bending stress acting in the tangential direction.
ε_θ	In general bending, the bending strain acting in the tangential direction (perpendicular to the bend radius)
σ_r	In general bending the transverse stress which acts in the radial direction
$\eta = t/to$	Relative thinning in general bending
$\rho = R_n/R_u$	Relative curvature of the neutral surface
$\kappa = \eta\ R_m = (R_y-R_i)/R_m$	Relative bending curvature in general bending
σ_0, Y^0	Uni-axial flow stress using Von Mises criterion
$\overline{\varepsilon_p}$	Von Mises effective plastic strain
k_L	Strength coefficient from the Ludwig work hardening equation
n_L	Work hardening coefficient from the Ludwig work hardening equation
C	Constant relating plane strain principle stress to uni-axial principle stress. For Von Mises criterion, is $C = \frac{\sqrt{3}}{2}$

$\bar{r}$, $\overline{R}$	Average Lankford coefficient from a weighted average of r_0, r_{45}, r_{90}
$\{d\}^e$	FEA notation for the nodal displacement (column) vector defining the nodal displacement component for "n" nodes bounding an element "e"
$[B]$	The "B" matrix which transforms the nodal displacement vector to the strain vector (assuming elastic deformation only)
{ }	Denotes a column vector
⌊ ⌋	Denotes a row vector
[ ]	Denotes a n x n matrix
$\{\varepsilon\}^e$	FEA notation for the nodal strain (column) vector defining the nodal displacement component for "n" nodes bounding an element "e"
N, N_i	Polynomial function (i.e. shape function) used to interpolate the displacement and strain field within an element "e", knowing the displacement and strain vectors, respectively
$\{u\}$	FEA notation for the displacement vector defining the nodal displacements
$\{\dot{u}\}$	FEA notation for the velocity vector defining the nodal velocities
$\{\ddot{u}\}$	FEA notation for the acceleration vector defining the nodal accelerations
$\{F\}$	Body force vector acting on all nodes
$[M]$	Mass matrix defining mass at each node

ω	Symbol for frequency in Hertz
ρ_d	Material density
c	Elastic sound wave speed in a material
$\{r^{int}\}$	Internally generated nodal forces due to the deformation resistance of the material
$\{r^{ext}\}$	External loads on a mesh, distributed to affected nodes.
$\{R(u)\}$, $\hat{R}$	Residual vector, difference between $\{r^{int}\}$ and $\{r^{ext}\}$ for a given nodal displacement vector.
du	Incremental change in the current displacement vector
$\hat{K}_T$	Tangent stiffness matrix describing the local variation in the residual vector for a given perturbation of the nodal displacement vector
$d\varepsilon_{ij}^{p}$	Plastic strain tensor
S_{ij}	Deviatoric stress tensor
$d\lambda$	The plastic multiplier (a scalar) which is a function of the plastic strain increment
$\lfloor P_\lambda \rfloor$	Plastic multiplier row matrix which is used to determine the current plastic multiplier knowing the current strain displacement increment vector
$[C_{ep}]$	The elastic-plastic constitutive matrix
[C]	The elastic modulus constitutive matrix
α_{ij}	Back stress parameter tensor used to define the current origin of the yield

	surface
$\{d\alpha\}$	Back stress vector increment
Hp	The local plastic hardening modulus from a uni-axial true stress-plastic strain curve
α	Mixed isotropic – kinematic hardening parameter used in LSDYNA MAT103. α varies from 0 (pure kinematic hardening) to 1 (pure isotropic hardening)
$BEF = \frac{S_{reverse\ yield\ stress}}{S_{forward\ flow}}$	Baushinger effect parameter, described the reduction in reverse flow stress compared to prior deformation in the opposite direction, along the same strain path.
$S_{forward\ flow\ stress}$	Flows stress in uni-axial tension at a prescribed pre-strain (i.e. 0.05)
$S_{reverse\ yield\ stress}$	Uni-axial compressive yield stress (0.2% offset) for a compression test preformed after a prescribed prestrain in tension.
$S = w^2/(Rt)$	Searle parameter which is a function of w, t, and $R=R_i$.
w	Bending specimen width

CHAPTER 1
INTRODUCTION

Net shape sheet metal forming is challenging because of the phenomenon of springback. Springback is an elastic recovery process resulting in a shape change, due to the removal of tooling forces. Springback guidelines for a variety of materials are generally available for process engineers, but they are at best, estimates for the expected springback (Eary and Reid, 1974; Frank et al., 1985). Currently, compensating for springback is a costly and often time-consuming process, consisting of trial and error. To reduce die tryout costs, and save time, recent efforts in the automotive sheet metal forming industry have been focusing on the use of finite element analysis (FEA) methods to predict springback, and to use these results for die compensation. Die compensation is an FEA technique in which the predicted springback is used to alter the original die geometry in order to design tooling capable of manufacturing near net shape stampings. Accurate springback predictions using FEA are therefore important.

A major challenge in sheet metal forming and springback FEA is the accurate modeling of material behaviors, especially for the new advanced high strength steel (AHSS) grades such as the Dual Phase (DP) steels. DP steels exhibit unique behaviors such as, high initial work hardening, good energy absorption at strain rates above 250 sec^{-1}, non-linear elasticity during springback, and pronounced Bauschinger effect. The American Iron and steel Institute (AISI) has stated that the FEA of springback in stampings of DP steels is currently not

accurate enough to be used as a production tool. Two issues have been identified that affect the accuracy of the springback FEA. The first is the accurate modeling of isotropic, mixed isotropic, and kinematic hardening behaviors. The second is that the 3D shell element fails to properly capture the forming and residual stresses, when the radius to thickness ratio (Rp/t) is small (AISI, 2006). Despite this, the 3D shell element is currently the recommended element for the FEA of forming and springback, using LSDYNA3D (Maker and Zhu, 2001).

Pure bending deformation has different kinematics, depending if bending occurs under simple (large radius) or general bending (small radius) conditions. In DP steels, the interaction of material hardening assumption with the kinematics of bending has not been studied. Further, the ability of a given element formulation to capture this interaction, as well as the effect on the accuracy of the springback from the FEA, has not been reported in the peer reviewed literature.

The objective of this thesis is to therefore examine bending and springback behaviors for two DP steels, DP780 and DP980, and to compare FEA results from separate models using 2D and 3D continuum elements, as well as 3D shells, for the blank. The behaviors of the various element formulations under simple and general bending conditions, and as a function of the hardening assumption, were therefore studied. Experiments were performed under simple bending conditions using a laboratory V-die, and for general bending using a commercial bending machine. Analytical and FEA models were both used to model the experiments, and all results were then compared. The FEA, in conjunction with the analytical

models, were used to investigate the interaction of the hardening assumption on the bending and residual stresses, as well as the effect on the accuracy of springback from the FEA.

This thesis is divided into 9 Chapters. Chapter 1 contains an introduction to the work. Chapters 2-4 review existing literature as applied to the understanding of bending and springback, as well as an overview of DP steels. Chapter 2 reviews simple and general bending theories, from which closed form solutions are shown for large radius (simple bending conditions) and small radius bending (general bending conditions) respectively. Chapter 3 is a literature review examining past and current understanding of plane strain bending and springback. In Chapter 4, general principles of non-linear FEA are reviewed.

Original work for this thesis is presented in Chapters 5-10. In Chapter 5, analytical and numerical procedures were developed that were used to model bending and springback for large radius and small radius bending. Regarding general bending, the original work in chapter 5 is in the modification of the general bending model by Tan et al., (2005) incorporating Ludwig work hardening and the pure isotropic hardening assumption. Chapter 6 describes the experimental aspects of this work. It describes the material characterization activities and aspects of the bending experiments performed. Chapter 7 outlines the development of FEA models used to model the bending and springback of the DP steels on a laboratory V-die, and a commercial bending machine. In Chapter 8, experimental, analytical and FEA results are presented and discussed, in order

to gain new insights into the bending and springback behaviors of these DP steels, and the limitations of FEA and analytical methods to predict bending stresses and springback. In Chapter 9, findings are summarized and conclusions are drawn from the work performed.

CHAPTER 2
SIMPLE AND GENERAL BENDING THEORY

2.1 Simple bending theory

In the bending of a wide sheet over a punch radius, the development of longitudinal bending stresses results in an internal bending moment. Springback is the release of the internal bending moment which manifest as a shape change. For simple bending conditions, assumptions regarding the mechanics of deformation (loading) and springback (unloading) are generally used to simplify the development of closed form solutions. These assumptions are summarized below for a wide blank bent to a given radius (Queener and De Angelis 1968; Wang, 1993; Marciniak et al., 2002).

1. Plane sections remain plane during bending.
2. The magnitude of the bending strain in a given bending fiber is proportional to the distance from the neutral axis.
3. The mid-surface is the neutral surface, and does not shift during bending.
4. There is no thinning of the sheet.
5. There are no axial or torsion forces present.
6. The bending curvature is such that the specimen conforms exactly to the bending tools used.
7. Work hardening of the blank material can be described by an analytical hardening law, and deformation theory is used to determine the final bending stresses-strains in the bent sheet.

8. The blank width to thickness ratio is sufficiently large such that transverse strains are zero (i.e., plane strain bending).
9. The blank material is isotropic and behaves according to Von Mises criterion, having the same stress strain curve in tension and compression.
10. Unloading or springack is linear elastic.

The assumptions for simple bending are generally applicable to bending conditions in which the ratio of R_m/t is greater than 4 to 5 (Wang, 1993; Marciniak et al., 2002). Under these conditions transverse (radial stresses), as well as shear stresses are negligible compared to the bending stresses. Pure bending conditions also imply the absence of torsion or axial forces. Axial tension has the effect of shifting the neutral axis towards the tooling surface.

2.1.1 Mechanics of simple bending and springback (Marciniak, 2002)

The geometry of simple bending is shown schematically in **Error! Reference source not found.**. Bending results in extension and compression of fibers above and below the neutral axis respectively. The neutral axis does not change in length and is the reference length in the determination of the through-thickness bending strain distribution. The engineering strain in fiber A'B', a distance "y" above the neutral axis is given by Eq. 1.

$$e_x = \frac{l_{A'B'} - l_{AB}}{l_{AB}} = \frac{\theta(R_m + y) - R_m\theta}{R_m\theta} = \frac{y}{R_m} \qquad \text{Eq. 1}$$

Since plane sections remain plane, the strain distribution is linear through the thickness reaching maximum tension-compression on the outside and inside fibers respectively (Eq. 2).

$$e_{\max/\min} = \frac{\pm(t/2)}{R_m} \qquad \text{Eq. 2}$$

The true bending strain is given by Eq. 3.

$$\varepsilon_x = \ln(\frac{l_{A'B'}}{l_{AB}}) = \ln(1+\frac{y}{R_m}) \qquad \text{Eq. 3}$$

The maximum-minimum true bending strains at the outermost fibers are given by Eq. 4. The true bending strain distribution is actually non-linear; however, for small ratios of y/R_m the true bending strain is linear, approximately equivalent to the engineering strain.

$$\varepsilon_{x\,\max/\min} = \pm\ln(1+\left|\frac{t/2}{R_i}\right|) \qquad \text{Eq. 4}$$

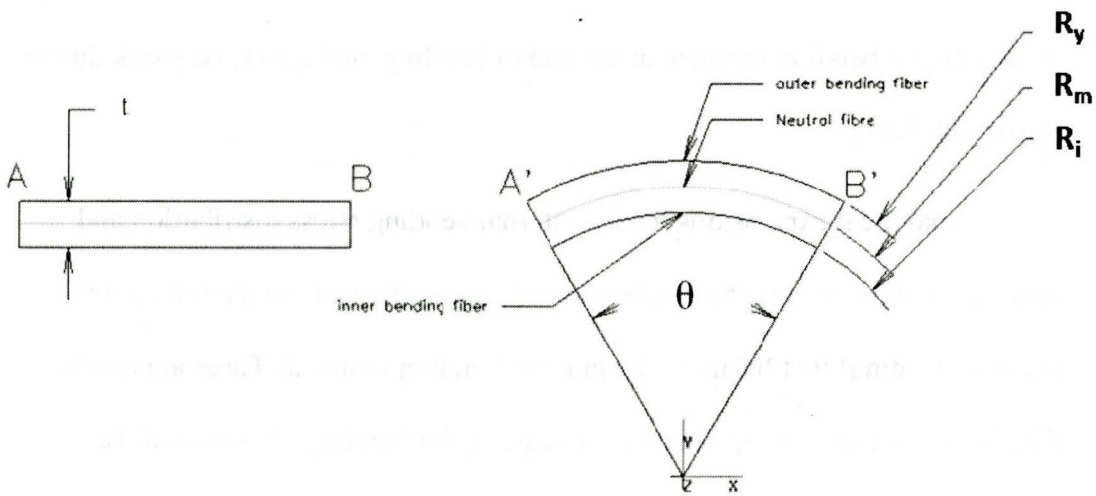

Figure 2.1 Geometry of simple bending

2.1.2 Bending stresses and work hardening

Bending stresses develop in response to bending strains. The assumption in simple bending is that the mid-surface is also the neutral surface, and that there is no net tension in the sheet. This necessarily restricts the stress distribution to be anti-symmetric about the neutral axis. This can be seen from Eq. 5.

$$\text{Tension} = \int_{-t/2}^{0} \sigma_x dx + \int_{0}^{t/2} \sigma_x dx = 0 \qquad \text{Eq. 5}$$

Bending stresses develop from the work hardening of the material during bending. In modeling work hardening, researchers have assumed analytical hardening laws such as Hollomon or Swift hardening (Queener and De Angelis, 1968; Hosford and Cadell, 1993; Wang et al., 1993; Tseng et al., 1994; Marciniak et al., 2002). The determination of bending stresses allows for the determination of the internal bending moment at the end of bending, and also springback due to elastic unloading.

Analytical expressions for the internal bending stress distribution and bending moment assume the application of a pure moment couple (i.e., pure moment bending) that balances the internal bending moment. Three approaches have been used to develop analytical equations for bending stresses and the internal bending moment. These are; plastic bending only in which the elastic portion of the hardening curve is ignored, elastic-plastic bending, and elastic-plastic bending using true strain (Queener and De Angelis, 1968; Wang et al.,

1993; Tseng et al., 1994). A comparison between the plastic and elastic-plastic bending approaches is shown in Figure 2.2.

2.1.3 Plastic bending

In plastic bending, a hardening law is assumed and the elastic portion of the work hardening curve is ignored. Work hardening in bending is also assumed to occur under a state of plane strain. For Hollomon hardening and assuming (Eq. 6), the plane strain deformation is related to the uni-axial state through Eq. 7, assuming Von Mises criterion.

$$\bar{\sigma} = k\bar{\varepsilon}^{n} \qquad \text{Eq. 6}$$

$$\sigma_1 = \left(\frac{4}{3}\right)^{1/2}\bar{\sigma},\ \varepsilon_1 = \left(\frac{3}{4}\right)^{1/2}\bar{\varepsilon} \qquad \text{Eq. 7}$$

From Eq. 7, the bending stress distribution through the thickness and the resulting internal bending moment is given by Eqs. 8 and 9 respectively.

$$\sigma_1 = \pm\left(\frac{4}{3}\right)^{(n+1)/2} k\left|\frac{y}{R_m}\right|^{n} \qquad \text{Eq. 8}$$

$$M_p = 2\int_0^{t/2}\sigma_1 y dy = 2\left(\frac{4}{3}\right)^{(n+1)/2}\frac{k}{R_m{}^{n}(n+2)}\left(\frac{t}{2}\right)^{n+2} \qquad \text{Eq. 9}$$

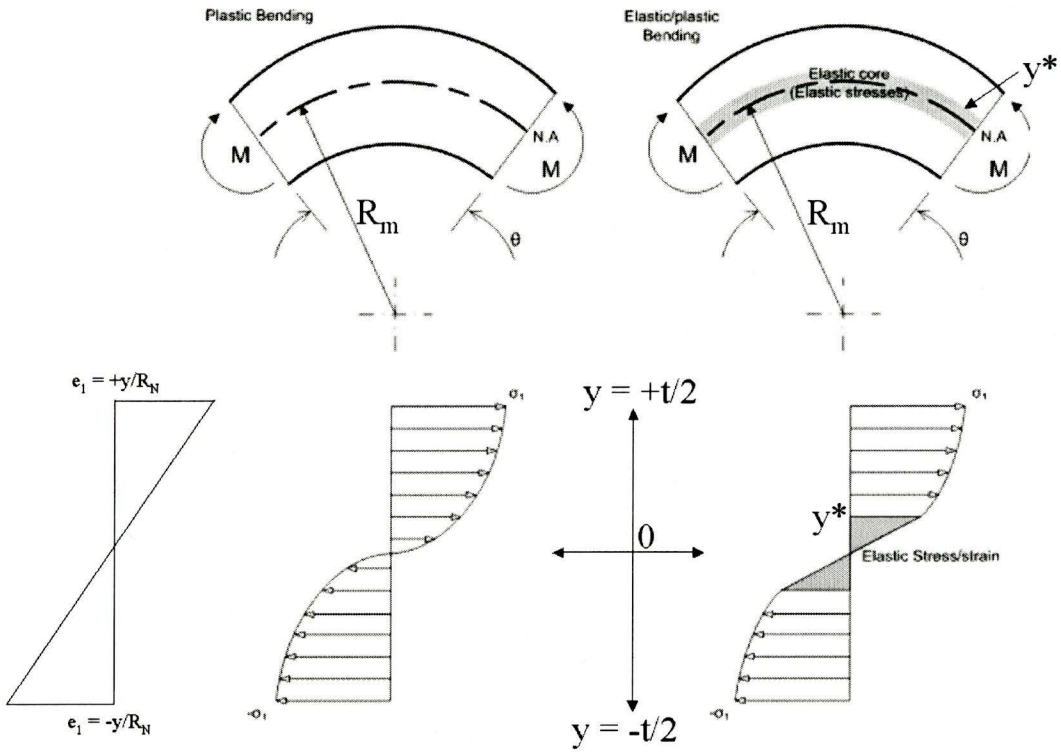

Figure 2.2 Schematic comparison of developed bending stresses assuming pure plastic bending (left) and elastic-plastic bending (right) in conjunction with an analytical hardening law such as Hollomon hardening. The bending fiber separating the elastic and plastic regions is at the position y* relative to the neutral axis. Note that $R_N = R_m$.

2.1.4 Elastic-plastic bending

In elastic-plastic bending, the total bending moment is determined by elastic and plastic regions of the work hardening curve. The elastic contribution is based solely on bending stresses less than or equal to the plane strain elastic limit for the material. In the elastic region, the bending stresses are given by Eq. 10, where y^* is the distance from neutral axis to the elastic-plastic interface (Figure 2.2), and ε_{1y} is the yield strain in plane strain. The plastic contribution is given by Eq. 8 for bending strains beyond the plane strain elastic limit.

$$\sigma_1 = \pm \frac{E}{(1-\nu^2)} \left| \frac{y^*}{R_m} \right| = \pm \frac{E}{(1-\nu^2)} \left| \varepsilon_{1y} \right| \qquad \text{Eq. 10}$$

Assuming Hollomon work hardening and Von Mises criterion, there is a discontinuity in the bending stress-strain distribution at the bending fiber corresponding to the position y* in Figure 2.2. This discontinuity arises from the difference between elastic and plastic theories, in defining the plane strain yield limit (Queener and De Angelis, 1968). This is due to the change in the Poisson's ratio from ≈ 0.3 (for steel) in the elastic region to 0.5 in the plastic region. The yield strain in uni-axial tension is given by Eq. 11. From plastic theory, the plane strain yield strain is given by Eq. 12. Using elastic theory, it is given by Eq. 13.

$$\overline{\varepsilon_y} = \left(\frac{k}{E} \right)^{1/(1-n)} \qquad \text{Eq. 11}$$

$$\varepsilon_{1y} = \left(\frac{k}{E} \right)^{1/(1-n)} \frac{\sqrt{3}}{2} \qquad \text{Eq. 12}$$

$$\varepsilon_{1y} = \left(\frac{k}{E} \right)^{1/(1-n)} \frac{(1-\nu^2)}{\sqrt{1-\nu+\nu^2}} \qquad \text{Eq. 13}$$

Plastic theory predicts a yield strain that is approximately 15% greater than elastic theory and this problem has been addressed by simply extending the elastic stress-strain distribution to the distribution given by plastic bending in Eq. 8 (Soldaat, 1985).

Assuming Hollomon hardening, the elastic and plastic components of the bending moment are given by Tseng et al., 1996, in Eqs. 14 and 15 respectively (see also Figure 2.2). The total bending moment is therefore given by Eq. 16.

$$M_e = 2\int_0^{y^*} \frac{E}{(1-\nu^2)}\varepsilon_1 y\, dy = \frac{2}{3}\frac{E}{(1-\nu^2)}(R_m)^2\varepsilon_{1y}^3 \qquad \text{Eq. 14}$$

$$M_p = 2\int_{y^*}^{t/2} \sigma_1 y dy = 2\int_{y^*}^{t/2}\left(\frac{4}{3}\right)^{(n+1)/2} k(\frac{y}{R_m})^n y dy$$
$$= 2\left(\frac{4}{3}\right)^{(n+1)/2}\frac{kR_m^2}{(n+2)}\left[\left(\frac{t/2}{R_m}\right)^{n+2} - \varepsilon_{1y}^{n+2}\right] \qquad \text{Eq. 15}$$

$$M_T = M_e + M_p \qquad \text{Eq. 16}$$

2.1.5 Elastic-plastic bending using true bending strain

At the R_m/t ratio of 4-5, the engineering strain is approximately .10-.12. At these levels, the difference between engineering strain and true strain can be significant. Wang et al., 1993, developed an expression for the maximum bending moment using the true bending strain using the Swift hardening law. If Hollomon hardening is used instead, the elastic bending moment is still given by Eq. 14, and the plastic bending moment is given by Eq. 17. As before, the total bending moment is the sum of elastic and plastic components given by Eq. 16.

$$\varepsilon_1 = \ln\left(1+\frac{y}{R_m}\right), \quad \sigma_1 = 2k\left(\frac{4}{3}\right)^{\frac{n+1}{2}}\varepsilon_1^{\,n}$$

$$M_p = 2k\left(\frac{4}{3}\right)^{\frac{n+1}{2}}\int_{y^*}^{t/2}\varepsilon_1^n y dy,$$

$$= 2k\left(\frac{4}{3}\right)^{\frac{n+1}{2}}\rho_n^2\sum_{j=0}^{\infty}\left[\frac{2^j-1}{j!(j+n+1)}\left(\left(\ln(1+\frac{t/2}{R_m})\right)^{j+n+1} - \varepsilon_{1y}^{j+n+1}\right)\right] \qquad \text{Eq. 17}$$

2.1.6 Elastic-plastic bending close to the plane strain yield limit

Previously, the equations used to determine the internal bending stresses and moments assumed that the material work hardened according to a Hollomon hardening law. Hollomon hardening does not provide a good fit to most materials at small bending strains (Marciniak et al., 2002). Sidebottom and Gebhardt (1979) showed that modeling hardening using a piece-wise linear curve from experimental tensile tests significantly increased the accuracy of the predicted springback, and therefore the internal bending moment, however, only at low bending curvatures. In light of these results, the work in this thesis also investigated piece-wise linear work hardening as applied to the experimental DP steels. Details of this method are described in Chapter 5.

2.1.7 Springback in simple bending

Springback is an elastic recovery process causing a decrease in the radius of curvature from the initial (formed) state to the final (sprung) state (Figure 2.3). The relative springback is given by $d\theta/\theta$, where $d\theta$is the change in springback angle and θ_i is the bend angle before springback. In this definition, θ_i is the angle of wrap of the blank around the punch radius as shown in Figure 2.4.

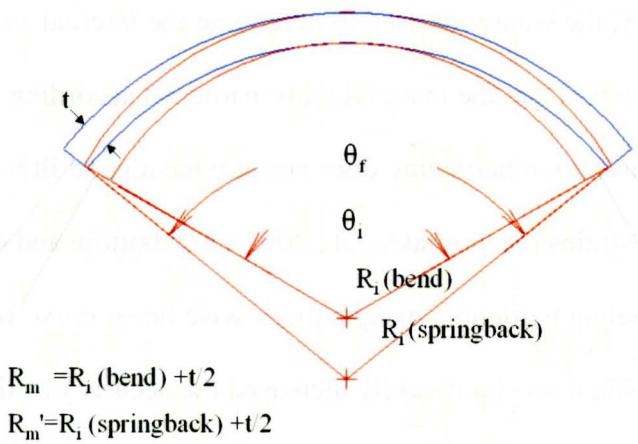

Figure 2.3 Schematic showing a decrease in curvature with springback.

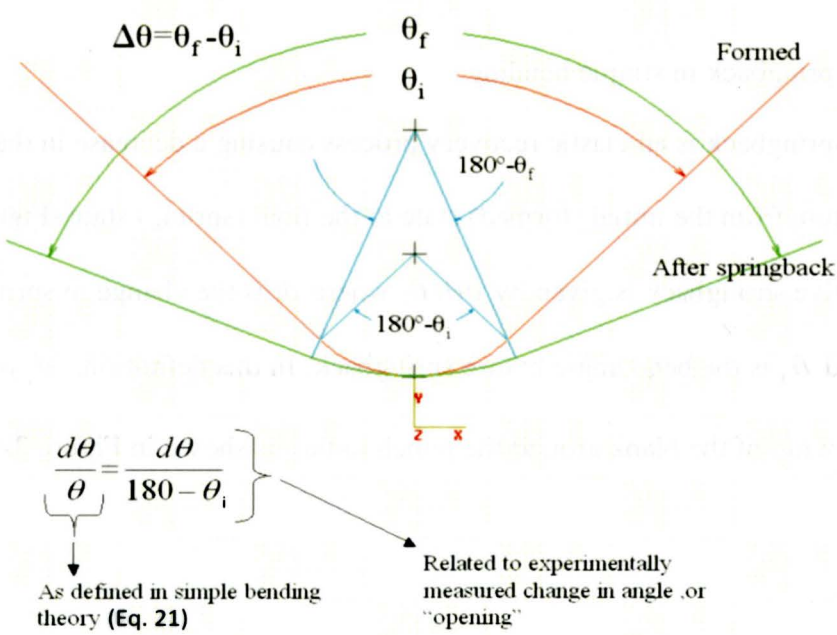

Figure 2.4 Nomenclature to describe springback in terms of the relative springback in relation to the usual experimentally measured angles.

In terms of V-die and small radius bending, the usual experimental angles before and after springback (i.e., θ_i and θ_f) are shown in Figure 2.3-2.4. The relative springback measure used in this thesis is determined from the experimentally measured angles, as shown in Figure 2.4. The advantage of this measure is that the relative springback can be directly related to the springback ratio K_s, which is the ratio of the initial bending curvature to the final bending curvature, using Eq. 19.

Analytically, springback is treated by applying an equal but opposite elastic moment to the blank, resulting in unloading to zero net bending moment. The unloading sequence is shown schematically in Figure 2.5. Springback is treated using the equations from Queener and DeAngelis (1968) in Eqs. 18-21.

$$\frac{\partial M}{\partial(1/R_m)} = \frac{2E}{3(1-\nu^2)}\left(\frac{t}{2}\right)^3 = \frac{M_t}{(1/R_m - 1/R'_m)} \qquad \text{Eq. 18}$$

$$K_s = 1 - \frac{d\theta}{\theta} = \frac{R_m}{R'_m} \qquad \text{Eq. 19}$$

$$K_s = 1 - M_t \frac{12(1-\nu^2)}{Et^3} R_m \qquad \text{Eq. 20}$$

$$\frac{d\theta}{\theta} = M_t \frac{12(1-\nu^2)}{Et^3} R_m \qquad \text{Eq. 21}$$

From the equations above, springback increases with increasing internal bending moment, bend radius, strength coefficient, and n-value. Springback also increases with decreasing Elastic modulus, and blank thickness. From Eq. 19, a

larger magnitude for K_s indicates less springback. In Eq. 21, a larger magnitude for the relative springback indicates more springback.

After springback, the bending stresses are re-distributed, due to the release of the elastic moment, with surface and near surface bending fibers undergoing a reversal of stress from tension to compression. An analytical expression for the residual stress after plastic bending as a function of position through the specimen thickness is shown in Eq. 22 , assuming Hollomon work hardening. In this equation y refers to the distance from the neutral surface to the top and bottom surfaces (y= ± t/2), where t is the blank thickness. The first and second terms on the right side of Eq. 22 represent the stress distribution at the end of bending and after elastic unloading respectively. The elastic unloading moment is equal in magnitude but opposite in sign to the bending moment in the loaded state.

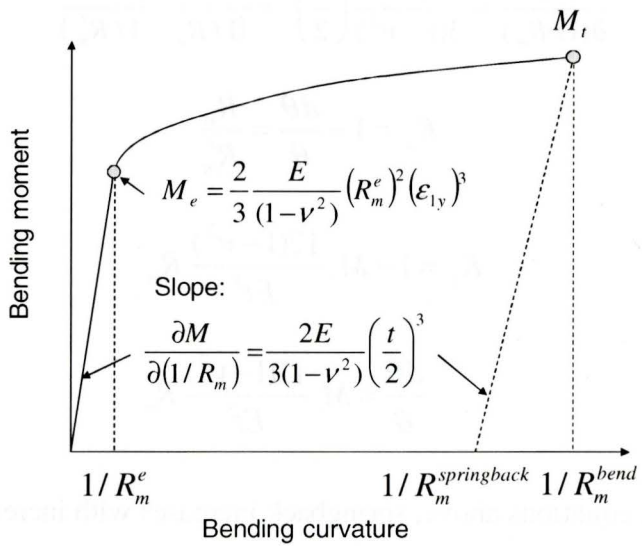

Figure 2.5 Schematic of the moment curvature relationships for bending and the unloading sequence during springback (adapted from Queener and DeAngelis 1968).

$$\sigma_{residual}(y) = \pm\left(\frac{4}{3}\right)^{\frac{n+1}{2}} k\left(\frac{|y|}{R_m}\right)^n - \left[\frac{3M_t}{2(t/2)^3}(y)\right] \qquad \text{Eq. 22}$$

2.2 General bending theory (from Tan et al., 1995)

General bending theory is used in small radius bending and the assumptions for simple bending theory do not apply. The nomenclature for general bending is shown in Figure 2.6, for the case of plane strain bending with a pure moment load. Also shown are three distinct zones through the thickness. Each zone has different deformation characteristics as bending progresses. Zone I is bounded by the unstretched surface and outer surface bending fibers. In this zone bending deformation is tensile. Zone II is bounded by the neutral surface and the surface at the inside bending radius. In this zone, bending deformation is compressive. Zone III is bounded by the unstretched surface and neutral surface fiber. This zone represents bending fibers that were prestrained in compression and undergo reverse loading into tension due to neutral axis shifting. The unstretched surface fiber is between the mid surface and neutral surface and represents the bending fiber that has a zero net strain. The predicted bending stresses in Zone III will, therefore, depend on whether or not deformation is modeled using isotropic or kinematic hardening. The application of isotropic and kinematic hardening in this bending zone will be explained further in this section.

General bending is therefore a complex forming process and different regions though the thickness experience, tension, compression, and compression –

tension deformation. There are non-linear geometric effects to consider such as neutral axis shifting towards the inside bend radius, and thinning deformation.

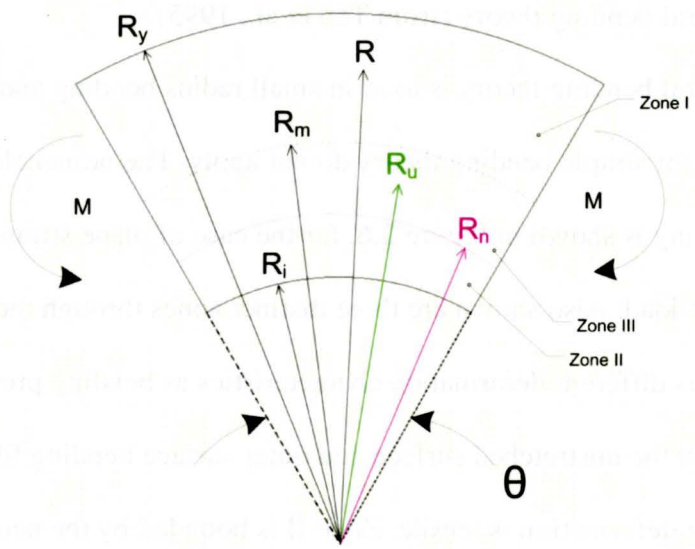

Figure 2.6 Nomenclature and deformation zones in general bending (from Tan et al., 1995).

2.2.1 Stress distribution

Using the convention from Tan et al. (1995), the principle stresses in small radius bending are designated by σ_θ in the tangential direction, σ_r in the radial direction, and σ_z in the transverse direction (z direction). The radial stress is continuous through the different thickness zones from Figure 2.6, having a value of zero at the free surfaces.

The governing differential equations for general bending can be found considering the state of equilibrium, as shown for the element in Figure 2.7. The resulting governing differential equation for general bending is then given by Eq. 23.

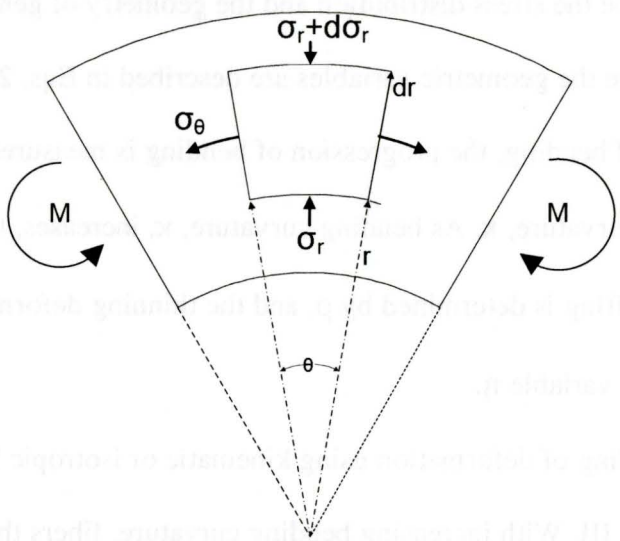

Figure 2.7 Stresses acting on a small volume element for small radius plane strain bending using a pure bending moment load.

$$r\frac{d}{dr}\sigma_r = \sigma_\theta - \sigma_r \qquad \text{Eq. 23}$$

Eq. 23 can be written as Eq. 24 (Proska 1959), to describe bending in terms of the key geometric parameters (Eqs. 25-27).

$$\frac{d\eta}{d\kappa} = -\frac{\eta}{2\kappa}\left(\frac{1-\kappa^2/4}{\eta^2\rho^2}-1\right) = -\frac{\eta}{2\kappa}\left(\frac{R_y R_i}{R_n^2}-1\right) \qquad \text{Eq. 24}$$

Relative curvature

$$\kappa = t/R_m = (R_y - R_i)/R_m \qquad \text{Eq. 25}$$

Thinning from bending

$$\eta = t/t_0 \qquad \text{Eq. 26}$$

Relative curvature of the neutral surface

$$\rho = R_n/R_u \qquad \text{Eq. 27}$$

Eqs. 23-24 describe the stress distribution and the geometry of general bending respectively, where the geometric variables are described in Eqs. 25-27. In terms of the geometry of bending, the progression of bending is measured by the relative bending curvature, κ. As bending curvature, κ, increases, the progression of neutral axis shifting is determined by ρ, and the thinning deformation is determined by the variable η.

The modeling of deformation using kinematic or isotropic hardening is important in Zone III. With increasing bending curvature, fibers that are prestrained in compression are eventually overtaken by the neutral surface and are then re-loaded in tension. For isotropic hardening, the cycle of loading and re-loading causes the yield surface to continually expand as shown in Figure 2.8. For kinematic hardening, the yield surface is translated resulting in the Baushinger affect as shown in Figure 2.9. Considering plastic deformation and Ludwig work hardening (Eq. 28), for pure isotropic hardening, the magnitude of the forward and reverse stress is equal (Eq. 29). The relationship between the forward and reverse stress under kinematic hardening is given by Eq. 30. For pure kinematic hardening, the substitution Ludwig's hardening equation for the forward stress into Eq. 30 yields Eq. 31.

$$\overline{\sigma} = \sigma_0 + k_L \left(\overline{\varepsilon}_p\right)^{n_L} \qquad \text{Eq. 28}$$

$$\left|\sigma_{forward}\right| = \left|\sigma_{reverse}\right| \qquad \text{Eq. 29}$$

$$|\sigma_{forward}| + |\sigma_{reverse}| = 2\sigma_0 \qquad \text{Eq. 30}$$

$$|\sigma_{reverse}| = |\sigma_0| - k_L(\bar{\varepsilon}_p)^{n_L} \qquad \text{Eq. 31}$$

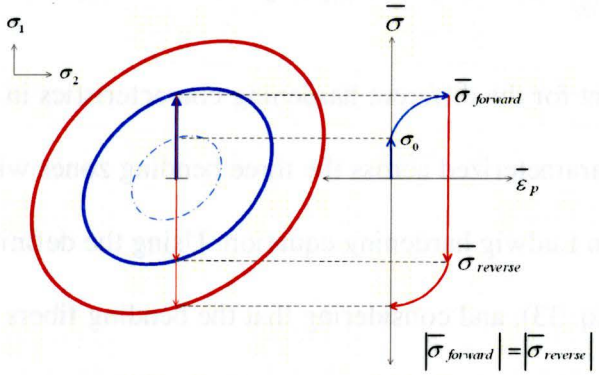

Figure 2.8 Pure isotropic hardening behavior showing expansion of the yield surface (left) with forward and reverse loading in uni-axial tension.

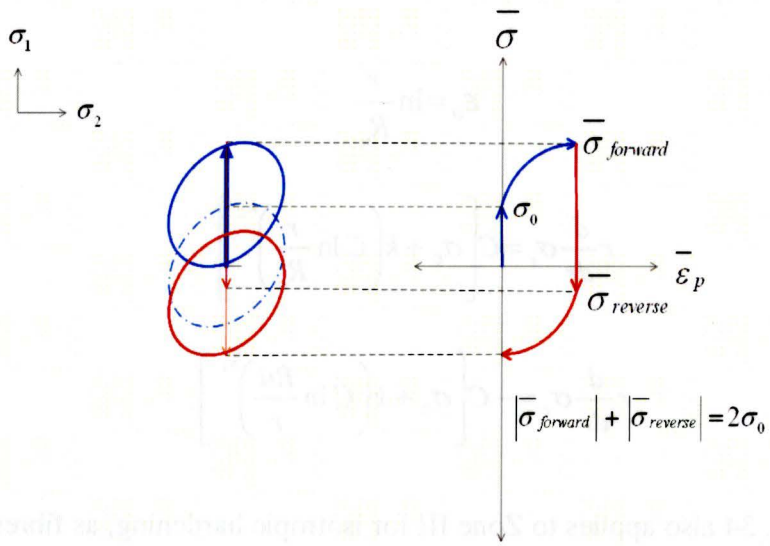

Figure 2.9 Pure kinematic hardening behavior showing translation of the yield surface (left) with forward and reverse loading in uni-axial tension.

Ludwig work hardening in the three bending zones can be incorporated into the governing differential equation for bending (Eq. 23). From the Levy-Mise

flow rule, assuming Von Mises criterion, and using ε_z=0 for plane strain bending, Eq. 23 can be written as Eq. 32 (Appendix A).

$$r\frac{d}{dr}\sigma_r = C\left[\sigma_0 + k(C\varepsilon_\theta)^{n_L}\right], \quad where \quad C = 2/\sqrt{3} \qquad \text{Eq. 32}$$

To account for the different hardening characteristics in each bending zone, Eq. 32 is parameterized across the three bending zones with different forms of the plane strain Ludwig hardening equation. Using the definition of the true bending strain (Eq. 33), and considering that the bending fibers in Zones I and II undergo tension and compression respectively, the differential equations for bending in Zones I and II, incorporating Ludwig hardening are given by Eq. 34 and Eq. 35 respectively.

$$\varepsilon_\theta = \ln\frac{r}{R_u} \qquad \text{Eq. 33}$$

$$r\frac{d}{dr}\sigma_r = C\left[\sigma_0 + k\left(C\ln\frac{r}{R_u}\right)^{n_L}\right] \qquad \text{Eq. 34}$$

$$r\frac{d}{dr}\sigma_r = -C\left[\sigma_0 + k\left(C\ln\frac{Ru}{r}\right)^{n_L}\right] \qquad \text{Eq. 35}$$

Eq. 34 also applies to Zone III for isotropic hardening, as fibres prestrained in compression are re-loaded in tension and the forward flow stress is equal in magnitude to the reverse flow stress (similar to Eq. 29). In contrast, under pure kinematic hardening, fibres that are re-loaded in tension after being prestrained in compression will have a flow stress that is less in magnitude,

compared to that for the pure isotropic hardening case. Under pure kinematic hardening, the concepts from Eq. 31 are applied, resulting in Eq. 36.

To solve for the bending stresses, Eqs. 34-36 are integrated and the boundary conditions in Eqs. 37-39 are applied. The resulting expressions for the bending stresses are given by Eqs. 40-44. The governing differential equations for general bending (Eq. 24) can be written as Eqs. 45-47. These equations can be solved numerically, yielding η, ρ as a function of κ. In determining this, the bending stresses for both pure isotropic and kinematic hardening assumptions can be found. Examples showing the calculation of the bending stresses, using MATHCAD sheets, are shown in Appendix D.

$$r\frac{d}{dr}\sigma_r = C\left[\sigma_0 - k\left(C\ln\frac{r}{R_u}\right)^{n_L}\right] \qquad \text{Eq. 36}$$

$$\sigma_r(Zone\,I)\big|_{R=Ry} = \sigma_r(Zone\,II)\big|_{R=Ri} = 0 \qquad \text{Eq. 37}$$

$$\sigma_r(Zone\,I)\big|_{R=Ru} = \sigma_r(Zone\,III)\big|_{R=Ru} \qquad \text{Eq. 38}$$

$$\sigma_r(Zone\,II)\big|_{R=Rn} = \sigma_r(Zone\,III)\big|_{R=Rn} \qquad \text{Eq. 39}$$

$$\sigma_r(Zone\,I) = -k1\left(\ln\frac{R_y}{R_u} - \ln\frac{r}{R_u}\right) - k2\left[\left(\ln\frac{R_y}{R_u}\right)^{n_L+1} - \left(\ln\frac{r}{R_u}\right)^{n_L+1}\right] \qquad \text{Eq. 40}$$

$$\sigma_r(Zone\,II) = k1\left(\ln\frac{R_u}{r} - \ln\frac{R_u}{R_i}\right) - k2\left[\left(\ln\frac{R_u}{R_i}\right)^{n_L+1} - \left(\ln\frac{R_u}{r}\right)^{n_L+1}\right] \qquad \text{Eq. 41}$$

Pure isotropic hardening

$$\sigma_r(Zone\,III) = k1\left(\ln\frac{R_n}{R_y} - \ln\frac{R_n}{r}\right) - k2\left[\left(\ln\frac{R_n}{r}\right)^{n_L+1} + \left(\ln\frac{R_y}{R_n}\right)^{n_L+1}\right] \quad \text{Eq. 42}$$

Pure kinematic hardening

$$\sigma_r(Zone\,III) = -k1\left(\ln\frac{R_y}{R_u} - \ln\frac{R_u}{r}\right) - k2\left[\left(\ln\frac{R_y}{R_u}\right)^{n_L+1} - \left(\ln\frac{R_u}{R_r}\right)^{n_L+1}\right] \quad \text{Eq. 43}$$

$$\sigma_\theta = r\frac{d}{dr}\sigma_r + \sigma_r \quad \text{Eq. 44}$$

$$\frac{d\eta}{d\kappa} = -\frac{\eta}{2\kappa}(\exp(-\Lambda) - 1) \quad \text{Eq. 45}$$

Pure isotropic hardening

$$\Lambda = \frac{k2}{k1}\left[(-2)\ln\left(\frac{1}{\rho}\right)^{n_L+1} - \ln\left(\frac{1+\kappa/2}{\eta}\right)^{n_L+1} + \ln\left(\frac{\eta}{1-\kappa/2}\right)^{n_L+1}\right] \quad \text{Eq. 46}$$

Pure kinematic hardening

$$\Lambda = \frac{k2}{k1}\left[\ln\left(\frac{1+\kappa/2}{\eta}\right)^{n_L+1} + \ln\left(\frac{\eta}{1-\kappa/2}\right)^{n_L+1}\right] \quad \text{Eq. 47}$$

$$k1 = C\sigma_0 \quad \text{Eq. 48}$$

$$k2 = \frac{k_L C^{n_L+1}}{n_L+1} \quad \text{Eq. 49}$$

A complete derivation of the differential equations is given in Appendix A, and the numerical procedure for solving them is described in Chapter 5 and Appendix B.

The solution to the general bending equations has been presented by Tan et al, (1995) for steel and aluminum. An example of their solution gives insights to the characteristics of general bending for the case of pure isotropic and pure kinematic hardening (Figure 2.10-2.11). General bending allows for neutral axis shifting, in contrast to simple bending. The bending stress distributions in Zone I

show a maximum at the surface fibres for the tensile portion of the bend. For the compression side (Zone II), the largest compressive bending stress is not at the innermost bending fibre, as it is for simple bending. The general bending model also shows increasing thinning deformation and neutral axis shifting, with increasing bending curvature. Thinning and neutral axis shifting is more pronounced for bending under pure kinematic hardening, compared to pure isotropic hardening. This is in contrast to simple bending theory in which thinning and neutral axis shifting is assumed to be negligible.

2.2.2 Bending moment and springback in general bending

The bending moment in general bending is given by Eq. 50. In this thesis springback after general bending was assumed to occur through elastic unloading of the bending fibres, similar to that in simple bending theory. An elastic unloading moment is mathematically applied to the total bending moment, as in the case shown for Eq. 22. Springback is then a function of the internal bending moment at the end of bending, and the cross- section properties, specifically thickness of the blank at the end of bending. For the general bending model presented here, material thinning, and internal bending moment at the end of bending depends on the bending curvature and hardening assumption (i.e. pure isotropic and kinematic hardening).

$$M_t = \int_{R_u}^{R_y} \sigma_\theta r dr + \int_{R_l}^{R_n} \sigma_\theta r dr + \int_{R_n}^{R_u} \sigma_\theta r dr \qquad \text{Eq. 50}$$

DP steels sheets are known to have pronounced Baushinger effect, compared to conventional steels, and the general bending behavior is therefore an important consideration in the determination of springback. Other considerations important to springback as well as work by other researchers are reviewed in Chapter 3.

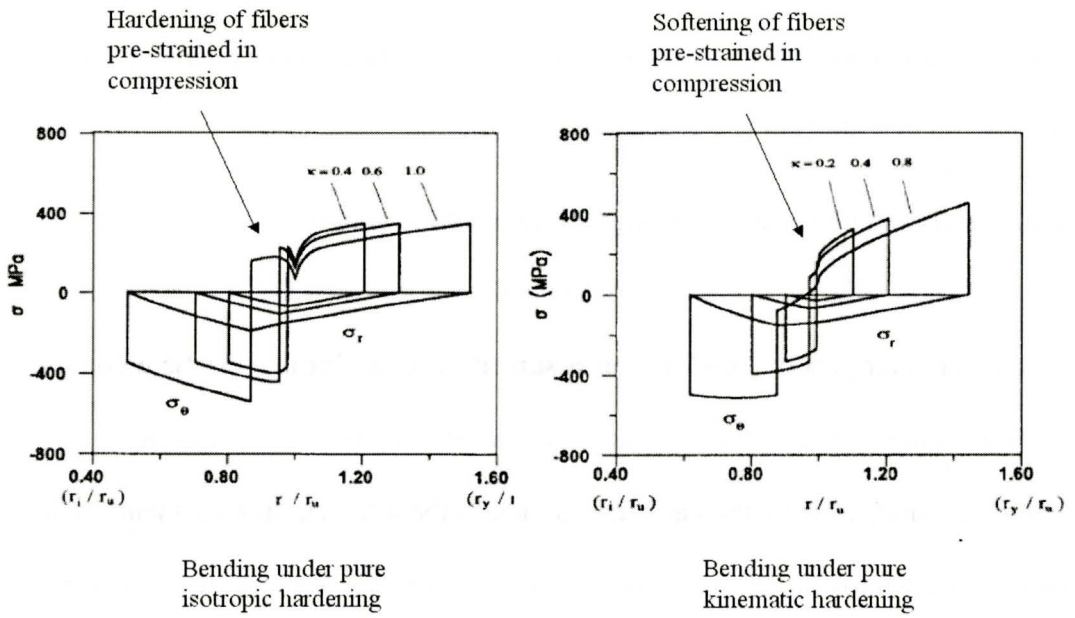

Figure 2.10 General bending under pure isotropic and kinematic hardening for an aluminum alloy (from Tan et al., 1995).

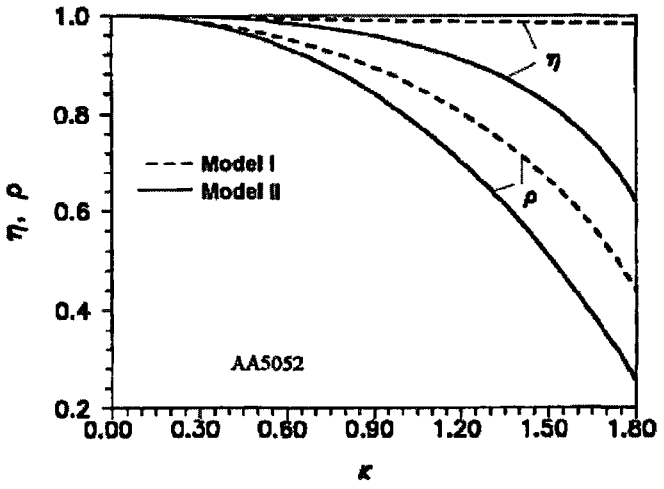

Figure 2.11 The geometry of bending (vis a vie Eq. 24) with increased bending curvature for the same aluminum alloy from Figure 2.10 (from Tan et al., 1995).

CHAPTER 3
LITERATURE REVIEW

3.1 Overview of advanced high strength steels (IISI, 2003)

Advanced high strength steels are being increasingly used in automotive applications such as automotive underbody, structural, and body panels, as a replacement for mild steel or micro-alloyed high strength low allow steels (HSLA). The motivation for the utilization of these steels is the ability to save weights because of superior energy absorption in impact events, higher tensile strength compared to traditional steel grades, and good formability. This allows material substitutions at lower thicknesses (gauge), especially between DP and HSLA steels in structural parts. A comparison of steel grades and properties in terms of tensile strength and total elongation highlights these substitution opportunities and as shown in Figure 3.1.

AHSS steel grades are classified in terms of their microstuctural composition, and on their physical behavior. In DP steels, the main microstructural constituents are ferrite phase and a varying volume fraction of martensite phase. Variations in the microstructures exist as many times intermediate complex phases such as bainite can also be present as a constituent phase. Complex phase (CP) steels have a microstructure composed primarily of ferrite and transformation products such as bainite and martensite, as well as fine precipitates that contribute to hardening. Martensitic (Mart) steels have a microstructure that is almost entirely martensite. Transformation induced plasticity steels (TRIP) have a microstructure primarily composed of ferrite,

retained meta-stable austenite and bainite. TRIP steels have unique behaviors in that the retained austenite transforms during deformation, resulting in higher work hardening at higher strain levels (compared to DP steels). The two DP steels studied in this thesis are DP780 and DP980, and are, therefore, emphasized in the sections below.

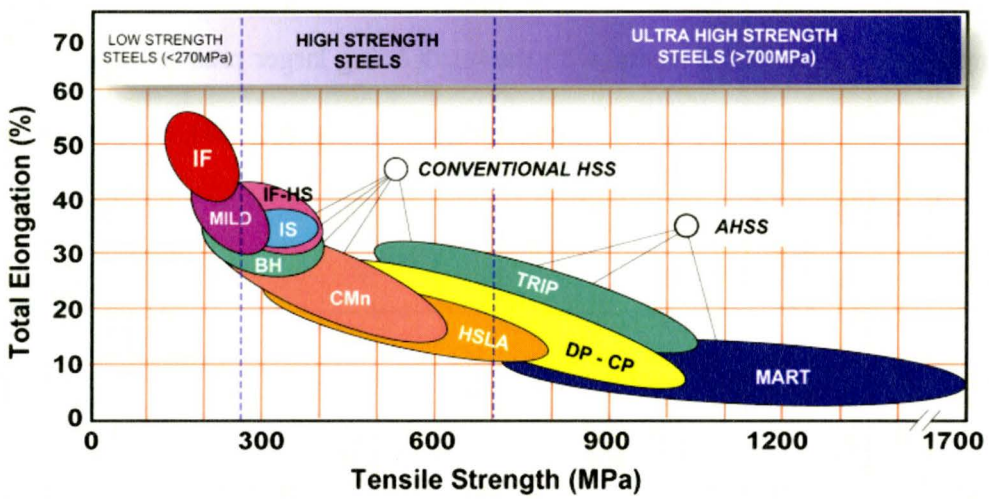

Figure 3.1 Overview of tensile properties of AHSS's in relation to other grades, showing potential material substitution opportunities (IISI, 2003)

3.1.1 Dual phase steels work hardening characteristics (IISI, 2003)

The microstructure of DP steels result in unique behaviors during forming, in terms of strength and work hardening. The control of tensile strength is determined by the volume fraction of marteniste in the ferrite matrix, with higher fraction martensite resulting in higher tensile strength. During initial deformation, strain is localized in the softer ferrite phase resulting in high initial work hardening compared to say high strength low allow (HSLA) steels. The high

initial work hardening benefits forming applications by reducing strain gradients at embossments or bends. Figure 3.2 -Figure 3.4 illustrate high initial work hardening through the instantaneous "n" values, or work hardening index from Hollomon's law. In these figures, DP800 and DP980 are compared to conventional high strength steels. The combination of high initial work hardening and high tensile strength has a significant impact on forming loads and springback compared to conventional steels, with the result being larger press tonnage requirements (Fekete, 2006) and more springback (Fekete, 2008), as shown in the example in Figure 3.5.

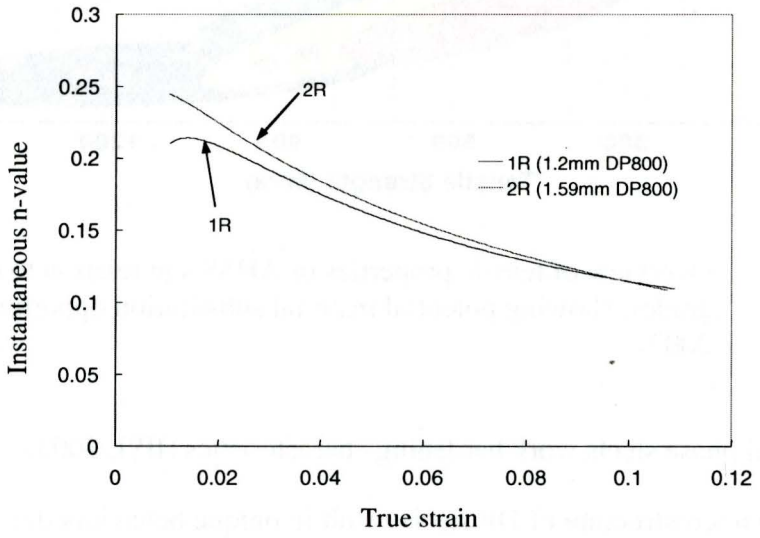

Figure 3.2 Instantaneous "n" values measured in a tensile test, according to ASTM E8, for DP800 (from Sadagopan, 2003).

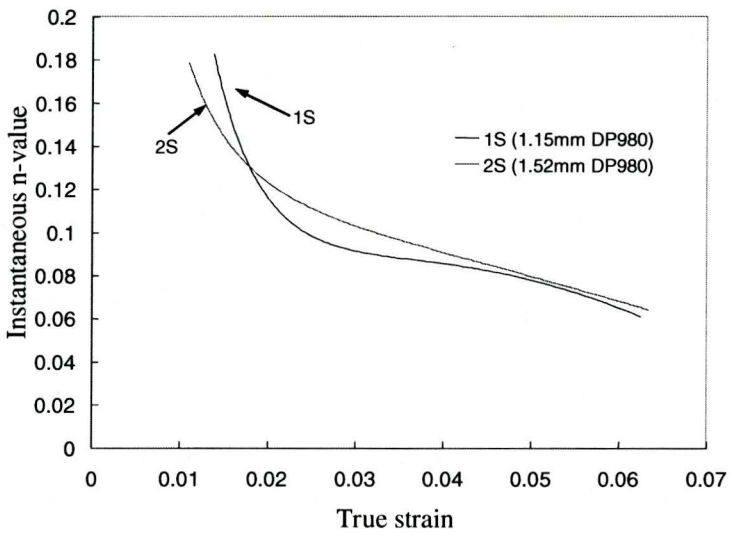

Figure 3.3 Instantaneous "n" values measured in a tensile test, according to ASTM E8, for DP980 (from Sadagopan, 2003).

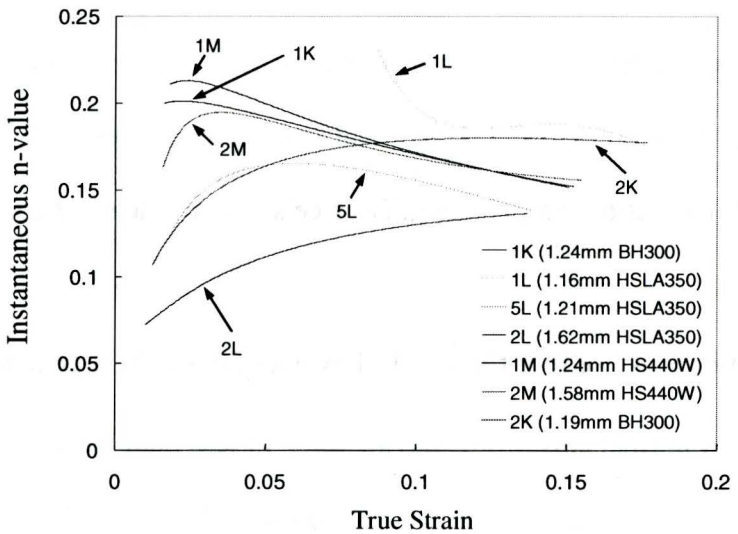

Figure 3.4 Instantaneous "n" values (measured in a tensile test using ASTM E8) for conventional high strength steels (from Sadagopan, 2003).

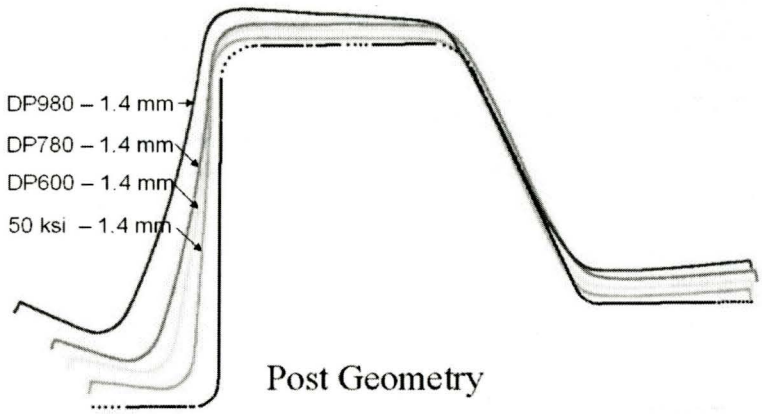

Figure 3.5 Laser scan data of a fender beam cross section showing springback as a function of steel grade strength (from Fekete, 2006).

3.1.2 Normal and planar anisotropy (AISI, 2002)

Sheet normal anisotropy is defined by the Lankford coefficient $\bar{r}$, which is the ratio of average in-plane strain to the thickness strain (Eq. 51 and Figure 3.6). For $\bar{r}$ greater than 1, deformation in the plane is preferred over the thickness direction, and therefore benefits sheet metal forming processes such as cup drawing, hole expansion, and bending. DP steels, are for the most part, considered to be planar isotropic and therefore are typically assumed to have a $\bar{r}$ value of 1. This assumption was used for this thesis, however DP steels in general do show a small degree of normal anisotropy, having an $\bar{r}$ of less than 1 (Figure 3.7). Normal anisotropy is important for describing the yield surface for the material. For a $\bar{r}$ value of 1, deformation can be described using Von Mises criterion.

$$r_0 = \frac{d\varepsilon_y}{d\varepsilon_z},\ r_{45} = \frac{d\varepsilon_{xy}}{d\varepsilon_z},\ r_{90} = \frac{d\varepsilon_x}{d\varepsilon_z},\ \bar{r} = \frac{r_0 + 2r_{45} + r_{90}}{4} \quad \text{Eq. 51}$$

3.1.3 Strain rate sensitivity

Stamping processes typically have a nominal strain rate of 10/s. DP steels have positive strain rate sensitivity, and in the typical stamping processes, the expected change in yield and tensile stress due to strain rate sensitivity is approximately 16-20 MPa (Figures 3.8-3.9). The strain rate sensitivity for DP steels is similar to that of conventional steels under medium strain rates of 10^{-3} to 10^{1}/s (Sadagopan, 2003).

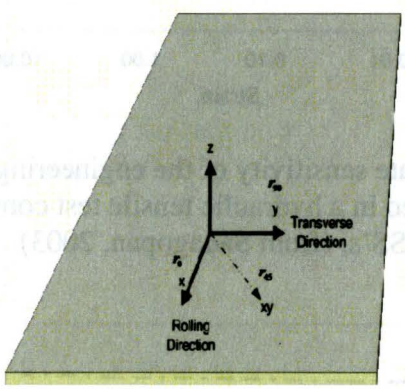

Figure 3.6 Sheet steel showing principle directions used to define r_0, r_{45}, and r_{90}.

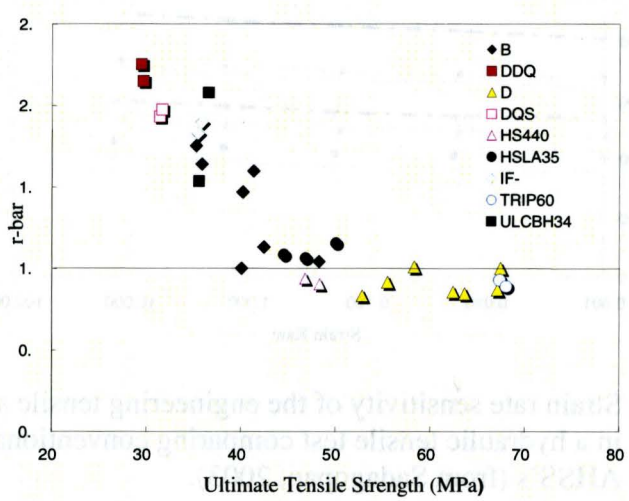

Figure 3.7 Normal anisotropy ($\overline{R}$) compared for conventional steels and AHSS's (from Sadagopan, 2003).

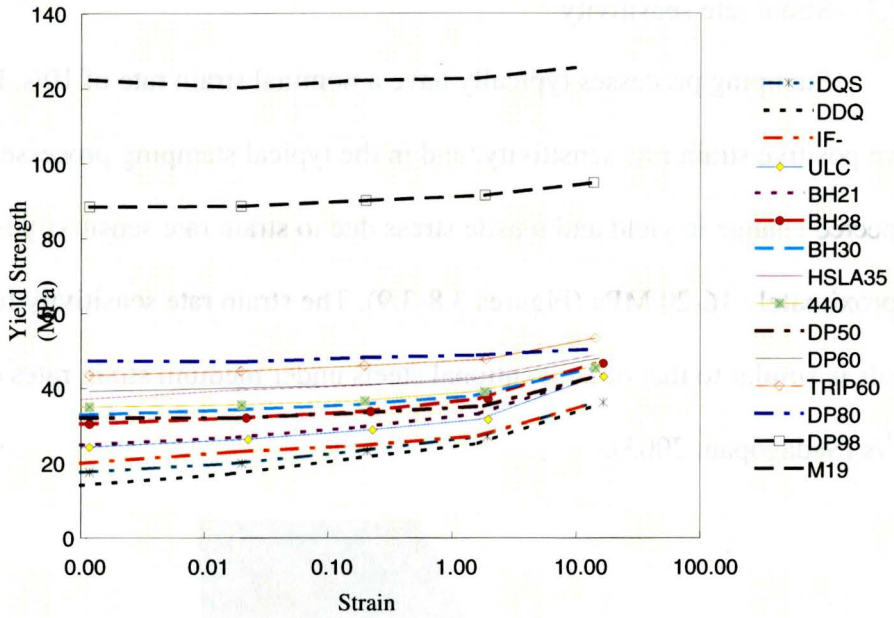

Figure 3.8 Strain rate sensitivity of the engineering yield stress (0.2% offset) measured in a hydraulic tensile test comparing conventional steels and AHSS's. (from Sadagopan, 2003)

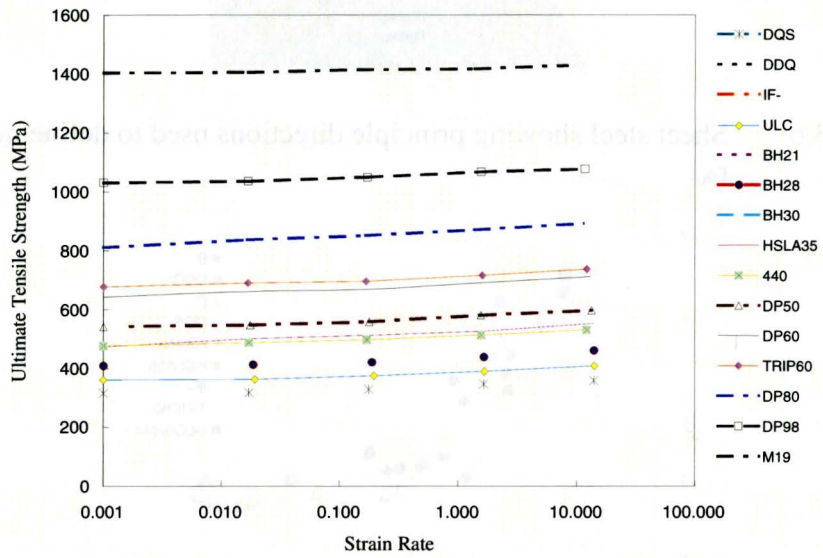

Figure 3.9 Strain rate sensitivity of the engineering tensile strength measured in a hydraulic tensile test comparing conventional steels and AHSS's (from Sadagopan, 2003).

3.1.4 Bauschinger effect

The Bauschinger effect manifests as a reduction in the flow stress due to prior deformation in the opposite direction. The AISI (American Iron and Steel Institute) has quantified Baushinger effect in terms of a Bauschinger effect parameter (BEF) (Sadagopan 2003). In this method uni-axial tension-compression tests are used in which the forward flow stress is compared to the reverse yield stress as measured using the 0.2% offset method (shown in Figure 3.10, and Eq. 52). Note that in Figure 3.10, the authors have re-plotted the compressive stage in order to better illustrate the differences between the forward flow stress and the reverse flow stress.

$$BEF = \frac{S_{reverse\ yield\ stress}}{S_{forward\ flow}} \qquad \text{Eq. 52}$$

From Eq. 52, a smaller value of BEF parameter implies larger Baushinger effect and DP steels generally show larger Baushinger effect, compared to conventional steels (Figure 3.11). The BEF is linear with material strength for most steels, however, the DP800 and DP980 steels, deviate from this linear behavior showing the largest degree of Bauschinger effect. These results highlight the importance of this material behavior, for the steels studied in this thesis. The BEF parameter is also dependent on the prestrain in the forward (tensile) direction, and saturates to a constant value, in this case between 2-5% prestrain. Figure 3.12 shows the BEF parameter as a function of strain in the forward flow direction for DP800, and DP980 steels.

Baushinger effect plays a significant role in springback. Springback is an unloading processes resulting from the removal of tooling forces from the stamping, causing a shape change in the part. Steels with larger Baushinger effect (or smaller BEF parameter) may potentially show more springback from larger recovery strains, compared to equivalent steels with smaller Baushinger effect (Figure 3.13).

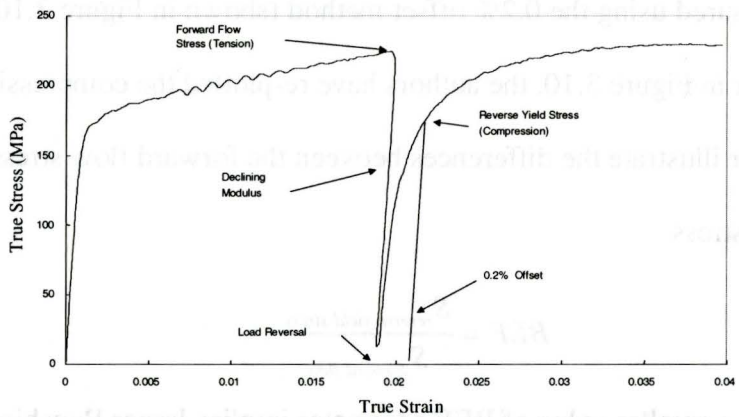

Figure 3.10 Bauschinger effect resulting from uni-axial (forward) tension, followed by uni-axial (reverse flow) compression (from Sadagopan, 2003)

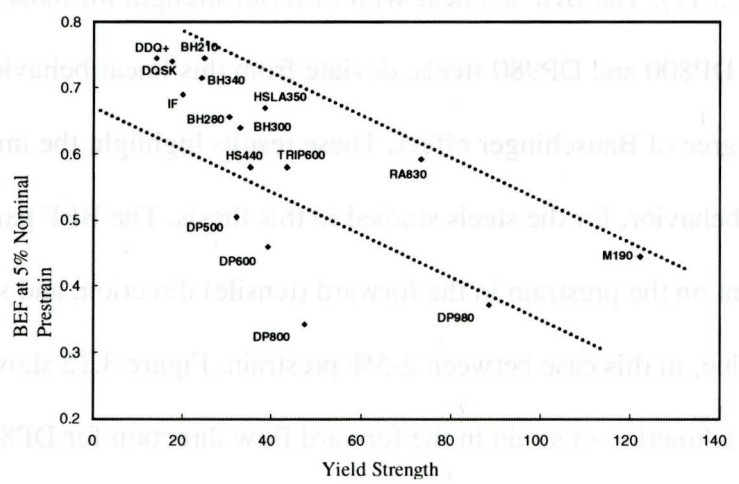

Figure 3.11 Bauschinger effect factor (BEF) for a wide range of steel grades at a prestrain of 5% (from Sadagopan, 2003).

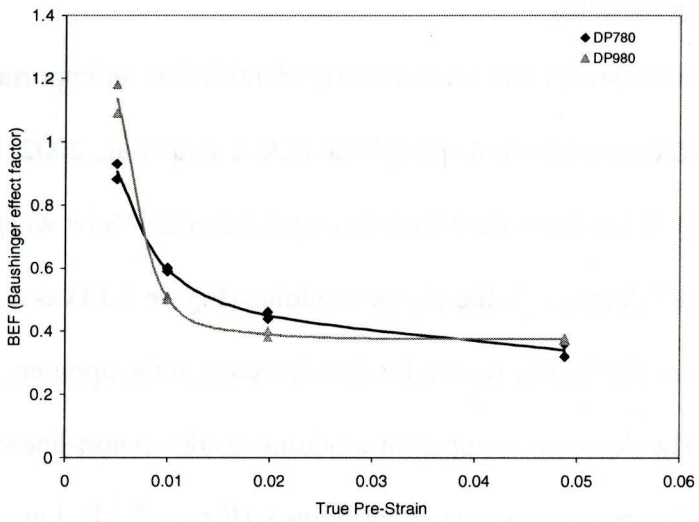

Figure 3.12 Bauschinger effect factor (BEF) as a function of forward prestrain comparing DP800 and DP980 (from Sadagopan, 2003).

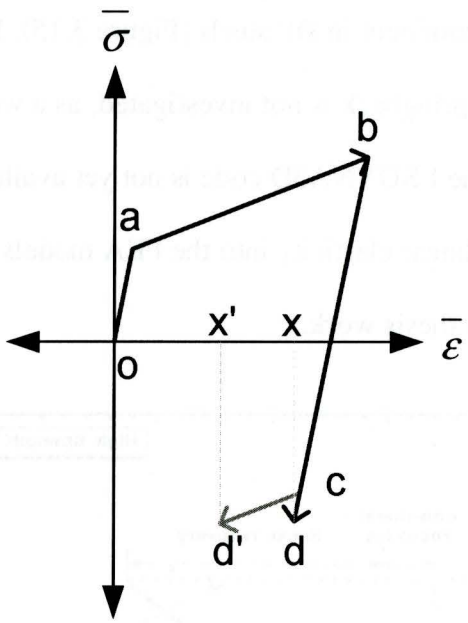

Figure 3.13 Schematic showing loading (oab) and linear unloading (bcd) resulting in recovery strain – x. Compared is non-linear unloading (bcd') due to Baushinger effect, resulting in greater recovery strain – x'.

3.1.5 Unloading modulus

Non-linear elasticity has been recently identified as an important consideration in the simulation of springback (Cleveland et al., 2002; Levy et al., 2006; Zhu, 2005). It has been identified that steel materials show what is referred to as an "apparent" decrease in the elastic modulus (Figure 3.14) as a function of prior strain (Figure 3.15). The reason for this decrease in the apparent modulus is not yet known. The decrease in apparent modulus results in non-linear unloading behavior and higher recovery strain in springback (Figure 3.14). Levy et al. (2006), has shown that the decrease in the apparent modulus is a function of prestrain, and is more prominent in DP steels (Figure 3.15). In this thesis, non-linear elasticity during springback is not investigated, as a working commercial material model within the LSDYNA3D code is not yet available. Further, the implementation of non-linear elasticity into the FEA models used in this thesis is beyond the scope of this thesis work.

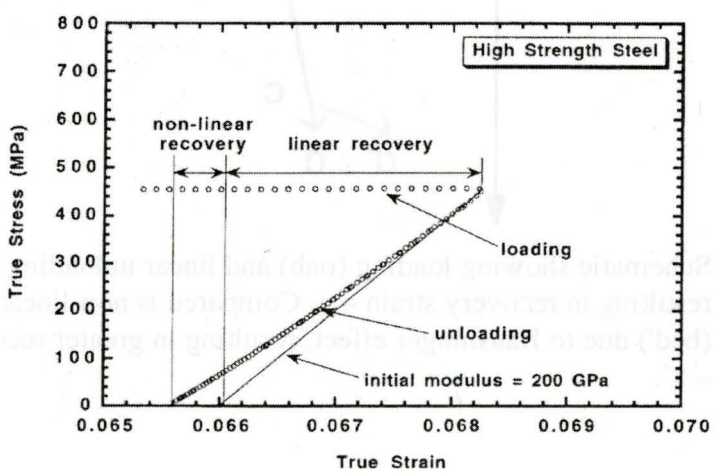

Figure 3.14 Experimentally observed non-linear unloading compared to assumed linear unloading (from Cleveland et al., 2002).

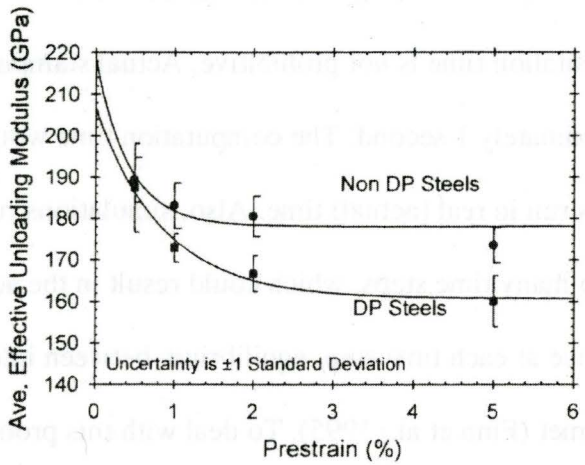

Figure 3.15 Effective unloading modulus for dual phase (DP) and conventional steels as a function of prestrain (from Levy et. al., 2006).

3.2 FEA modeling of sheet metal forming and springback using shell Elements

Towards the late 1980's the explicit-dynamic FEA (finite element analysis) method, using the shell element formulation, emerged as a numerical method applied to commercial sheet metal forming problems. Explicit dynamic codes have found wide use because of the ability to provide good solutions for problems involving contact, large degrees of freedom, and also large deformations, translations, and rotations (Finn et al., 1995). The current state of the art is to simulate forming and springback in two separate stages. The forming stage is simulated using the explicit dynamic codes (such as LSDYNA3D) and the springback stage is simulated using a static implicit code (such as LSDYNA3D Implicit). Historically, springback was simulated using the dynamic relaxation technique, using a dynamic explicit code, and today, this technique is not commonly used (Maker and Zhu, 2001).

In industrial explicit forming simulations, the simulation time is scaled so that the total computation time is not prohibitive. Actual stamping processes are in the order of approximately 1 second. The computation time would be prohibitive if a simulation was run in real (actual) time. Also, simulations run in real time would result in too many time steps, which could result in the accumulation of numerical error since at each time step, equilibrium between internal and external forces is not truly met (Finn et al., 1995). To deal with this problem, a number of techniques are used. First, the punch velocity is scaled upward, for example, a typical punch velocity would have a peak value of 2 m /sec. Also, mass scaling is selectively applied to the smallest elements to maintain a minimum acceptable time step according to the courant conditions as will be explained later in Chapter 4. Scaling the velocity or time step unfortunately creates excessive dynamic effects in the simulation, which in turn can alter forming stresses or create areas showing artificial plasticity. These effects degrade the quality of the predicted stress distribution within the part at the end of forming and are therefore detrimental to the quality and accuracy of the springback simulation (Galbraith, 1998). As a quality check in an explicit simulation, it is assumed that quasi-static conditions are achieved if the kinetic energy of the part is less than 5% of its internal energy (Galbraith, 1998). Guidelines have also been established by LSTC (Livermore Software technology Corporation) that account for the combined effect of mass scaling in combination with velocity scaling on the time step in the simulations. The effect of mass scaling and punch velocity scaling should be such

that the number of cycles per mm of deformation (or punch displacement) is in the area of 500-1000, where 1 cycle represent one time step calculation in the FE differential equations. To properly capture the deformation history, more cycles are required for deformation that changes rapidly, and less is required for a gradual forming process (Maker and Zhu, 2001).

Over a period of 20 years a high level of confidence has been established for FEA to predict strains, thickness and wrinkling in sheet metal stamping processes. The prediction of springback still remains a challenge (Du et al., 2007). Typically, FEA of springback under predict actual springback, and the reported accuracies are in the order of 70% or better (i.e. predicting 70% of the actual springback) (Maker and Zhu, 2001). Efforts by the sheet metal forming simulation community have therefore been focused on improving the accuracy and reliability of springback FEA. The approaches taken by researches have been in two key areas; the first is examining the effects of numerical parameters in the forming simulations, and more recently, incorporating more complex material behaviors.

3.2.1 FEA parameters and their effect on the predicted springback

Earlier studies suggest that certain key variables in the forming simulations that influence the accuracy of springback simulations. For example, higher punch velocity, increased mass scaling, large element sizes (in areas of the part with high curvature), and fewer though-thickness integration points, all have been demonstrated to degrade the accuracy of springback simulations (Du et al., 2001; Yao et al., 2002; Du et al., 2004; Chen et al., 2005).

The required number of through-thickness integration points for the 3D shell element used in the FEA, has been a subject of study over the last few years (Li et al., 2002; Xu et al., 2004; Wagoner et al., 2007). The integration points capture the stress distribution though the thickness and therefore in springback FEA, affect shape changes such as wall curl. Xu et al., (2004) performed FEA simulations of forming and springback for the Numisheet 93 benchmark hat channel part using a high strength steel. The FEA simulations used the explicit technique for forming and the explicit dynamic relaxation technique to calculate springback. They put forth a number of recommendations with respect to improving the accuracy of the FEA. For example, they recommended that the punch velocity should be less than 1 m/sec, mesh resolution should be sufficient to ensure that 5 elements are around each corner radius, and that 7 integration points through thickness of the shell element should be used. They also found that too many or too few integration points created error in the predicted springback. Li et al., (2002) demonstrated that for coupled forming and springback simulations, the predicted springback magnitude oscillates depending on the number of integration points used. The oscillation is due to sampling of the through thickness stress distributions using fixed integration point schemes and they argued that their findings may explain the results by Xu et al., (2004). Li et al. also argued that 25-56 integration points are required for accurate springback FEA. In response to Li's work, Zeng et. al., (2006) performed a numerical analysis and demonstrated that 5-9 integrations points is sufficient. Previously,

Zeng et al., (2006) shared their results with the Li and Wagoner prior to the publication of their paper (Wagoner et al., 2007). In the 2007 paper, Wagoner and Li performed a numerical analysis using a simple beam problem bent under tension. By comparing the analytical (closed form) solution for the bending moment, to that determined using numerical integration (both Gaussian and Simpson's integration) they were able to quantify the error when using numerical integration. Their results showed that for a given number of integration points through the thickness, the error increases with decreasing R_m/t, and increasing tension. The error also depends on the shape of material hardening curves. They presented the concept of an assured limit for sufficient integration points through the thickness. This limit assures a given error in the numerical calculation of the bending moment. For example, for an IF steel from their study bent to R_m/t of 5, the assured limit of 26 Gaussian integration points through the thickness was necessary to have a maximum error of 5% between the numerical and analytical bending moment. In general, more integration points were required using Simpson's rule. Wagoner et. al., (2007) softened his recommending of 26-56 through thickness integration points, and instead recommended that the use of 3-9 integration points should be critically examined for the given forming process simulated. Currently, the correct number of through thickness integration points is still a topic of research.

In industrial sheet metal forming and springback simulations, Coulomb friction is conventionally used, and typical values of the coefficient of friction are

from 0.10 to 0.20. The effect of friction on springback is usually part and process specific. For some parts, the effect on friction can be small (De Souza et al., 2007). In other parts, friction affects springback through the interaction with the blank holder force (BHF), creating more membrane tension during forming (Samual, 2000). Springback in parts with large BHF and large surface areas of contact between the tooling and blank, are therefore affected more. For example, Lim et al., (2006) demonstrated using the Numisheet2006 benchmark II part (a high strength steel cross member), that springback was particularly sensitive to the coefficient of friction.

The contact penalty stiffness factor is another factor that can affect springback results. In LSDYNA3D, contact in sheet metal forming FEA is typically modeled using a penalty method in which a restoring force is applied to penetrating nodes in the blank, preventing them from penetrating into the tooling surface mesh (Maker and Zhu, 2001). The contact penalty stiffness factor within the code ultimately controls the magnitude of this restoring force. For sheet metal forming FEA, a contact stiffness of 0.01 to 0.1 is generally recommended (Maker and Zhu, 2001). Excessive penetration of the blank nodes into the tooling surface results from a contact interface with low contact stiffness. If the penetration is severe, it can create a condition in which the final formed part geometry does not reflect the actual tooling geometry. A large contact stiffness factor can lead to contact instabilities and more often large restoring forces for penetrating nodes that in turn can create numerical stress artifacts. This can affect the accuracy of

the springback simulation. Parametric studies by Lee et al., (1998) demonstrated that for a hat channel part, the effect of contact penalty stiffness in the range from 0.01 to 0.1, on springback accuracy was small, when compared to the effect of element size. Du et al. (2001) showed similar results.

3.3 Material modeling

3.3.1 Yielding

Accurate springback predictions require accurate stress predictions. The use of appropriate yield criterion is therefore critical. Hills 1948 yield function is probably the most popular criterion applied to sheet metal forming simulations for steel materials (Wagoner and Chenot, 1996; Barlat et al., 1997; Mattiasson et al., 2007). Mattiasson et al., (2007) proposed several possibilities for its popularity such as; simplicity in implementation, numerical efficiency, and general lack of awareness among industrial FEA analysts regarding the effect of yield criterion choice on the FEA results.

This section focuses mainly on material modeling and yielding of steel sheets which is commonly modeled using Hill's 1948 quadratic yield surface. It is well known that this yield surface fails to describe yielding in other materials such as aluminum (Barlat et al., 1997). Regarding steel materials, Kuwabara et al., (2007) published a review of their experimental work in which anisotropic plastic behavior of various metals were studied using a specially designed cruciform specimen to achieve different load paths under bi-axial tension. Tests were performed for various load paths in which the stress ratio was varied (σ_x σ_y, x,y

coincide with the sheet rolling and transverse direction respectively, Figure 3.6). They argued that the flow stress evolution over a specific range of plastic deformation was more important in understanding deformation and anisotropy, than the initial yield surface. They produced so called "contours of equivalent work in stress space" for various metals. This representation is the locus of stress pairs having equivalent plastic work to that from the uni-axial tensile test in the rolling direction. They also compared the evolution of these stress contours, with various yield criterion for initial yielding, including that of Von Mises (Eq. 53), Hosford's 1979 criterion with exponent M=6 recommended for bcc materials (Eq. 54), and Hill's 1948 planar anisotropic criterion (Eq. 55).

$$\sigma_0^2 = \sigma_x^2 + \sigma_y^2 + (\sigma_x - \sigma_y)^2 \qquad \text{Eq. 53}$$

$$\sigma_0^M = \frac{r_{90}\sigma_x^M + r_0\sigma_y^M + r_{90}r_0(\sigma_x - \sigma_y)^M}{r_{90}(1+r_0)} \qquad \text{Eq. 54}$$

$$\sigma_0^2 = \frac{r_{90}\sigma_x^2 + r_0\sigma_y^2 + r_{90}r_0(\sigma_x - \sigma_y)^2}{r_{90}(1+r_0)} \qquad \text{Eq. 55}$$

Figure 3.16 shows the results from Kuwabara et al. (2007) for an IF steel. For a uni-axial tension of plastic 0.002, the contours of equivalent work are essentially equal to the initial yield surface of the material. In this case, the initial yielding of the IF steel is close to Von Mises criterion. With increasing work, the evolution of the stress contours shows preferential hardening in the bi-axial load path, and the experimental results are close to Hosford's yield criterion. Hill's

1948 yield criterion overpredicted hardening. The authors proposed that the differential hardening observed was probably due to crystallographic texture. Hosford (1998) also showed experimental evidence that supported the argument that a non-quadratic form of the yield surface is superior to the quadratic form (i.e. Hill's 1948 criterion). Kuwabara's results for DP590 steel are also shown in Figure 3.17. In this case, hardening in the equal-biaxial load path is not as prominent as in the IF steel from Figure 3.16, and both the Hosford and Von Mises criterion showed better agreement to the experimental data, when compared to Hill's 1948 criterion. This is apparent under plane strain deformation.

Previously, Kuwabara et al., (2004) performed plane strain tension tests on a high strength IF steel and found that Hill's 1948 criterion overpredicts hardening for the entire plastic strain range tested. In contrast to this, Von Mises and Hosford's criterion were close to the experimental points up to a plastic strain of approximately 0.015. Beyond this strain, both Von Mise's and Hosford's criterion predicted hardening that was slightly below the experimental curves. The effect of yield criterion on the predicted springback was also examined. Bending under tension experiments were performed for the same high strength IF steel, and the results were then compared to FEA analysis for various yield criterion (Figure 3.19). The author's results showed that the FEA analysis using Hill's criterion overpredicted springback to a large degree, whereas Von Mises and Hosford's criterion showed better agreement with the experiments (but slightly underpredicting springback (Figure 3.20)). Kuwabara's work points to the

inadequacy of Hill's 1948 criterion, specifically for the case in which the $\overline{R}$ >1.0. There is little or no published information regarding the appropriate yield criterion for DP steels.

Gomes et al., (2005), performed FEA forming and springback simulations for a hat channel part using a high strength steel, but did not specify if it was a DP or conventional steel. They examined the effect of different yield criterion such as, Von Mises, Hill's 1948 transversely anisotropic, and the Barlet-Lian 3-parameter planar anisotropic criterion (Barlet et al., 1997). They demonstrated that the FEA of the planar isotropic models did not agree with the experiments, specifically, in predicting differences in springback with respect to different orientations to the rolling direction. The Barlet and Lain model, however, was able to predict these differences and overall showed better agreement with the experiments. Geng et al., (2002) investigated 6000 series aluminum and HSLA steels. They used draw bend tests and simulations to show that the predicted springback is dependent on material planar anisotropy. They argued that planar anisotropy affects anticlastic curvature through the second principle stress, which in turn affects the predicted springback. This effect, however, was more dominant at high in-plane tension forces. Delanney et al. (2003) performed tests as well as FEA for of simple bending experiments using textured aluminum. They found that the FEA in general underpredicted springback. The aluminum sheet itself was not strongly planar anisotropic, and no significant differences in the springback with respect to the sheet orientation were found in the experiments and FEA. Leu

(1997) derived springback equations for simple bending using Hill's normal anisotropic yield criterion, and demonstrated that the predicted springback increases linearly with increasing value of $\bar{r}$. His work did not consider the dependence of anticlastic curvature and springback discussed previously. Papeleux et al., (2002) performed FEA of the Numisheet 2002 U- channel benchmark for high strength steel (but did not specify if it was a DP grade) and found that including planar anisotropy (using Hill's 1948 yield criterion) improved the predicted springback accuracy. Alves et al. (2004) performed forming and springback FEA for the Numisheet 2002 unconstrained bending problem using an aluminum alloy. They found that a non-quadratic planar anisotropy yield criterion resulted in better agreement between the experiments and FEA.

In general the literature of peer reviewed journals provides little information regarding the appropriate yield criterion for DP steel. The use of Von Mises criterion has provided reasonably good agreement between experiments and FEA, for example, the case studied by Du et al, (2007) for a part manufactured using DP600 steel sheet. At present there are no published experimental yield surfaces for DP780 and DP980 which are the focus of this thesis. Von Mises criterion is a reasonable compromise and generally describes yielding in low carbon steels as shown in Figure 3.21. Further, Von Mises criterion is also closer to Hosford's non-quadratic yield criterion under plane strain deformation (Figure 3.18).

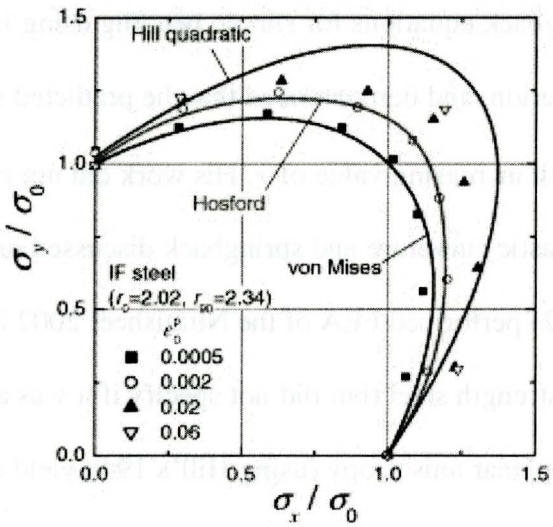

Figure 3.16 Experimental contours of equivalent plastic work for an IF steel showing the evolution of the curves with increasing plastic work (equivalent to the given uniaxial prestrain). Experimental points are compared to Hill's 1948 quadratic (planar anisotropic) and Hosford's (1979) yield criterion with exponent M=6 (from Kuwabara et al., 2004).

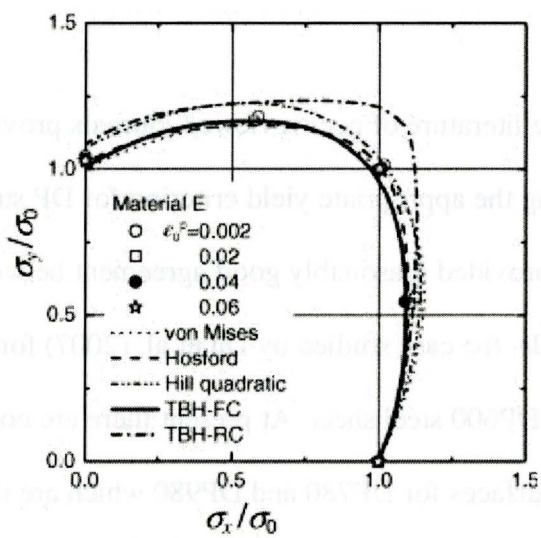

Figure 3.17 Experimental Contours of equivalent plastic work for a DP590 (r_0=0.82, r_{45}=r_{90}=1.08) steel showing the evolution of the curves with increasing plastic work (equivalent to the given plastic strain, ε_0^P). Experimental points are compared to Hill's 1948 quadratic (planar anisotropic) and Hosford's (1979) yield criterion with exponent M=6 (from Kuwabara et al., 2007).

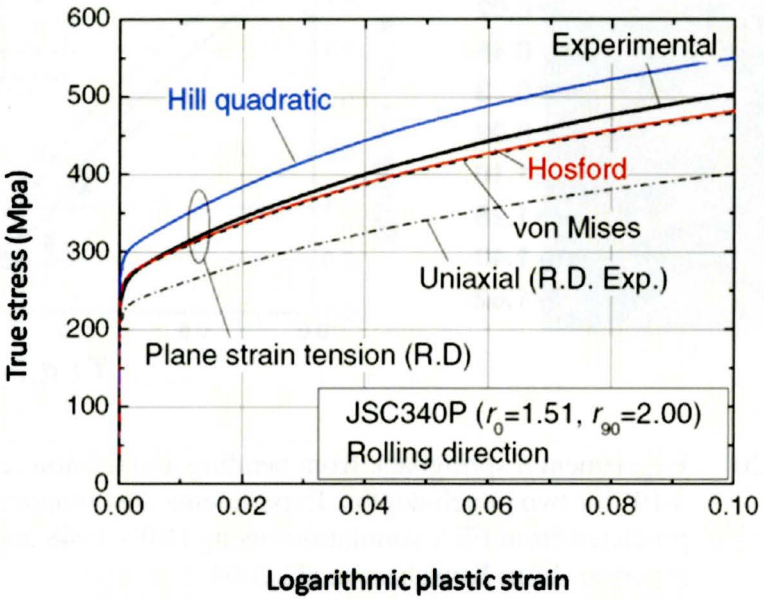

Figure 3.18 Plane strain tension test for a high strength IF steel, comparing experimental to predicted curves using various yield criterion, including Hosford's criterion with exponent M=6 (from Kuwabara et al., 2004).

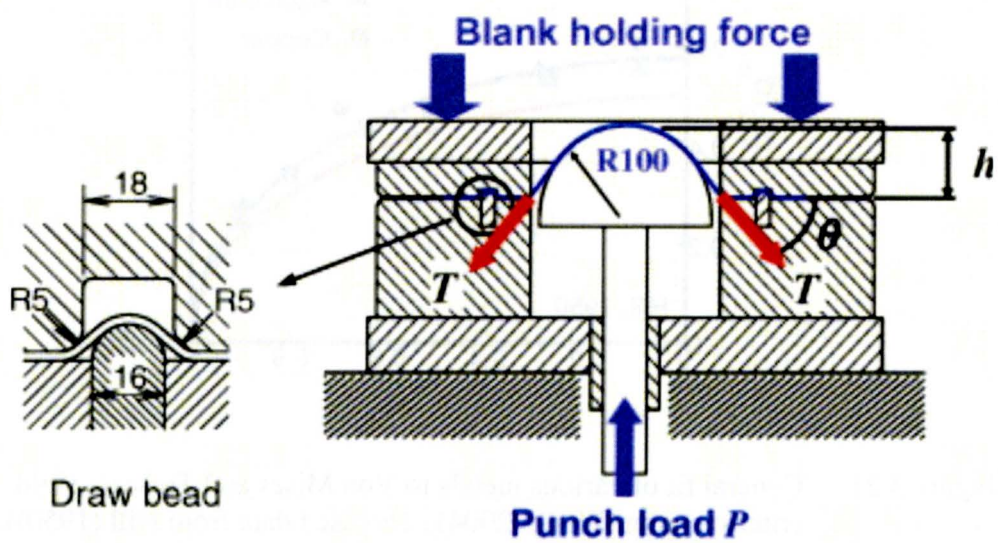

Figure 3.19 Schematic apparatus used for stretch bend springback tests (from Kuwabara et al., 2004).

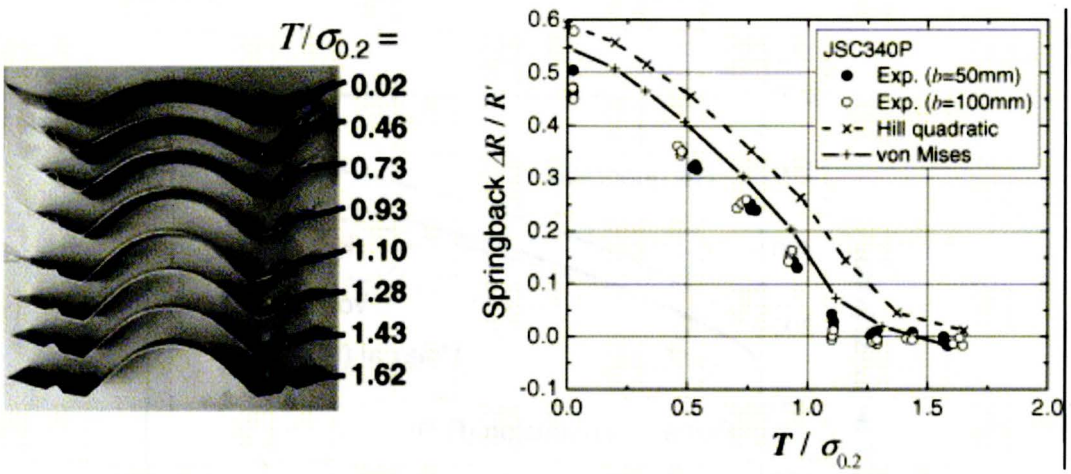

Figure 3.20 Experimental springback from bending and tension test (Figure 3.19) for two punch depths. Experiments are compared to that predicted from FEA simulations using Hill's 1948 and Von Mises criterion (from Kuwabara et al., 2004).

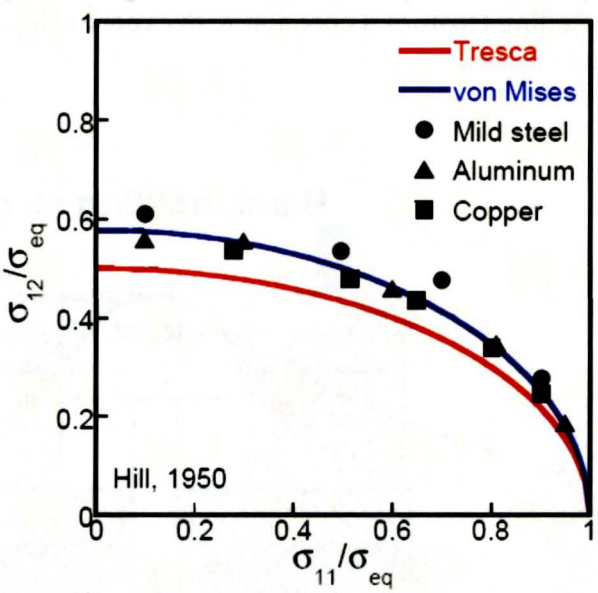

Figure 3.21 General fit of various metals to Von Mises and Tresca's yield criterion (from Wang (2004), who used data from Hill (1950)).

3.3.2 Unloading modulus experiments and FEA

Zhu et al., (2004) performed uni-axial tension-compression tests and their finding agreed with those from Clevland et al., (2002). Namely, a decrease in the apparent unloading modulus as a function of tensile prestrain was observed. Zhu et al. implemented an experimentally determined unloading modulus into the FEA springback benchmark developed by Demeri et al (2002). In this benchmark a cup is drawn, and then a ring is machined from the cup. The ring is then cut open to release the residual stresses and the subsequent diameter is measured. Zhu performed FEA for DQSK and BH (bake hardening) steels and the results were compared to that from Demeri's study. In Demeri's study the predicted (FEA) springback was in error by a factor of almost 50%. In Zhu's work, the implementation of the effective unloading modulus resulted in a predicted (FEA) springback error of only 11-20%.

Levy et al. (2006) compared the unloading modulus for a wide variety of conventional and DP steels (Figure 3.15). He found that the unloading modulus saturates to a fixed level at a prestrain of 1-2%. Also it was found that the decrease in the unloading modulus was greater for DP steels compared to conventional steels (i.e. approximately a 20% decrease from the initial value of the elastic modulus). Luzin et al., (2005), used several techniques to measure Young's modulus in 1mm thick sheet, as a function of rolling direction, and found that tensile testing has an uncertainty of about 5%. In terms of Luzin's work, the

uncertainty in measuring the modulus associated with tensile testing is not large enough to negate the independent work by Levy, Ghosh, and Zhu.

Fei et al., (2006) measured the effective unloading modulus as a function of pre-strain in uni-axial tensile tests for three different TRIP steels, with tensile strengths ranging from 745 to 883 MPa . They did not observe a level at which the unloading modulus saturated. They implemented the effective unloading modulus into their FEA simulations of V-die bending and compared predicted springback results to experiments. It was found that the error in the FEA, using elastic unloading vis a vie the elastic modulus, was 15%. The error was decreased to 7% by implementing an effective unloading modulus. Li et al. (2002) found similar improvements when simulating air bending of an aluminum alloy.

In summary, the inclusion of nonlinear elasticity in the FEA may be important. Future developments of material models to support this capability could be forthcoming.

3.4 Plane strain bending

Bending along a straight line is a common sheet metal forming operation used in the fabrication of various components (Marciniak et al. 2002). Typical processes using this operation are; air bending, V-die bending, wiping (straight line flanging), and U-die bending (Mielnik, 1991), as shown in Figure 3.22 from Eary et al., (1974). Many of the experiments and analytical models in the literature were developed specifically for these bending operations.

Accurate springback predictions require accurate modeling of the bending stresses and strains during the loading (bending) and unloading (springback) process. These are influenced by material strength, hardening and yielding, as well as the assumed physics of the bending process (as well as the underlying assumptions presented in Chapter 2). Accordingly, much of the previous research has focused on these main characteristics.

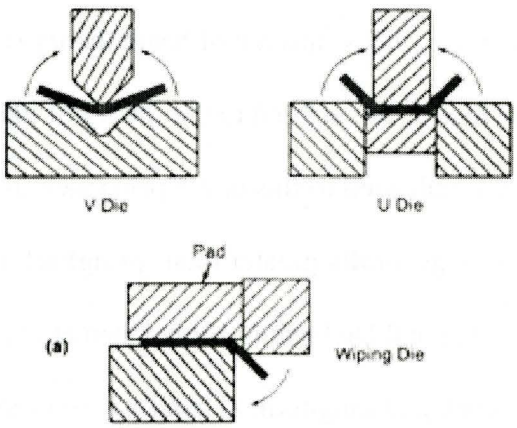

Figure 3.22 Typical "straight line" bending operations showing V-die, U-die bending as well as flanging-wiping (Eary et al., 1974).

3.4.1 Development of analytical closed from solutions to predict springback in simple bending

One of the earliest closed form solutions for predicting springback in bending was developed by Gardiner (1957). Bending and springback was modeled for the bending of narrow strips (i.e. using beam theory), and the material was assumed to be planar isotropic, with perfectly plastic hardening behavior. Gardiner's equation is given by Eq. 56. This equation predicts that springback increases with yield strength and bending radius. Springback also

increases with lower elastic modulus and increasing thickness. Gardiner also performed cylindrical bending experiments for bend radii from approximately 10 mm to 220 mm for a number of metals.

$$Ks = 4\left(\frac{\sigma_{ys}R_i}{Et}\right)^3 - 3\left(\frac{\sigma_{ys}R_i}{Et}\right) + 1 \qquad \text{Eq. 56}$$

In examining an addendum to Gardiner's work, Crandell (in Gardiner, 1957) proposed that the bending stress development and springback be treated using plate theory (i.e. wide plates) instead of beam theory (narrow plate). This was an important contribution since it led to the theory of plane strain bending and springback, which is still used to this day. Springback in plane strain (wide sheet) bending (Eq. 57) is generally greater than springback in narrow sheet bending (Eq. 58) (Queener and DeAngelis 1968; Chen et al., 1994). Under plane strain conditions the developed longitudinal bending stress in the elastic region are greater than that for beam theory by a factor of $1/(1-\nu^2)$, where ν is Poisson's ratio. For steel, ν is approximately 0.3, and therefore under elastic deformation, the bending stress is approximately 10% greater than that for beam theory. In the plastic region of the stress strain curve, the bending stress is greater than beam theory by a factor of $(4/3)^{(n+1)/2}$ if Hollomon work hardening and Von Mises criterion is assumed. The result is that the magnitude of springback is 6-10% greater for plane strain bending, compared to the case for plane stress or uni-axial deformation.

$$K_s = \frac{\Delta M}{EI}\left(1-\nu^2\right) \quad \text{Eq. 57}$$

$$K_s = \frac{\Delta M}{EI} \quad \text{Eq. 58}$$

Further analytical developments of closed form solutions for springback focused on incorporating more accurate equations to describe material hardening. Rolf et al., (1978), Johnson et al., (1981), and Tseng et al (1996) derived analytical models for bending stress development and springback assuming bi-linear work hardening. Queener and DeAngelis (1968) and Johnson et al., (1972) derived equations for bending stresses, springback, and residual stresses assuming Hollomon work hardening. In the work of Queener and DeAngelis (1968) two bending cases comprising of fully plastic and elastic-plastic deformation were presented. They recommended that when the bending radius to thickness ratio is less than 30, plastic bending could be assumed, ignoring the elastic bending moment. They also compared their analytical results with V-die experiments for a range of metals, which showed fair agreement in terms of the springback ratio and experimentally measured residual stresses after springback. Hosford et al., (1983), also derived an analytical expression for the springback ratio using Hollomon hardening, which agreed with that from Queener and DeAngelis (1968). Tseng et al. (1994) applied the analytical equations from Queener and DeAngelis (1968) to experiments involving V-die bending of Invar sheets. His results showed that the analytical predictions were within the range of springback measured experimentally.

It was recognized that the use of analytical hardening equations in closed form springback equations can sometimes result in large errors. Sidebottom et al., (1979) criticized the work by Queener and DeAngelis (1968) and showed that the predicted springback could be markedly improved for situations where the maximum bending strain is close to the yield strain of the material, only if work hardening was modeled using piece-wise linear curve. Their assertion was based on the fact that the Hollomon hardening used in Queener's work, under predicted bending stresses at or near the yield point. Sidebottom developed a method to model material hardening using a piece-wise linear discretization of actual experimental tensile curves. For this they developed an iterative technique based on the Prandtl Ruess flow rule, previously described by Mendelson (1968). They assessed Queener's results and predicted more springback for cases with large bending radii, in which the maximum bending strains were close to the plane strain yield for the material. Their development was necessarily restricted to materials that obey Von Mises criterion and was unnecessarily complex. Chapter 5 shows an alternative method to incorporate material hardening from uni-axial stress strain tests into a bending-springback analytical model. In general, it has been recognized that analytical hardening equations have the disadvantage of misrepresenting actual (experimental) hardening. For example, Holloman hardening gives a poor fit to tensile data at low strains (Marciniak et al., 2002), and Swift hardening is not accurate at higher strains (Wang, 1993).

Other workers have made small improvements to analytical solutions, for example, using true strain instead of engineering strain, incorporating planar or normal anisotropy, or using yield criterion other than Von Mises criterion. Tseng et al. (1994) claimed that their closed form solution using true strain (instead of engineering strain) showed better agreement with their experimental V-die results predicting 75-95% of the experimental springback. Wang (1993) developed expressions for true bending stress and strain using Hill's 1978 non-quadratic yield criterion. His equations are shown below.

$$\varepsilon_1 = \bar{\varepsilon} / F \qquad \text{Eq. 59}$$

$$\sigma_1 = F \bar{\sigma} \qquad \text{Eq. 60}$$

$$F = \left[\frac{2\left(1+\bar{r}\right)^{1/M}}{2}\right]\left[1+\left(1+2\bar{r}\right)^{1/(1-M)}\right]^{(M-1)/M} \qquad \text{Eq. 61}$$

Referring to the equations above, ε_1 and σ_1 are the principal true bending strain and stress respectively in a given fiber. The factor "F" (derived from Hill's non-quadratic yield criterion with normal anisotropy $\bar{r}$) can be modified to represent common yield criterion used for steels. In Eq. 61, Von Mises criterion is applied for M=2, $\bar{r}$=1, Tresca's yield criterion applies for M=1, $\bar{r}$=1, Hill's 1948 yield criterion applies when M=2, and Hosford's yield criterion applies for M=6 (for bcc metals). Eq. 59-61 show that bending stresses increase with increasing normal anisotropy. In Chapter 3, anticlastic curvature in bending is reviewed. Wang's work did not account for the effect of $\bar{r}$ on lateral strains and anticlastic curvature, which hinders springback in bending (Wang et a; Barlat, 2005). It is

generally assumed that the effect of anticlastic curvature is negligible for a blank width to thickness ratio greater than 10 (Tan et. al., 1995).

It was Wang (1993) that first developed analytical models of bending and springback that incorporated the geometry of the bending process, in addition to different material models (Eq. 59-61). An example for V-die bending is shown in Figure 3.23 and Figure 3.24. Wang introduced a coordinate system that tracks the specimen segment length and this was used to define three distinct zones in the bending process. Referring to Figure 3.24, plastic bending occurs directly under the punch along segment O-A, and the bending moment is constant. Segment A-B represents a transition zone in which the bending moment decreases linearly to a value of zero at point B, where the blank contacts the die wall. In Wang's model, the total bending moment contributing to springback is due to the contributions from segments O-A and A-B. This is an important distinction compared to the simple bending theory outlined in Chapter 2, in which the bending moment that contributes to springback is due only to the specimen curvature directly underneath the punch. Wang's model also illustrated the effect of die gap C on the blank angle of wrap around the punch. For any value of C greater than the specimen thickness t, the angle of wrap is less than the die angle α. As the die gap C approaches the specimen thickness, the length of the segment A-B (the transition zone) falls to a value of zero. When C exactly equals the specimen thickness t, the angle of wrap is equal to α, and the moment distribution along the entire sample length is the same as that assumed by simple bending theory.

3.4.2 Analytical solutions for general bending

General bending analytical models have been previously developed for describing the through thickness bending stress distribution (Hill, 1950; Lubahn et al.,1950; Proska, 1959; Crawford, 1970; Verguts et al., 1975; Dadras et al., 1982). If linear unloading is assumed, then springback can be calculated using Eq. 58. Unlike simple bending, deformation in general bending is not proportional, and therefore the strain history in each fiber directly affects the stress distribution. Tan et al. (1995) briefly reviewed the historical development of analytical solutions to general bending, and much of their review is described below. Analytical equations of general bending were described in Chapter 2, and are not repeated here.

Many of the models developed differed in complexity by adapting non-linear hardening, different yield criterion and incorporating planar anisotropy. Hill (1950) presented a solution to general bending for a perfectly plastic material. His model ignored thinning, anisotropy, and Baushinger effect, but accounted for neutral axis shifting, non-linear through thickness stress distribution, and transverse or normal stresses. Lubahn et al., (1950) performed a similar analysis to Hill (1950) and also considered perfectly plastic material behavior. Nagpal et al., (1978) presented a solution considered linear hardening, which was also reproduced in Meilnik (1991). Wang's (1993) model accounted for neutral axis shifting, anisotropy, but not thinning. Zhang et al. (1998) developed a model that used Swift hardening and incorporated Hill's 1979 non-quadratic yield surface,

and accounted for thinning. The solution, however, required an iterative technique to solve the differential equation of general bending. Their model was extended to bending-unbending deformation in which kinematic hardening was used to model alternate tension-compression cycles in the outer bending fibers. However, the Baushinger effect was not considered (and kinematic hardening was not used) in the modeling of neutral axis shifting.

Crawford (1970) was first to consider the Baushinger effect from neutral axis shifting. However, his model used a constant yield stress to model reverse straining of fibers overtaken by the neutral axis. Dadras et al., (1982) considered linear strain hardening for fibers overtaken by the neutral axis. Tan et. al., (1995) developed an analytical models to predict stress distributions, bending moments, and thinning. Their models considered pure isotropic and pure kinematic hardening for fibers overtaken by the neutral axis. However, for the case of pure isotropic hardening, Voce's work hardening law was used in their model. For the case of pure kinematic hardening, Ludwig's work hardening was used. Their models also incorporated Hill's 1948 yield criterion and therefore accounted for planar anisotropy. To validate their models, bending experiments were performed for an aluminum alloy, and two high strength steels, in which thinning and bending moment verses curvature, was measured. Their experimental results showed good agreement with their analytical models.

3.4.3 Previous studies on plane strain bending and springback

Early work such as that by Chapman et al. (1942), Shanley (1942), and Brown et al. (1944) had established basic trends in terms for springback. Namely, that springback increases with yield strength, lower Young's modulus, and larger punch radius to thickness ratio (Rp/t). Sachs (1966) also generated experimental results and proposed empirically based methods for springback compensation. Others have generated experimental data in order to compare springback in different materials. Queener and DeAngelis (1968) performed V-die bending experiments for a range of materials under conditions of simple bending, and found good correlation between their analytical model and experimental results. However, for the case of 1095 high strength steel, their analytical model underpredicted the amount of springback (Figure 3.25). Davies (1981) performed experiments examining springback in straight flanging for a number of steel grades, including DP600, SAE980X, SAE950, and a generic cold rolled low carbon steel. His results showed that springback increases with bend radius, die gap, material strength, and with decreasing sheet thickness. Experimental work from Inamadar et al., (2002) for an aluminum alloy and a low carbon steels at various punch radii, also showed increasing springback with increasing punch radii and die clearance. Davies (1981) experimental work was one of the earliest that compared DP steels to conventional steels. His work showed that springback was proportional to yield stress for conventional steel, but not for a DP600 steel. The DP600 in his study had a similar springback to the SAE950X grade. Other

workers performed bending-springback experiments with the intention of producing calibration curves. Levy (1984) created empirical equations for springback under pure bending. He performed regression analysis on data obtained from three different experiments; bending into an elastomer, die forming-flanging, and simulated die flanging. His regression equations were a function of the variables; die geometry, yield strength, sheet thickness and bend radius. The experiments were performed for a low carbon cold rolled grade and 3 martensitic grades of sheet steel (Martensite M130, M160 and M220). Similar to Levy, Fekete (2003) presented empirical equations for springback based on flanging experiments, comparing HSLA and DP steels. His regression equations showed that the bend ratio (R_m/t), yield point elongation, and a term he called the "material strength" were important variables affecting springback. By material strength, Fekete (2003) was describing the work hardening of the material in the final bend configuration, or the final maximum bending stress. In light of the work of Davies (1981), the differences in material work hardening probably accounted for the differences in springback between DP steels and HSLA steels of similar yield strength. Fekete's results showed that springback increases with material work hardening and bend ratio, and decreases with increasing yield point elongation (YPE). Interestingly, his results also showed that the magnitude of springback for a DP600 grade was more than twice that of an HSLA grade of equivalent yield strength.

Wang (1993) applied his model to small radius bending of a 2000 series aluminum alloy sheet, bent to a R_m/t less than 5. His bending-springback model incorporated true strain, the effect of neutral axis shifting and Hill's non-quadratic yield criterion. His model showed good agreement with his experimental results. Magnusson and Tan (1994) applied Wang's model to V-die bending for a variety of steels having yield strengths ranging from 182 MPa to 370 MPa. The agreement between experiments and analytical models was good with error ranging from 0.6% to 13%. In general, the analytical model tended to underpredict actual springback. Leu, (1997) derived springback equations for simple bending using Hill's normal anisotropic yield criterion and demonstrated that the predicted springback increases linearly with increasing $\bar{r}$, but a comparison to experiments was not performed.

Mori et al. (2007) used a CNC press to accurately control the punch motion in V-die bending experiments. Three materials were studied, namely, an ultra high strength steel with tensile strength of 1GPa, a high strength steel with tensile strength of 800 MPa and a mild steel with tensile strength of 340 MPa. Their experimental results showed increasing springback with material strength and decreased springback with greater punch bottoming or coining. They also studied the effect of varying the punch velocity from 0.003 m/sec to 0.047 m/sec, on springback. There results showed no significant effect. The authors also performed 2D plane strain FEA simulations of the bending process but focused on coining and they did not report the springback from FEA. Ling et al., (2005)

examined flange-bending and springback in an aluminum alloy (AL3034-T3), and performed FEA corresponding to their experiments. They found that springback increases with punch to die clearance, and that the most important variable affecting springback was the bend radius. Unfortunately, their FEA was focused on springback countermeasures using coining, and a comparison to the experimental results was not discussed. Nilsson et al. (1997) performed FEA springback simulations of V-die bending. Their FEA utilized 2D continuum elements, simulating pure plane strain bending and springback. Corresponding experiments were performed using and an aluminum alloy , and low and medium strength steels with yield strengths ranging from 158MPa. The springback FEA was performed using the LSDYNA-NIKE3D finite element implicit code. Their experiments showed no difference in springback between dry and lubricated bending conditions using oil and plastic film. On this basis, bending and springback simulations were performed with Coulomb friction of 0. In general, their FEA predicted springback errors ranged from 0 to 22%. The simulations tended to underpredicted springback. The material models used in their FEA were not described.

Schikorra et al. (2005) studied the air bending of DP600 steels, both experimentally and using FEA. They compared the springback from FEA using 2D and 3D continuum elements as well as 3D shell elements, to that measured experimentally. The analysis code used was ABAQUS, and both pure isotropic and kinematic hardening assumptions were used. The results showed that that in

terms of the effect of the element formulation, the springback magnitude was in the following order: 2D continuum > 3D continuum> 3D shells. The results also showed that the FE using the pure kinematic hardening assumption predicted more springback than the corresponding simulations using isotropic hardening. However, they did not calibrate the FEA material model to account for the actual mixed isotropic-kinematic hardening behavior of their experimental DP steels.

3.4.4 Anticlastic curvature in bending and springback

In the pure bending of steel blanks, uniform plane strain deformation across the blank width is never achieved as plane stress persists at the blank edges and extends approximately a distance equal to the material thickness into the specimen (Horrocks and Johnson, 1967). If the blank is wide enough, compared to the cross sectional thickness, the effect of plane stress at the edges on the average internal bending moment per unit width (and springback), is minimal. Anticlastic curvature forms at the edges of the blanks as a result of plane stress and uni-axial deformation. Persistent anticlastic curvature increases the cross section moment of inertia, with the effect of suppressing springback (Carden et al., 2002).

The blank width to thickness ratio is an important consideration in promoting plane strain deformation. Sachs (1950) demonstrated that plane strain bending conditions occur when the ratio of width to thickness (w/t) is greater than 8. There is little or no literature on anticlastic formation in plastic bending (Wang et al., 2005). Ashwell (1950) developed a closed form solution to predict anticlastic curvature deflection and shape for elastic bending. His results showed

that for Poisson's ratio (ν) of 1/3, the elastic bending moment saturates to a level of 91% of the plane strain value when the Searle parameter equal to $w^2/(Rt)$, is greater than 150, where w, t, and R_m are the specimen width, thickness and mid-surface bending radius respectively. Wang et al. (2005) defined the Searle parameter as $(w/t)^2/(R/t)$, which highlighted that the conditions for plane strain bending depends on the normalized width and the normalized bending radius. Wang et al. (2005) revisited Ashwell's elastic solution, and stated that with increasing Searle parameter, bending deformation is closer to plane strain and anticlastic curvature concentrates more towards the free edges of the blank (Figures 3.26-3.27). Horrocks and Johnson, (1967) performed elastic-plastic bending experiments using wide plates of aluminum and mild steel. They found that with higher Searle parameter, anticlastic curvature become more concentrated at the free edges of the blank. They also found that the measured anticlastic curvature depth (or deflection) was greater than that predicted using the elastic solution by Ashwell (1950). They reasoned that this was due to larger Poisson's ratio in plastic deformation compared to elastic deformation, resulting in a corresponding difference in the lateral bending strains. For elastic bending, the maximum deflection due to anticlastic curvature is approximately 10% of the material thickness (Wang et al., 2005).

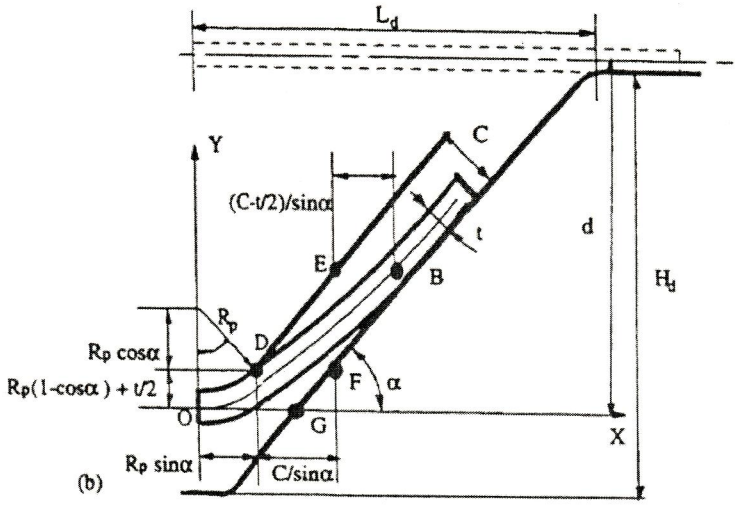

Figure 3.23 Geometry of V-die bending showing the relationship between die gap (C), material thickness, and tooling geometry (from Wang, 1993).

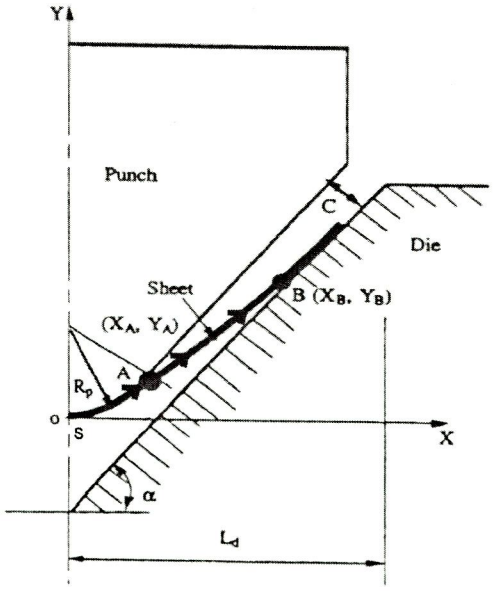

Figure 3.24 Coordinate system "S" used to describe V-die bending (from Wang, 1993). The "S" coordinate is the arc length along the specimen length, as indicated by the arrows, and represents the distance along a curved "line length".

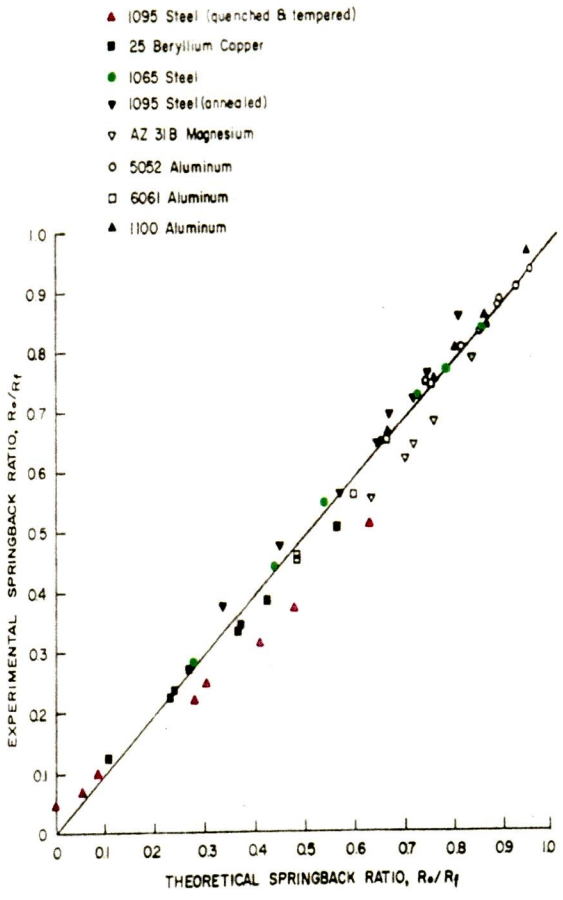

Figure 3.25 Predicted springback ratio (Ks) verses that from experiments for 90 degree V-die bending (from Queener and DeAngalis, 1968).

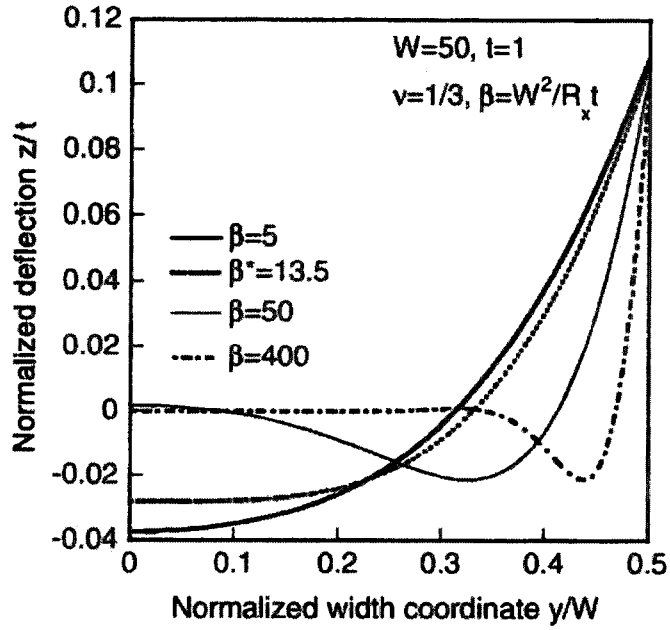

Figure 3.26 Predicted elastic anticlastic deformation as a function of Searle parameter (β), based on the solution by Ashwell (1950) (from Wang et al., 2005).

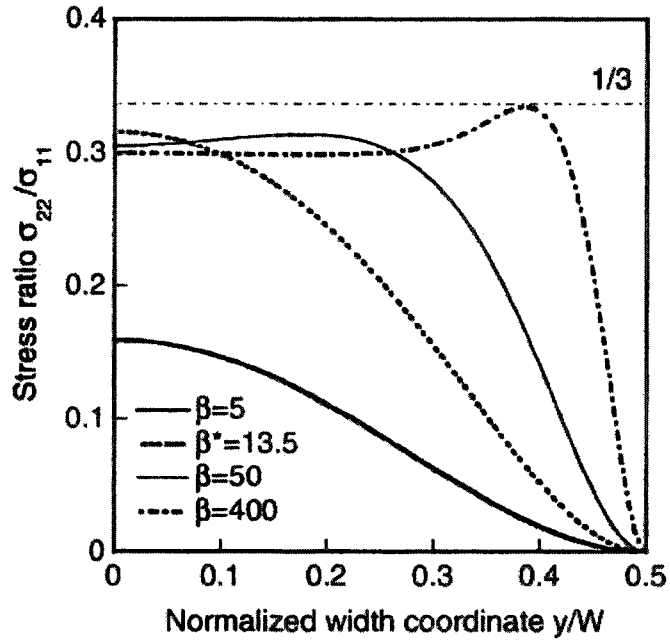

Figure 3.27 Predicted stress ratio (elastic deformation) as a function of Searle parameter (β) based on the solution by Ashwell (1950) (from Wang et al., 2005).

3.5 Summary

DP steels have unique behavior in forming and springback, compared to conventional steels. Their higher strength and initial work hardening contributes to larger springback, and press tonnage requirements. In stamping processes, the strain rate sensitivity of DP steels is similar to that of conventional steels. DP steels however show more pronounced Baushinger effect and decrease in the "unloading modulus" compared to conventional steels, both of which have the potential to contribute to greater recovery strains and increased springback. The steel grades DP780 and DP980 steels show the most pronounced Baushinger effect compared to all typical automotive steels. Both Bauschinger effect and "unloading modulus" are a function of prior strain and these behaviors have the potential to be important in the application of FEA, and analytical models used to predict springback. Non-linear elasticity is not investigated as it is beyond the scope of this thesis work.

The yield criterion is an important factor in modeling bending stresses, bending moment, and therefore springback. Currently there are no experimental results that provide guidance as to the appropriate yield criterion for DP780 and DP980. In this thesis work, Von Mises criterion is assumed in the modeling of DP780 and DP980 because of its universality in fitting a variety of metals including mild steels. The experimental results from Kuwabara (2004) supports this assumption.

Sheet metal forming FEA typically use the explicit (dynamic) method for forming and (static) implicit method for springback respectively. Various studies have identified important numerical parameters such as element size, and number of through thickness integration points, yet many FEA simulations of bending cited do not report these parameters. The majority of FEA simulations use shell elements, or 2D continuum elements. Only one study was found that used 3D continuum elements, and the results showed that the predicted springback was greater in the 3D continuum element models compared to that using 3D shells. In using 2D continuum elements, researchers have justified the assumption of plane strain bending using the width to thickness ratio; however, plane strain bending conditions are also a function of the Searle parameter. A higher magnitude of Searle parameter implies conditions approaching plane strain bending. Many of the FEA studies reviewed, that used 2D continuum elements, did not evaluate bending conditions in terms of the Searle parameter.

Historically, plane strain bending experiments on a variety of materials have found that the springback magnitude is a function of yield strength, tensile strength, clearance, bend radius, and thickness. DP steels have shown significantly more springback compared to those HSLA steels of similar yield strength. This has been attributed to high initial work hardening resulting in larger bending stresses. This implies that accurate modeling of work hardening is important for the prediction of springback.

Analytical simple bending models have grown in complexity and have included improvements such as non linear strain hardening, and incorporating the effect of punch to die clearance. Most studies have shown fair to good agreement with corresponding experiments. There no studies in the literature that examine plane strain bending of DP780 and DP980 accounting for the effect of kinematic hardening on bending and springback. Given that DP780 and DP980 have the highest degree of Baushinger effect for all steels, this may be an area of interests. Simple bending models have assumed isotropic hardening, and a few general bending models have incorporated kinematic hardening.

From the late 1990's onward, many workers have turned to FEA to model bending and springback. Studies have identified numerical parameters that affect springback, but material modeling is still a challenge, especially for DP steels.

CHAPTER 4
NON-LINEAR FEA IN SHEET METAL FORMING

4.1 Introduction

Finite element modeling of sheet metal forming considers deformation at a macroscopic level. Deformation is such that infinitesimal deformation theory does not apply, and large deformation measures of stress and strain are used within the finite element code. In the following, the concepts of non-linear FEA are presented with an emphasis on plasticity, keeping in mind that the definition of stress and strain are not the usual definitions used for infinitesimal deformation. The information presented in this chapter is condensed from the works of Cook et al., (2001) and Zienkiewicz et al., (2000); as well as from LSTC published manuals (Weimer, 2001; LSTC, 2003; LSTC, 2006).

4.2 Linear momentum equilibrium and the equations of motion (Cook et al., 2001)

In the FEA method, the equations of motion are derived from a discritized representation of the volume or continuum. The continuum is discritized into a number of connecting elements. Each element is bounded by a set of nodes, and each node has a designated degree of freedom. Using the convention by Cook et. al., (2001), the nodal displacements in an element is given by a column vector $\{d\}^{(e)}$. Polynomial functions, N, are used to interpolate the displacements within the element, in reaction to loads applied to the volume. The strain in an element is

then calculated (Eq. 62) knowing the nodal displacements and the B matrix (Eq. 63).

$$\{\varepsilon\}^{(e)} = [B]\{d\}^{(e)} \quad \text{Eq. 62}$$

$$[B] = [\partial][N] \quad \text{Eq. 63}$$

Again using the notation from Cook et. al. (2001), the stress and strains are written in matrix form according to Eq. 64 and Eq. 65 respectively, and the shear strains are represented in the strain matrix using Eq. 66.

$$\sigma = [\sigma_{11} \quad \sigma_{22} \quad \sigma_{33} \quad \sigma_{12} \quad \sigma_{23} \quad \sigma_{31}]^T \quad \text{Eq. 64}$$

$$\varepsilon = [\varepsilon_{11} \quad \varepsilon_{22} \quad \varepsilon_{33} \quad \gamma_{12} \quad \gamma_{23} \quad \gamma_{31}]^T \quad \text{Eq. 65}$$

$$\gamma_{ij} = 2\varepsilon_{ij} \quad \text{Eq. 66}$$

For the entire volume, the nodal displacements and strains are represented by a matrix with a single column, with the number of rows equal to the number of nodes times the degree of freedom for each node. The nodal displacements, velocities, accelerations and strains are therefore represented by Eqs. 67-70.

$$\{u\} = \sum_{All\ elements} [N]^{(e)} \{d\}^{(e)} = [N]\{d\} \quad \text{Eq. 67}$$

$$\{\dot{u}\} = [N]\{\dot{d}\} \quad \text{Eq. 68}$$

$$\{\ddot{u}\} = [N]\{\ddot{d}\} \quad \text{Eq. 69}$$

$$\{\varepsilon\} = [B]\{d\} \quad \text{Eq. 70}$$

From these equations the shape functions describe the nodal quantities as a function of space, and the nodal displacements. The velocities and accelerations are themselves functions of time. The shape functions are also used to distribute

loads, tractions and mass to the nodes. Therefore partitioning of the continuum is achieved through the elements and nodes, and their associated shape functions. Again using the element shape functions, the global mass of the volume is distributed to the nodes using Eq. 71.

$$[M] = \int_{\Omega} [N]^T \rho [N] d\Omega \qquad \text{Eq. 71}$$

Tractions at the surface of the volume are distributed to nodes using Eq. 72.

$$\int_{S} [N]^T \{t\} dS \qquad \text{Eq. 72}$$

Body forces and loads are distributed to the nodes according to Eq. 73.

$$\int_{\Omega} [N]^T \{F\} d\Omega \qquad \text{Eq. 73}$$

Dynamic equilibrium is therefore represented by the equation of motion for the finite element system, neglecting damping, in Eq. 74. In this equation, the first term represents the inertial forces, the second term represents the deformation resistance of the material, and the right hand side represents all external loads on the volume. This state of dynamic equilibrium in the volume is therefore the result of the inertial and internal forces, in balance with the external loads.

$$[M]\{\ddot{u}\} + \{r^{int}\} = \{r^{ext}\} \qquad \text{Eq. 74}$$

From Eq. 71, the inertial forces arise from the mass matrix and nodal accelerations. The internal forces, $\{r^{int}\}$, are a function of the material constitutive law, which describes the developed internal stresses as a response to the nodal strains. The internal force terms is also called the stress divergence term (LSTC, 2003).

$$\{r^{int}\} = \int_{\Omega} [B]^T \{\sigma\} d\Omega \qquad \text{Eq. 75}$$

In elastic deformation, stress is related to the strain through the elastic modulus, and the substitution of Eq. 70, into Eq. 75 results in the linear stiffness matrix, $[K]$ (Eq. 77).

$$\{\sigma\} = [E]\{\varepsilon\} \quad \text{Eq. 76}$$

$$\{r^{\text{int}}\} = \int_{\Omega} [B]^T [E][B]\{d\} d\Omega = [K]\{d\} \quad \text{Eq. 77}$$

In elastic –plastic deformation, the stress is a non-linear function of strain. The stiffness matrix is therefore non-linear.

Numerical integration of the equations of motion is used to solve for the nodal displacements. From nodal displacements, the derived quantities of stress and strain are then found.

4.3 Explicit integration of the finite element equations of motion

In the explicit method, the central difference scheme is used for the direct integration of the equations of motion with respect to time. In this method, the equation of motion is linearized using the finite difference form of each derivative term in Eq. 74.

LSDYNA3D uses the half step central difference method where velocities lag the accelerations by ½ the time step (Weimer, 2001). Cook et. al. (2001) describes this method in which the current nodal velocities, displacements and accelerations are given by Eqs. 78-80, respectively. The substitution of these equations into Eq. 74 yields the equations of motion, in a form that can be readily integrated (Eq. 81).

$$\dot{u}_{n+1/2} = \dot{u}_{n-1/2} + \Delta t \ddot{u}_n \quad \text{Eq. 78}$$

$$u_{n+1} = u_n + \Delta t \dot{u}_{n+1/2} \quad \text{Eq. 79}$$

$$\ddot{u}_n = M^{-1}\left(r_n^{ext} - r_n^{\text{int}}\right) \quad \text{Eq. 80}$$

$$\frac{1}{\Delta t^2} M u_{n+1} = \left(r_n^{rxt} - r_n^{\text{int}}\right) + \frac{1}{\Delta t^2} M \left(u_{n-1} + \Delta t u_{n-1/2}\right) \quad \text{Eq. 81}$$

To start the integration at n=0 (or time =0), the backward difference form for $\dot{u}_{-1/2}$ is used as shown in Eq. 78.

$$\dot{u}_{-1/2} = \dot{u}_0 - \frac{\Delta t}{2} \ddot{u}_0 \quad \text{Eq. 82}$$

In Eq. 80, the mass matrix M is a diagonally lumped mass matrix in which the mass of the volume is distributed to each node. This matrix is easily inverted by taking the inverse of the diagonal elements (Eq. 83). Integration of Eq. 81 then proceeds by stepping through time. The explicit integration scheme does not require a matrix inversion step, nor does it multiple iterations, as in the implicit method to be discussed shortly. It is therefore computationally efficient. A detailed procedure for the explicit integration method is shown in Figure 4.1.

$$M_{ii}^{-1} = \begin{bmatrix} 1/m_{11} & & & & \\ & 1/m_{22} & & & \\ & & 1/m_{33} & & \\ & & & .. & \\ & & & & .. \end{bmatrix} \quad \text{Eq. 83}$$

The central difference method is conditionally stable in that the time step must be less than a critical value. Beyond this value, the solution becomes unstable. In elastic deformation, the time step limit is governed by the Courant

condition in which the stable time step is governed by the highest natural frequency of the mesh (Eq. 84, from LSTC, 2003).

$$\Delta t = \frac{2}{\omega_{Max}} \qquad \text{Eq. 84}$$

For example (LSTC, 2003), in a 2 noded bar element of length "l", the highest natural frequency is given by Eq. 85, and depends on the element length "l" as well as the wave speed of sound in the bar (Eq. 86). The stable time step limit for the bar element is therefore given by Eq. 87. This shows that the allowable time step increases with the size of the element, but decreases with the sound wave speed in the material.

$$\omega_{\max} = \frac{2}{l}\sqrt{\frac{E}{\rho_d}} \qquad \text{Eq. 85}$$

$$c = \sqrt{\frac{E}{\rho_d}} \qquad \text{Eq. 86}$$

$$\Delta t = \frac{l}{c} \qquad \text{Eq. 87}$$

For plastic deformation, an analytical form of the Courant condition does not exist (LSTC, 2006). In the LSDYNA3D code, Eq. 88 is adopted in which "l_e" is a characteristic measure of the element size and c is the elastic sound wave speed for the material. The physical interpretation of this is that the times step is less than the time required for a sound wave to propagate across the smallest deforming element (LSTC, 2003).

$$\Delta t = 0.9\frac{l_e}{c} \qquad \text{Eq. 88}$$

Step 1 Initialize at t=0

$\sigma^0 = \sigma|_{t=0}$,

$\dot{u}_{-1/2} = \dot{u}_0 - \frac{\Delta t}{2}\ddot{u}_0$

$\ddot{u}^0 = M^{-1}\left(r^0_{ext} - r^0_{\text{int}}\right)$

Step 2 Update velocities and displacements

$\dot{u}_{n+1/2} = \dot{u}_{n-1/2} + \Delta t_n \ddot{u}_n$

Update displacements, mesh geometry

$u_{n+1} = \dot{u}_{n+1/2}\left(\Delta t_{n+1/2}\right) + u_n, \quad x_{n+1} = x_0 + u_{n+1}$

Step 3 loop over all elements

Determine internal forces

Strain rates $\dot{\varepsilon}_{n+1/2} = B\dot{u}_{n+1/2}$, and B is the strain displacement matrix (Eq. 63).

$\dot{\sigma}_{n+1} = f\left(\dot{\varepsilon}_{n+1/2}\right)$

$f\left(\dot{\varepsilon}_{n+1/2}\right)$ returns the stress due to non-linear elastic plastic hardening (Section 4.6)

Stress update $\sigma_{n+1} = \sigma_n + (\Delta t)(\dot{\sigma}_{n+1/2})$,

Update internal forces $r^{\text{int}}_{n+1} = \int_{\Omega} B^T \sigma_{n+1} d\Omega$

Step 4 Compute external forces (due to loads and contact)

r^{ext}_{n+1}

Step 5 Calculate new accelerations $\ddot{u}^{n+1} = M^{-1}\left(r^{n+1}_{ext} - r^{n+1}_{\text{int}}\right)$

Go to step 2 for the next time increment

Figure 4.1. Flowchart for the explicit integration of the equations of motion (adapted from LSTC, 2003).

4.4 Implicit integration of the equations of motion (LSTC, 2003)

In LSDYNA3D the non-linear static implicit solution procedure is often used to solve the equations of motion in springback problems. The following discussion is therefore focused on this topic.

In the implicit method, the nodal displacements at the current time step are the unknowns to be determined. The change in the external load vector from time "n" to time "n+1", results in a change in the nodal displacements and therefore strains. Through the constitutive model, this gives rise to the internal stress distribution and the internal force vector (Eq. 75). At equilibrium, the internal force vector is equal to the external force vector. The Newton method is a common numerical method used to determine equilibrium conditions and therefore the nodal displacement increments. For a given load increment, the internal and external load vectors are out of balance (Eq. 89) resulting in a residual vector $\{R(u)\} \neq 0$. The objective is to find Δu in Eq. 90, such that the residual is reduced to 0, or a user defined tolerance.

$$\{R(u_{n+1})\} = \{r^{ext}(u_{n+1})\} - \{r^{int}(u_{n+1})\} \qquad \text{Eq. 89}$$

Eq. 90 represents the desired nodal displacements in the next time increment. By expanding this equation as a Taylor series and keeping lower order terms, the equilibrium equation can be re-written as Eq. 91. This equation can then be written in terms of the residual vector as in Eq. 92 (Zienkiewicz et. al., 2000).

$$u_{n+1} = u_n + \Delta u_n \quad \text{Eq. 90}$$

$$r^{\text{int}}(u_n + du_n) = r^{\text{int}}(u_n) + \left[\frac{\partial r^{\text{int}}}{\partial u_n}(u_n)\right](du_n) + 0(du_n)^2 = r^{ext}(u_{n+1}) \quad \text{Eq. 91}$$

$$\left[\frac{\partial r^{\text{int}}}{\partial u_n}(u_n)\right](du\ ) = r_{n+1}{}^{ext} - r^{\text{int}}(u_{n+1}) = \hat{R}_{n+1} \quad \text{Eq. 92}$$

Eq. 92 can be written as a system of linear equations, Eq. 93, where $\hat{K}_T$ is called the tangent stiffness matrix (Zienkiewicz et. al., 2000).

$$\hat{K}_T(du_n) = \hat{R}_{n+1} \quad \text{Eq. 93}$$

Applying Newton's method at time "n+1", "i" iterations are performed until the residual vector meets the convergence tolerance. At the start of the iterations, $\hat{K}_T^1$ (where 1 denotes the first iteration) is evaluated using u_n (i.e., the displacement vector at time "n" or the previous converged solution). The residual vector $\hat{R}_{n+1}^1$ is set to the load increment (Δf_n), and the change in displacement vector Δu_{n+1}^1 is calculated using Eq. 94. The displacement vector after the first iteration, u_{n+1}^1, is determined using Eq. 95 and Eq. 96. From this, the internal force vector is updated using Eq. 75. The residual vector $\hat{R}_{n+1}^2$, is then calculated from the difference between the updated internal force vector and the external force vector for time "n+1". The next iteration starts with the evaluation of $\hat{K}_T^2$ at the displacement vector u_{n+1}^1 (Eq. 97), and the process continues until $\Delta u_{n+1}^i \to 0$ and $\hat{R}_{n+1}^i \to 0$. This is also illustrated in Figure 4.2.

$$du_n^i = \left[\hat{K}_T\right]^{-1} \hat{R}_{n+1}^{i+1} \quad \text{Eq. 94}$$

$$\Delta u_{n+1}^i = \sum_i du^i \quad \text{Eq. 95}$$

$$u_{n+1} = u_n + \Delta u_{n+1}^i \quad \text{Eq. 96}$$

$$\hat{K}_T\left(u_{n+1}^i\right) du_n^i = \hat{R}_{n+1}^{i+1} \quad \text{Eq. 97}$$

Though the Newton method rapidly converges, it is computationally expensive (Zienkiewicz, 2000). At each new iteration "i", the tangent stiffness matrix is inverted (Eq. 94) and then reformed (Eq. 97). The modified Newton method addresses the problem of reforming the tangent stiffness matrix after each iteration.

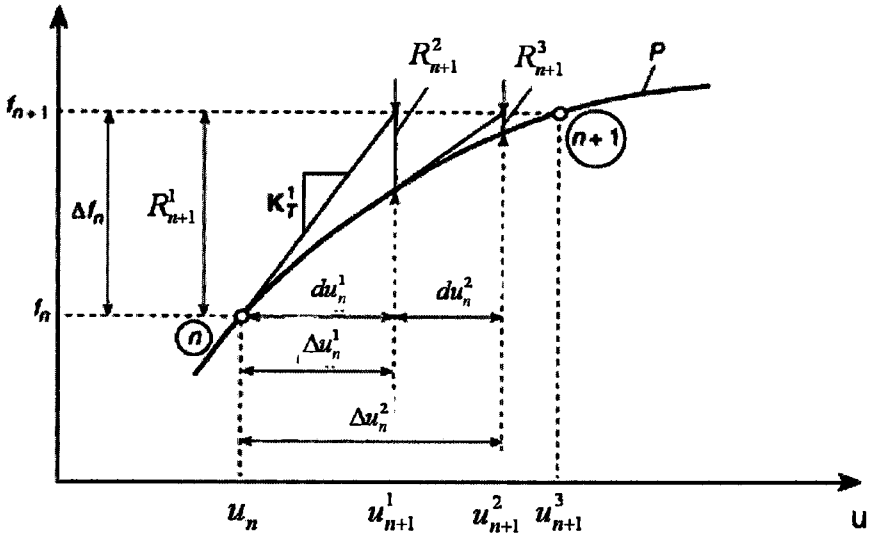

Figure 4.2. Newton – Raphson method for 3 iterations used to determine the displacement increment (from Zienkiewicz et. al., 2000).

The modified Newton method reduces the computation time as the tangent stiffness matrix (Eq. 97) is reformed after "j" iterations, instead of after every iteration "i", as is the case in the Newton method. Convergence is slower, than the

Newton method; however, the overall simulation time can be reduced because of the savings from not reforming the tangent stiffness matrix. This method can have problems however. If the dependence of the internal force vector norm with the displacement norm changes slope from positive to negative, than the use of the fixed tangent stiffness matrix will result in a non-converging solution (Zienkiewicz et. al., 2000).

Ideally, iterations in the Newton method proceed until $\Delta u_{n+1}^{i} \to 0$ and $\hat{R}_{n+1}^{i} \to 0$. Within finite element codes, the implementation of this criterion is through the use of predefined convergence criterion. In LSDYNA3D three criterion are used. Namely, the energy convergence tolerance (ECTOL), the residual convergence tolerance (RCTOL), and the displacement convergence tolerance (DCTOL). The energy and displacement tolerances are activated by default, whereas the user has to activate the residual convergence tolerance (LSTC, 2003).

The equations for energy, residual and displacement convergence criterion are shown in Eqs. 98-101, respectively (LSTC, 2003). Convergence at a given iteration is achieved once these criterion have values less than the set tolerances (ECTOL, RCTOL, DCTOL). In LSDYNA3D, it is common to use the energy and displacement tolerances to check for convergence at a given iteration (Eqs. 98-100). The interpretation of these equations with the aid of Figure 4.2 is as follows. The energy convergence equation compares the current energy norm to that found at the beginning of the iteration sequence. By default, ECTOL is set to 0.001.

Similarly, the residual convergence tolerance compares the current residual norm, to that at the beginning of the iteration sequence. This criterion is not commonly used (LSTC, 2003).

There are two criteria for the displacement convergence. These criteria relate the incremental displacement norm at the current iteration (i) compared to the total accumulated displacement norm (Eq. 100) or the incremental displacement norm for the step (Eq. 101). The component norms used to evaluate these criteria are shown schematically in Figure 4.3. In LSDYNA3D, the default criterion is the one given by Eq. 100, and the default tolerance (DCTOL) is 0.001. By inspection, the criterion from Eq. 101 is more stringent than that using Eq. 100.

$$\left\| \frac{\left(\Delta u_n^i\right)\left(\hat{R}_{n+1}^i\right)}{\left(\Delta u_n^1\right)\left(\hat{R}_1\right)} \right\| < ECTOL \qquad \text{Eq. 98}$$

$$\left\| \frac{\left(\hat{R}_{n+1}^i\right)}{\left(\hat{R}_1\right)} \right\| < RCTOL \qquad \text{Eq. 99}$$

$$\left\| \frac{du^i}{u} \right\| < DCTOL \qquad \text{Eq. 100}$$

$$\left\| \frac{du^i}{\Delta u_n} \right\| < DCTOL \qquad \text{Eq. 101}$$

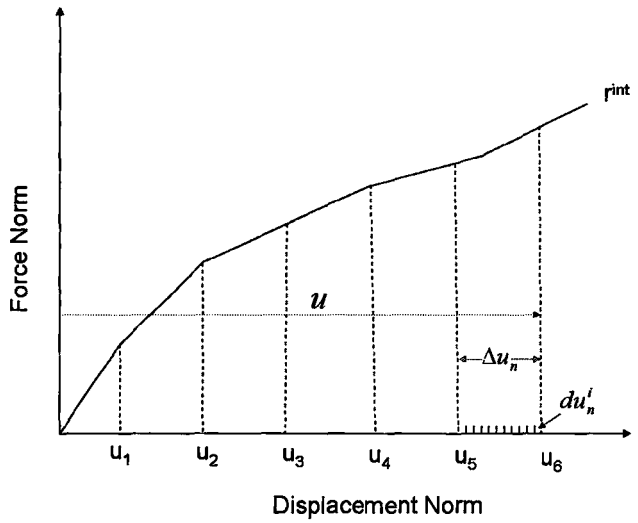

Figure 4.3 Illustration of components used to determine the displacement convergence criterion in Eq. 100-Eq. 101 (adapted from LSTC, 2003).

4.5 Comparison between (static) implicit and explicit solutions (LSTC, 2003)

The implicit solution is unconditionally stable and convergence is not guaranteed. It is well suited for simulations of long durations (simulation times) as the time step is typically larger than that in the explicit solution. An implicit solution does, however, require large amount of memory and there can be difficulties in achieving convergence in strongly non-linear problems. The implicit solution is well suited for the simulation of static loading of structures, springback, and gravity loading simulations. Though not discussed in this thesis, the implicit dynamic solution is also well suited for low rate dynamic and eigenvalue analysis (LSTC, 2003).

The explicit solution is computationally fast as there is no requirement for the matrix inversion using (lumped matrices) at each time step. However, the time

step is limited by stability requirements. For this reason, simulations of long duration are computationally expensive. Simulations are, however, robust having the ability to find solutions to strongly non-linear problems. The explicit method is well suited to problems involving high rate dynamics. Examples are car impact/crashes, explosions, and projectiles penetration. The explicit method has been used successfully to model quasi-static loading commonly used in metal forming problems. As a rough guide, a quasi-static analysis can be performed by ensuring that the total kinetic energy of the model is less than 5% of the internal energy of the structure being analyzed (LSTC, 2003).

4.6 Modeling of elastic plastic deformation in the FEA method (Cook et al., 2001)

The implicit and explicit schemes described previously solve for the change in nodal displacement such as for the static and dynamic equilibrium respectively between the external loads and internal forces (Eq. 75). The internal forces arise from the nodal displacements responding to the external loads, which in turn result in the developed strain and the internal stress distribution. The developed internal stresses are therefore a function of the material's constitutive equations, hardening law and yield function. The yield function and the associated flow rule for the steels used in this thesis are Von Mises criterion, and Levy – Mises associative flow rule, respectively.

4.6.1 Pure isotropic hardening (Cook et. al., 2001)

Assuming pure isotropic hardening, the yield function is given by Eq. 102, where Von Mises effective stress and strain in tensor notation (for convenience) is given by Eq. 103 and Eq. 104 respectively.

$$F(\{\sigma\},Y(\bar{\varepsilon}_p))=\bar{\sigma}-Y(\bar{\varepsilon}_p) \quad \text{Eq. 102}$$

$$\bar{\sigma}=\sqrt{\frac{3}{2}S_{ij}S_{ij}} \quad \text{Eq. 103}$$

$$d\bar{\varepsilon}^p=\sqrt{\frac{2}{3}(d\varepsilon_{ij}^p)(d\varepsilon_{ij}^p)} \quad \text{Eq. 104}$$

In the above equations, S_{ij} is the deviatoric stress tensor. It is defined in matrix (column notation), which is convenient for FEA, is defined by Eq. 105 (Cook et. al., 2001). Using the same conventions, a similar column vector can also be constructed for $d\varepsilon_{ij}^p$.

$$\{S\}=\begin{Bmatrix}S_{11}\\S_{22}\\S_{33}\\S_{12}\\S_{23}\\S_{31}\end{Bmatrix}=\frac{1}{3}\begin{Bmatrix}2\sigma_{11}-\sigma_{22}-\sigma_{33}\\2\sigma_{22}-\sigma_{33}-\sigma_{11}\\2\sigma_{33}-\sigma_{11}-\sigma_{11}\\\tau_{12}\\\tau_{23}\\\tau_{31}\end{Bmatrix} \quad \text{Eq. 105}$$

Reverting back to the column vector notation, the Levy Mises flow rule is given by Eq. 106, where $d\lambda$ is called the plastic multiplier. This condition necessarily implies that the plastic strain increment is perpendicular to the yield surface F.

$$\{d\varepsilon\}^p = \left\{\frac{\partial F}{\partial \sigma}\right\} d\lambda \qquad \text{Eq. 106}$$

For a given material point inside the yield surface (F), the stress state is defined by the elastic strains and the elastic modulus matrix. For plastic deformation the stress point remains on the yield surface, either remaining fixed or sliding along it through the redistribution of the stress components. This is called the consistency condition and mathematically the condition of loading is given by Eq. 107, which implies that the change in stress occurs tangent to the yield surface (Eq. 108). The condition of unloading is given by F <0 (and $d\lambda = 0$). The loading and unloading conditions previously described are also shown schematically in Figure 4.4.

$$F(\sigma + d\sigma) = F(\sigma) + \nabla F^T d\sigma = 0 \qquad \text{Eq. 107}$$

$$dF = \nabla F^T d\sigma = 0 \qquad \text{Eq. 108}$$

Strain hardening results in expansion or "evolution" of the yield surface. An evolution law to describe this phenomenon is given by Eq. 109, where the slope H_p is the slope of the $\bar{\sigma} / \overline{\varepsilon^P}$ curve obtained from an experimental uniaxial tensile test (see Figure 5.1, Chapter 5) and is a function of the accumulated plastic strain.

$$dY(\bar{\varepsilon}_p) = H_p d\bar{\varepsilon}_p = H_p \, d\lambda \qquad \text{Eq. 109}$$

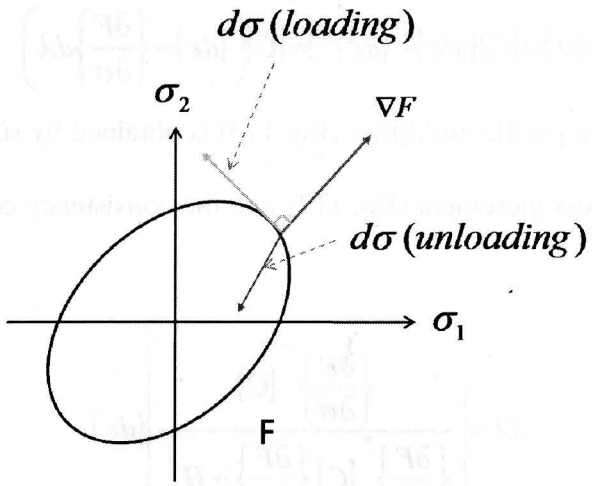

Figure 4.4 Schematic showing plastic loading and elastic unloading.

In terms of FEA, the yield surface, evolution law and consistency condition are used to determine the stress increment in response to the strain increment, and therefore allowing for the determination of the internal force vector (Eq. 75). The consistency condition applied to Eq. 102 is shown in Eq. 110. Inserting the expression for the evolution of the yield surface into this equation gives Eq. 111.

$$dF = \left\{\frac{\partial F}{\partial \sigma}\right\}^T \{d\sigma\} + \left[\frac{\partial F}{\partial d\bar{\varepsilon}^p}\right] d\bar{\varepsilon}^p = \left\{\frac{\partial F}{\partial \sigma}\right\}^T \{d\sigma\} + \frac{\partial F}{\partial \lambda}(d\lambda) = 0 \qquad \text{Eq. 110}$$

$$dF = \left\{\frac{\partial F}{\partial \sigma}\right\}^T \{d\sigma\} - H_p d\lambda = 0 \qquad \text{Eq. 111}$$

Hooke's law is used to give the expression relating the stress increment to the elastic and plastic strains. By applying the flow rule, Eq. 106, the stress increment is therefore given by Eq. 112, where $[C]$ is elastic modulus matrix and $\{d\varepsilon\}$ is the total strain increment.

$$\{d\sigma\}=[C]\left(\{d\varepsilon\}-\{d\varepsilon\}^{p}\right)=[C]\left(\{d\varepsilon\}-\left\{\frac{\partial F}{\partial \sigma}\right\}d\lambda\right) \qquad \text{Eq. 112}$$

The equation for the plastic multiplier (Eq. 113) is obtained by substituting the equation for the stress increment (Eq. 112) into the consistency condition (Eq. 111).

$$d\lambda=\left[\frac{\left\{\frac{\partial F}{\partial \sigma}\right\}^{T}[C]}{\left\{\frac{\partial F}{\partial \sigma}\right\}^{T}[C]\left\{\frac{\partial F}{\partial \sigma}\right\}+H_{p}}\right]\{d\varepsilon\} \qquad \text{Eq. 113}$$

Cook et. al (2001) also defined the term in the "square" brackets (Eq. 114) as "$\lfloor P_{\lambda} \rfloor$" which is a row matrix. The equation defining the incremental stress-strain relationship (Eq. 114) is then found by substituting the equation for the plastic multiplier back into Eq. 112. This relationship can be used to update the internal stress vector (Eq. 75) for the explicit and implicit solutions previously discussed.

$$\{d\sigma\}=\left[[C]-\frac{[C]\left\{\frac{\partial F}{\partial \sigma}\right\}^{T}\left\{\frac{\partial F}{\partial \sigma}\right\}[C]}{\left\{\frac{\partial F}{\partial \sigma}\right\}[C]\left\{\frac{\partial F}{\partial \sigma}\right\}^{T}+H_{p}}\right]\{d\varepsilon\}=[C_{ep}]\{d\varepsilon\} \qquad \text{Eq. 114}$$

The expression $[C_{ep}]$ is the elastic-plastic matrix. The substitution of the elastic-plastic matrix for the elastic modulus matrix [C] in Eq. 75 yields the stiffness matrix for elastic-plastic deformation (Eq. 115) and therefore also provides a means to update internal forces required for the solution methods described in Sections 4.3 and 4.4. This equation is analogous to the case for pure elastic deformation shown in Eq. 77.

$$[K]=\int[B]^T[C_{ep}][B]\,dV \qquad \text{Eq. 115}$$

4.6.2 Mixed isotropic-kinematic hardening (Cook et. al., 2001)

The elastic-plastic incremental stress strain expressed by Eqs. 112-114 can also be derived for more complex material behavior such as mixed isotropic-kinematic hardening. For example, the model described by Cook et al., (2002), is given by Eqs. 116-117.

$$F(\sigma_{ij},\alpha_{ij},\bar{\sigma}_e)=0 \qquad \text{Eq. 116}$$

$$F(\sigma_{ij},\alpha_{ij},\bar{\sigma}_e)=\sqrt{\frac{3}{2}(S_{ij}-\chi\alpha_{ij})(S_{ij}-\chi\alpha_{ij})}-\chi Y^0-(1-\chi)\bar{\sigma}_e \qquad \text{Eq. 117}$$

Now focusing on this model, the center of the yield surface is defined by the back stress parameter "α_{ij}", and at time =0, α_{ij}=0. Hardening results from the translation of the yield surface as shown schematically in Figure 2.9 (Chapter 2), and allows for the modeling of Baushinger effect as described in Chapter 2. Cook et al., (2002) describes the parameter "Y^0" as the uni-axial yield stress for the material, and $\bar{\sigma}_e$ is the maximum Von Mises stress reached in the previous straining. The parameter "χ" defines the degree of mixed hardening. For $\chi = 0$, Eq. 117 reduces to pure isotropic hardening whereas for $\chi = 1$, Eq. 117 reduces to pure kinematic hardening. Values of χ between 0 and 1 therefore described mixed states of hardening.

Prager type hardening is used to describe the evolution of the back stress parameter and therefore the shift in the yield surface. The evolution of the of the

back stress parameter is given by Eq. 118 (Cook et al.), where H_p is the plastic hardening modulus from the uni-axial tensile curve described previously in Eq. 109. From this, the direction of the shift in the origin of the yield surface is parallel to the plastic strain vector. If the hardening modulus is constant, Prager hardening results in linear hardening of the material, for example, a bi-linear tensile curve composed of linear and elastic and plastic regions. In experimental tensile tests of steels, the actual work hardening is such that Hp is a non-linear function of the accumulated plastic strain. To model this, the hardening modulus, H_p, can be represented as a piecewise linear approximation of the actual hardening. The Prager hardening treatment using the local hardening modulus therefore provides a piecewise linear representation of the non-linear hardening seen in a tensile test. This can be visualized as a series of linear incremental shifts of the yield surface in the direction of the plastic strain increment vector.

$$\{d\alpha\}=[\mathrm{H}]\{d\varepsilon^p\} \text{ where } [\mathrm{H}]=\frac{2}{3}H_p\begin{bmatrix} 1 & 0 & 0 & 0 & 0 & 0 \\ 0 & 1 & 0 & 0 & 0 & 0 \\ 0 & 0 & 1 & 0 & 0 & 0 \\ 0 & 0 & 0 & 1/2 & 0 & 0 \\ 0 & 0 & 0 & 0 & 1/2 & 0 \\ 0 & 0 & 0 & 0 & 0 & 1/2 \end{bmatrix} \quad \text{Eq. 118}$$

From Cook et al., the consistency condition is again applied to Eq. 116 in order to derive the elastic plastic tangent matrix. Substituting Eq. 112, Eq. 118, and Eq. 119, into Eq. 120 yields Eq. 121.

$$\left\{\frac{\partial F}{\partial \alpha}\right\}^T = -\chi\left\{\frac{\partial F}{\partial \sigma}\right\}, \quad d\bar{\sigma}_e = H_p d\lambda, \quad \frac{\partial F}{\partial \bar{\sigma}_e} = -(1-\chi) \qquad \text{Eq. 119}$$

$$dF = \overbrace{\left\{\frac{\partial F}{\partial \sigma}\right\}^T \{d\sigma\}}^{1} + \overbrace{\left\{\frac{\partial F}{\partial \sigma}\right\}^T \{d\alpha\}}^{2} + \overbrace{\left[\frac{\partial F}{\partial \bar{\sigma}_e}\right] d\bar{\sigma}_e}^{3} = 0 \qquad \text{Eq. 120}$$

$$\overbrace{\left\{\frac{\partial F}{\partial \sigma}\right\}^T [C](\{d\varepsilon\} - \{d\varepsilon^p\})}^{1} + \overbrace{\left[-\chi\left\{\frac{\partial F}{\partial \sigma}\right\}^T [H]\{d\varepsilon^p\}\right]}^{2} + \overbrace{[-(1-\chi)H_p d\lambda]}^{3} = 0 \qquad \text{Eq. 121}$$

Substituting the flow rule (Eq. 106) for $\{d\varepsilon_p\}$ and rearranging terms gives the plastic multiplier (Eq. 122). The elastic-plastic tangent matrix (Eq. 123) is found by substituting the plastic multiplier into Eq. 112. Again using the terminology from Cook et al., the term in the square brackets in Eq. 122 is defined as $\lfloor P_\lambda \rfloor$. For pure isotropic hardening ($\chi = 0$), Eq. 122 reduces to Eq. 113, and the expansion of the yield surface is governed through the local plastic hardening modulus H_p. For kinematic hardening ($\chi = 1$), the term relating to H_p is "0", and hardening is controlled through the shift of the yield surface via the [H] matrix in Eq. 118.

$$d\lambda = \overbrace{\left[\frac{\left\{\frac{\partial F}{\partial \sigma}\right\}^T [C]}{\left\{\frac{\partial F}{\partial \sigma}\right\}^T ([C] + \chi[H])\left\{\frac{\partial F}{\partial \sigma}\right\} + (1-\chi)H_p}\right]}^{\lfloor P_\lambda \rfloor} \{d\varepsilon\} \qquad \text{Eq. 122}$$

The final incremental stress strain relationship is found by substituting $d\lambda$ from Eq. 122 into Eq. 112 to give the results shown in Eq. 123 and Eq. 124.

$$[C_{ep}]=[C]\left([I]-\left\{\frac{\partial F}{\partial \sigma}\right\}\lfloor P_{\lambda}\rfloor\right), \text{ where [I] is the identity matrix.} \quad \text{Eq. 123}$$

$$\{d\sigma\}=\lfloor C_{ep}\rfloor\{d\varepsilon\} \quad \text{Eq. 124}$$

4.7 Incremental stress-strain relations and elastic-plastic loading conditions

For a given load increment during the analysis, the displacement increments, are determined either explicitly or implicitly as previously described in Sections 4.3 and 4.4 respectively. The displacement increments are used to determine the strain and therefore stress increments in order to update the internal force vector (Eq. 75). For a given strain increment, the stress path must be considered in order to properly determine the stress increments. There are four stress paths to consider (Table 4-1), each defined by the initial stress state, the value of the yield function (for example, Eq. 117) and the plastic multiplier.

4.7.1 Stress update methods

In the FEA method, the update of the stress increment first starts with the evaluation of an elastic trial stress from the strain increment (Eqs. 125-126). The loading conditions are then determined using the appropriate yield criterion, F, as shown in Eq. 117. If $F(\{\sigma_{Trial}\}) < 0$, then elastic loading is indicated and Eq. 126 can be used to update the stress state. If $F(\{\sigma_{Trial}\})= 0$ then the plastic multiplier $(d\lambda)$ is determined (Eq. 127). If the plastic multiplier is equal to "0" ($d\lambda = 0$) then elastic unloading is indicated and again Eq. 126 can be used to update the stress state. These two situations correspond to cases 1 and 2 in Table 4-1.

Table 4-1 Possible stress paths for a given strain increment.

Case	Initial stress point position	Yield Function for the final stress point	Plastic Multiplier	Comment
1	Below the Yield surface (Elastic stress state)	F<0	----	Pure elastic deformation
2	On the current Yield surface	F=0	$d\lambda=0$	Elastic unloading (i.e. springback)
3	On the Yield surface (Elastic stress state)	F=0	$d\lambda<0$	Pure elastic deformation followed by plastic deformation
4	On the current yield surface	F=0	$d\lambda>0$	Plastic deformation

$$\{\Delta\varepsilon\}_{A\to B}=[B]\{\Delta d\}_{A\to B} \quad \text{Eq. 125}$$

$$\{\sigma\}_B=\{\sigma\}_A+[C]\{\Delta\varepsilon\}_{A\to B} \quad \text{Eq. 126}$$

$$d\lambda=\lfloor P_\lambda \rfloor_A\{\Delta\varepsilon\}_{A\to B} \quad \text{Eq. 127}$$

For case 3 in Table 4-1, the portion of the strain increment corresponding to pure elastic deformation is determined using an iterative secant procedure (Cook et al., 2001). This procedure is described as follows. Consider the strain increment from state "A" to state "B" in which the stress state "A" is below the yield surface (Figure 4.5). The trial stress (Eq. 128) is portioned using a constant "β" in Eq. 129 such that an intermediate stress state "b" (Eq. 130) is on the current

yield surface (Eq. 131).The objective of the iterative procedure is to determine the parameter β.

$$\{\Delta\sigma\}_{Trial}=[C]\{\Delta\varepsilon\}_{A\to B} \quad \text{Eq. 128}$$

$$\{\Delta\sigma\}_b=\beta\{\sigma\}_{Trial} \quad \text{Eq. 129}$$

$$\{\sigma\}_b=\{\sigma\}_A+\beta\{\sigma\}_{Trial} \quad \text{Eq. 130}$$

$$F(b)=F(\{\sigma\}_b)=0 \quad \text{Eq. 131}$$

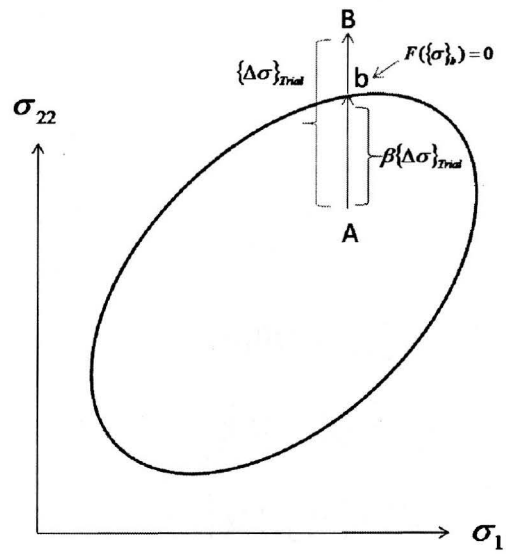

Figure 4.5 Portion of trial stress increment ($\beta\{\sigma\}_{Trial}$) that changes stress state from point A to a point on the current yield surface "b" (adapted from Cook et al., 2001).

The Iterative procedure used to determine β is shown in equations Eqs. 132-136, as well as illustrated in Figure 4.6. Through successive approximations of the secant, a value of β is obtained such that stress state "b" is found usually in 4 to 5 iterations (Cook et. al., 2001)

Start of iteration i=0

$$\beta_0 = 0, \{\sigma_b\}_0 = \{\sigma_A\} \quad \text{Eq. 132}$$

i=1

$$\beta_1 = \frac{F(\{\sigma_A\})}{F(\{\sigma_A\}) - F(\{\sigma_{Trial}\})} \quad \text{Eq. 133}$$

$$\{\sigma_b\}_1 = \{\sigma\}_A + \beta_1[C]\{\Delta\varepsilon\}_{A\to B} \quad \text{Eq. 134}$$

Remaining iterations i

$$\beta_{i+1} = \beta_i - \frac{F(\{\sigma_b\}_i)}{\sec ant_i} \quad \text{Eq. 135}$$

$$\sec ant_i = \frac{F(\{\sigma_b\}_{i-1}) - F(\{\sigma_b\}_i)}{\beta_{i-1} - \beta_i} \quad \text{Eq. 136}$$

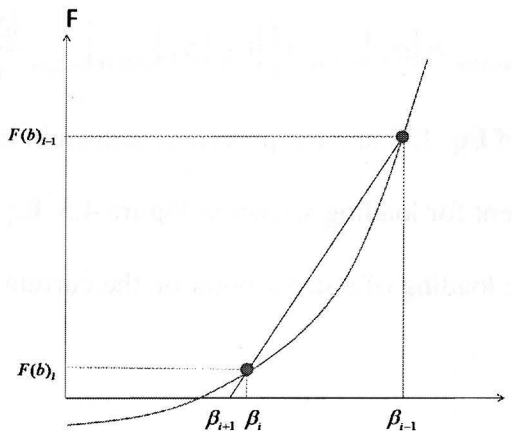

Figure 4.6 Secant iterative procedure to determine β using Eqs. 132-136 (adapted from Cook et al., 2001).

Once an estimate for β is known, the strain increment causing yield surface expansion (or shifting) is then given by the expression $(1-\beta)\{\Delta\varepsilon_{A\to B}\}$. The corresponding stress increment can then be determined using the process of subincrementation, in which the strain increment is subdivided into intervals (m).The elastic-plastic modulus is then used to calculate the sum of stresses in the sub increments corresponding to the strains in the subincrements (Eq. 137). For example, Eq. 138 -Eq. 140 show the first three results using Eq. 137. The

calculation is explicit as the elastic-plastic modulus is determined at the previous estimate of the stress point.

$$\{\Delta\sigma_{bB}\}_n = \sum_{j=0}^{m-1}\left([C_{ep}]_{n+j/m}\frac{\{\Delta\varepsilon\}}{m}\right) \quad \text{Eq. 137}$$

j=0 $$\{\sigma_B\}_n = \{\sigma_b\} + \left([C_{ep}\{\sigma_b\}]_n\frac{\{\Delta\varepsilon\}}{m}\right) \quad \text{Eq. 138}$$

j=1 $$\{\sigma_B\}_{n+1/m} = \{\sigma_B\}_n + \left([C_{ep}\{\sigma_B\}_n]_{n+1/m}\frac{\{\Delta\varepsilon\}}{m}\right) \quad \text{Eq. 139}$$

j=2 $$\{\sigma_B\}_{n+2/m} = \{\sigma_B\}_{n+1/m} + \left([C_{ep}\{\sigma_B\}_{n+1/m}]_{n+2/m}\frac{\{\Delta\varepsilon\}}{m}\right) \quad \text{Eq. 140}$$

Together, the results of Eq. 137 and the procedure shown in Eqs. 132-136 provide the total stress increment for loading shown in Figure 4.5. Eq. 137 also can be used for elastic-plastic loading of a stress point on the current yield surface (see case 4 in Table 4-1).

4.7.2 Radial return method (Zienkiewicz et al., 2000)

Because of potential accumulation of numerical error, the subincrementation procedure does not guarantee that $F(\{\sigma\})=0$. The accumulation of numerical error can be reduced by reducing the size of the load increment (Cook et al., 2001). An alternative procedure that addresses this problem is the radial return algorithm, as shown in Figure 4.7.

The method is based on Eq. 112, in which the stress increment is updated assuming pure elastic deformation, and then corrected such that the final stress point lies on the yield surface, satisfying the condition that $F(\{\sigma\})=0$. The elastic

predictor and the plastic corrector vector returns the point to the yield surface. This path is also apparent through the integration of Eq. 112, giving Eq. 141. From Eq. 141, it is apparent that the plastic corrector term is determined by the scalar plastic multiplier $\Delta\lambda$, and the gradient of the yield surface that gives the direction for the projection.

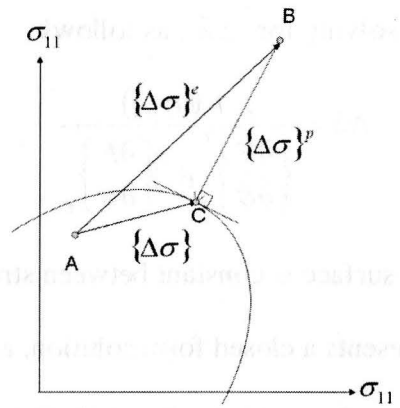

Figure 4.7 Schematic of radial return algorithm showing elastic predictor $\{\Delta\sigma\}^e$ and plastic corrector $\{\Delta\sigma\}^p$ used to map the stress vector onto the yield surface at the next strain increment (adapted from Zienkiewicz et al., 2000).

$$\{\Delta\sigma\} = \overbrace{[C]\{\Delta\varepsilon\}}^{\text{Elastic preditor}} + \overbrace{\int_{\lambda}^{\lambda+\Delta\lambda} [C]\left\{\frac{\partial F}{\partial\sigma}\right\} d\lambda}^{\text{Plastic corrector}} \qquad \text{Eq. 141}$$

In terms of the final stress point "C" in Figure 4.7, Eq. 141 can be approximated using Eq. 142, where the plastic multiplier is unknown.

$$\{\Delta\sigma\} = [C]\{\Delta\varepsilon\} - \Delta\lambda[C]\left\{\frac{\partial F}{\partial\sigma}\right\}_C \qquad \text{Eq. 142}$$

Using Figure 4.7 as a reference, the magnitude of $\Delta\lambda$ can be determined by considering the Taylor series expansion of the yield function around stress point "B", as follows.

$$F(\{\sigma_C\}) = F\left(\{\sigma_B\} - \{\Delta\sigma\}^p\right) \approx F(\{\sigma_B\}) - \left\{\frac{\partial F}{\partial \sigma}\right\}_B^T \{\Delta\sigma\}^p = 0 \qquad \text{Eq. 143}$$

The plastic multiplier is then determined by using the flow rule for the plastic strain increment, and then solving for $\Delta\lambda$, as follows

$$\Delta\lambda = \frac{F(\{\sigma_B\})}{\left\{\frac{\partial F}{\partial \sigma}\right\}_B^T [C] \left\{\frac{\partial F}{\partial \sigma}\right\}_C} \qquad \text{Eq. 144}$$

If the gradient of the yield surface is constant between stress point C and stress point B, then Eq. 144 represents a closed form solution, and the stress correction to the yield surface can be performed using Eq. 142. If the gradients are different, than an iterative procedure such as the Newton Raphson method can be used (Zienkiewwicz et. al., 2000).

4.8 General FEA procedure for stamping simulation (Gailbraith, 1998)

The basic steps in the FEA analysis are; preprocessing, solving the equations of motion, and post-processing (Figure 4.8). In the preprocessing stage the tooling geometry and blank are discretized into nodes and elements. Material and section properties (for example, shell thickness) are assigned to the elements, as well as various boundary conditions such as loads, velocities (or displacements) and constraints. In the solution step, the equations of motion are assembled and solved. In the post-processing step, the solution to the problem is

analyzed. Some common variables examined are displacements, velocities, accelerations, deformed geometry, strains and stresses. Other outputs include reactions forces and energies associates with deformation and motion of the work piece as well as the motion of the tooling.

The FEA analysis is an idealization of the actual processes as many variables are not accounted for, and therefore the solution may not exactly predict actual behavior. A comparison between FEA and the actual stamping process is shown in Table 4-2.

At the end of the forming the deformed work piece mesh, with associated stresses-strains, and resulting shell thicknesses, are in theoretical equilibrium with the restraining forces imposed by the tooling. Springback is simulated vis a vie an instantaneous removal of the tooling resulting in relief and redistribution of forming stresses. The inputs for the springback simulation are therefore the work piece in the deformed state, as well the appropriate material properties (i.e. Elastic modulus and unloading curve).

4.9 General parameters used in forming and springback FEA using LSDYNA3D

LSDYNA3D is a general purpose FEA code primarily used in the simulation of impact and crash events. The second most frequent use of LSDYNA3D is for the FEA of sheet metal forming (Dutton, 2005). Most forming simulations are performed using the explicit code, and a typical model is composed of the blank, a punch and a blank holder and a die (depending on the

stamping process of interest). The FEA of the forming system is essentially a virtual die in which the tooling actions (punch and blank holder) are assigned prescribed loads or displacements, resulting in the deformation of the blank mesh. To reduce the CPU times, mass scaling and/or artificially high punch velocities are used. Mass scaling is a technique whereby mass is added to the smallest elements limiting the time step according to Eq. 88. Forming simulations are essentially displacement driven problems, and therefore increasing the punch velocity results in shorter simulation times. Metal forming problems are considered to be "quasi-static". The effect of mass scaling and punch velocity scaling is an increase in the dynamics or inertial forces, which result in inaccuracies in the predicted stresses and strains in the blank. As stated earlier, quasi-static conditions are achieved if the kinetic energy of the deforming blank is less than or equal to 5% of the internal energy due to plastic work (Gailbraith, 1998).

Table 4-2 Contrast between FE Simulation and the actual forming processes (adapted from, Blumel et al., 1999).

	Die stamping inputs	
	Simulation	Actual Process
Geometry	CAD model	Tooling after die tryout
Material	Material models	Mild steel, AHSS's, microsturctural effects, burrs, material variation etc.
Tribology	Coulomb friction	Dynamic friction, different lubricants, area of contact variation (spotting)
Environment	Not accounted for	Temperature variations, moisture, cycle times
Numerical Influences on the solution process	Mesh size, implicit-explicit solver, dynamic effects in explicit codes, contact, mesh adaptivity	none

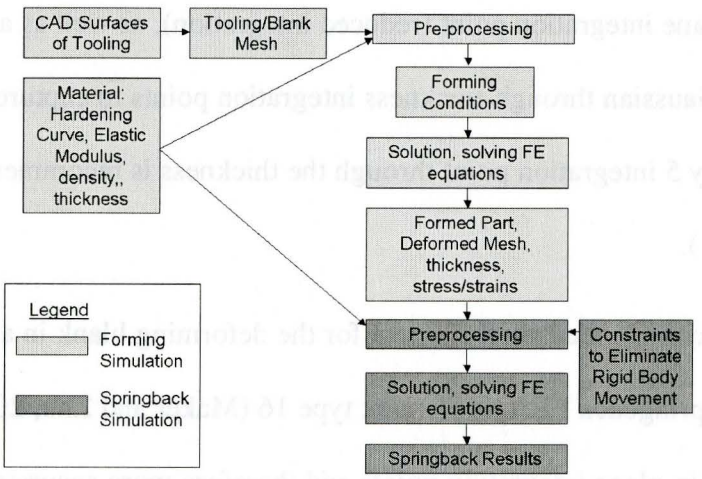

Figure 4.8 Flow chart showing overview of tasks to perform in a FEA analysis of forming and springback

4.9.1 Meshing

In sheet metal forming models, discritization of the tooling and blank geometry is typically performed using shell elements. Shell elements are also used to model the tooling as rigid bodies providing the contact surface to the blank. For the blank, shell elements model membrane, shear and bending stresses. Shell elements are well suited for sheet metal forming problems because stresses normal to the plane of the sheet are considered to be insignificant, which is also the assumption used in most sheet metal forming simulations (Marciniak et al., 2001), .

For forming, shell elements type 2 and 16 are used. Both are 4 noded Mindlin type shells (C^0 continuous), and are capable of modeling, membrane, bending, shear, and thinning deformation (LSTC, 2003). The elements have 6 degrees of freedom per node (3 translations and 3 rotations), and each node can represent a specified thickness. Element type 2 is the Belytschko-Tsay element, with one in-plane integration point (reduced integration), as well as a number of user defined Gaussian through-thickness integration points to capture bending effects (usually 5 integration point through the thickness is recommended (Maker and Zhu, 2001).

The recommended shell element for the deforming blank in a coupled forming and springback FEA, is element type 16 (Maker and Zhu, 2001). This element has 4 in-plane integration points and therefore more accurately captures

stresses due to forming. It also has a user defined number of through thickness integration points to capture bending effects.

4.9.2 Tooling Mesh (Maker and Zhu, 2001)

The tooling mesh forms the basis for modeling contact and sliding between the work piece and the tools. For this reason, only a mesh of the tooling surface is required. The tooling mesh is modeled as a perfectly rigid body and therefore mesh quality is not an important factor. Within LSDYNA3D, the mesh can also be disjoint, as long as automatic contact options are used to model contact with the blank.

An important consideration in the tooling mesh is capturing curvature, for example at die and punch radii. Industry practices are a minimum of 5 elements in a radius. Software preprocessors used to create tooling meshes from CAD surfaces, such as Hyperform or Dynaform, use a specified chordal deviation between the mesh and the CAD surface, and standard values for chordal deviation are 0.10 or less. This usually results in at least 5 elements in a radius. However, as discussed in Section 3.2, a finer mesh can lead to improved springback predictions.

4.9.3 Blank Mesh (Maker and Zhu, 2001)

Blank meshing is critical in terms of element size and shape, thereby minimizing discritization error (Figure 4.9). Element aspect ratios should approach the value of 1, and one should avoid using triangle (at least in areas of the blank that are of particular interest). By default, LSDYNA3D treats triangles

as degenerate quadrilateral shell elements, which are considerably stiff and therefore could lead to inaccuracies in the solution. If the use of triangles is necessary, a good practice is to place them at or near the blank boundary, in which their participation in deformation is minimized. The exception to this is in stretch or shrink flanging deformation. The user can also set a flag within the input deck to use the C^0 triangle shell formulation, which is more accurate than the degenerate quadrilateral element.

Mesh size is also critical for resolving the effects of tooling curvature and adequate modeling contact in these areas. If care in the tooling mesh was used to create a fine mesh in areas of high curvature, then the blank mesh should also reflect this in terms of matching the element size. (Gailbraith, 1998)

4.10 Contact in Sheet Metal Forming Simulations (Gailbraith, 1998)

The modeling of contact between the work-piece and tooling is an integral part of the FE model used to simulate sliding, separation and friction at interfaces. It is industry standard practice to model interface sliding using Coulomb friction, mainly, because it is fast and reliable.

During forming, the sheet will thicken or thin in response to the strain state in the sheet. The work piece thickness is considered in modeling contact. LSDYNA3D calculates shell (work piece) thicknesses at each part of the solution (time step) and contact is then based on the work piece shell surface located ½ the shell thickness away from the shell mid plane. The tooling surface is modeled with no thickness.

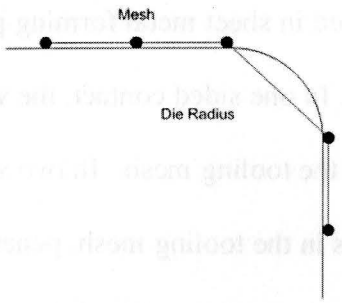

Figure 4.9 Blank mesh and tooling profile view showing discretization error due to a coarse blank mesh.

The modeling of contact is generally performed using the penalty method. In the penalty method nodes actually penetrate the contacting surface (shell surfaces) and a restoring force is applied to prevent further penetration. The amount of penetration therefore depends on the restoring force or interface stiffness. The restoring force results from the application of normal interface springs between all penetrating nodes and the contacting surface. The restoration stiffness is shown in the equation below (Eq. 145) and is a function of the bulk modulus (K), element size (A is the element area, V the element volume), and a user defined scale factor (δ) which by default has a value of 0.2. The stiffness of this interface is therefore of the same order of magnitude as the work piece material, and therefore minimizes hourglassing. Hourglassing is a zero energy mode found in reduced integration shell elements which results in nonphysical deformation states and are essentially numerical artifacts.

$$k = \delta K \frac{A^2}{V} \qquad \text{Eq. 145}$$

Contact interfaces used in sheet metal forming perform one sided or two sided checks for penetration. In one sided contact, the work piece nodes are checked for penetration into the tooling mesh. In two sided contact, an additional check is performed for nodes in the tooling mesh, penetrating into the work piece surface. One way contact is commonly used in sheet metal forming simulations, mainly because of the reduced CPU cost.

Contact between the blank and the tools is typically modeled using two methods Figure 4.10. The first uses a segment based projection, used in "surface to surface" type contact. Segment based projection is efficient computationally, but can create gaps or overlaps, leading to noisy contact interface forces during sliding. The second method uses nodal based projection, used in "node – to-surface" contact, and in this method the gaps-overlaps are eliminated. However it is computationally more expensive. Typical metal forming simulations use segment based projection (or surface to surface contact).

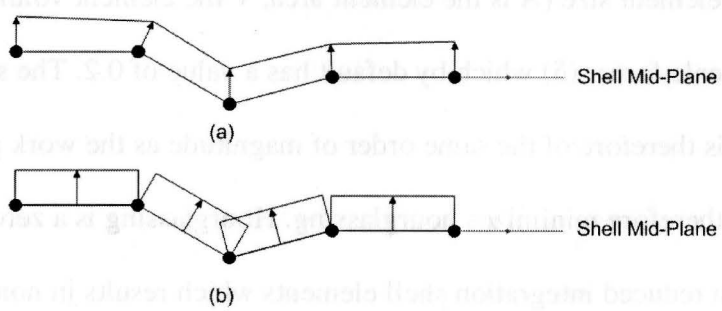

Figure 4.10 Thickness offset of shell midplane for the purpose of determining contact with the tooling mesh. In (a) nodal based projection provides a continuous contact surface. In (b) segment based projection results in gaps and overlaps (adapted from Weinmar, 2001).

CHAPTER 5
DEVELOPED NUMERICAL PROCEDURES TO MODEL BENDING AND SPRINGBACK

5.1 The modeling of simple bending using piece-wise linear hardening

The motivation for modeling bending stresses using piece-wise linear hardening comes from the inability of analytical hardening laws to accurately represent actual material hardening. For example, Hollomon hardening does not adequately model actual hardening at low strains. Voce's law, on the other hand, does not adequately model work hardening of steels at larger strains. A computer program was developed to predict bending stresses using piece-wise linear hardening from the experimental stress strain curve (Figure 5.1). The work hardening in bending was then modeled using the hardening modulus from successive stress-plastic strain pairs.

The plane strain yield function for this problem is shown Eq. 146. In Chapter 4, Von Mises criterion, the associative flow rule, and the consistency condition were all used in the development of the elastic-plastic tangent modulus [C_{ep}], the latter was used to determine the tangent stiffness matrix for the non-linear FEA method (Cook et al., 2002). The substitution of the yield function for plane strain simple bending into Eq. 114 from Chapter 4, yields the incremental stress-strain relationship. More details on the derivation of Eq. 147 are shown in Appendix D.

$$F(\sigma_{ij},\sigma_0)=\left(\frac{3}{2}S_{ij}S_{ij}\right)^{1/2}-\sigma_0=0 \qquad \text{Eq. 146}$$

$$d\sigma_1=\left[\frac{1-\nu^2}{E}+\frac{3}{4Hp}\right]^{-1}d\varepsilon_1 \qquad \text{Eq. 147}$$

In Eq. 147, the plastic hardening modulus Hp is a function of the current effective plastic strain as shown in Figure 5.1 below.

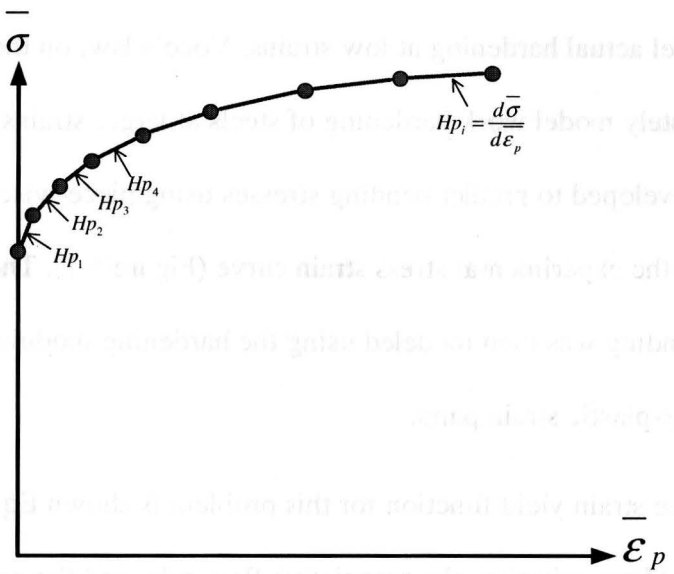

Figure 5.1 Piece-wise linear hardening based on the experimental stress-plastic strain curve.

A program for plane strain simple bending, incorporating the incremental stress-strain relationship (Eq. 147) and piece-wise linear work hardening, was written using MATLAB®. The program is documented in Appendix D. The flowchart for the program is shown in Figure 5.2. The program uses the experimental uni-axial true stress-true strain curve as an input, with the first

stress-strain pair corresponding to the yield stress and strain. This curve is then converted to the true stress-plastic strain curve, from which the plastic hardening modulus is determined for successive stress-strain pairs.

For the calculation, the ½ thickness is divided into 200 bending fibers. From the target bending radius (R_i), the maximum bending strain in each fiber is determined in step 7 of the flowchart. The bending stress distribution is then initialized in step 8, with the elastic stresses for the elastic bending fibers. The plastic bending fibers are initially assigned a bending stress and strain equivalent to that of the plane strain yield point for the material. The bending strain is incremented in each plastic fiber, and the corresponding stress increment is determined from Eq. 147. The current stress and strain in a bending fiber is then updated in step 8 using the stress-strain increments. After each stress update, the effective plastic strain is calculated and the appropriate value for the hardening modulus H_p is chosen (step 10). This process continues for all bending fibers until the maximum (target) bending strain is reached as determined by the target bending radius (R_i). The strain increment for each bending fiber is small enough such that the consecutive values of H_p are used (Figure 5.1). In this case 1000 steps or strain increments were adequate. A comparison between bending stresses using piecewise linear hardening to that from Hollomon hardening is shown in Figure 5.3. These results show differences near the neutral surface, at low bending strains. The results are similar to those observed in comparing actual uni-axial tension test data to the curve fit of Hollomon hardening (Figure 8.20).

5.2 Numerical routine for solving for the bending geometry in general bending

In Chapter 2, the bending geometry as a function of bending curvature is described using the governing differential equation (Eq. 45). The bending geometry is affected by the choice of hardening assumption, i.e., if pure isotropic or pure kinematic hardening is modeled (Eq. 46 and Eq. 47 respectively). Tan and Magnusson (1995) developed a computer scheme to solve this problem and their methods have been adopted here using the computational procedure shown in Figure 5.4. The corresponding computer program was written using MATLAB® and is documented in Appendix B.

The numerical routine can be described as follows. The bending geometry is initialized in step 1 with zero bending curvature ($\kappa = 0$), thinning ($\eta = 1$) and neutral axis shifting ($\rho = 1$). Von Mises criterion is assumed for the yield surface, and the parameters for Ludwig work hardening are given by strength coefficient (k_L), work hardening exponent (n_L) and initial flow stress (σ_0). Elastic strains are ignored and only plastic strains are modeled. At the first bending increment, the differential equation is integrated using the adaptive step Runge Kutta solver in MATLAB®, and the interval of integration is from κ_{i-1} to κ_i. The ode45 routine in MATLAB® was used, having a relative error tolerance of 10^{-5}. This routine adjusts the step size to meet the error tolerance. Once η_i is determined for the current κ_i, the bending geometry parameters are updated in step 3.

Steps

1 Input E, R_i (target punch radius), t (thickness), true stress-true strain curve $R_m = R_i + t/2$

2 True stress-plastic strain curve using $\bar{\varepsilon}_p = \bar{\varepsilon} - \bar{\sigma}/E$

3 $Hp_i = \left(\bar{\sigma}_{i+1} - \bar{\sigma}_i\right) / \left(\bar{\varepsilon}_{p,i+1} - \bar{\varepsilon}_{p,i}\right)$, piece-wise plastic hardening modulus for each $\bar{\varepsilon}_{p,i}$

4 Yield $\varepsilon_{1Y} = \frac{1-\nu^2}{\sqrt{1+\nu^2-\nu^2}} \bar{\varepsilon}_Y$, $\sigma_{1Y} = \frac{2}{\sqrt{3}} \bar{\sigma}_Y$

5 Divide ½ thickness into 200 bending fibres

6 $\Delta t = t/200$

bending fibre position vector $\lfloor y \rfloor = y_j = j\Delta t \;,\; j = 1:200$

7 Maximum Bending Strain in a given fibre $\lfloor \varepsilon_1(Max) \rfloor = \frac{\lfloor y \rfloor}{R_m}$

8 Initialize through thickness bending stress-strain distribution

$\sigma_1(elastic\_Core) = \frac{E}{1-\nu^2} \lfloor \varepsilon_1(Max) \rfloor$ *for* $\lfloor \varepsilon_1(Max) \rfloor \le \varepsilon_{1Y}$

$\varepsilon_1(elastic\_Core) = \lfloor \varepsilon_1(Max) \rfloor \le \varepsilon_{1Y}$

$\sigma_1(Plastic) = \sigma_{1Y}$ *for* $\lfloor \varepsilon_1(Max) \rfloor > \varepsilon_{1Y}$

$\varepsilon_1(Plastic) = \varepsilon_{1Y}$

9 Increment bending strains in plastic fibres up to $\lfloor \varepsilon_1(Max) \rfloor$

Steps = 1000

Strain increment for each plastic fibre $\lfloor d\varepsilon_1 \rfloor = \lfloor \varepsilon_1(Max) \rfloor / Steps$

10 For k=1 steps

Stress increment in each plastic fibre, $d\sigma_{k+1} = \left[\frac{1-\nu^2}{E} + \frac{3}{4Hp}\right]^{-1} d\varepsilon_1$

Update stress-strain

$\sigma_{1,k+1} = \sigma_{1,k} + d\sigma_{1,k+1}$

$\varepsilon_{1,k+1} = \varepsilon_{1,k} + d\varepsilon_1$

$\varepsilon^p_{1,k+1} = \varepsilon_{1,k+1} - \sigma_{1,k+1} / \left(E/(1-\nu^2)\right)$

$\bar{\varepsilon}_{p,k+1} = \frac{2}{\sqrt{3}} \varepsilon^p_{1,k+1}$

Find new Hp from $\bar{\varepsilon}_{p,k+1}$ in the interval $\left(\bar{\varepsilon}_{p,i+1} - \bar{\varepsilon}_{p,i}\right)$ in 3

End

Output bending stress-strain, bending moment

11 $Output\ \sigma_1, \varepsilon_1, y_i \;\; M_t = 2\sum_i \sigma_{1i}(y_i + \Delta t/2)dt$

Figure 5.2 Incremental bending flow chart to determine principle bending stresses and bending moment prior to springback from a piece-wise linear hardening curve.

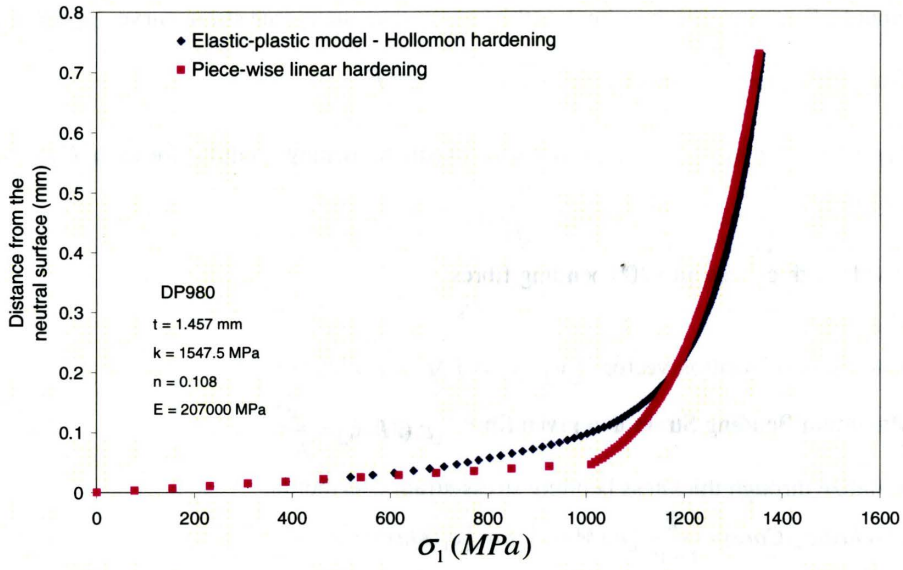

Figure 5.3 Predicted bending stress for DP980 comparing Hollomon hardening (elastic-plastic bending) to piece wise linear hardening from the MATLAB® computer program.

The position of the neutral surface is found in step 4 by using continuity of the radial stresses at the interface of bending Zones II and III (Figure 2.6). Once the radius of the neutral surface is determined, the bending geometry parameter ρ_i is found. In summary, each cycle through the loop in step 2 determines η_i and ρ_i by the integration of Eq. 35 from K_{i-1} to K_i. Once κ_i, ρ_i, and η_i are known, bending stresses can be calculated using the equations from the general bending theory discussed in Chapter 2 (Eqs. 25-27 and Eqs. 40-44). Appendix C shows an example of the bending stress calculation using MATHCAD, as well as the calculation of the internal bending moment.

Steps

1 Initialization
Initial bending geometry, $\kappa = 0$, $\eta = \rho = 1$
Material Ludwig parameters in plane strain, $t_0, k_L, n_L, \sigma_0, C = 2/\sqrt{3}$

2 Loop to increment bending curvature κ

For κ =0.02 1.8, in steps of 0.02
Integrate using the Runge-Kutta method with variable step size. $\frac{d\eta}{d\kappa} = -\frac{\eta}{2\kappa}(\exp(-\Lambda) - 1)$,
output η *for the current* κ
Where " Λ "is from Eq. 46, or Eq. 47 for pure isotropic or kinematic hardening respectively.

3 Determine ρ for the current bending curvature
Update current bending geometry
Current thickness $t = \eta\, t_0$
$R_m = t/\kappa$
$R_u = \eta R_m$
$R_i = (1 - \kappa/2)R_m$
$R_y = (1 + \kappa/2)R_m$

4 Find R_N by checking for continuity of radial stresses at the boundary between Zone II and Zone III
R=Ri
While Loop
Check to see if σr_ZoneII(Ri,Ru,R)>σr_ZoneIII(Ri,Ru,R)
Yes – continue and increment R by .001 mm
No – last used R is approximately Rn
end
$\rho = \frac{R_n}{R_u}$

5 Output κ, η, ρ

end

Figure 5.4 Incremental bending routine to determine the solution to Eq. 45 (adapted from Tan et al., 1995).

CHAPTER 6
MATERIALS CHARACTERIZATION AND EXPERIMENTAL METHODOLOGY FOR BEND TESTING

6.1 Introduction

The experimental phase of this work involved pure bending of DP780 and DP980 under simple and general bending conditions, and then measuring the resulting springback. Springback under simple bending conditions were studied in an experimental V-die, having a punch radius (R_i) of 10.0 mm. For the DP780 and DP980 steels, the R_i/t ratio was 5.0 and 6.86 respectively. Springback under general bending conditions was studied in a commercial bending machine having a bending radius of 1.0 mm. The DP780 steel was used in these experiments as the DP980 steel cracked under these bending conditions.

The experimental work was composed of 2 main phases. In the first phase, the steels were compositionally identified as DP780 and DP980. Also, mechanical property (tensile testing) was required in order to provide work hardening curves for the FEA analysis of the bending experiments. The materials characterization and mechanical testing was performed at the ArcelorMittal-Dofasco Research and Development center (Van Riemsdijk, 2005). In the second phase, bending specimens were prepared from the steel sampled, and bending experiments were subsequently performed.

6.2 Materials characterization and coil sampling

Material characterization activities were performed by Van Riemsdijk (2005) on CR (cold rolled) DP780, and DP980 grades, having sheet thickness of 2.00 mm and 1.457 mm respectively. The materials were obtained from test coils, from ArcelorMittal (formerly Mittal Ispat Inland Steel). Descriptions of the steel coils are shown in Table 6-1. Test coupons for the mechanical, chemical and bending tests were cut at or near the centerline of the coil (also corresponding to the slit edge for the DP980 coil). Bending coupons were obtained close to the vicinity of the tensile coupons in order to minimize differences in the material properties between them, due to mechanical property variation across the coil width. Samples were taken from 1 meter long sheets, which were in turn sampled from the first 60 meters of the coil (i.e., coil lead). The sampling scheme is shown in Figure 6.1.

Table 6-1. Descriptions of coils, from which the DP780 and DP780 steels were sampled for the bending-springback experiments.

DP780 • Cold Rolled, grade DiForm T780 from Mittal Ispat Inland Steel. • Heat #528893 coil id# 857-593451. • Dimensions 58" x .079" x ~ 1880 ft. (29,319 lbs). 58" represents the full coil width.
DP980 • Cold Rolled, grade DiForm 140T from Mittal Ispat Inland Steel. • Heat #417405 coil id# 00900050703. • Dimensions 23.2" x .055" x ~1940 ft. (8,404 lbs). 23.2" represents an edge slit width (one edge had been cut; the other edge was the mill edge).

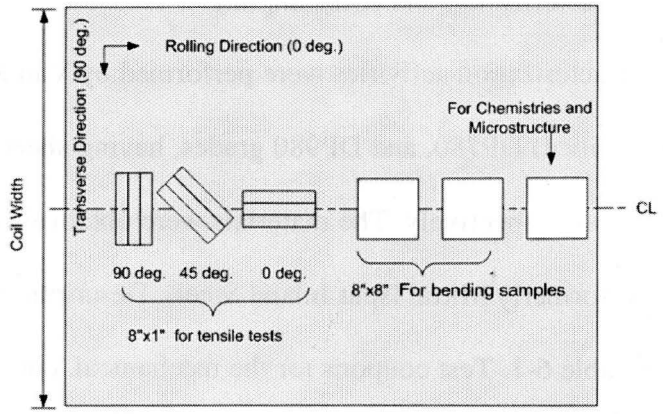

Figure 6.1 Sampling coupon scheme for various tests from a 1 meter long sheet, taken from the first 60 meters of the coil.

6.2.1 Chemical analysis

Optical emission spectrometry was performed on the steel coupons and the results are shown in Table 6-2 and Table 6-3. The chemistry of these steels can be described as carbon-manganese, with small additions of silicon. In DP steels, carbon and manganese are used to increase the hardenability of the steel allowing for the formation of martensite at cooling rates seen in steel mill operations (i.e., hot mill, or continuous annealing lines). Silicon also acts to strengthen ferrite through solid solution strengthening (AISI, 2006).

Table 6-2. Chemical analysis (wt %) of DP780 steel by optical emission spectrometry (coil lead, centerline position).

C	Mn	P	S	Si	Cu	Ni	Cr	Sn
0.10	1.79	0.009	0.005	0.332	0.04	0.01	0.02	0.008

Al_{sol}	Al_{tot}	N	Mo	V	Nb	Ti	Ca	B
0.036	0.042	0.0065	0.016	0.002	0.0029	0.0026	0.0022	0.0002

Table 6-3. Chemical analysis (wt %) of DP980 steel by optical emission spectrometry (coil lead, centerline position).

C	Mn	P	S	Si	Cu	Ni	Cr	Sn
0.15	1.41	0.014	0.005	0.314	0.03	0.01	0.03	0.004

Al_{sol}	Al_{tot}	N	Mo	V	Nb	Ti	Ca	B
0.043	0.050	0.0058	0.014	0.002	0.0029	0.0031	0.0024	0.0001

6.2.2 Microstructure

Coupon cross-sections, through the thickness and in the rolling direction, were obtained for microstructural analysis. The cross-sections were mounted, polished and then etched to reveal the microstructure. They were etched with 4% Nital etchant to reveal grain boundaries for metallographic imaging. A 4% picral etch was used to prepare samples for SEM (scanning electron microscopy) imaging in order to detect martensite. The resulting micrographs are shown in Figure 6.2.

Image analysis was also performed in order to quantify the martensite area fraction and ferrite grain size. Image analysis was performed using the Clemex Vision 3.0 image analysis software. Samples were etched with Nital and LePera's etchant in order to determine ferrite and martinsite grain sizes respectively. The results for the DP780 and DP980 steels are shown in Table 6-4.

SEM images confirmed the presence of martensite in the steel samples. Image analysis showed that the area fraction of martensite was larger in the DP980 sample compared to the DP780 sample. The microstructure of the DP780 steel was composed of uniformly distributed ferrite (α) grains and fine martensite.

The ferrite grains were coarser in the DP980 steel compared to the DP780 steels, and the distribution of martensite was non-uniform (Figure 6.2).

Table 6-4 Image analysis results for the DP780-980 steels.

	Sample Size	ferrite grain size		Martensite % area fraction	Martensite grain size (μm)
		ASTM	μm		
DP780	2	12.5	4.0	28	1.4
DP980	4	12.3	4.3	34	2.3

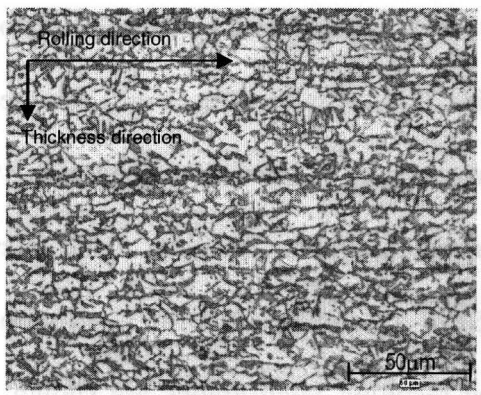

DP780, 4% Nital etchant

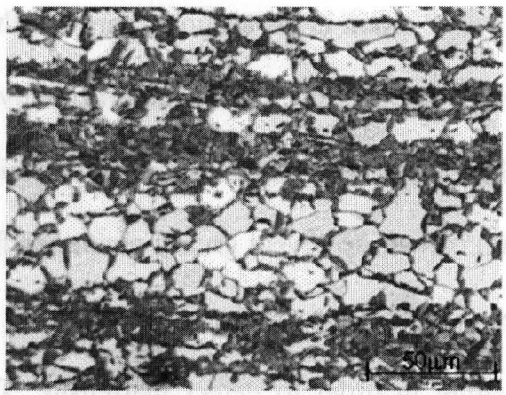

DP980, 4% Nital etchant

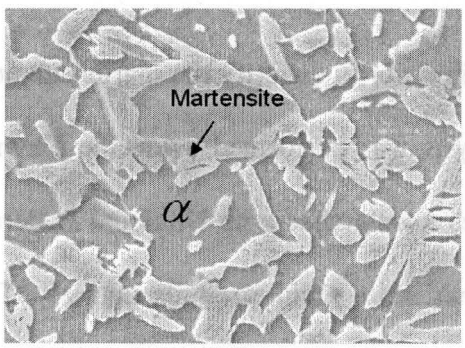

DP780 SEM 5000x, 4% picral

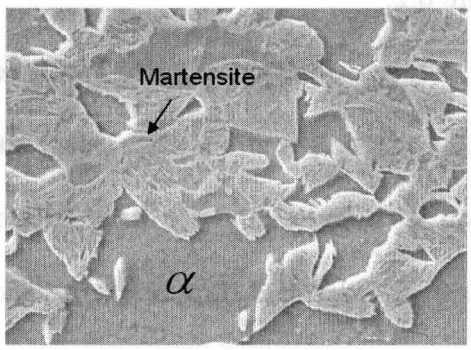

DP980 SEM 5000x, 4% picral

Figure 6.2 Metallographic and SEM images showing the underlying microstructure for the DP780 and DP980 steels. In the optical metallographic images, the dark and light phases are martensite and ferrite respectively. In the SEM image the martensite is angular, as shown.

6.2.3 Mechanical properties (tensile testing)

Tensile coupons were milled to standard dimensions according to the ASTM E8 standard. Tensile tests were performed on a screw driven mechanical testing machine using a constant crosshead speed of 0.1 inch per minute, up to approximately 2% engineering strain. After this point, the crosshead speed was changed to 0.5 inches per minute. Three samples per direction (i.e. 0°, 45°, and 90° to the rolling direction) were tested resulting in raw engineering stress-engineering strain curves. Standard engineering mechanical properties were also determined, for example, the 0.2% offset yield strength, ultimate tensile strength, elongation, n-value and r-value. The n-values were reported at 4-6% elongation, and r-values were measured at or just before uniform elongation using a laser based extensometer capable of measuring both axial and width strains. The average r value (or $\bar{R}$) was determined using the standard weighted averaging formula (Eq. 51 in Chapter 3). All tensile testing was performed at the ArcelorMittal Dofasco Research and Development Center in Hamilton, Ontario, Canada. The engineering mechanical property results are shown in Chapter 8 (Tables 8-1 to 8-2). These results show that the DP780 and DP980 steels are essentially isotropic.

The uni-axial true stress-plastic strain hardening curves in the rolling direction were used for the FEA models as hardening curves. The hardening curves were obtained from the raw engineering tensile curves using the formulas shown below. For example, Eq. 148 converts engineering strain to true strain. Eq.

149 converts engineering stress to true stress, and equation Eq. 150 calculates the effective plastic strain by subtracting the elastic portion of the effective strain. These equations and the true stress strain curve are valid up to the point of uniform elongation, which is just prior to diffuse necking in the tensile test.

$$\varepsilon_1 = \ln(1 + e_1) \qquad \text{Eq. 148}$$

$$\sigma_1 = S(1 + e_1) \qquad \text{Eq. 149}$$

$$\varepsilon_1^p = \varepsilon_1 - \frac{\sigma_1}{E} \qquad \text{Eq. 150}$$

Figures 8.18-8.20 (in Chapter 8) show representative tensile curves (true stress-true strain) from a tensile coupon in the sheet rolling direction.

6.3 V-die bending experiments

6.3.1 Bending samples preparation

Bending samples were rectangular in shape having the dimensions of 25.4 mm x 400 mm x thickness (in mm). Samples were cut from the coil pieces shown in Figure 6.1 using a commercial shear. Twisting and warping of the samples due to shearing was avoided by using a low blade angle and small clearance. Any samples with visible twist or warp were discarded. Once the bending samples were cut, the edges were deburred on a wet belt sander using 320 and then 600 grit sand paper. Samples were cut with the bending axis perpendicular (transverse coupons) and parallel (longitudinal coupons) to the sheet rolling direction for both the DP780 and the DP9890 steels. In the V-die bending experiments, two longitudinal and three transverse coupons were used from each steel grade.

6.3.2 V-bending die assembly

A CAD model of the V-die used for the experiments is shown in Figure 6.3. The V-die was designed and constructed specifically for this work, at the Manufacturing Research Institute (MMRI) at McMaster University. The die is equipped with varying punch inserts and a roller mechanism for the punch as shown in Figure 6.3. The tooling itself is composed of 2 main components. These are the punch assembly, and the die shown below. The dimensions of the V-die are shown in Figure 7.13 (Chapter 7) and the punch radius, which determines the nominal (engineering) bending strain, was 10 mm. The V-die dimensions were used in the development of the FEA models for V-die bending and springback.

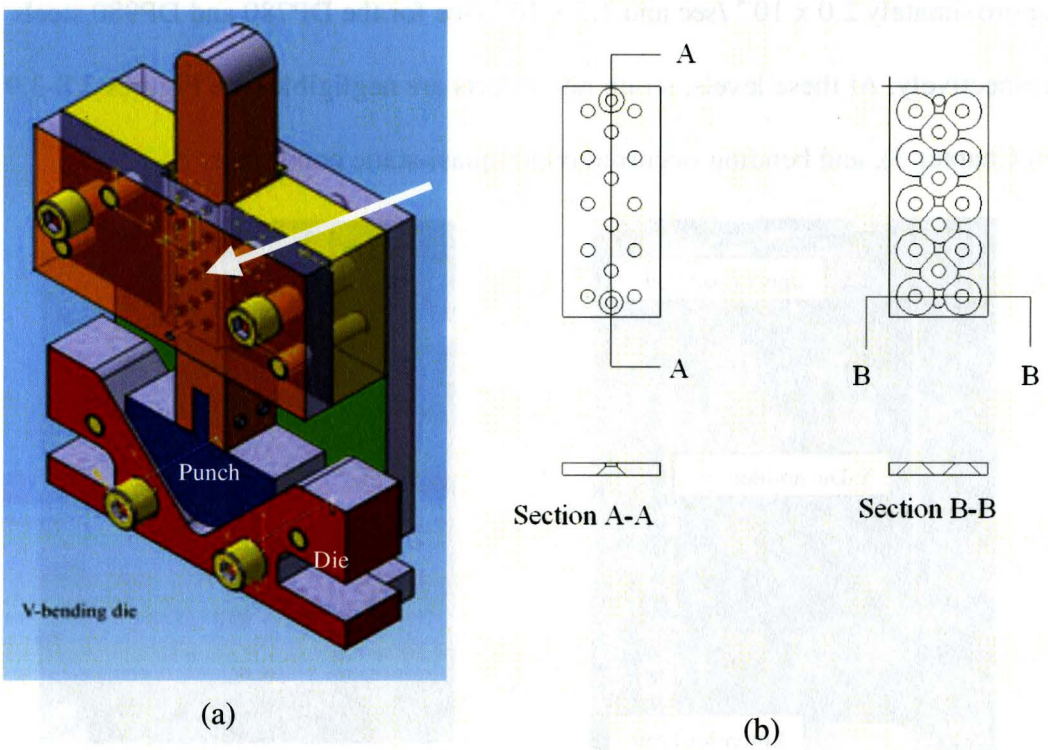

Figure 6.3 CAD model of V-Die assembly (a) showing punch slide mechanism that uses ball bearings to limit friction (b).

6.3.3 Experimental procedure

The V-die assembly was positioned inside a servo-hydraulically controlled mechanical test system (MTS), between the upper and lower load cells (Figure 6.4). Each bending specimen was placed in the V-die and pre-loaded with 30.5 N of force, from the weight of the punch assembly itself (Figures 6.5-6.7). The pre-load ensured that the bending sample was firmly fixed in the bending die prior to testing. Bending was accomplished by the vertical downward movement of the punch assembly (Figure 6.6) while keeping the die at a fixed position. The duration of a given bend test was approximately 115 seconds. From the nominal bending strain (Eq. 2), the maximum strain rate in bending was therefore approximately 2.0×10^{-4} /sec and 1.5×10^{-4} /sec for the DP780 and DP980 steels respectively. At these levels, strain rate effects are negligible (see Figures 3.8-3.9 in Chapter 3), and bending occurred under quasi-static conditions.

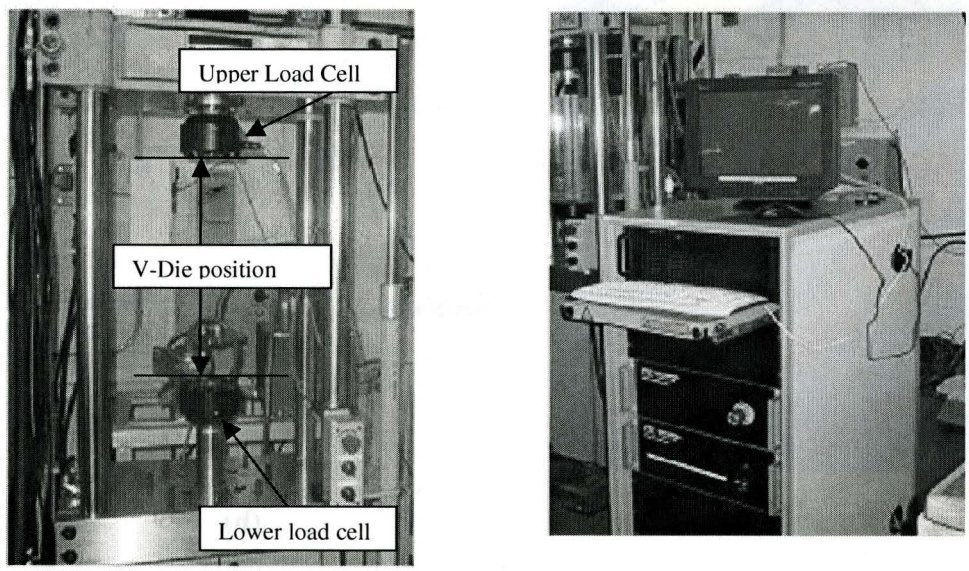

Figure 6.4 MTS Frame showing placement of V-die assembly (a) as well as the controller and data acquisition unit.

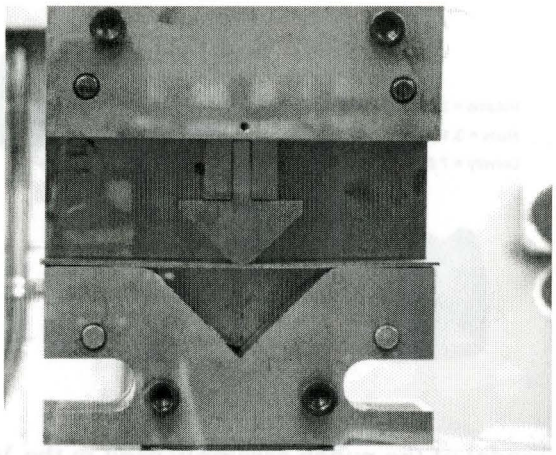

Figure 6.5 Placement of bend specimen in the V-die showing initial deflection due to the weight of the punch.

The sequence of events in the V-die bending experiments is shown in Figure 6.6. At the start of testing, the bending sample is preloaded as mentioned previously. The punch is then displaced a fixed distance, which has been previously programmed into the MTS controller, until the end of the bending stage. In the springback stage, the punch is manually retracted to allow springback to occur.

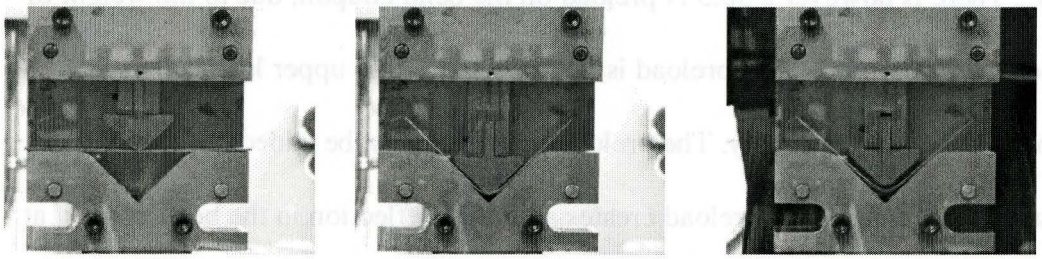

(a) (b) (c)

Figure 6.6 V-die bend testing sequence showing (a) start and (b) end of bending, and unloading of the punch resulting in springback (c).

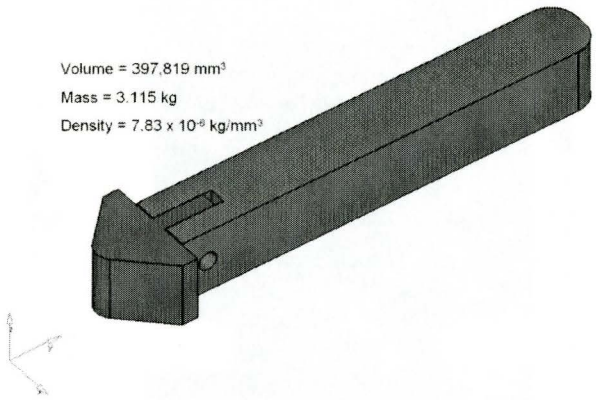

Figure 6.7 CAD model of the punch assembly used in the V-die assembly used to calculate the preload due to the weight of the punch.

The punch movement during a test was controlled by an MTS controller. Punch reaction forces were recorded in real time by the upper load cell. The punch displacement was also recorded in real time by recording the position of the punch actuator. Data files for each test were created and saved to the computer attached to the test system.

At the start of a test, the recorded punch force and displacement are both "0". There is however a 30.5 N preload on the bend coupon, due to the weight of the punch assembly. This preload is not detected by the upper load cell as it is above the punch assembly. The preload therefore must be added to the recorded punch forces. Also, the preload creates an initial deflection in the bend coupon at the start of the bend test. The initial deflection from the preload must be added to the recorded punch displacements. An FEA of the preload condition on the test specimen was used to estimate the initial displacement of the blank under the preload (or weight of the punch). The results are shown in Figures 6.8-6.9.

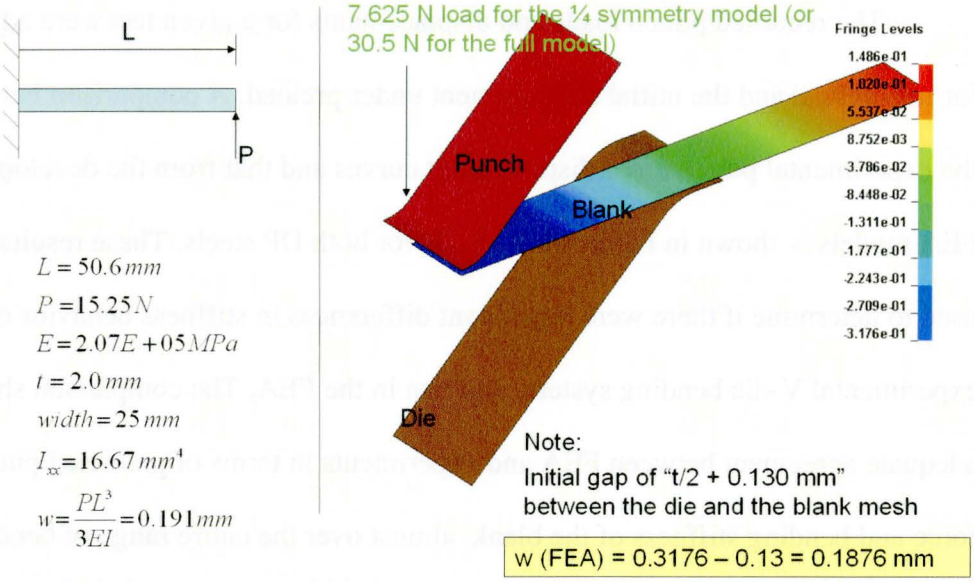

Figure 6.8 DP780, FEA predicted blank deflection due to the punch assembly weight of 30.5 N. Shown also for comparison is the analytical (beam model) prediction.

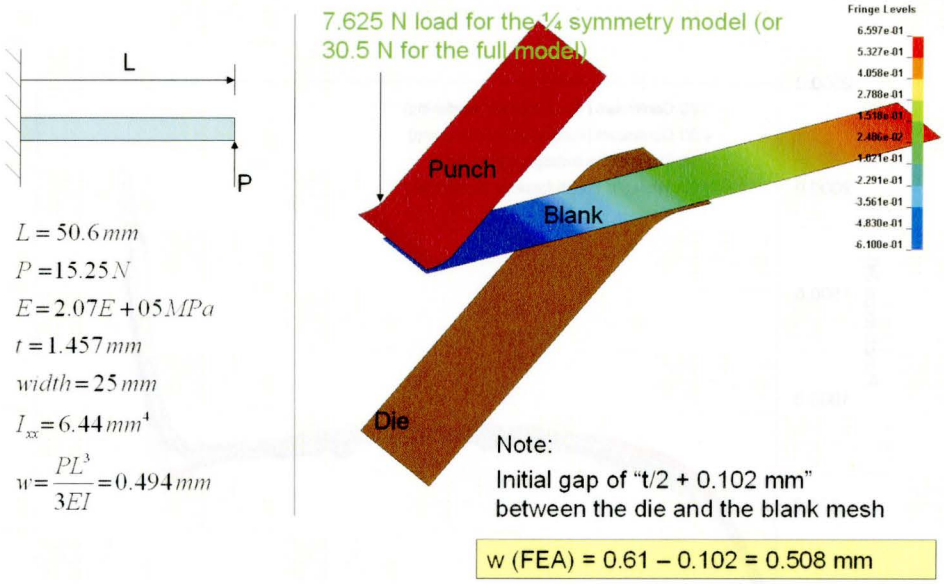

Figure 6.9 DP980, FEA predicted blank deflection due to the punch assembly weight of 30.5 N. Shown also for comparison is the analytical (beam model) prediction.

The recorded punch loads and displacements for a given test were adjusted for the preload and the initial displacement under preload. A comparison between the experimental punch force-displacement curves and that from the developed FEA models is shown in Figures 6.10-6.11, for both DP steels. These results were used to determine if there were significant differences in stiffness behavior of the experimental V-die bending system, and that in the FEA. The comparison showed adequate agreement between FEA and experiments in terms of predicted punch force and bending stiffness of the blank, almost over the entire range of bending (forming). There are discrepancies at the end point of the curves (or end of the bending test); however, at this point the punch force is extremely sensitive to the punch displacement.

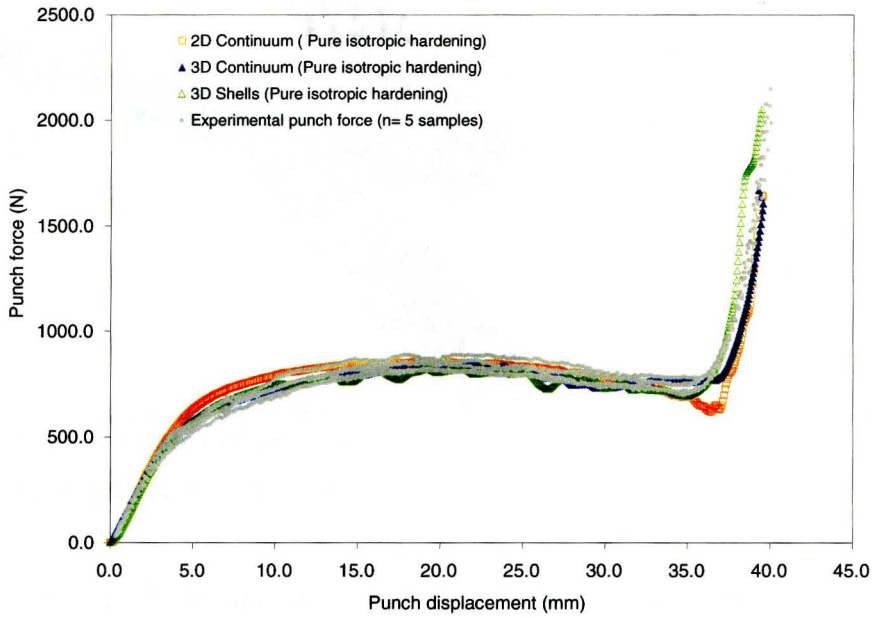

Figure 6.10 Punch force as a function of punch displacement for the DP980 steel V-die bend tests, compared to FEA. The experimental curves have been corrected for the preload and initial displacement under the preload.

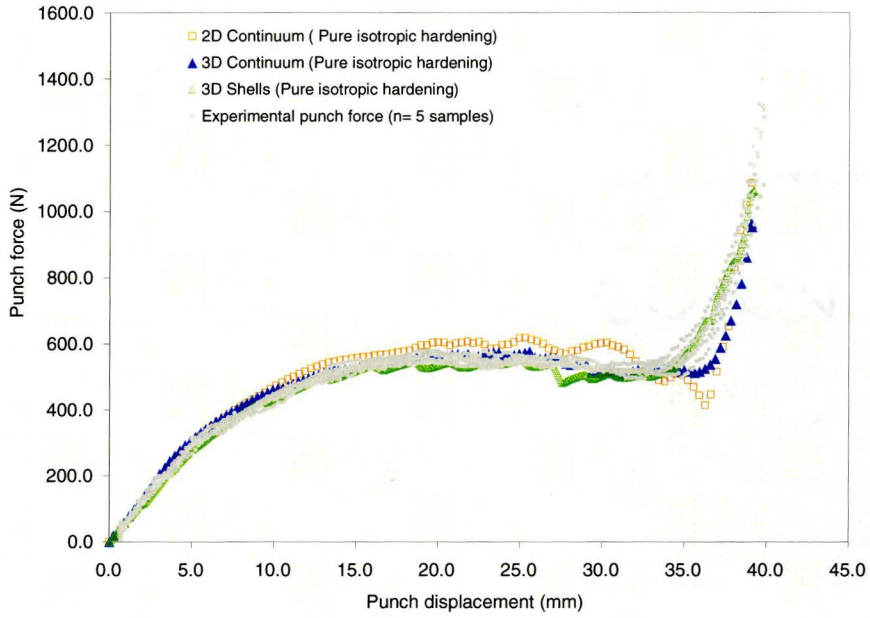

Figure 6.11 Punch force as a function of punch displacement for the DP980 steel V-die bending tests, compared to FEA. The experimental curves have been corrected for the preload and initial displacement under the preload.

6.4 In-situ digitization of the punch position at the end of each bending test using a coordinate measuring machine (CMM)

A FARO arm (model Silver series) portable CMM was used to digitize the final punch position at the end of each bend test (prior to springback), as well as the deformed (bent) shape of the blank. By knowing the experimental final punch position, the appropriate punch motion boundary conditions can be determined and therefore used in the development of the FEA models. The average punch positions, from 5 tests for each of the DP steels, are shown in Table 6-5.

The FARO arm CMM is shown in Figure 6.12 and has a rated accuracy of ± 0.078 mm (2 sigma) for a single point digitization. A "point probe" tip having an effective radius of 0.1 mm was used in the experiments.

Table 6-5 Average punch position at the end of bending as measured by CMM.

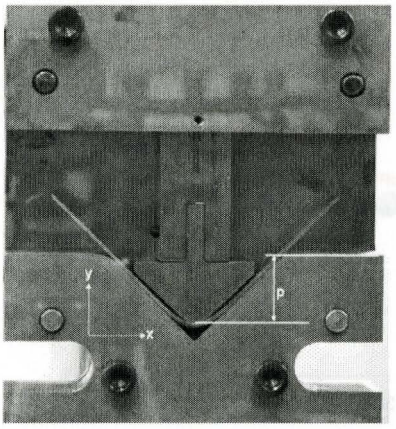

	Punch position relative to die face (mm)
DP780 V-die bend tests	Avg. = 37.8 mm Std. = 0.08 N = 5
DP 980 V-die bend tests	Avg. = 37.5 mm Std. = 0.33 N = 5

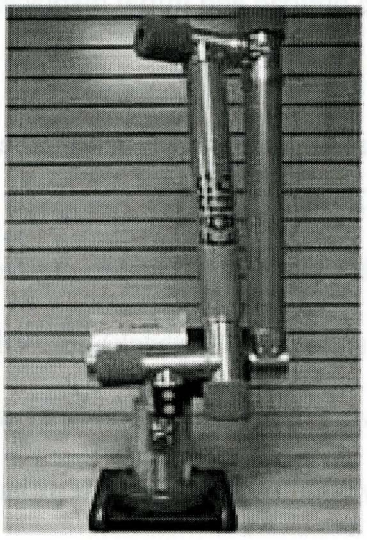

(a) (b)

Figure 6.12 Silver Series FARO Arm (a) and 0.1 mm diameter point probe used in the digitization of bend specimens.

Prior to testing, the FARO arm was placed near the MTS load frame, and the point probe was calibrated against a 25 mm reference sphere. At this point in the calibration, the effective probe tip diameter was determined by the CMM software.

Data acquisition of all digitized points was performed using a laptop computer and the CALIPER3D software, designed for the FARO arm. All data points were saved to the computer and then converted to an AUTOCAD "DXF" file for input into a CAD system. In addition to the point probe calibration against the 25 mm diameter sphere, before each test, a reference coordinate system was created using the CMM on the top surface of the V-die. Referring to Figure 6.13, the reference coordinate system was created by first digitizing points 1, 2, and 3 to form the level plane or XY plane. All points on this plane will have a z-coordinate of "0". Next, the edge of the V-die is digitized (points 1 and 2) to form the x-axis. Point 4 is digitized to define the point x=0. Once the coordinate system is set up, bend testing proceeds until the maximum punch displacement is reached.

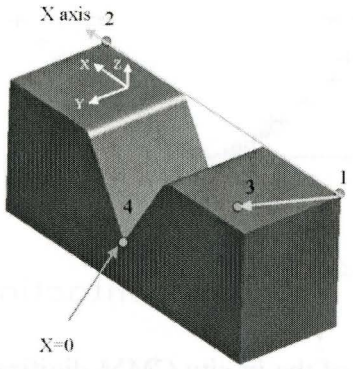

Figure 6.13 CMM digitization procedure for alignment and creation of a coordinate system on the die, prior to testing.

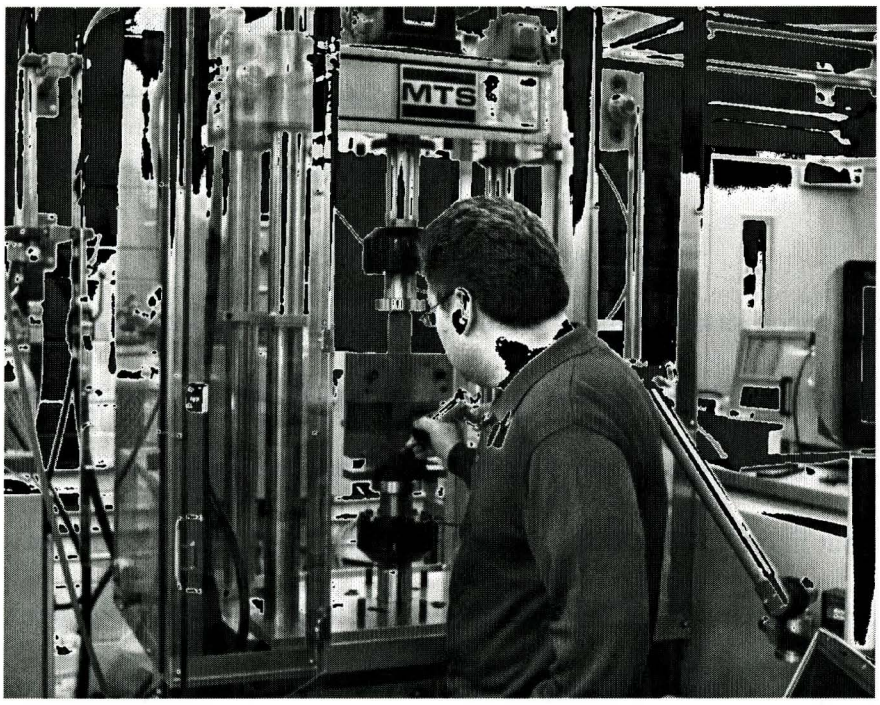

Figure 6.14 V-die assembly positioned inside the MTS frame during an actual bending test. Also shown is the in-situ digitization of the deformed specimen using a Silver Series portable CMM (FARO arm).

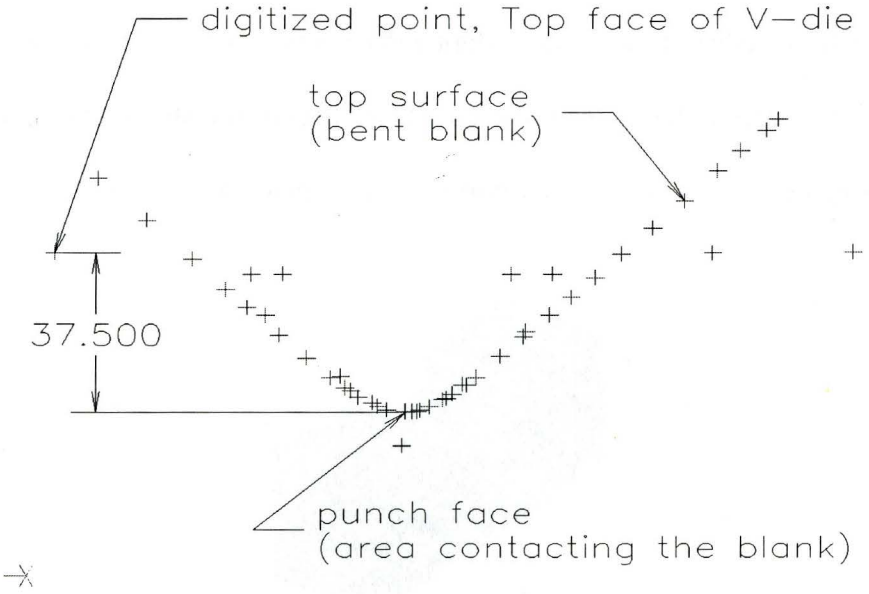

Figure 6.15 An example of the in-situ CMM digitization of key features, including the top die face, punch face, and bending sample (dimensions in mm).

Figure 6.14 is a view of the in-situ CMM digitization process at the end of bending, and Figure 6.15 shows the corresponding sample output from the CMM. From the CMM measurements the punch position relative to the top die face is apparent. The CMM data was also used to measure the bend angle in a blank, just prior to springback. The digitized data that was saved to a DXF file was converted to XYZ data using the Hypermesh preprocessing software. The data was then read into Microsoft Excel, and linear regression analysis was performed in order to calculate the slopes along the two flanges of the sample. This is shown in Figure 6.16 for three DP780 samples, and in this case the data from the different bending tests were shifted in the vertical coordinate in order to fit 3 curves on one plot. The bend angle for a given test was then calculated using Eq. 151.

$$\tan(\theta)=\frac{m_2-m_1}{1+m_1m_2},\ m_2>m_1 \qquad \text{Eq. 151}$$

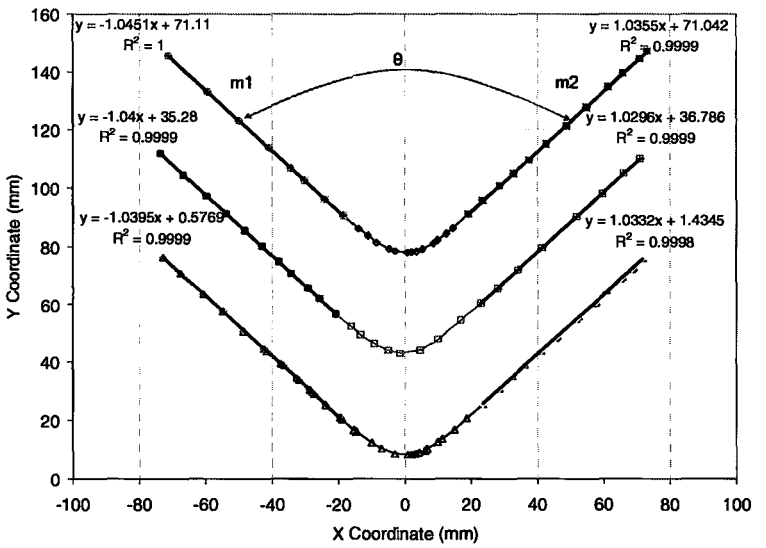

Figure 6.16 CMM point data in excel used to calculate the bend angle in the V-die bending experiments.

6.5 Small radius bending experiments using a commercial bending machine

6.5.1 Bending samples preparation

Bending samples for the small radius bending experiments were prepared having the dimensions of 100 mm x 25 mm x thickness. These samples were prepared from the V-die bending samples for both DP steels, by shearing them in half. Similar to the V-die samples, the edges were deburred and sanded to a 600 grit finish. Three bending samples were tested for each DP steel, all having the bending axis perpendicular to the sheet rolling direction.

6.5.2 Small radius bending machine

The bending machine used was a Brown and Boggs manual bender (circa 1960), equipped with a number of segmented bending blocks. The machine is located in the ArcelorMittal Research and Development Center in Hamilton Ontario, Canada (Figure 6.17). In a given bending experiment, a 25 mm wide specimen was bent around a bending block having a radius of 1 mm, and an inclination of 40° (Figure 6.18). Unlike the earlier V-die experiments, there was no instrumentation for real time data acquisition during a bending test. Also it was assumed that the blanks were bent to an inclination angle of 40° just prior to springback. The sequence of events in a test are; clamping of the blank between the bending block and the base, and then manually bending the sample until the upper flange just contacts the bending block. Bending was timed to occur over a period of 60 seconds. This implies a strain rate of approximately 8×10^{-3} /sec and

as in the case of the V-die bending experiments, stain rate effects were therefore negligible.

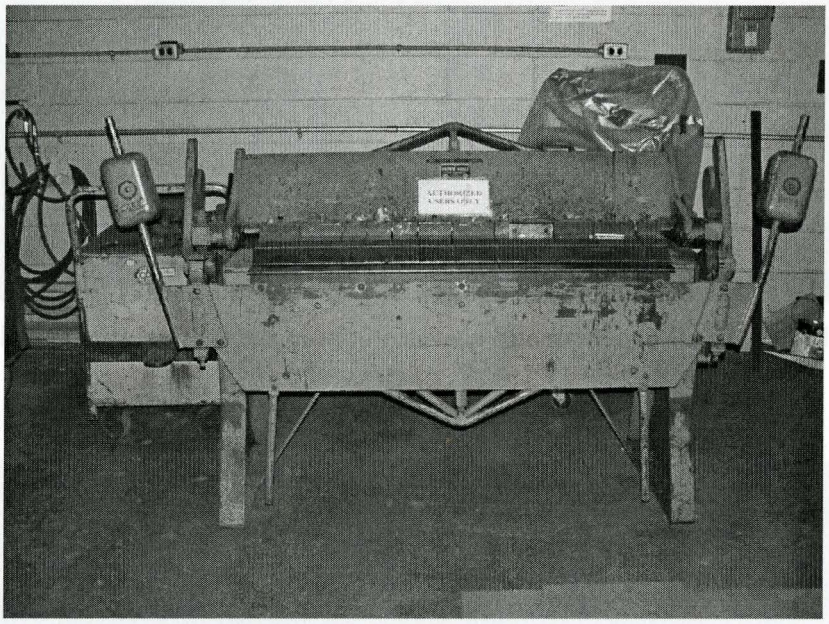

Figure 6.17 Brown and Boggs manual bending machine circa 1960.

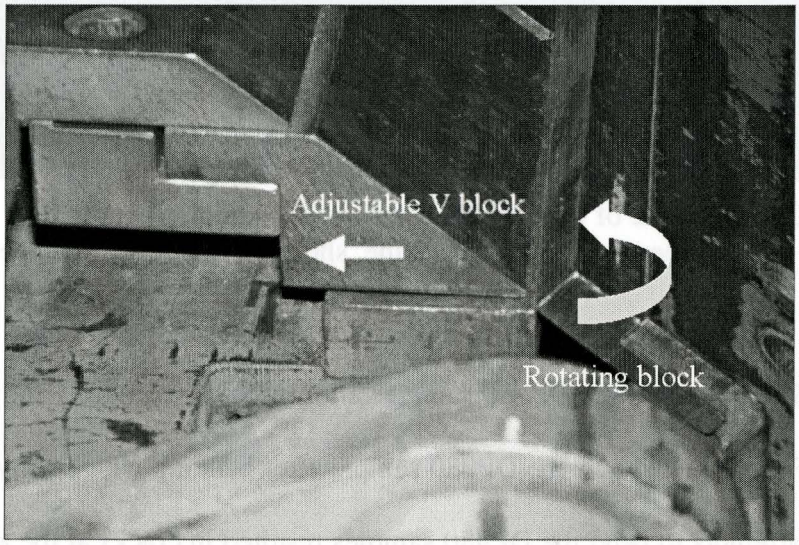

Figure 6.18 Commercial (manual) bending machine used to bend DP780 samples around a 1 mm radius, and an inclination of 40°.

Figure 6.19 DP780 experimental samples bent in the commercial bending machine.

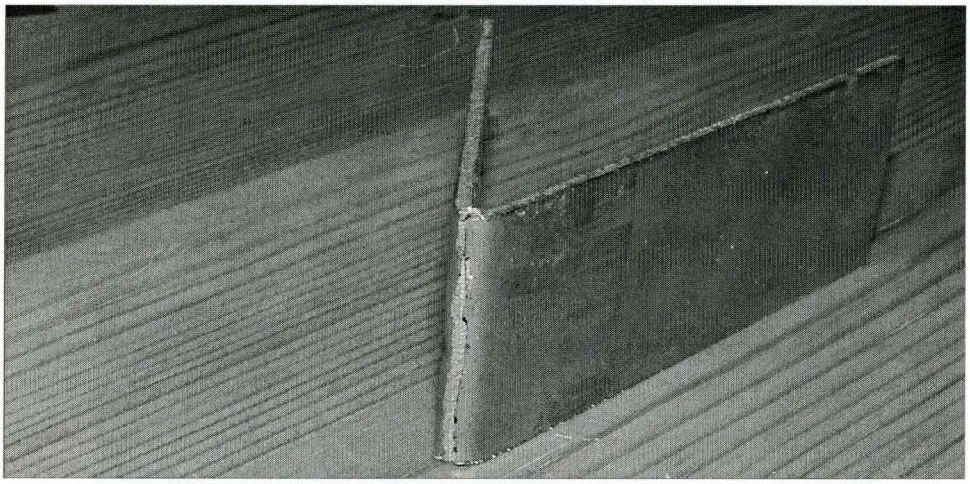

Figure 6.20 Example of the DP980 experimental samples bent in the commercial bending machine, showing fracture at the apex of the bend.

Figure 6.19 shows the three DP780 samples after removal from the bending machine. Figure 6.20 shows the DP980 sample after bending which shows a crack. All attempts to bend the DP980 samples resulted in cracks at the apex of the bend, and therefore the analysis of bending and springback was restricted to the DP780 steel only.

6.6 Springback measurements in bent samples from V-die bending and small radius bending

The FARO arm portable CMM was also used to digitize bent samples after removal from the V-die and the small radius bending tooling. Samples were placed on a toolmakers magnetic base which firmly fixed the flanges of the samples. The magnetic force from the base was enough to stop any sample movement or deflection of the flanges during CMM digitization.

Similar to the procedure of the in-situ CMM measurement in V-die bending, a 0.1 mm point probe was used (Figure 6.22). The probe was first calibrated against a 25 mm reference sphere in order to determine the effective tip diameter of the probe. A reference coordinate system was also created for the magnetic base. The level or XY plane was determined from 3 digitized points on the face of the magnetic base. An X axis was created by digitizing two points on the edge of the base. The approximate center of the base was digitized to create the origin.

CMM digitization was performed along the approximate centerline of the sample (perpendicular to the bending axis). All digitized points were essentially projected to the XY plane, or in this case the magnetic base. The centerline of the specimen was digitized in order to avoid the sample edge areas, where the bending sample geometry was affected by anticlastic curvature. As earlier, the digitized data was saved to a DXF file, and converted to XYZ data using the Hypermesh preprocessing software. The data was then read into Microsoft Excel

and the angle after springback was calculated using the slope method from section 6.4. An example using the CMM data from the small radius bending experiments is shown in Figure 6.22.

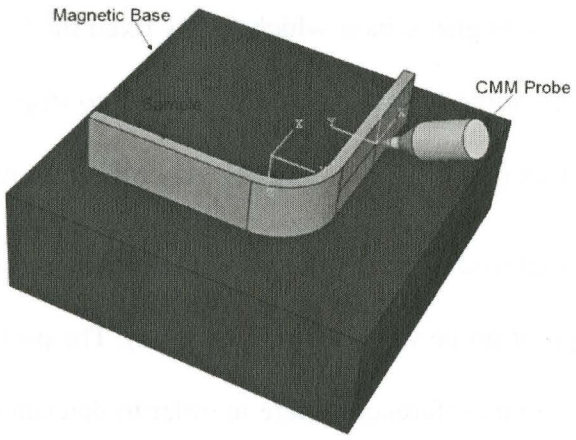

Figure 6.21 Schematic of the CMM inspection of a bending sample firmly fixed to a toolmakers magnetic base.

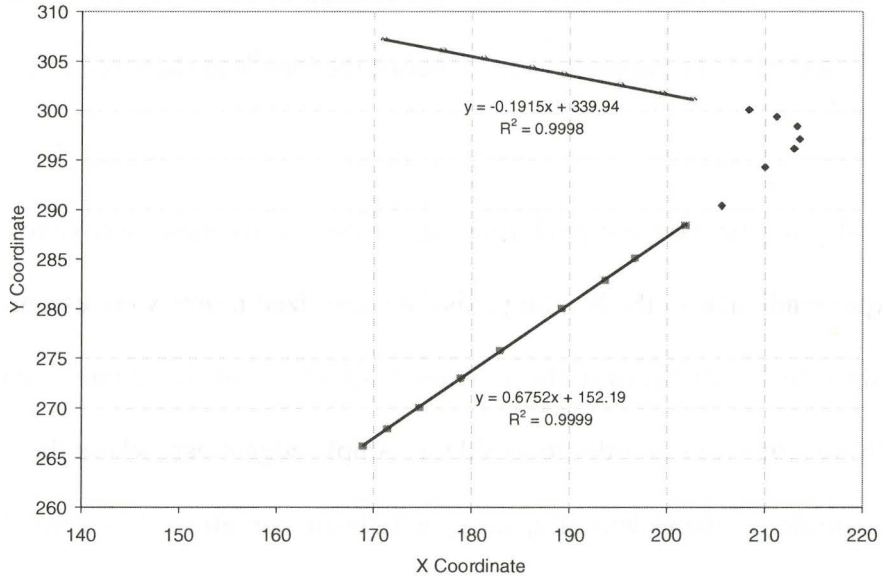

Figure 6.22 CMM point data example in Microsoft Excel, used to calculate the bend angle in the small radius bending experiments.

CHAPTER 7
DEVELOPMENT OF FEA MODELS FOR BENDING AND SPRINGBACK

7.1 Introduction

In Chapter 4 an overview of FEA modeling of sheet metal forming and springback using LSDYNA3D was presented along with descriptions of the FEA parameters used. This chapter applies the concepts from Chapter 4 in describing the development of FEA models used for this thesis.

The FEA of V-die bending in the work by Queener and De Angelis (1968) was performed using the LSDYNA3D FE code. The models were constructed using the recommended practices for FE modeling of sheet metal forming and springback by the software vendor, Lawrence Livermore Software Corporation (Maker and Zhu, 2001). These models used shell elements exclusively.

In the FEA of the small radius and V-die bending experiments, other approaches were used. The development of these models involved the use of advanced material models, continuum and 3D shell elements. Also, convergence analysis was used to minimize mesh discretization error in terms of the predicted springback. All the FEA analysis of the experimental work was performed at the ArcelorMittal –Dofasco offices using a single CPU workstation. The FEA code LSDYNA3D (version 971) was used for all simulations. The FEA using the explicit method was performed using the single precision explicit version of LSDYNA3D. The FEA using the implicit method used the double precision version of LSDYNA3D.

7.2 FEA study of V-die bending in the work by Queener and DeAngelis (1968)

The FEA study of V-die bending and springback in the work by Queener and DeAngelis (1968) was performed for the 1095 steel in their study. Baseline FEA models were first constructed in order to compare FEA to Queeners's experimental and analytical results. Other FEA models were then made using minor changes to the baseline FEA models, in order to investigate the effects of tooling friction, FEA solution procedure, bending moment distribution, and anticlastic curvature on springback. A summary of all FEA models used for the study is shown in Table 7-1. Descriptions of these models are presented in the following sections.

7.2.1 Material properties used in the FEA

Limited material property data was provided in Queener's study. For the FEA, the blank material was assumed to yield according to Von Mises criterion, and obeyed the Hollomon hardening law. The material was assumed to have the same yield in tension and compression (i.e. pure isotropic hardening behaviour). These assumptions are consistent with those used by Queener and DeAngelis in their study for simple bending conditions. The material properties used for the 1095 steel are shown in Table 7-2. Based on these material properties, the work hardening curve for the FEA was generated as a true stress-plastic strain curve (Figure 7.1). The material model used in the FEA was MAT37, which is based on Hill's 1948 transverse anisotropic yield criterion. To model Von Mises criterion,

the $\bar{r}$ input to MAT37 was set to a value of 1. All tooling was modeled as perfectly rigid.

Table 7-1 Overview of models used in the FEA study of the work by Queener and DeAngelis (1968).

FEA Model	Description	FEA solution procedure	
		bending	springback
1	Baseline Ri =13.46 mm, μ =0.0	explicit	implicit
2	Baseline , Ri =33.82 mm, μ =0.0	explicit	implicit
3	Baseline , Ri =52.93 mm, μ =0.0	explicit	implicit
4	Baseline , Ri =72.04 mm, μ =0.0	explicit	implicit
5	Baseline , Ri =89.91 mm, μ =0.0	explicit	implicit
6	Ri =13.46 mm, μ =0.125	explicit	implicit
7	Ri =33.82 mm, μ =0.125	explicit	implicit
8	Ri =52.93 mm, μ =0.125	explicit	implicit
9	Ri =72.04 mm, μ =0.125	explicit	implicit
10	Ri =89.91 mm, μ =0.125	explicit	implicit
11	Ri =13.46 mm, μ =0.20	explicit	implicit
12	Ri =33.82 mm, μ =0.20	explicit	implicit
13	Ri =52.93 mm, μ =0.20	explicit	implicit
14	Ri =72.04 mm, μ =0.20	explicit	implicit
15	Ri =89.91 mm, μ =0.20	explicit	implicit
16	Ri =13.46 mm, μ =0.125	implicit	implicit
17	Ri =33.82 mm, μ =0.125	implicit	implicit
18	Ri =52.93 mm, μ =0.125	implicit	implicit
19	Ri =72.04 mm, μ =0.125	implicit	implicit
20	Ri =89.91 mm, μ =0.125	implicit	implicit
21	Ri =13.46 mm, μ =0.0, plane strain edge restraints	implicit	implicit
22	Ri =33.82 mm, μ =0.0, plane strain edge restraints	implicit	implicit
23	Ri =52.93 mm, μ =0.0, plane strain edge restraints	implicit	implicit
24	Ri =72.04 mm, μ =0.0, plane strain edge restraints	implicit	implicit
25	Ri =89.91 mm, μ =0.0, plane strain edge restraints	implicit	implicit

Table 7-2 Available material properties for a 1095 steel from the study by Queener and DeAngelis (1968).

Material	Thickness (mm)	Elastic Modulus (MPa)	Strength coefficient (MPa)	n-value
AISI 1095 steel	2.49	207000	2447	0.085

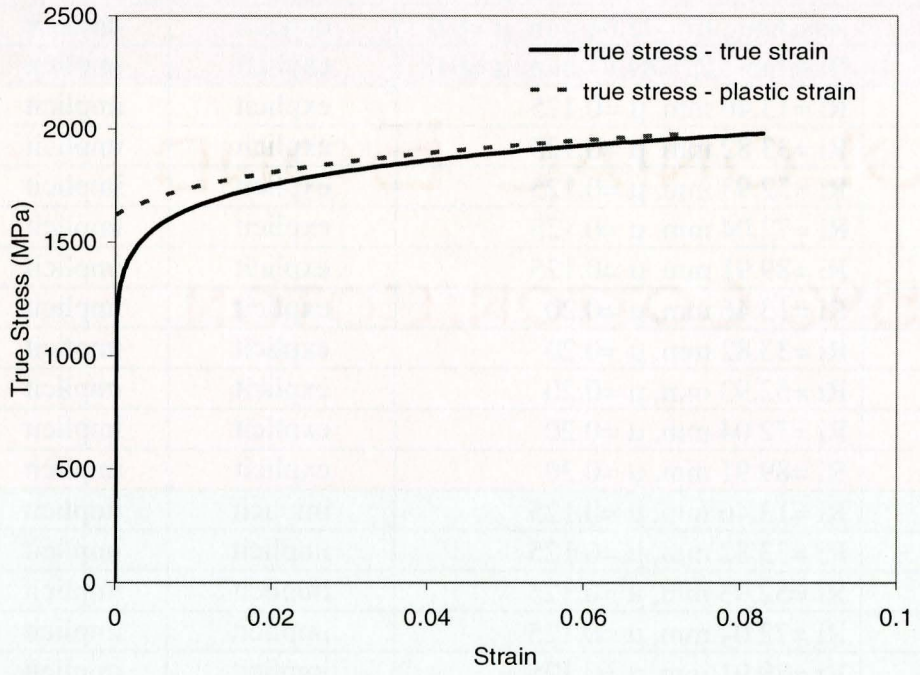

Figure 7.1 True stress-plastic strain hardening curve for AISI 1095 steel, derived from the Hollomon hardening law (Table 7-2).

7.2.2 V-die tooling mesh

There were limited details provided with respect to the V-die geometry in Queener's study. Five punch radii ranging from 13.46 mm to 89.91 mm were used. For the FEA, the V-die tooling geometry was therefore assumed as shown in Figure 7.2. Accordingly 5 FEA meshes were constructed from CAD models such as that shown in Figure 7.3, which shows the CAD model for a punch radius of 33.82 mm. The theoretical punch displacement for each punch radius case was also calculated from the CAD data. The punch displacement from the CAD therefore assumed that the blank shape after bending was described by a series of arcs and lines. The deformed blank shape is actually parabolic (Asnafi, 2000).

In the explicit forming FEA technique, the punch displacement is an important input to the FEA model which also determines the simulation time for the determined punch velocity. The FEA of V-die bending used punch velocity profiles that were trapezoidal, having a maximum punch velocity of 2 m / s, and a 0.002 second ramp, at the beginning and the end of the simulation (Figure 7.4).

The punch displacements for each FEA model in Table 7-1 were calculated from CAD (Figure 7.2). These calculated values represent the punch displacements in the absence of tooling clearance. In the construction of the tooling meshes, the punch was placed 0.025 mm above the top surface of the blank to avoid contact instabilities at the start of the simulation. This effectively created a 0.025 mm clearance between the punch and the blank at the end of the simulation, while the punch displaced a total distance as calculated from CAD.

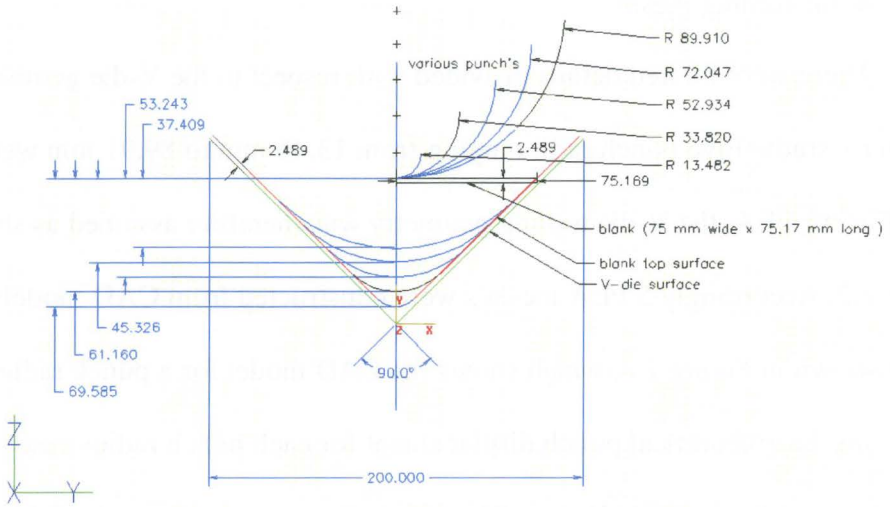

Figure 7.2 2D CAD drawing of V-die tooling geometry used for the FEA study of the work by Queener and DeAngelis (1968). Shown are theoretical (CAD) punch displacements (in mm) for various punch radii.

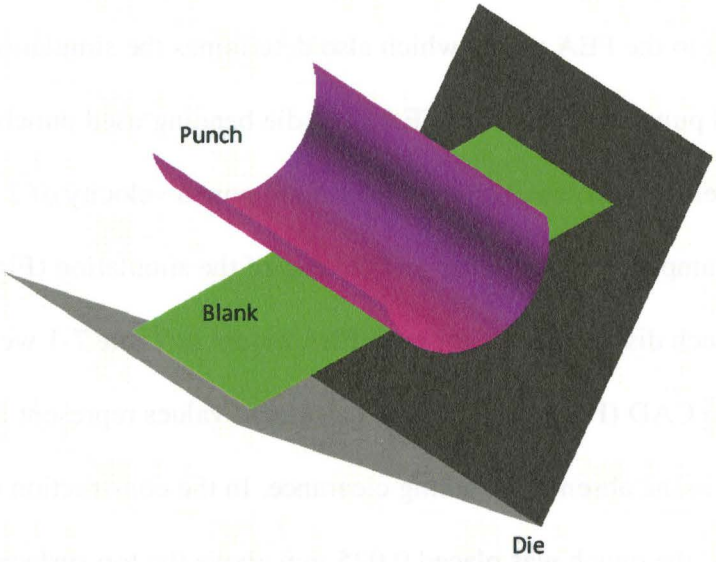

Figure 7.3 3D CAD model of the V-die tooling for the punch radii (R_i) of 33.82 mm.

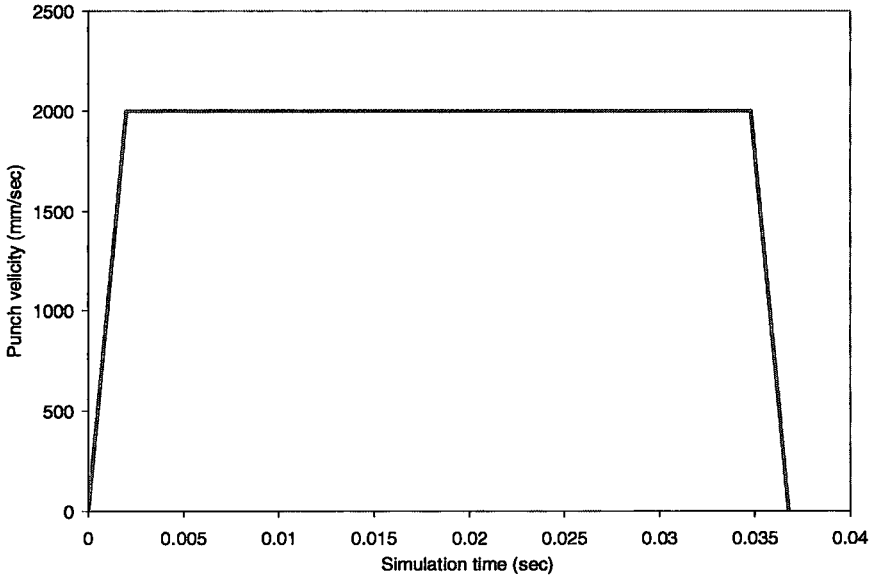

Figure 7.4 Punch velocity profile used for the baseline forming FEA for the punch radius of 13.46 mm.

LSDYNA3D explicit was used for the FEA of bending (forming). The V-die tooling was modeled as perfectly rigid and the blank was modeled as elastic-plastic using MAT37. The V-die bending mesh was constructed exclusively of shell elements. The blank mesh was constructed using the recommended fully integrated element "type 16", with 9 Gaussian through-thickness integration points. This element formulation is based on the work of Simo and Aremero (1992), having a 2 x 2 array of in- plane integration points. Historically, the Belytschko-Tsay element (type 2 in LSDYNA) was recommended for the forming simulation, and the fully integrated element type 16 for the springback simulation. The Belytschko-Tsay element is an under integrated element having one in-plane integration point. Having only one in-plane integration point for the forming simulation is inferior to full integration, giving inferior resolution of forming

stresses. This can lead to poor convergence behavior in the springback FEA (Maker and Zhu, 2001).

The blank mesh was constructed using a uniform element size of 2.0 mm x 2.0 mm. This ensured at least 5 elements in the bending portion of the blank. For this part of the FEA, convergence analysis was not performed as the element size used was based on the recommendations from the software vendor LSTC (Maker and Zhu, 2001). The tooling mesh was constructed using the Belytschko-Tsay shell element and also using the guidelines from LSTC. Such as having at least 5 elements were around the punch and die radii. All FEA models used ½ symmetry to reduce the model size. The mesh for the FEA model using a punch radius (R_i) of 33.83 mm is shown in Figures 7.5-7.6. A plan view of the blank mesh with the symmetry boundary conditions on the blank mesh is shown in Figure 7.6.

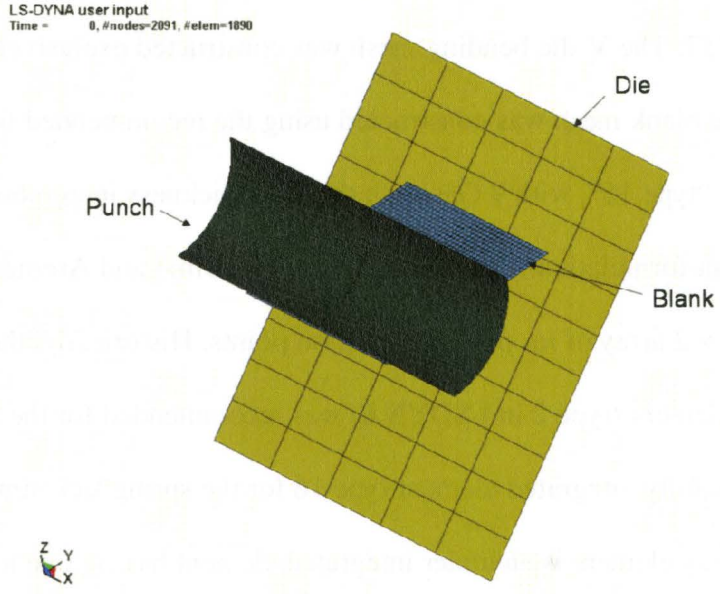

Figure 7.5 FEA mesh for the tooling using Ri of 13.46 mm. Note that XZ plane symmetry is used in the FEA.

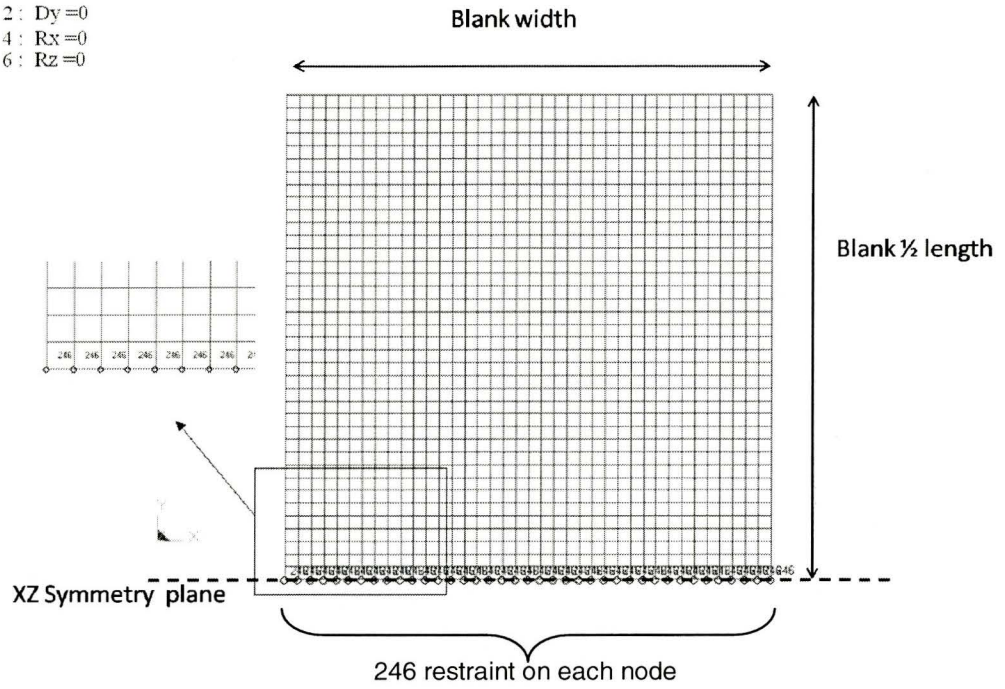

Figure 7.6 FEA mesh for the blank showing symmetry boundary conditions.

Contact between the deformable blank and rigid tools was modeled using the penalty method, and in LSDYNA, the contact card "one way forming surface contact", was used. The global contact interface stiffness was set at the standard value of 0.01. A standard damping of 20% of the critical value was used to eliminate "chattering" in the contact interface between the blank and tools. The elastic modulus and Poisson's ratio for the tooling was 207,000 MPa, and 0.3 respectively, the same values for the blank. Although the tooling was modeled as perfectly rigid, these material parameters are used in LSDYNA to determine the contact interface stiffness between the blank and the tools. Friction in contact was modeled as Coulomb friction, and in the baseline FEA a friction coefficient of "0"

was used. A summary of the important FEA numerical parameters used is shown in Table 7-3.

Table 7-3 FEA parameters used in the baseline simulations for the forming-bending FEA (based on recommended practices as described by Maker and Zhu, 2000)

V-die forming simulation parameters	
Time integration	explicit
Element	Type 16 (fully integrated shell)
Contact Penalty Stiffness factor	0.01
Contact Type	Forming one way surface to surface, with 20% damping
Maximum Punch Velocity and velocity profile	2 m/sec, using a trapezoidal velocity profile.
Number of elements in the bend (radii)	At least 7
Through thickness integration	9 points, Gaussian –Legendre
Number of cycles/time steps per mm of punch stroke.	At Least 500
Friction	Coulomb type, 0.0
Material Model	Type 37, Von Mises criterion for =1

7.2.3 FEA of Springback

At the termination time of the forming simulation, the FEA results for the blank are output to a file (Dynain file) for the subsequent springback FEA. Contact interfaces are also deleted. The Dynain file contains the deformed mesh, stress and strain state, as well as symmetry boundary conditions. Additional springback constraints must be added to the blank model in the "Dynain" file, in order to eliminate rigid body motions. Without this step the global stiffness matrix would be singular. Physically, this would mean that a small load applied to the model would create an infinite displacement without any change in the stress

state. The addition of springback constraints at the optimal locations implies that springback evolves during the analysis, without developing significant reaction forces at the constraint points. The recommended practice in LSDYNA is to eliminate rigid body motion by constraining translational degrees of freedom only. This is performed at 2 nodes on the symmetry line for models using ½ symmetry, or at 3 nodes for other models without symmetry. The use of rotational constraints is not recommended, as this leads to large numerical errors and problems with convergence (Maker and Zhu, 2001). For the FEA of springback of Queener's work, the required constraints are shown in Figure 7.7.

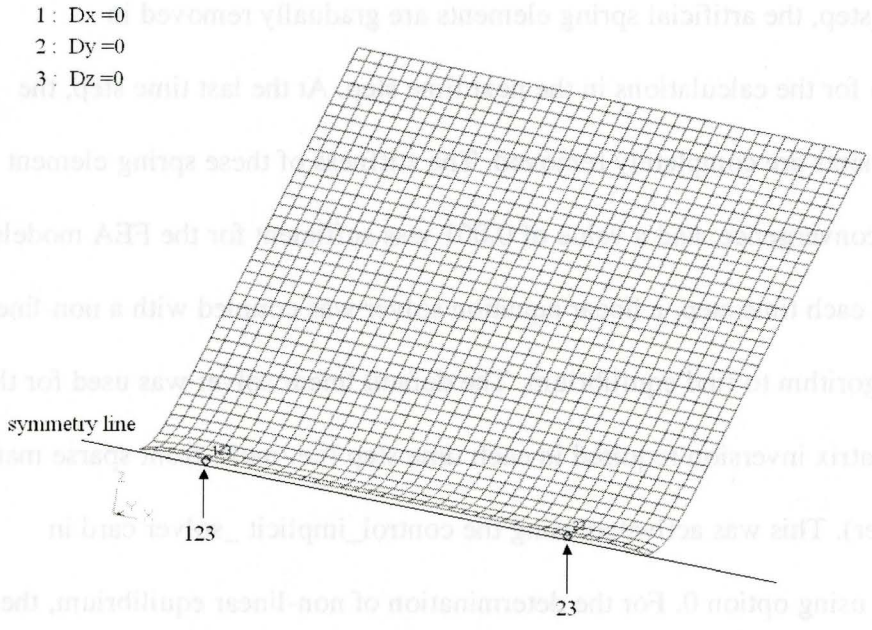

Figure 7.7 Deformed mesh after forming (stresses, strains not shown) from the Dynain FEA output file. Shown are constraints required to eliminate rigid body motion for the springback FEA. These constraints are used in addition to those from the forming FEA shown in Figure 7.6.

Numerical details regarding the static implicit method were described in Chapter 4, and this section augments the description. The procedure for the FEA of springback requires modeling non-linear unloading or redistribution of the forming stresses in the deformed blank. For the FEA, the solution was divided into 4 times steps, with a termination time of 0.004 seconds. The actual simulation time has no physical meaning, but allows for the analysis to be divided into smaller steps to improve convergence. Artificial stabilization was also used at each time step to help improve convergence. Artificial stabilization is a technique in which spring elements are applied to the model to limit the magnitude of the springback displacements for each time step. When convergence is reached in a given time step, the artificial spring elements are gradually removed in preparation for the calculations in the next time step. At the last time step, the spring elements are completely removed. The stiffness of these spring element can affect convergence, and a value of 0.001 was sufficient for the FEA models.

For each time step, a linear equation solver was coupled with a non-linear solution algorithm to find equilibrium. The default linear solver was used for the stiffness matrix inversion required in each time step (i.e. multi-front sparse matrix linear solver). This was activated using the control_implicit _solver card in LSDYNA, using option 0. For the determination of non-linear equilibrium, the default Newton non-linear solver with BFGS updates (Broyden-Fletcher-Goldfarb-Shanno) was used. This solver was activated using the control_implicit_solution card, using option 0 for the card. For the springback

FEA, the non-linear solution procedure employed the full Newton method in which the stiffness matrix was reformed after every iteration. A maximum limit of 200 iterations was used to find equilibrium at each time step. This is the recommended method for the FEA of springback. Automatic time step control was also used in case there were difficulties in convergence. Automatic time step control decreases the time step if convergence for the current time step fails. Equilibrium convergence was based on default values for the displacement and energy norms, of 0.001, and 0.01 respectively. Details on the numerical parameters used for the static implicit springback FEA are shown in Table 7-4.

Table 7-4 FEA parameters used in the baseline simulations for the springback FEA.

Springback simulations	
Time integration	Implicit, double precession
Number of springback steps	4
Element	Type 16 (fully integrated shell)
Through thickness integration	9 points, Gaussian –Legendre
Linear solver	default
Non-linear solver	default
Iteration method	Full Newton method.
Material Model	Type 37, Transversely anisotropic
Displacement norm	0.001
Energy norm	0.01

7.2.4 The effect of friction

The baseline models from the previous section were used to study the effect of Coulomb friction on springback. New FEA models were created from the baseline models by modifying the Coulomb friction in the contact interface

definitions. The FEA models with varying friction are listed in Table 7-1, for FEA runs 6 to 15.

7.2.5 Fully implicit forming and springback FEA

A series of fully implicit simulations were also created (runs 16 to 20, in Table 7-1). The fully implicit FEA, modeled the entire forming and unloading process, as opposed to separate explicit forming and implicit springback simulations used in the baseline FEA models. The implicit parameters used are equivalent to those used in the baseline springback FEA models, and one half symmetry was also used (Figure 7.6). The major difference, however, is that the additional constraints necessary for the explicit forming-implicit springback method (Figure 7.7) were not required. In the fully implicit method the blank motion is constrained by the tooling throughout the entire simulation. At the end of unloading, just at the point where the punch no longer contacts the blank, there are no inertial forces on the blank to cause convergence problems.

7.2.6 Uniform plane strain bending FEA models

FEA models simulating uniform plane strain bending were created from the implicit forming-implicit springback models (models 16-20 in Table 7-1). Coulomb friction was set to a value of 0 for the FEA. Constraints were applied to the blank edges to simulate the bending of an infinitely wide plate. These constraints are shown in Figure 7.8.

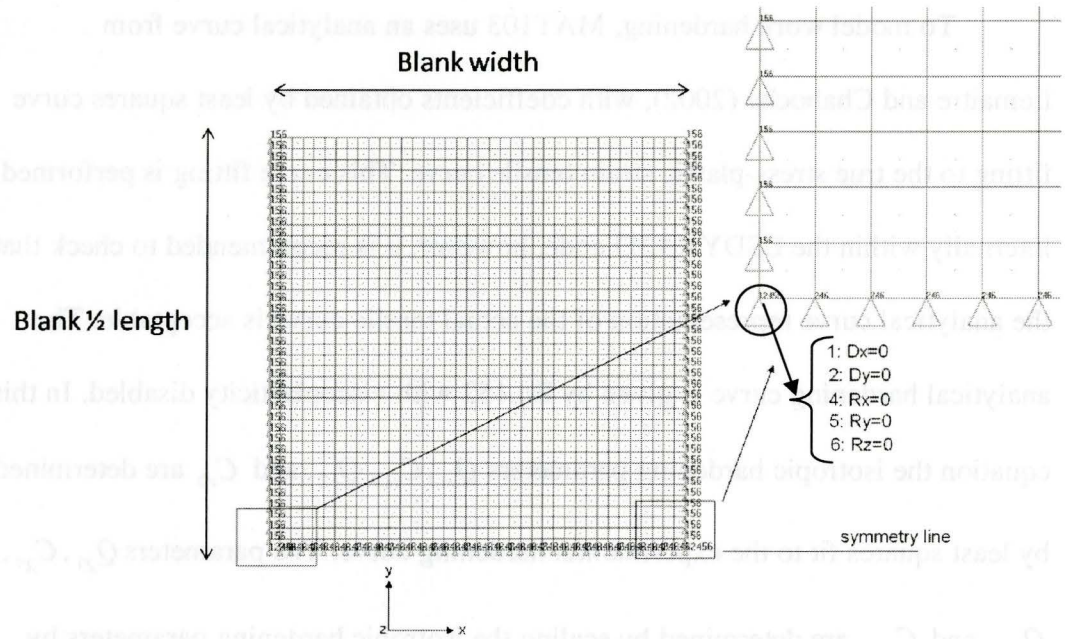

Figure 7.8 Blank mesh with edge constraints to simulate bending of an infinitely wide plate.

7.3 Calibration of DP780 and DP980 for Baushinger effect using MAT103

LSDYNA3D-MAT103 was the material model used in the FEA analysis of the V-die bending and small radius bending experiments. MAT103 was developed by Berstad et al., (1994), and is a planar anisotropic viscoplastic formulation with non-linear kinematic hardening capability. Viscoplasticity in this model is accounted for by using the effective plastic strain rate. However, for the simulations in this work, viscoplasticity was disabled; therefore the model behavior was elastic-plastic. Yield surface expansion and translation is controlled by the parameter "α" which ranges from 0 to 1 for pure isotropic and pure kinematic hardening respectively. Mixed hardening is modeled using a value of "α" between 0 and 1.

To model work hardening, MAT103 uses an analytical curve from Lemaitre and Chaboche (2002), with coefficients obtained by least squares curve fitting to the true stress-plastic strain tensile curve. This curve fitting is performed internally within the LSDYNA3D code, however, it is recommended to check that the analytical curve representation of the actual tensile curve is acceptable. The analytical hardening curve is given by Eq.152 with viscoplasticity disabled. In this equation the isotropic hardening parameters Q_{r1}, C_{r1}, Q_{r2}, and C_{r2} are determined by least squares fit to the experimental hardening curve. The parameters $Q_{\chi 1}, C_{\chi 1}$, $Q_{\chi 2}$, and $C_{\chi 2}$, are determined by scaling the isotropic hardening parameters by $(1-\alpha)$, where α is the mixed hardening parameter described earlier. The values for the coefficients are inputs to the material model for a given state of hardening, from pure isotropic, to mixed, and to pure kinematic hardening.

$$\bar{\sigma}(\bar{\varepsilon}^p)=\sigma_0+Q_{r1}(1-\exp(-C_{r1}\bar{\varepsilon}^p))+Q_{r2}(1-\exp(-C_{r2}\bar{\varepsilon}^p))+Q_{\chi 1}(1-\exp(-C_{\chi 1}\bar{\varepsilon}^p)) + Q_{\chi 2}(1-\exp(-C_{\chi 2}\bar{\varepsilon}^p)) \quad \text{Eq.152}$$

FEA models of a sub-size tensile test were developed in order to calculate the Baushinger effect as defined by Sadagopan (2003), as a function of the parameter α. This in effect was a method to calibrate the hardening behavior (i.e. isotropic to pure kinematic hardening) for the experimental DP780 and DP980 steels against Baushinger effect values from the literature.

The dimensions of the sub size tensile specimen as well as the FEA mesh with boundary conditions are shown Figures 7.9-7.10. The models were run using

the static implicit solver using the same numerical parameters shown in Table 7-4, with the exception that material MAT103 was used. A check of the experimental tensile data and the least squares fit to Eq.152 is shown in Figure 7.11 and Figure 7.12 for the DP780 and DP980 steels respectively. The least squares fit shows good agreement with a maximum deviation from the experimental data of 5.5%. Note that the curve fit was performed for tensile data only, as opposed to tension-compression data. The use of MAT103 for the FEA in this thesis therefore assumes that the shape of the hardening curve in tension and compression is identical. This is an approximation as experimental tension curves from Sadagapan (2003) can show different curve "shapes" in tension verses compression.

A series of FEA models of the sub-size tensile specimens were used in the material calibrations as shown in Table 7-5. In MAT103, the parameter "α" was varied for the different FEA models from a value of 1 for pure isotropic hardening, to a value of 0 for pure kinematic hardening.

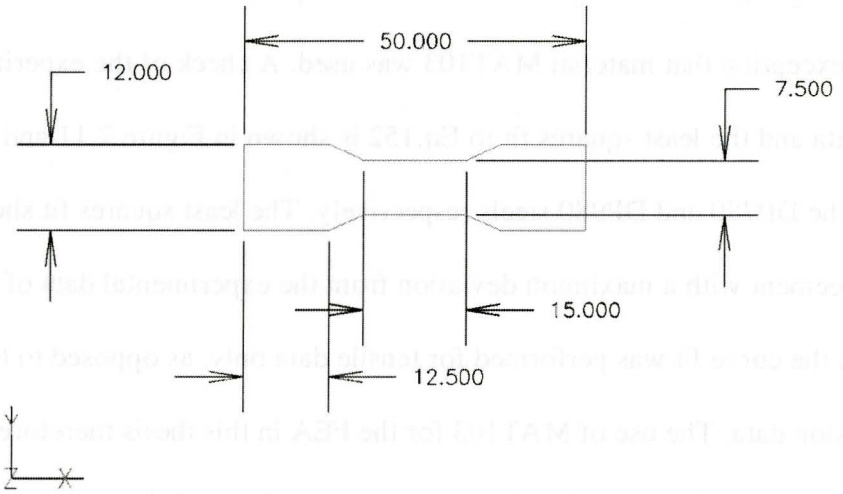

Figure 7.9 Sub-size tensile specimen geometry used for the FEA models (dimensions in mm).

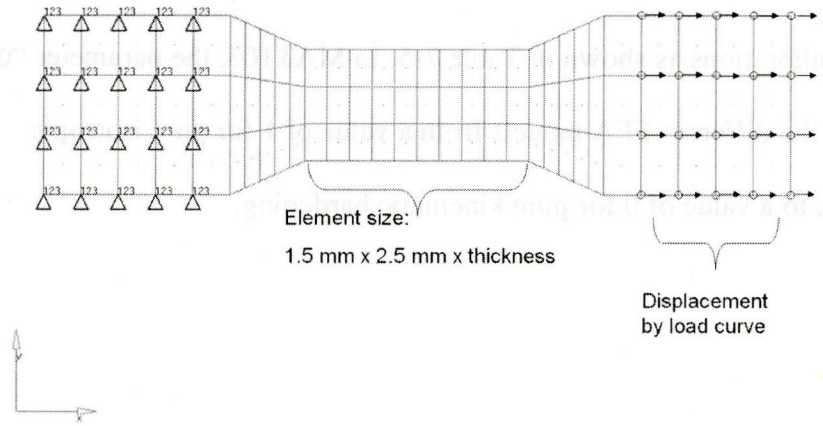

Figure 7.10 Sub-size tensile FEA model showing mesh and boundary conditions.

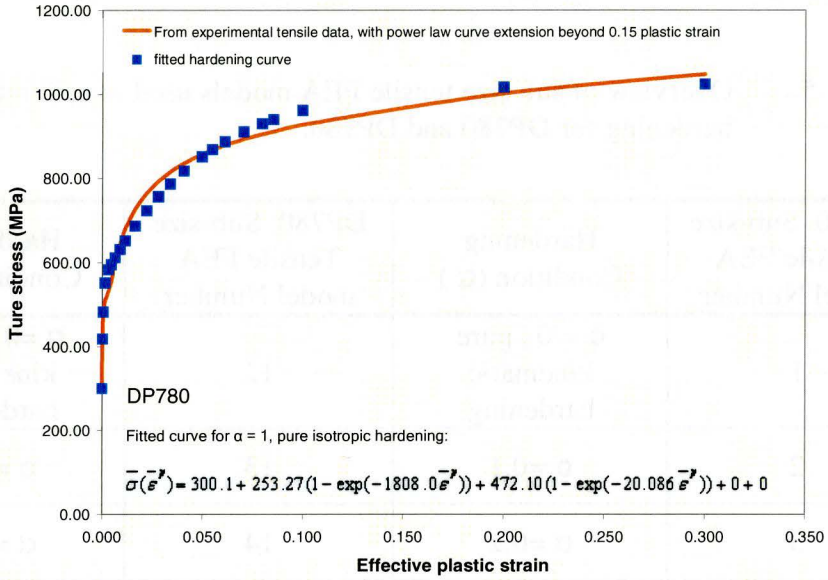

Figure 7.11 Comparison of fitted hardening curve in MAT103 for DP780 (for pure isotropic hardening) compared to data from the experimental tensile test.

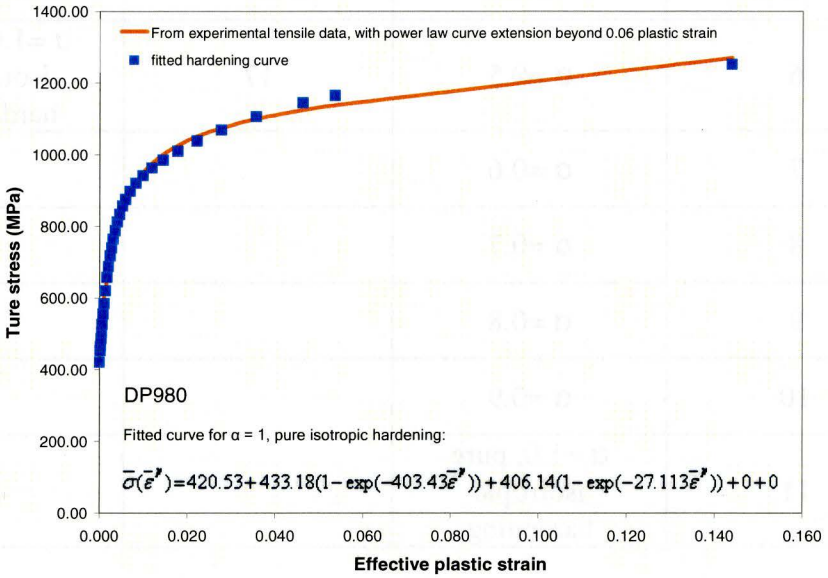

Figure 7.12 Comparison of fitted hardening curve in MAT103 for DP980 (for pure isotropic hardening) compared to data from the experimental tensile test.

Table 7-5 Overview of sub size tensile FEA models used to calibrate hardening for DP780 and DP980.

DP980 Sub-size Tensile FEA model Number	Hardening Condition (α)	DP780 Sub-size Tensile FEA model Number	Hardening Condition (α)
1	α = 0 , pure kinematic hardening	12	α =0 , pure kinematic hardening
2	α =0.1	13	α =0.2
3	α =0.2	14	α =0.4
4	α =0.3	15	α =0.6
5	α =0.4	16	α =0.8
6	α =0.5	17	α =1.0, pure isotropic hardening
7	α =0.6		
8	α =0.7		
9	α =0.8		
10	α =0.9		
11	α =1.0, pure isotropic hardening		

7.4 FEA models of the V-die bending and springback experiments

FEA models of the V-die bending and springback experiments were constructed for both the DP780 and DP980 steels, using a common tool mesh for the 3D models and a separate mesh for the 2D continuum models (Figures 7.13-7.16). The tooling mesh discretization around radii was the same for the 3D and 2D models having 9 elements around the die radius, and 16 elements around the punch radius. The tooling mesh was constructed from the CAD geometry of the V-die shown in Figure 7.13. The tooling mesh was modeled as perfectly rigid using MAT20 with the elastic modulus of 207000 MPa and a Poisson's ratio of 0.3. Note that the elastic properties are utilized in the contact algorithm. Contact between the blank and the tooling was modeled using the penalty method, using the "contact_forming_ nodes_ to_surface" card. The global contact stiffness factor was set at a value of 0.01, which was within the standard range for metal forming FEA.

The punch displacement used in the FEA models for steel was determined from in-situ CMM measurements of the punch position during the experimental testing (see Chapter 6). CMM measurements at the end of bending (just prior to springback and release of the tooling forces) showed a punch to die gap of 3.95 mm and 3.85 mm for the DP780 and DP980 steels respectively. In the FEA, the punch was moved using displacement control and linear ramp for the punch velocity. All FEA models used the static implicit method and for forming and springback, and were simulated in a single FEA run. For example, at the end of

forming, the punch was gradually retracted allowing the blank to manifest springback, similar to the fully implicit FEA described in the FEA study of Queener's work. The implicit solution used the Newton-Raphson method and the same numerical parameters as used in the FEA study of Queener's work (see Table 7-4). In the implicit solution, automatic time step control was used with a maximum time step of 0.001 seconds. On average, the punch was displaced 0.18 mm per 0.001 seconds during the simulation. Since the forming and springback FEA was performed together in one run and automatic time step control was used, there is no guarantee that a plot (or stress strain state) will be written by the code at the end point of forming. To solve this problem, the key point method was used. In the key point method, a load curve is used that defines the maximum time step verses simulation time used. As the simulation approaches the end point of forming, the time step is adjusted to the target "key point" simulation time. An example of this process is shown in Figure 7.17.

Fully integrated elements were used for all elements in the FEA models. The shell elements were modeled using the type 16 shell with 9 through-thickness integration points. The 3D continuum elements were of type 2, and the 2D continuum elements were of type 13. As mentioned earlier, fully integrated elements facilitate improved convergence behavior for the implicit method.

MAT103 was the material model used for the FEA of the V-die bending experiments. The results of the hardening calibration study were then used in the FEA of V-die bending to simulate the appropriate mixed hardening for both the

DP780 and DP980 steels. V-die bending simulations were also performed for the cases of pure isotropic and kinematic hardening.

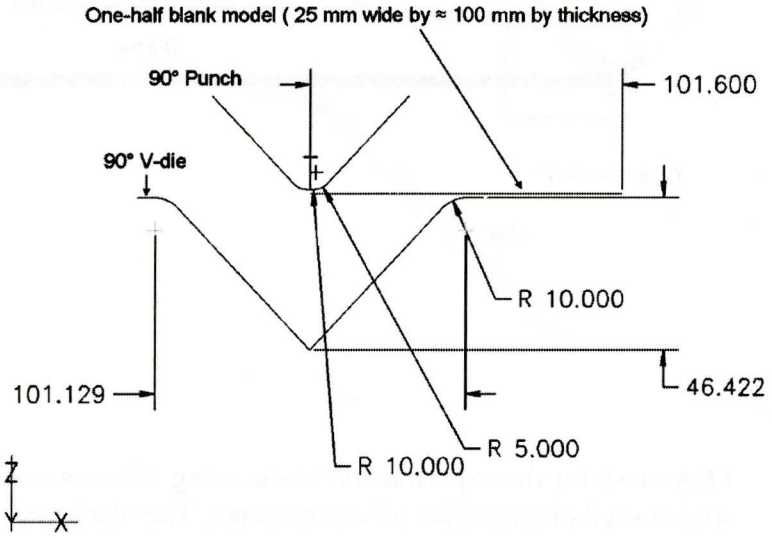

Figure 7.13 2D CAD drawing of the experimental V-die tooling geometry (all dimensions are in mm).

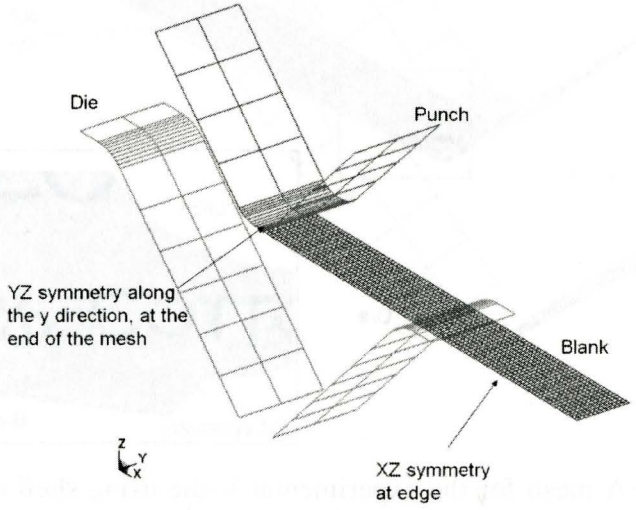

Figure 7.14 FEA mesh for the experimental V-die using shell elements for the tooling components. The blank was modeled using shell elements and one-quarter symmetry was used.

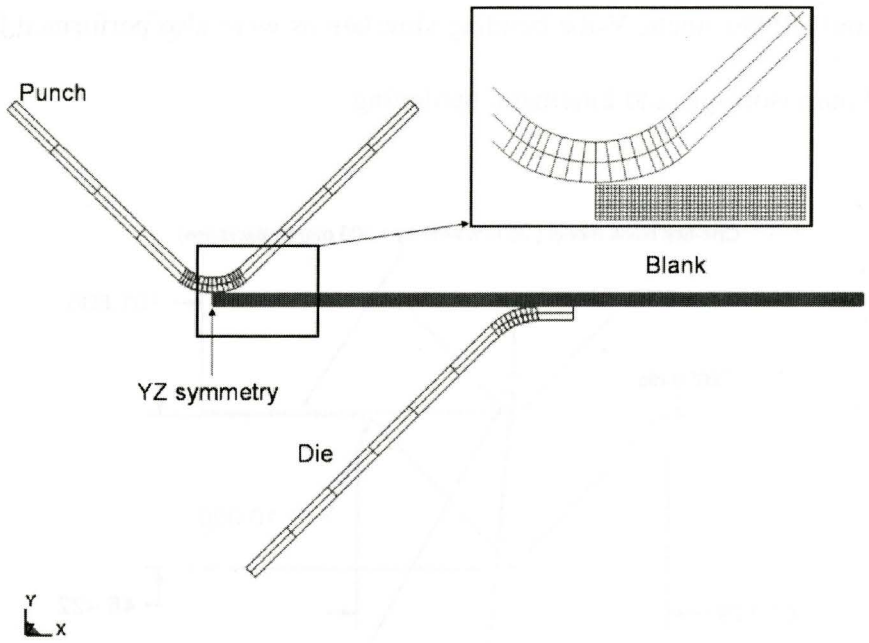

Figure 7.15 FEA mesh for the experimental V-die using 2D continuum (plane strain) shell elements for all components. The blank was modeled using one-half symmetry.

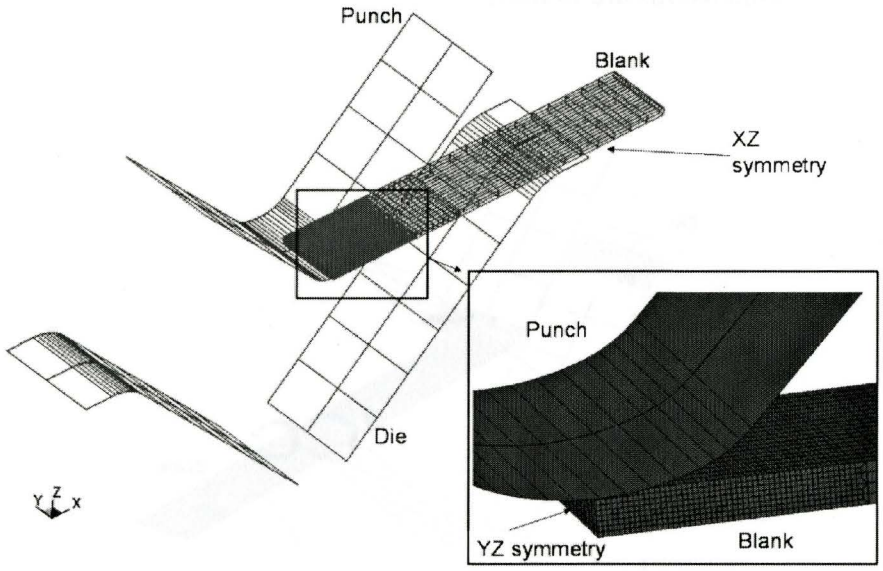

Figure 7.16 FEA mesh for the experimental V-die using shell elements for the tooling. The blank was modeled using 3D continuum elements and one-quarter symmetry was used.

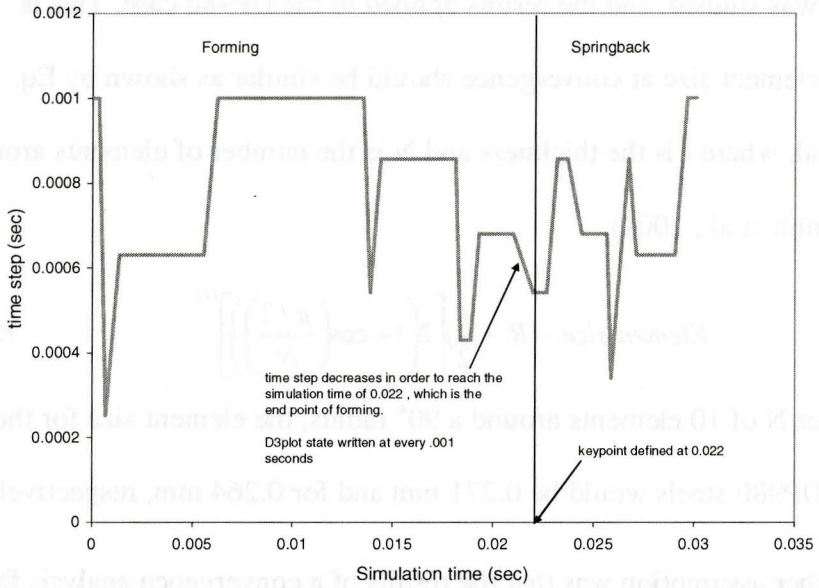

Figure 7.17 Example of time step variation in a static implicit FEA with automatic time step control. The key point definition at the end of the forming stage forces a solution at a prescribed simulation time of interest, in order to capture stress-strain data at that point.

7.4.1 Mesh discretization and convergence analysis in the development of the blank mesh

The effect of the element formulation on forming stresses and the resulting springback was investigated for blank meshes utilizing 2D and 3D continuum elements, as well as 3D shell elements (Figures 7.14-7.16). From Section 3.2, an important parameter affecting the springback magnitude is the number of elements around a bend radius as springback increasing with more elements around the bend radius, or a smaller element size. For example 7 elements around the bend radius is the recommendation by Maker and Zhu (2001). For each of the blank meshes used, the element size is therefore an important factor for predicting a stable springback magnitude. In the convergence analysis to follow, only the

DP780 case was studied, and the results applied to the DP980 case. This is because the element size at convergence should be similar as shown by Eq. 153 for a 90° bend, where t is the thickness and N is the number of elements around the bend (Smith et al., 2004).

$$Elementsize=(R_i+\frac{t}{2})\left[2\left(1-\cos\left(\frac{\pi/2}{N}\right)\right)\right]^{1/2} \quad \text{Eq. 153}$$

In Eq.152, for N of 10 elements around a 90° radius, the element size for the DP780 and DP980 steels would be 0.271 mm and for 0.264 mm, respectively.

Another assumption was that the results of a convergence analysis for the 3D continuum blank mesh, would also apply to the 2D continuum blank mesh, in terms of the mesh discretization through the thickness. The convergence analysis was therefore also performed for the DP780 models using the 3D continuum blank meshes only. For all cases, the convergence analysis was performed for the case of isotropic hardening only.

The results from the convergence analysis are shown in Figure 7.18-7.21. The maximum Von Mises stress at the end of forming is shown in Figures 7.18-7.19 for the simulations using shells and continuum elements respectively. For the shell elements the maximum Von Mises stress stabilizes for the element size of 1.0 x 1.0 mm. The change in maximum Von Mises stress from the model using 2.0 mm compared to 1.0 mm is less than 1%. For the continuum elements, the maximum Von Mises stress stabilizes at 8 elements through the blank thickness.

The change in the maximum Von Mises stress from 4 to 8 elements is approximately 3.5%.

The effect of springback on the element size is shown in Figure 7.20 and Figure 7.21 for the shell element and continuum element models respectively. Springback stabilizes in the shell element models at the element size of 1.0 mm. The change in the relative springback is approximately 3% from the model using 2.0 mm to the model using the 1.0 mm element size. For the continuum element models, the relative springback stabilizes at 8 elements through the thickness. The change in relative springback from the models using 4 elements through the thickness to the models using 8 was approximately 5%. The parameters used in the FEA of V-die bending and springback are therefore summarized in Table 7-6 and Table 7-7 for the DP780 and DP980 steels respectively.

Table 7-6 FEA parameters for the V-die bending and springback of DP980 and DP780 using shell elements.

Time integration	Implicit, double precision
Time step control	Automatic, Dt max=0.001 sec, key point method
Bending and springback	Within the same simulation
Element	Type 16 (fully integrated shell)
Element size	1.0 mm x 1.0 mm
Through thickness integration	9 points, Gaussian –Legendre
Linear solver	default
Non-linear solver	default
Iteration method	Full Newton method.
Material Model	MAT103, Von Mises criterion, isotropic and kinematic hardening parameter "α" according to the FEA calibration (see Table 8-3)
Displacement norm	0.001
Energy norm	2.0×10^{-3}

Table 7-7 FEA parameters for the V-die bending and springback of DP980 and DP780 using 2D and 3D continuum elements.

Time integration	Implicit, double precision
Time step control	Automatic, Dt max=0.001 sec, key point at the end of forming defined by load curve
Bending and springback	Within the same simulation
Element	3D continuum Type 2 (fully integrated) 2D continuum Type 13 (plane strain shell)
Element size	0.25 mm x 0.25 mm x 1 mm (3D) 0.25 mm x 0.25 mm (2D continuum)
Linear solver	default
Non-linear solver	default
Iteration method	Full Newton method.
Material Model	MAT103, Von Mises criterion, isotropic and kinematic hardening parameter "α" according to the FEA calibration (see Table 8-3)
Displacement norm	0.001
Energy norm	2.0×10^{-3}

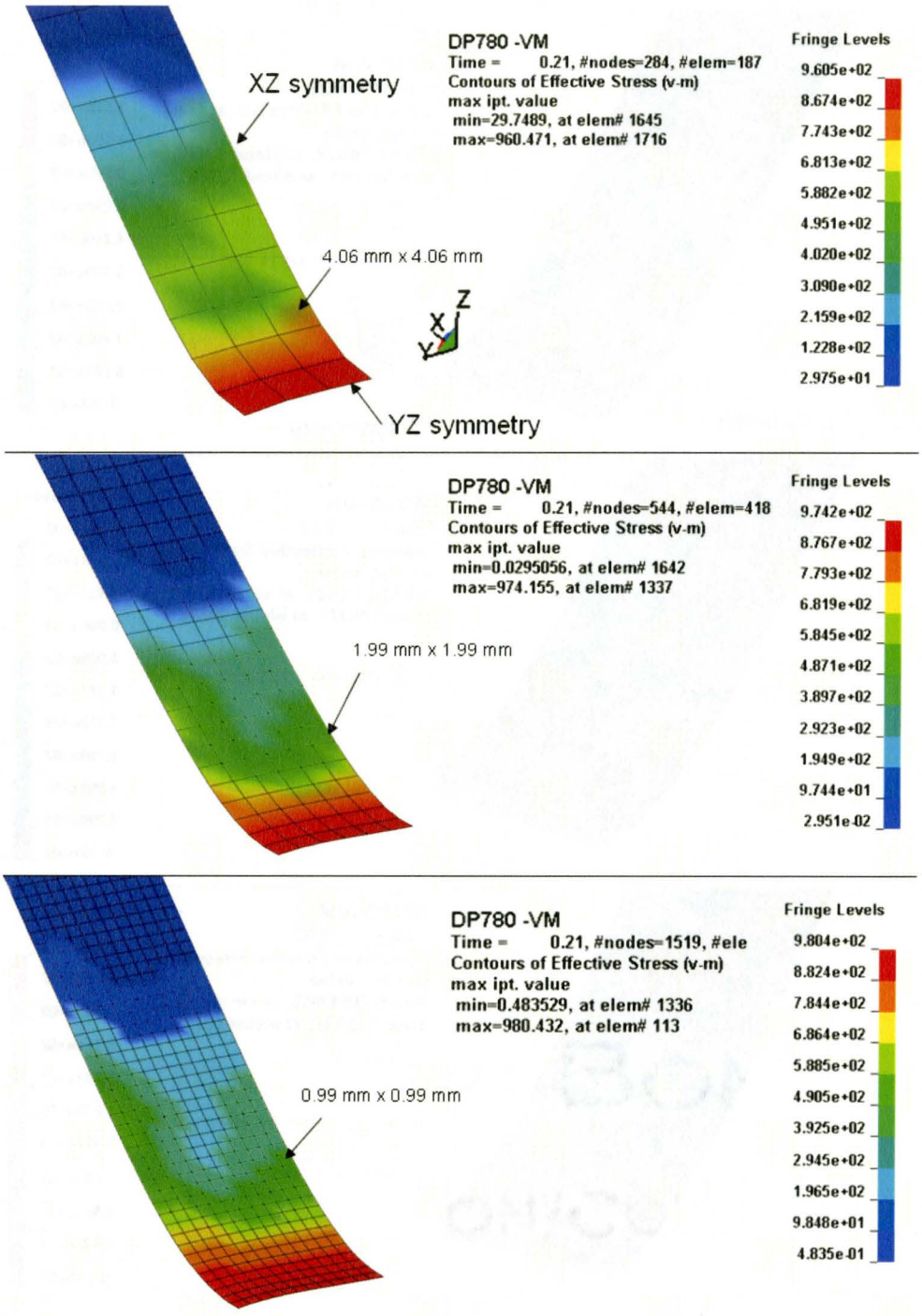

Figure 7.18 V-die bending simulation for DP780 (prior to springback) using shell elements with 1:1 aspect ratio and various element sizes. Pure isotropic hardening was assumed.

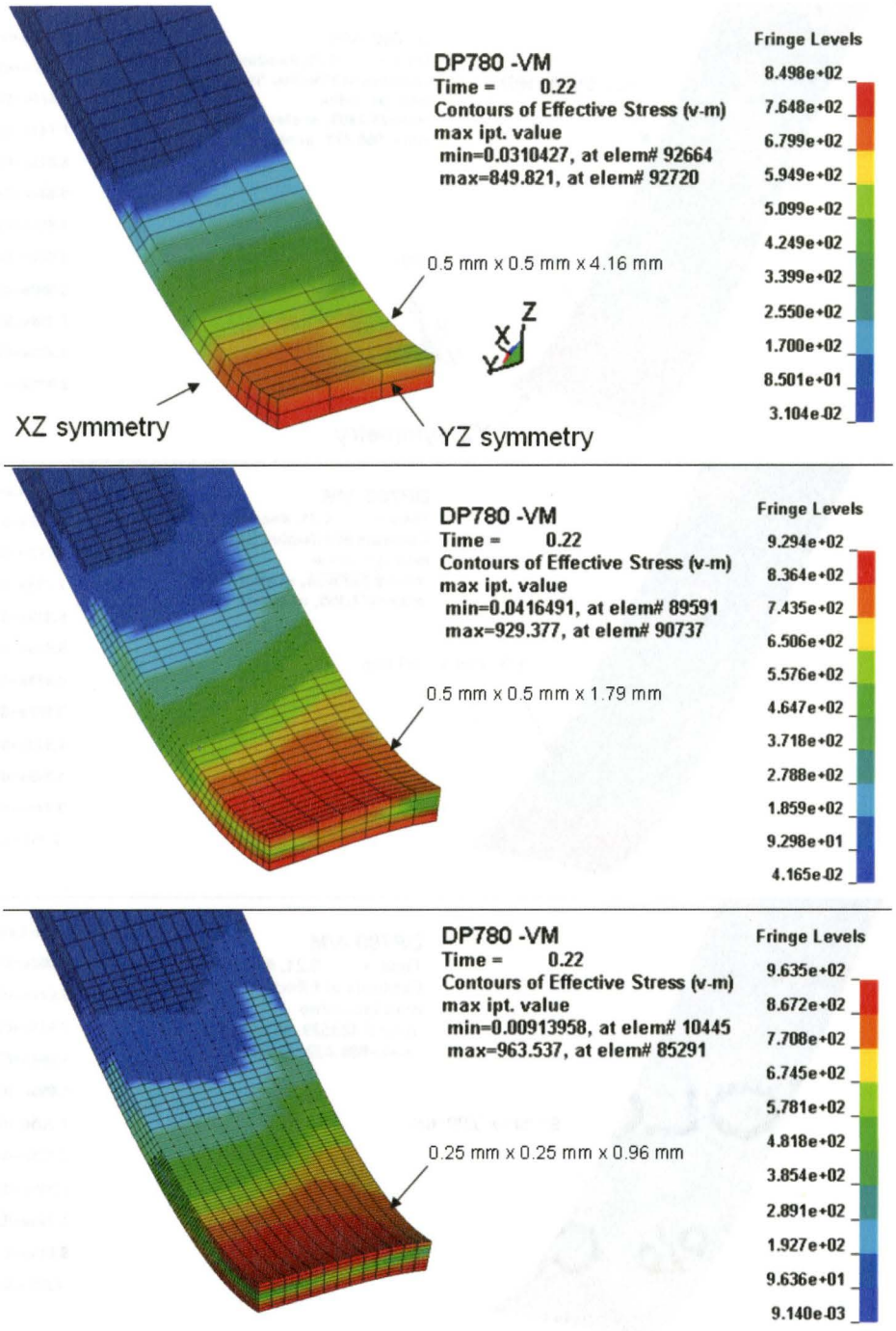

Figure 7.19 V-die bending simulation for DP780 using 3D continuum elements of aspect ratio of approximately 1:1:4, as a function of element size. Pure isotropic hardening was assumed.

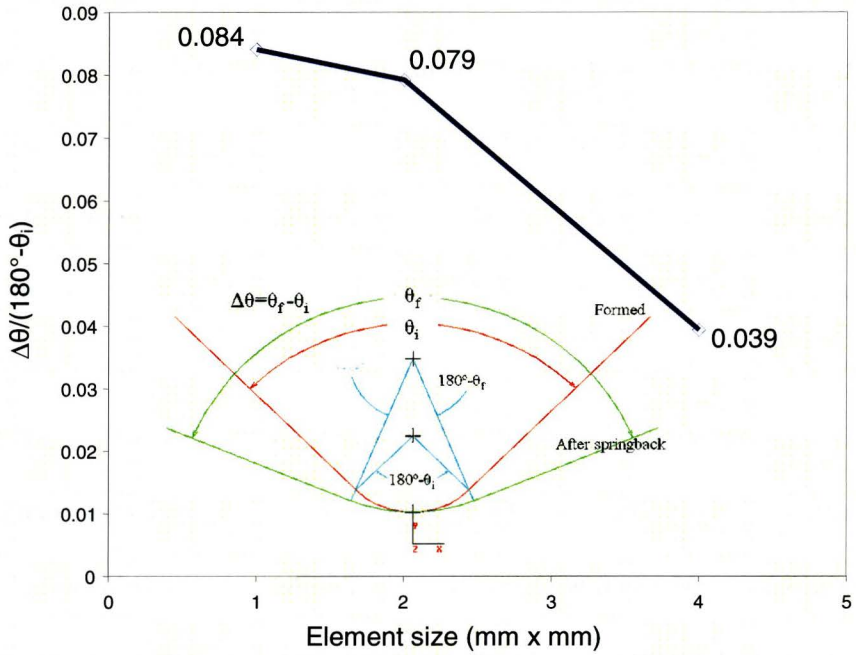

Figure 7.20 DP780 springback results using shell elements with 1:1 aspect ratio. Relative springback is plotted as a function of element size

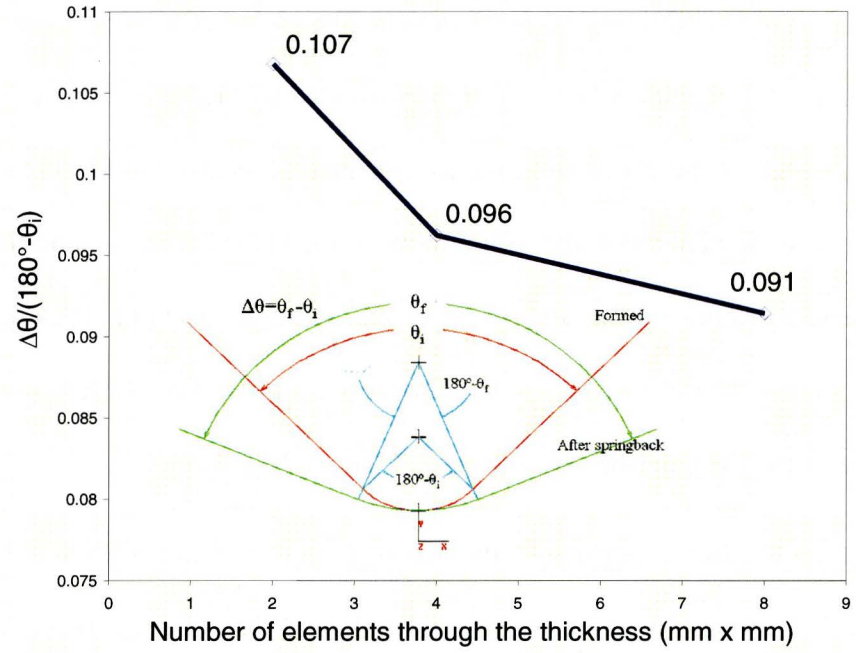

Figure 7.21 DP780 springback results using 3D continuum elements with approximately 1:1:4 aspect ratio. Relative springback is plotted as function of number of elements through the thickness.

7.5 FEA models of small radius bending in a commercial bending machine

FEA modeling of small radius bending was performed for the DP780 material only, as the DP980 cracked during bending. The FEA was based on the bending machine geometry which is shown in Figure 7.22, and modeled the bending action shown in Figure 7.23. FEA models were constructed for different cases in which the blank was modeled using 2D and 3D continuum elements, as well as 3D shell elements. The tooling mesh for the 3D FEA was modeled using shell elements, and as in the V-die FEA, the material of the tool was treated as perfectly rigid using MAT20 with the elastic modulus of 207000 MPa and a Poisson's ratio of 0.3. Contact between the blank and the tooling was modeled using the penalty method and node to surface contact was used by selecting the "contact_forming_ nodes_ to_surface" option. The global contact stiffness factor was set to a value of 0.01, which was within the standard range for metal forming FEA. In the case of the 2D models, the tooling mesh was also modeled using the 2D continuum elements. For all tooling meshes, the element size around the critical bending radius on the bending block die was approximately 0.24 mm, therefore minimizing differences in bending conditions across all FEA models. Examples of the FEA meshes are shown in Figures 7.24-7.26.

In the bending experiments, the blank measured 45 mm x 25 mm. For the FEA, one-half symmetry was used for the blank, and therefore, the blank mesh measured 12.5 mm wide. Translational constraints were applied to the blank in the area 14 mm at the end of the blank in order to simulate the clamping action in

the experimental bending machine. The constraints used for the various blank meshes are shown schematically in Figure 7.27.

The bending action in the FEA was modeled using the *Part_inertia card, where the center of rotation was redefined at point "A" shown in Figure 7.23. Conventionally, parts are defined using the *Part card and, by default, the center of rotation is at the centroid of the part mesh. The *Part_inertia card technique is typically used to model bending die actions in rotary tube bending.

All FEA models used the static implicit method and forming and springback were simulated in a single FEA run. To obtain springback in the FEA, the bending mechanism is gradually rotated back towards its initial position. In addition, contact between the bending block die and the blank is disabled when the bending mechanism is no longer in contact with the blank.

The implicit solution used the Newton Raphson method and the same numerical parameters as in the V-die bending FEA. Automatic time step control using a key point load curve to define the end point of bending was used, as explained previously for the V-die bending FEA. The maximum allowable time step used was 0.003 seconds.

Fully integrated elements were used for all elements in the FEA models. The shell elements were modeled using the Type 16 shell with 21 through thickness integration points. Since bending was more severe (higher $_{Ri/t}$ ratio) compared to V-die bending, it was anticipated that more integration points would

be required to capture the through thickness stress distribution. The 3D continuum elements were of Type 2, and the 2D continuum elements were of type14. As mentioned earlier, fully integrated elements facilitate convergence in the implicit method.

Bending and springback was modeled for the cases of pure isotropic and kinematic hardening using MAT103. FEA was performed using for the parameter "α" set to a value of 0 for pure kinematic hardening and a value of 1 for pure isotropic hardening. To model actual material hardening, the appropriate values of "α" were used from the material calibration FEA, described previously (Section 7.3).

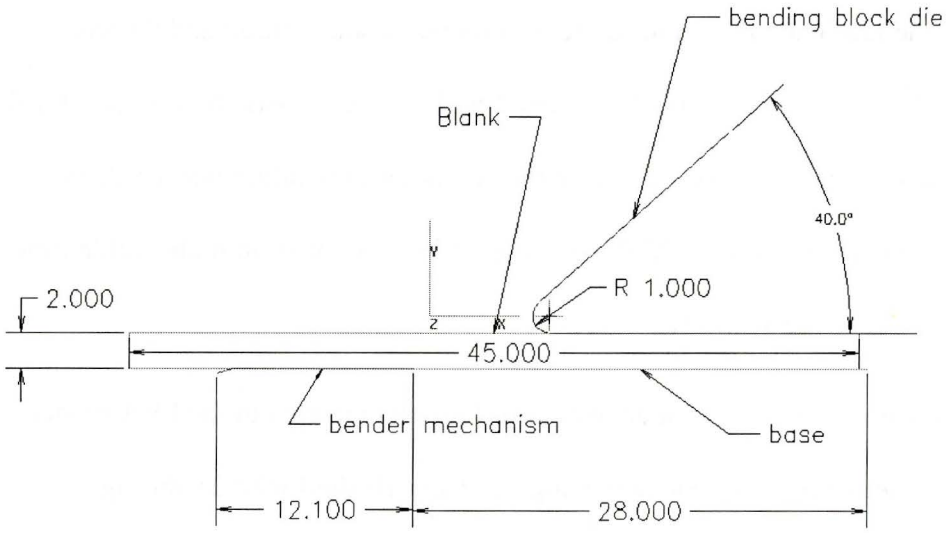

Figure 7.22 2D CAD model of the bending geometry used for the small radius bending FEA.

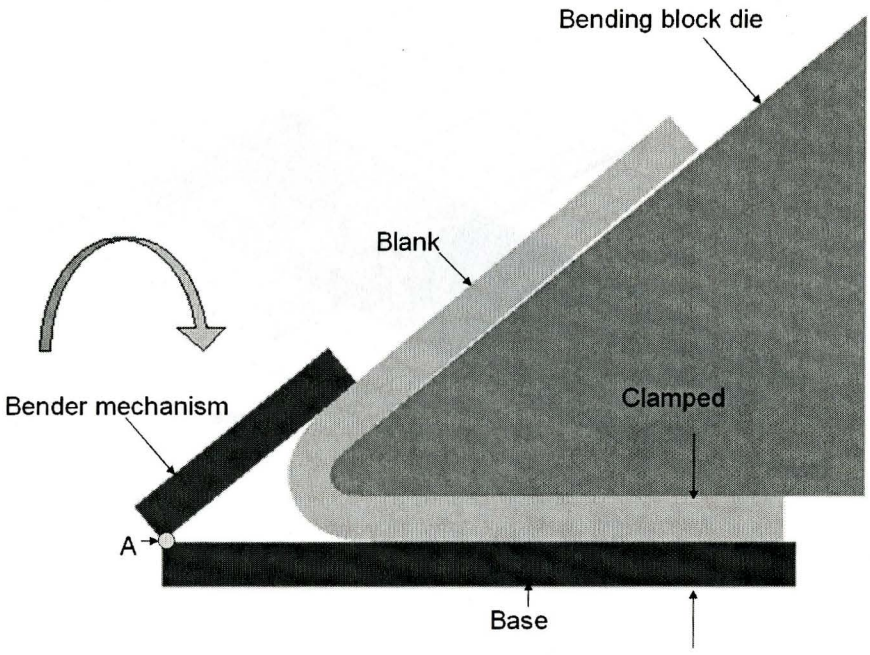

Figure 7.23 Schematic showing bending actions used in the FEA to model small radius bending.

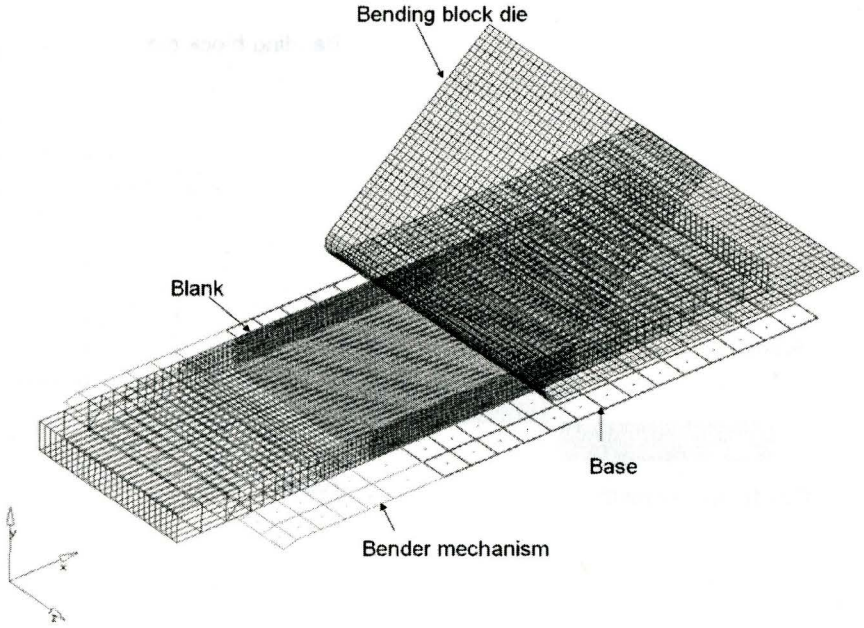

Figure 7.24 3D continuum element FEA mesh of small radius bending.

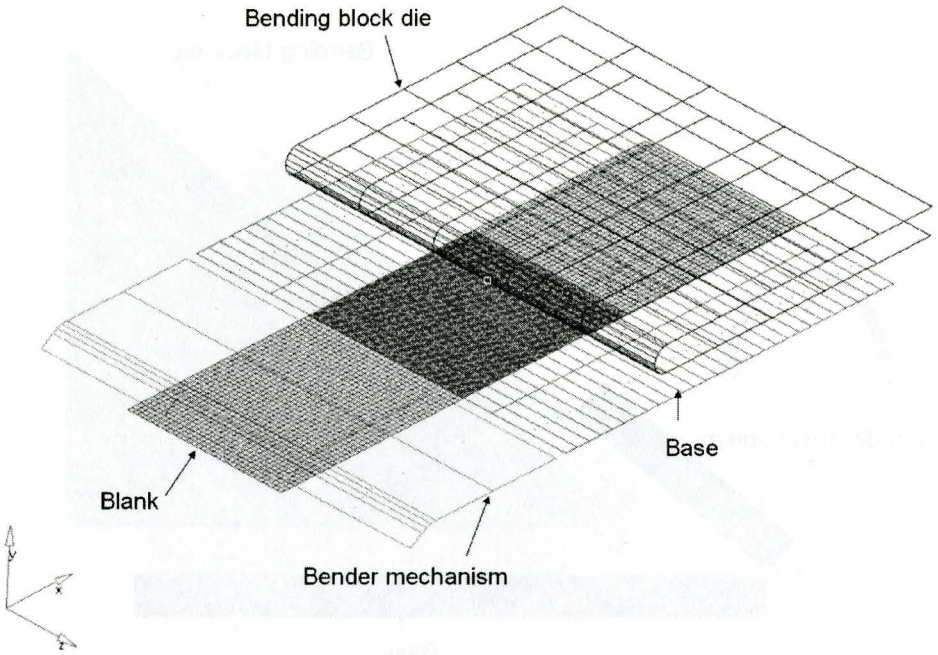

Figure 7.25 3D shell element FEA mesh of small radius bending.

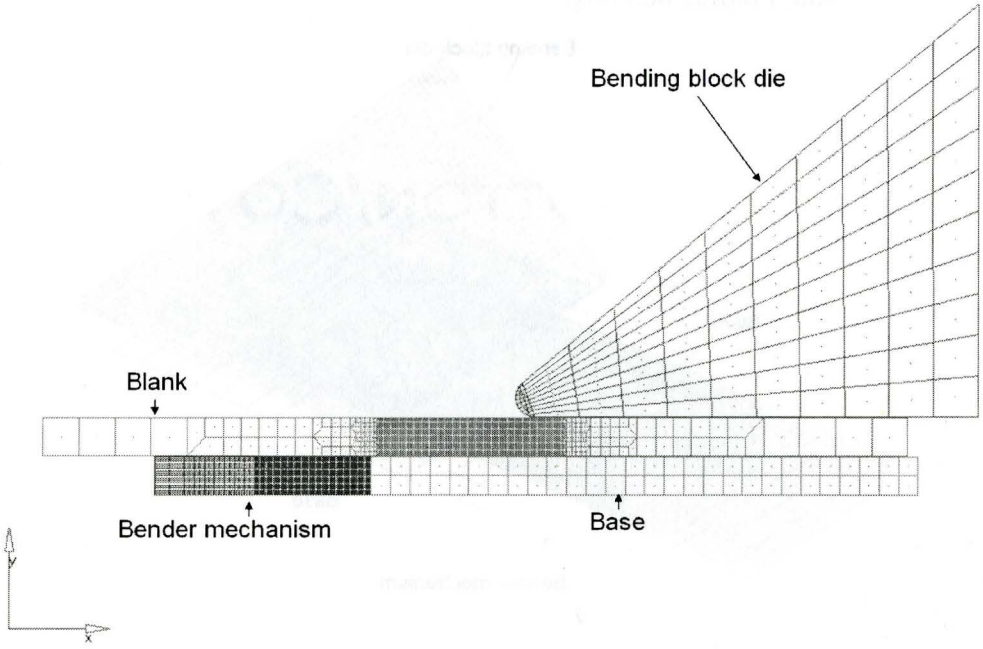

Figure 7.26 2D continuum, element FEA mesh of small radius bending.

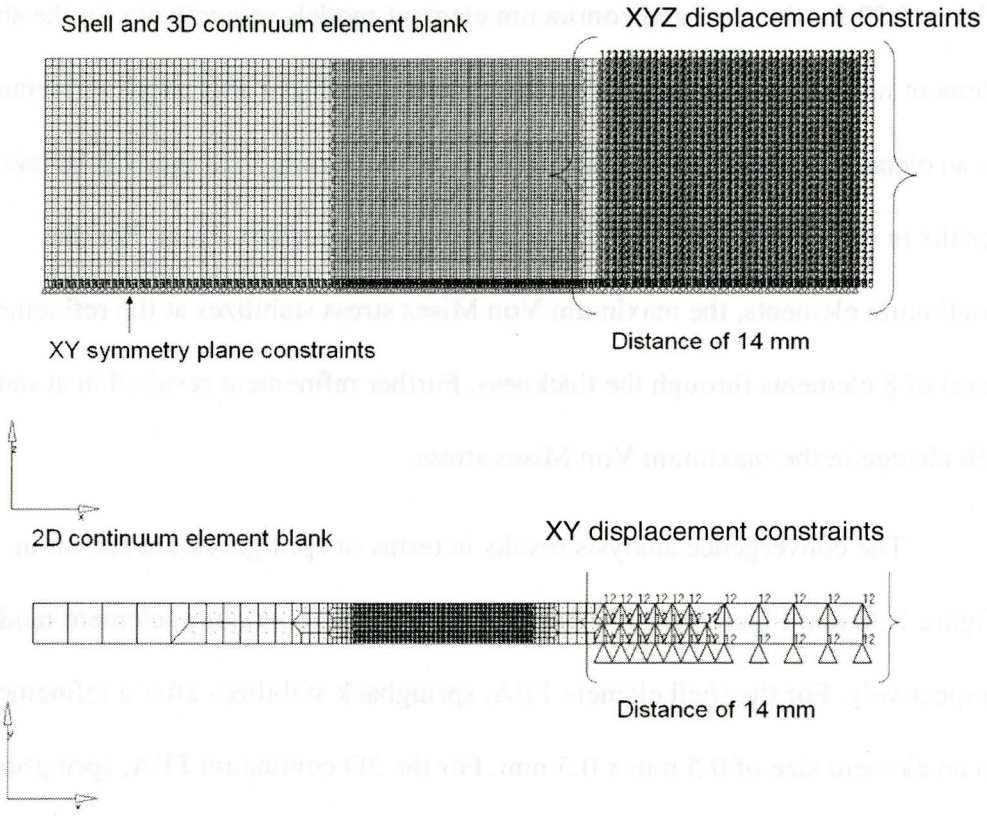

Figure 7.27 FEA model constraints for the 3D and 2D FEA blank meshes.

7.5.1 Mesh discretization and convergence analysis in the development of the blank mesh

A convergence analysis was performed for the FEA using 3D continuum elements, and 3D shell elements for the blanks. It was assumed that the results from the 3D continuum element convergence analysis would apply to the 2D continuum FEA in terms of the required discretization through the blank thickness.

The results of the convergence analysis are shown in Figures 7.28-7.31. The convergence analysis was performed for the case of isotropic hardening only. The maximum Von Mises stress at the end of forming is shown in Figure 7.28 and

Figure 7.29 for the shell and continuum element models respectively. In the shell element models the maximum Von Mises stress stabilizes after mesh refinement to an element size of 0.5 x 0.5 mm. Further refinement to 0.18 mm x 0.18 mm results in essentially no change in the maximum Von Mises stress. For the continuum elements, the maximum Von Mises stress stabilizes at the refinement level of 8 elements through the thickness. Further refinement resulted in at most 2% change in the maximum Von Mises stress.

The convergence analysis results in terms of springback are shown in Figure 7.30 and Figure 7.31 for the shell element and continuum element models respectively. For the shell element FEA, springback stabilizes after a refinement to an element size of 0.5 mm x 0.5 mm. For the 3D continuum FEA, springback stabilizes at the level of 16 elements through the blank thickness. These results represent minimum blank mesh requirements for stable springback. It is to be noted that they are more restrictive compared to the convergence analysis results for maximum Von Mises stress.

A summary of the parameters used in the FEA of small radius bending, incorporating the convergence analysis are given in Tables 7-8 to 7.9. These were the parameters used in the FEA modeling of small radius bending in this thesis.

Table 7-8 FEA parameters for the modeling of small radius bending and springback for DP780 using shell elements.

Time integration	Implicit, double precision
Time step control	Automatic, Dt max=0.003 sec, key point at the end of forming defined by load curve
Bending and springback	Within the same simulation
Element	Type 16 (fully integrated shell)
Element size	0.18 mm x 0.18 mm
Through thickness integration	21 points, Gaussian –Legendre
Linear solver	default
Non-linear solver	default
Iteration method	Full Newton method.
Material Model	MAT103, Von Mises criterion, isotropic and kinematic hardening parameter "α" according to the FEA calibration (see Table 8-3)
Displacement norm	0.001
Energy norm	2.0×10^{-3}

Table 7-9 FEA parameters for the modeling of small radius bending and springback for DP780 using 2D and 3D continuum elements.

Time integration	Implicit, double precision
Time step control	Automatic, Dt max=0.003 sec, key point at the end of forming defined by load curve
Bending and springback	Within the same simulation
Element	3D continuum Type 2 (fully integrated) 2D continuum Type 13 (plane strain shell)
Element size (16 elements through the blank thickness)	0.125 mm x 0.125 mm x 0.5 mm (3D) 0.125 mm x 0.125 mm (2D continuum)
Linear solver	default
Non-linear solver	default
Iteration method	Full Newton method.
Material Model	MAT103, Von Mises criterion, isotropic and kinematic hardening parameter "α" according to the FEA calibration (see Table 8-3)
Displacement norm	0.001
Energy norm	2.0×10^{-3}

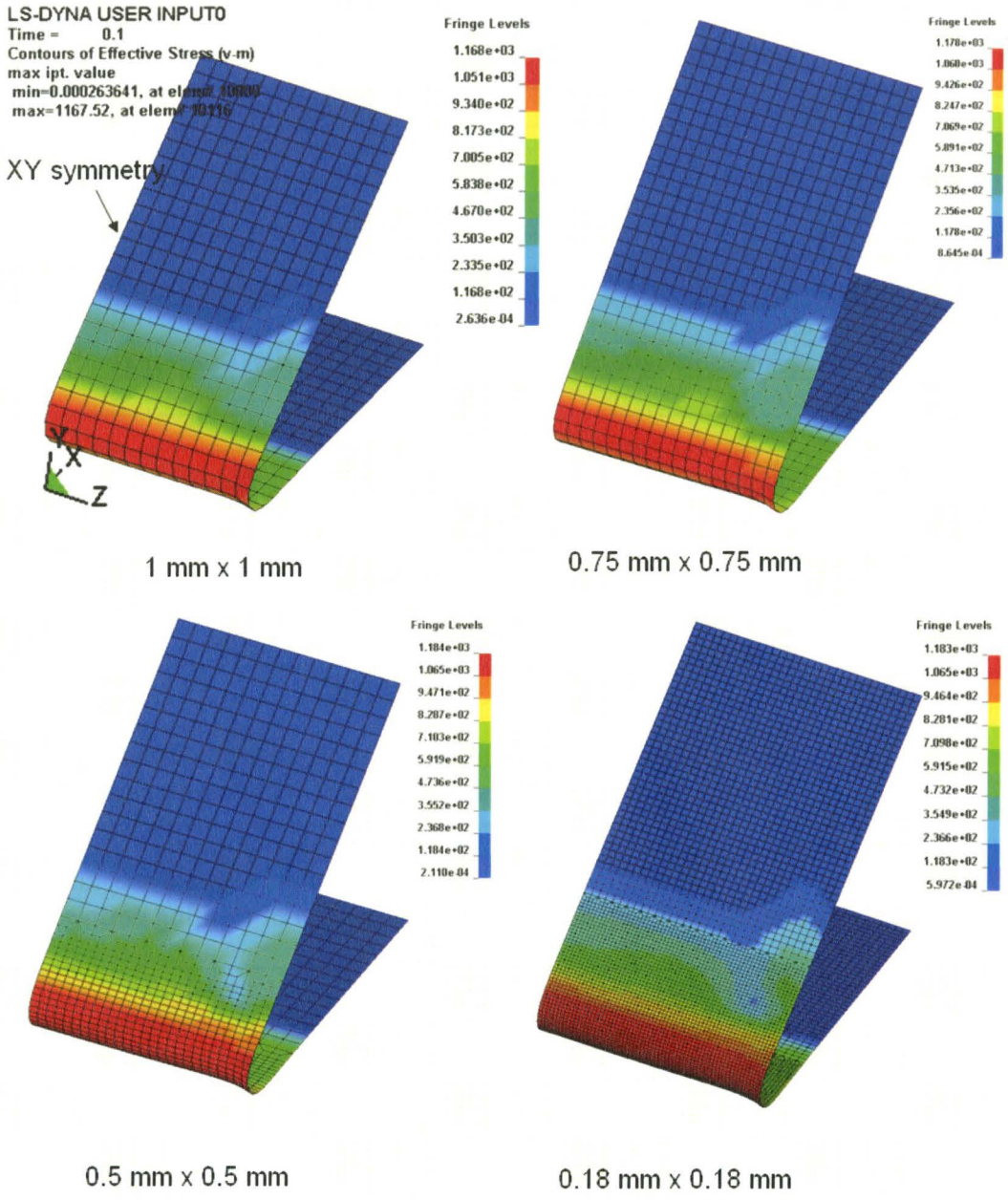

Figure 7.28 V-die bending simulation for DP780 (prior to springback) using 3D shell elements of aspect ratio of approximately 1:1, as a function of element size. Pure isotropic hardening was assumed.

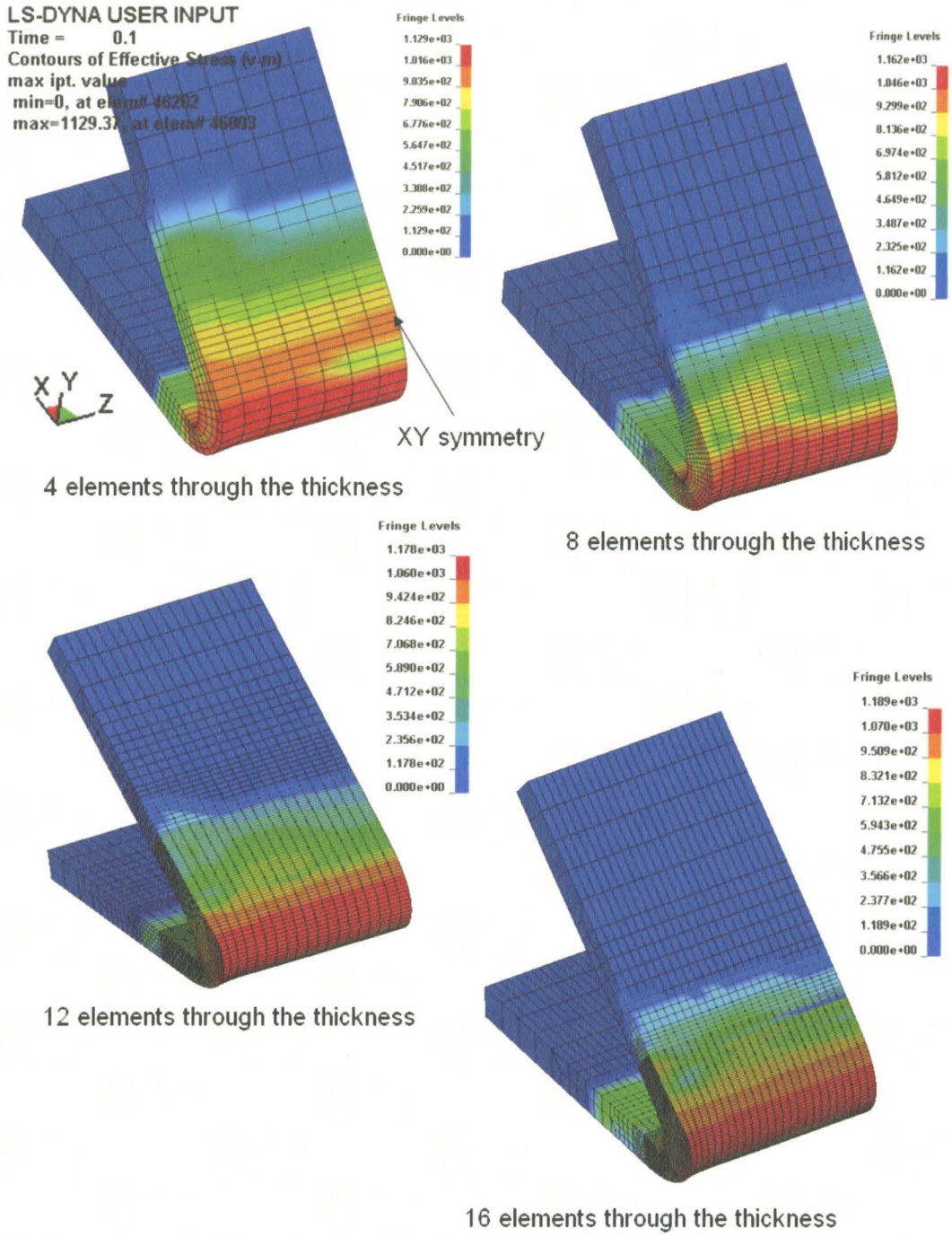

Figure 7.29 V-die bending simulation for DP780 (prior to springback) using 3D continuum elements of aspect ratio of approximately 1:1:4, as a function of element size. Pure isotropic hardening was assumed.

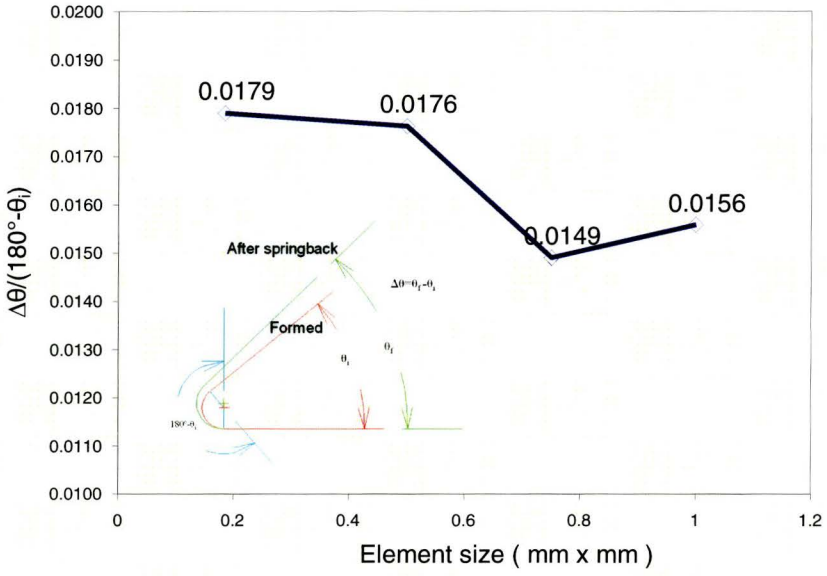

Figure 7.30 DP780 springback results using shell elements with 1:1 aspect ratio. Relative springback as plotted as a function of element size

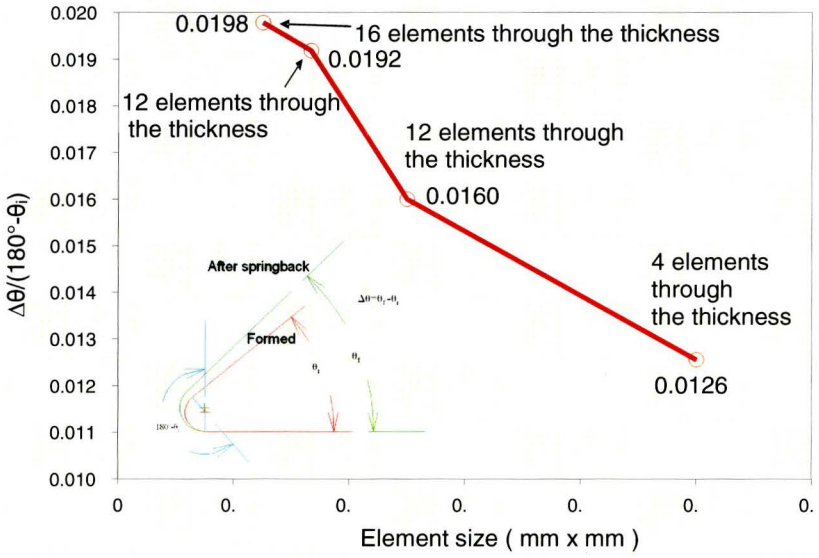

Figure 7.31 DP780 springback results using 3D continuum elements with 1:1:4 aspect ratio. Relative springback plotted as function of element size through the sheet thickness.

CHAPTER 8
NUMERICAL AND EXPERIMENTAL RESULTS

8.1 Introduction

The results within this thesis focus on the application of FEA and simple and general bending theories, in modeling the bending and spring back behavior of DP980 and DP780 steel sheet in plane strain bending.

The results are divided into four major sections. In Section 8.2, an FEA study of V-die bending and springback of the experimental work performed by Queener and DeAngelis (1968) was performed. The work was performed in order to assess the accuracy of simple bending theory and FEA as applied to this problem. In addition, the study was performed to demonstrate bending and springback behaviors using conventional FEA practices, that is, using 3D shell elements and the pure isotropic hardening assumption (Maker and Zhu, 2000). The FEA results were also used to examine the effect of tooling friction, the assumption of uniform plane stain deformation across the specimen width, and the assumption of a uniform bending moment distribution under the punch from simple bending theory. Results are also shown that compare the effect of the FEA solution method. Springback from FEA was compared between the coupled explicit forming-implicit springback and the implicit forming-implicit springback method, presented earlier in Chapter 4. The FEA results were then compared to those from analytical models using simple bending theory.

In Section 8.3 a purely numerical analysis was performed in which simple bending theory was applied to the bending and springback of the DP780 and DP980 steels used in the experimental portions of this work. These results compare the effect of Hollomon hardening versus "piece-wise" linear hardening. Also shown are results which show the effect of the true bending strain compared approach to the engineering strain on the predicted springback.

In Section 8.4, experimental V-die bending springback results for the DP780 and DP980 are compared to that from FEA and simple bending theory. In the experiments, the punch radius to thickness ratio (R_p/t) was 5, and 6.9 for the DP780 and DP980 steels respectively, both of which were at or within the limit for simple bending theory (Marciniak and Duncan, 2002). The FEA results compared the effect of element formulation (i.e., 2D continuum, 3D continuum, and 3D shell), as well as the effect of the hardening assumption (i.e., pure kinematic, isotropic, and where applicable, mixed hardening). The steels were assumed to obey Von Mises yield criterion and strain rate effects were ignored, as the experiments were performed under quasi-static conditions. A comparison was made between FEA and Queener's analytical model, in terms of the predicted bending stress distributions before and after springback, and the predicted bending moment distribution along the length of the blank prior to springback.

Section 8.5 examines experimental, FEA, and numerical results for the bending and springback of the DP780 steel in a commercial bending machine. In the bending experiments, the radius of the experimental bending block was 1 mm

and corresponding to a R_p/t ratio of 0.5, well below the limiting ratio for simple bending. At this bending radius, the DP980 steel fractured and therefore was not included in the analysis. The FEA results compared the effect of the element formulation (i.e., 2D continuum, 3D continuum, and 3D shell), and the effect of the hardening assumption (i.e., pure kinematic and isotropic hardening) on the bending stress distribution and springback. As earlier, the DP780 steel was assumed to obey Von Mises yield criterion and strain rate effects were ignored since the experiments were performed under quasi-static conditions. The predicted springback from FEA and the general (analytical) models based on the work of Tan et al. (1995) were compared, assuming linear unloading. The bending stresses from the general bending model also were compared to those from FEA, and from simple bending theory. These results examined the bending behavior of DP780 and the interaction of the material hardening assumption with the predicted bending stresses, bending moment, thinning deformation, and springback.

8.2 FEA of the experimental V-die bending and springback by Queener and De Angelis (1968)

8.2.1 Baseline 3D shell FEA using LSDYNA3D

The baseline simulations were initially performed using the conventional modeling techniques for forming and springback described by Maker and Zhu (2001). Tooling friction (Coulomb friction) of 0.0 was assumed, and the blank dimensions were 75 mm wide x 200 mm long x 2.49 mm thick. Five simulations

were performed for a range of punch radii, from 13.46 mm to 89.91 mm, in accordance with the experiments by Queener and De Angelis (1968), for the 1095 steel. The blank material was modeled using the isotropic hardening assumption. Work hardening was modeled using the Hollomon hardening law (Eq. 154). The FEA boundary conditions were such that the blank edges were unconstrained, allowing anticlastic curvature to form. The FEA results are shown in Figure 8.1, and are compared to analytical results from the simple bending model and experiments from Queener and DeAngelis (1968).

$$\bar{\sigma}=2447\bar{\varepsilon}^{0.085}\ (MPa) \qquad \text{Eq. 154}$$

The predicted springback from the baseline FEA models were comparable to that from simple bending theory. The relative difference between the springback ratio from the analytical models compared to FEA, ranged from 0.5% to approximately 20%. The springback ratio (Ks) from the FEA was generally lower than that from the simple bending model at lower punch radius to blank thickness ratio (R_p/t). The reverse was found at higher R_p/t ratios, and agreement was very good at intermediate R_p/t ratio. At the R_p/t ratios of 5.4 and 13.6, the springback ratio (Ks) from the FEA was 4% to 5% less than that calculated from the analytical model. At the R_p/t ratios of 29 and 36, Ks from the FEA was larger than that from than the analytical model by 10% and 20% respectively.

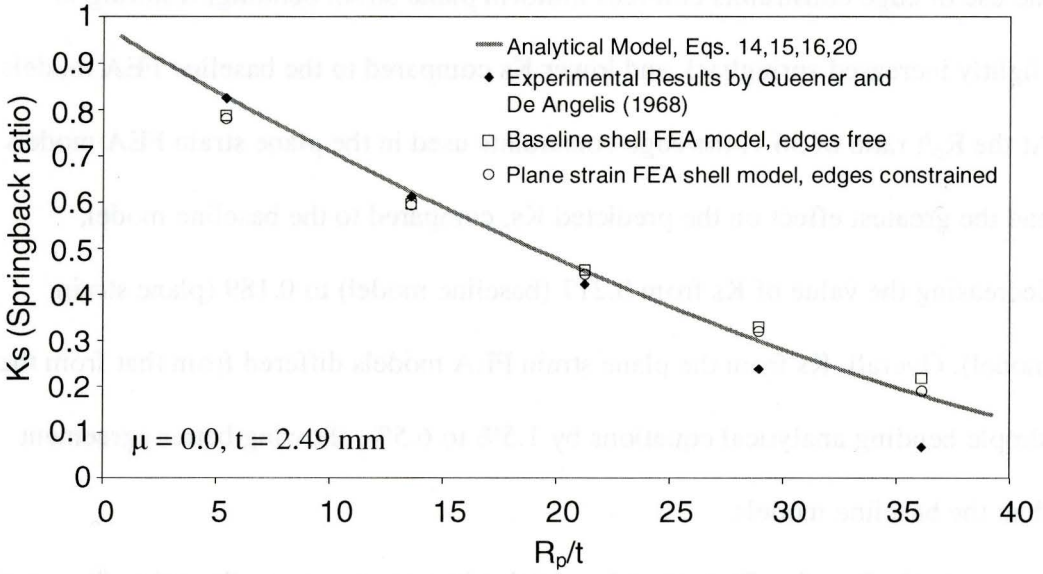

Figure 8.1 FEA predicted springback (explicit forming-implicit springback simulations, μ =0) for V-die bending experiments performed by Queener and De Angelis (1968).

The experimentally measured Ks from Queener and De Angelis (1968) showed good agreement with simple bending theory, up to the R_p/t ratio of 21.3. Up to this point, the error in the Ks from simple bending ranged from 0.4 to 6.8%. At the Rp/t ratios greater than 21.3, Ks was larger than that from experiments, by 26% to 166%.

8.2.2 3D Shell plane strain FEA

FEA of pure plane strain bending conditions were modeled by constraining the edges of the baseline FEA models, suppressing the formation of anticlastic curvature. The predicted Ks for the these FEA models were compared to that from the baseline FEA, as well as that from simple bending theory and experiments by Queener and De Angelis (1968) (Figure 8.1).The results show that

the use of edge constraints enforces uniform plane strain bending, resulting in slightly increased springback and lower Ks compared to the baseline FEA models. At the R_p/t ratio of 36.1, the edge constraints used in the plane strain FEA models had the greatest effect on the predicted Ks, compared to the baseline model, decreasing the value of Ks from 0.217 (baseline model) to 0.189 (plane strain model). Overall, Ks from the plane strain FEA models differed from that from the simple bending analytical equations by 1.5% to 6.5%, showing better agreement than the baseline models.

In the baseline FEA models, anticlastic curvature was allowed to form and was measured using transverse cross sections of the FE mesh (Figure 8.2). At the largest punch radii of 89.91 mm, anticlastic curvature was convex. At smaller punch radii (i.e. 13.46 mm) the shape was more complex. These results show that the relationship between anticlastic curvature shape and punch radii is complex.

Anticlastic curvature affected the bending stress distribution across the blank width (Figures 8.3-8.6). The plane strain FEA models predicted a uniform bending stress distributions across the width of the blank, before and after springback. In contrast, the baseline models showed non-uniform bending across the blank width, with the minimum bending stress occurring at the blank edges. The maximum residual stress after springback was predicted to occur near the blank edges. The plane strain FEA results predicted lower residual stresses (in magnitude) compared to the baseline models.

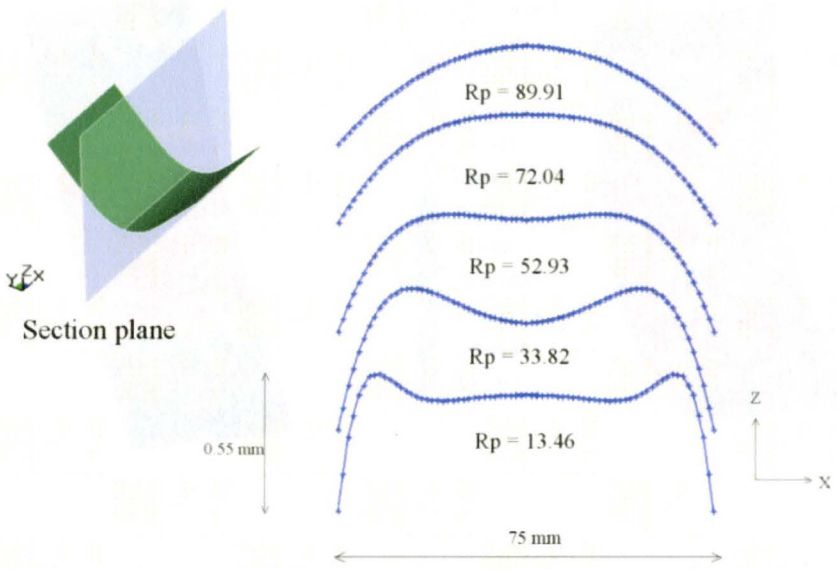

Figure 8.2 FEA predicted cross section of the blank (at the punch apex) showing anticlastic curvature as a function of punch radii.

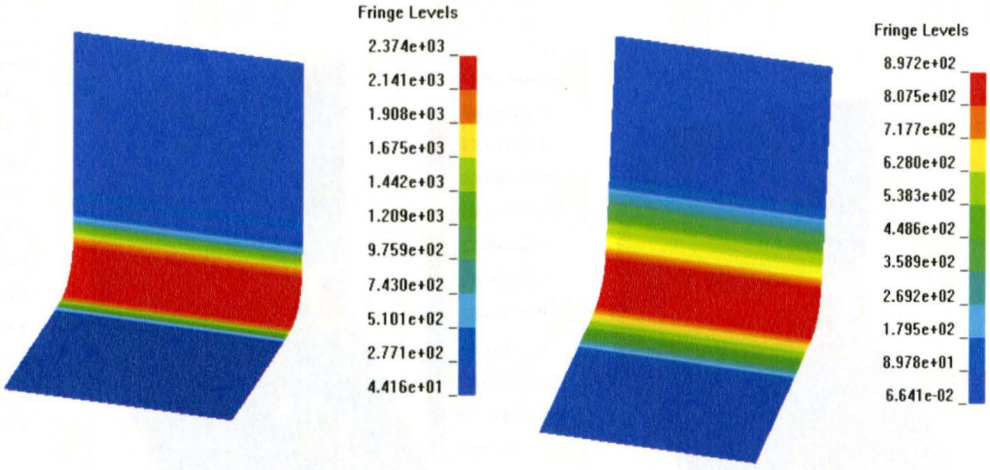

Figure 8.3 Plane strain FEA simulations for a punch radius of 13.46 mm of Queener's V-die bending and springback experiments. Shown are predicted (maximum) principle bending stress distributions before (left) and after (right) springback for 2.49 mm thick, 1095 steel (Stress is in MPa.).

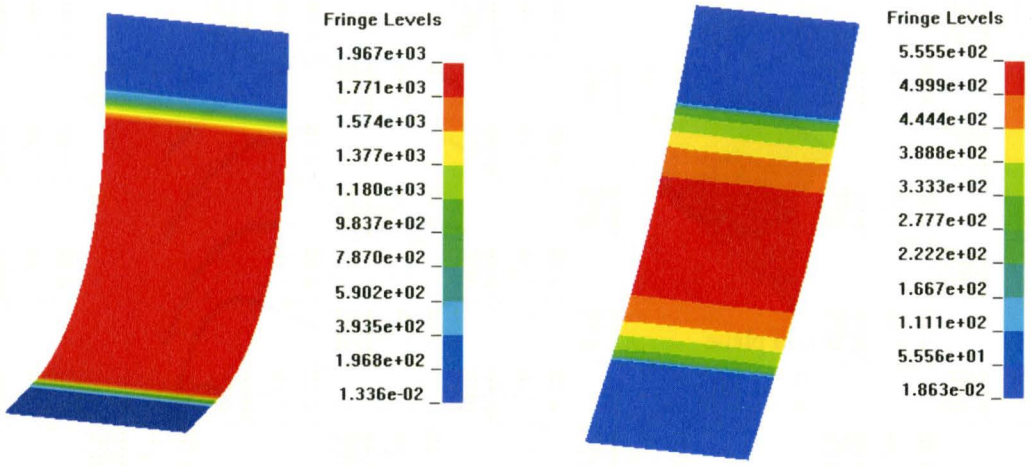

Figure 8.4 Plane strain FEA simulations for a punch radius of 89.91 mm of Queener's V-die bending and springback experiments. Shown are predicted (maximum) principle bending stress distributions before (left) and after (right) springback for 2.49 mm thick, 1095 steel.

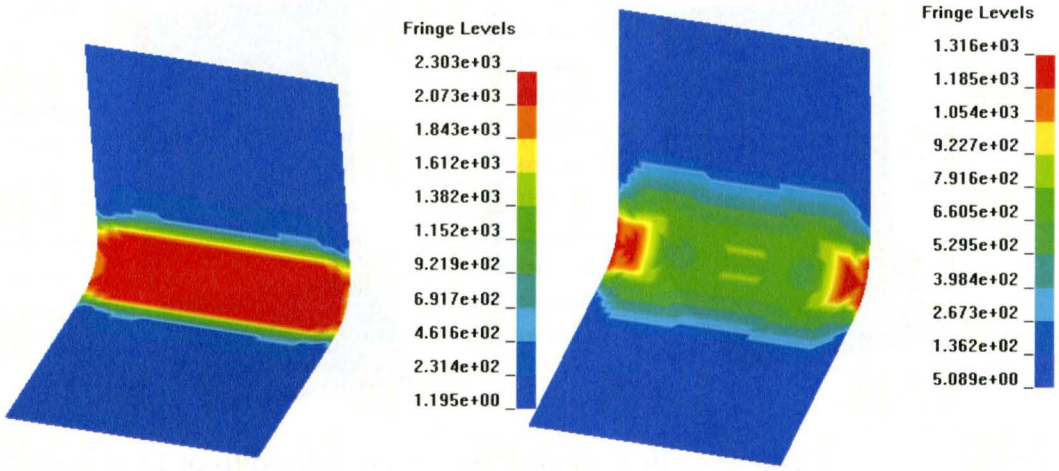

Figure 8.5 Baseline FEA simulations for a punch radius of 13.46 mm (without plane strain constraints at the blank edges) of Queener's V-die bending and springback experiments. Shown are predicted (maximum) principle bending stress distributions before (left) and after (right) springback for 2.49 mm thick, 1095 steel.

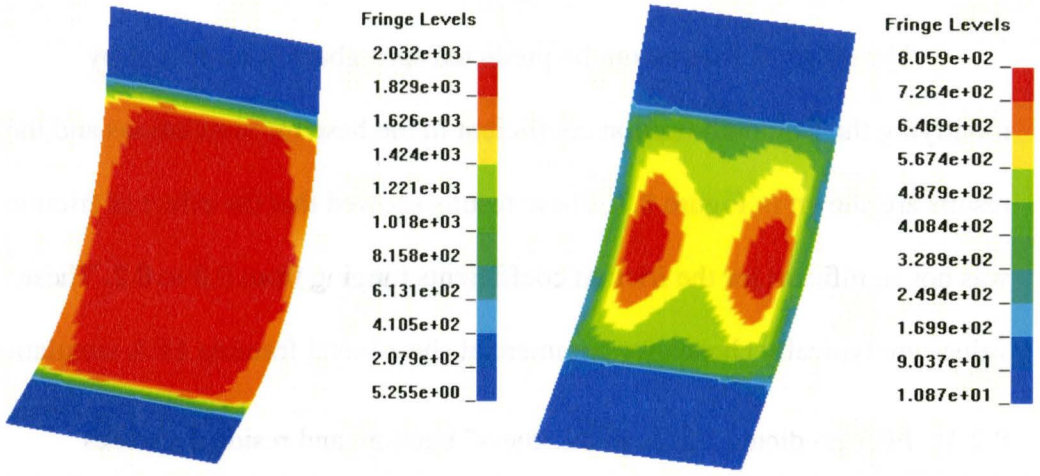

Figure 8.6 Baseline FEA simulations for a punch radius of 89.91 mm (without plane strain constraints at the blank edges) of Queener's V-die bending and springback experiments. Shown are predicted (maximum) principle bending stress distributions before (left) and after (right) springback for 2.49 mm thick, 1095 steel.

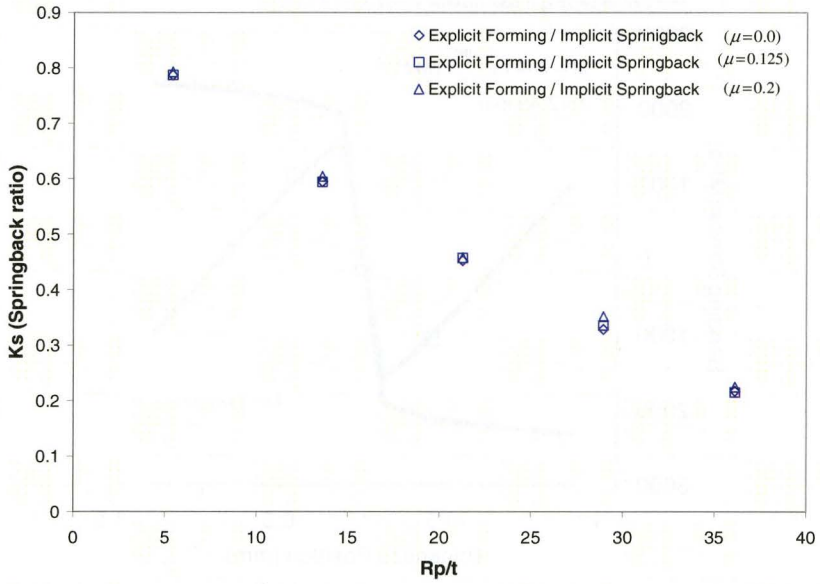

Figure 8.7 FEA predicted springback for sheet (Coulomb) coefficient of friction ranging from 0.0 to 0.2, typically used in sheet metal forming simulations (blank edges are "free").

8.2.3 FEA predicted effect of tooling friction

The effect of friction on the predicted springback was studied by modifying the Coulomb friction coefficient in the baseline simulations and the results are shown in Figure 8.7. These results showed that the effect of friction was not significant for the friction coefficients ranging from 0.0 to 0.2. These values are typically chosen for commercial sheet metal forming FEA simulations.

8.2.4 FEA predicted "through thickness" bending and residual stresses

Figures 8.8-8.12 show bending and residual stresses from the baseline FEA models, at the mid-width location of the blank, and at the apex of the bend for the range of punch radii as per the work of Queener and DeAngelis (1968).

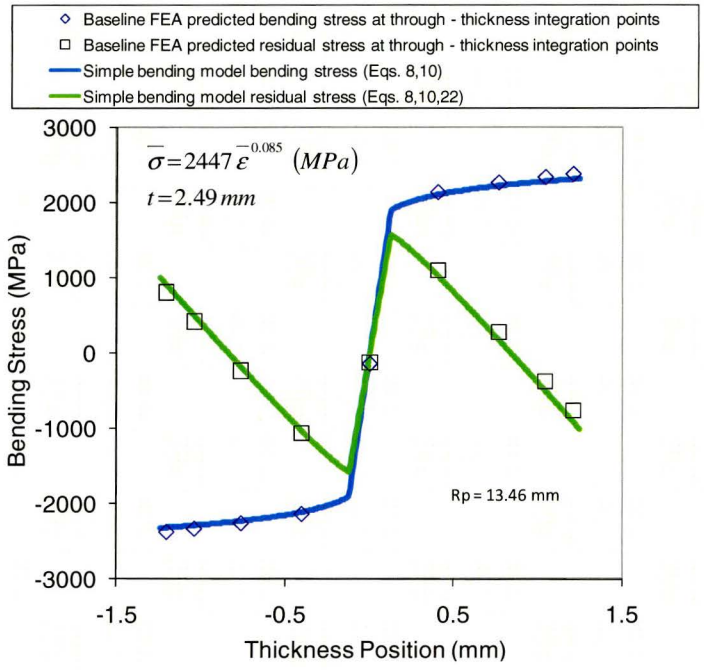

Figure 8.8 Through thickness bending and residual stresses after springback, FEA compared to analytical models using simple bending theory, 2.49 mm, thick 1095 steel (Rp=13.46 mm).

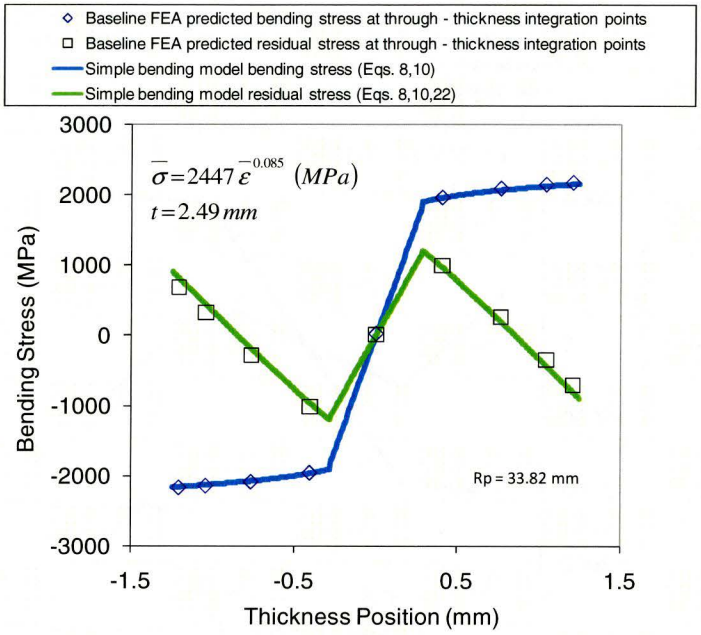

Figure 8.9 Through thickness bending and residual stresses after springback, FEA compared to analytical models using simple bending theory, 2.49 mm thick, 1095 steel (Rp=33.82 mm).

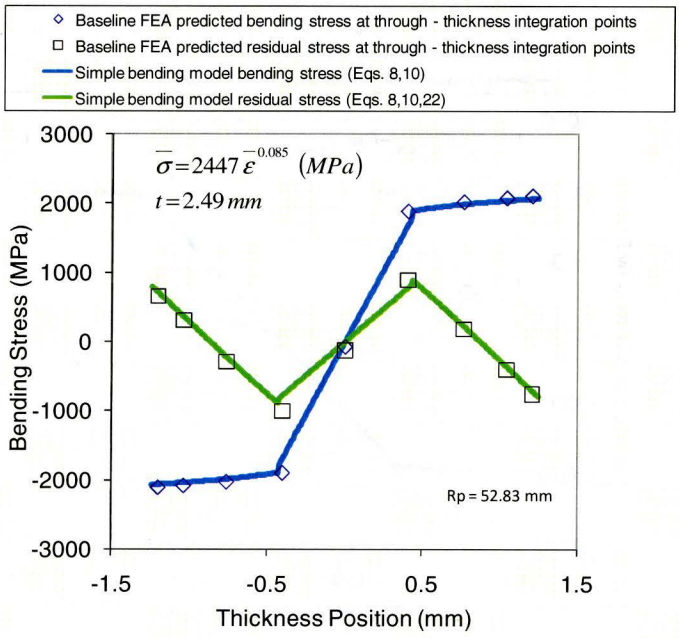

Figure 8.10 Through thickness bending and residual stresses after springback, FEA compared to analytical models using simple bending theory, 2.49 mm thick, 1095 steel (Rp=52.93 mm).

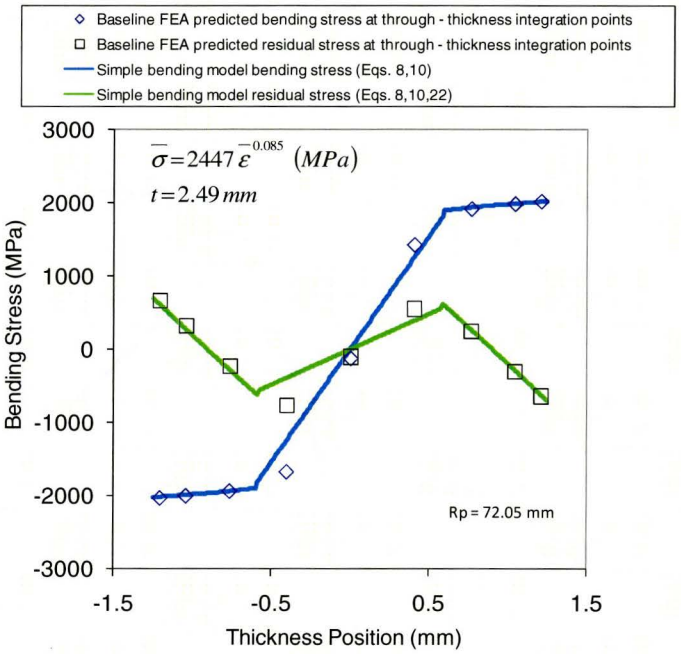

Figure 8.11 Through thickness bending and residual stresses after springback, FEA compared to analytical models using simple bending theory, 2.49 mm thick, 1095 steel (Rp=72.05 mm).

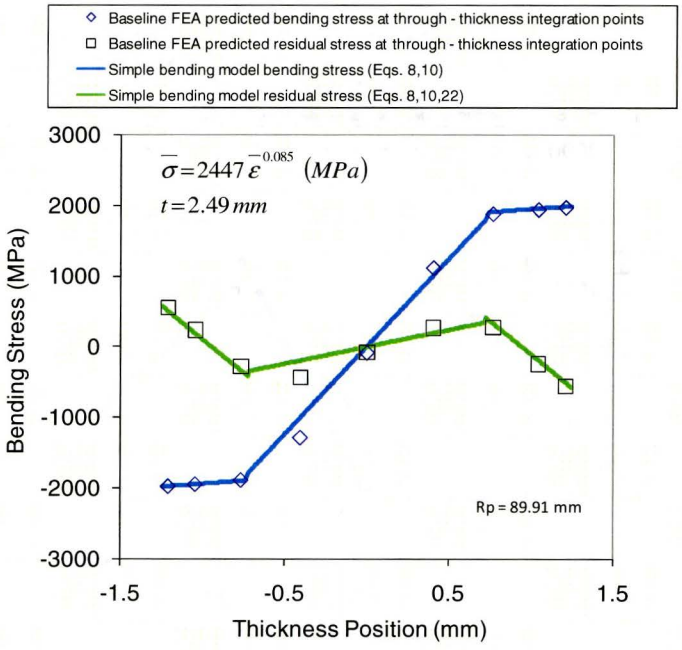

Figure 8.12 Through thickness bending and residual stresses after springback, FEA compared to analytical models using simple bending theory, 2.49 mm thick, 1095 steel (Rp=89.91 mm).

In the FEA models, the through thickness bending stresses are calculated at the through thickness integration points in the shell element. In this case, 9 integration points were used. The bending and residual stresses predicted from the FEA and simple bending theory showed good agreement for all punch radii investigated.

8.2.5 Bending moment distribution along the blank length in the baseline simulations

The baseline FEA were performed using a punch to die clearance of 0.1 mm plus the blank thickness, to avoid contact instabilities at the end of the punch stoke. The punch to die clearance was therefore less than 5% of the blank thickness. The FEA predicted bending moment distributions over the length of the blank, just prior to springback, for the punch radii in the range of 13.46 to 89.91 mm, are shown in Figures 8.13-8.17. The distributions were taken at the mid-width position of the blank.

To facilitate the interpretation of these results Figure 8.13 illustrates a longitudinal cross section of the blank shell model; displayed using the "thicken option" in the post processor LSPOST. The "thicken option" displays the stress distribution through the thickness at a distance "± half the blank thickness" from the mid-surface of the shell elements. The bending moment is therefore shown as a function of position along the blank "arc" length. These results were compared with the predicted bending moment distribution from simple bending theory. The results show that as the punch radius increases, the maximum bending moment

under the punch decreases. The agreement between the maximum bending moment from FEA compared to simple bending theory was very good. There were, however, differences observed between in the bending moment distributions. The FEA showed a region directly under the punch in which the bending moment is at a maximum, and an adjacent transition region in which the bending moment decreases from a peak value near the punch to 0 at the point of contact with the die. In contrast, the bending moment distribution assumed by simple bending theory is constant under the punch, and has a magnitude of 0 elsewhere.

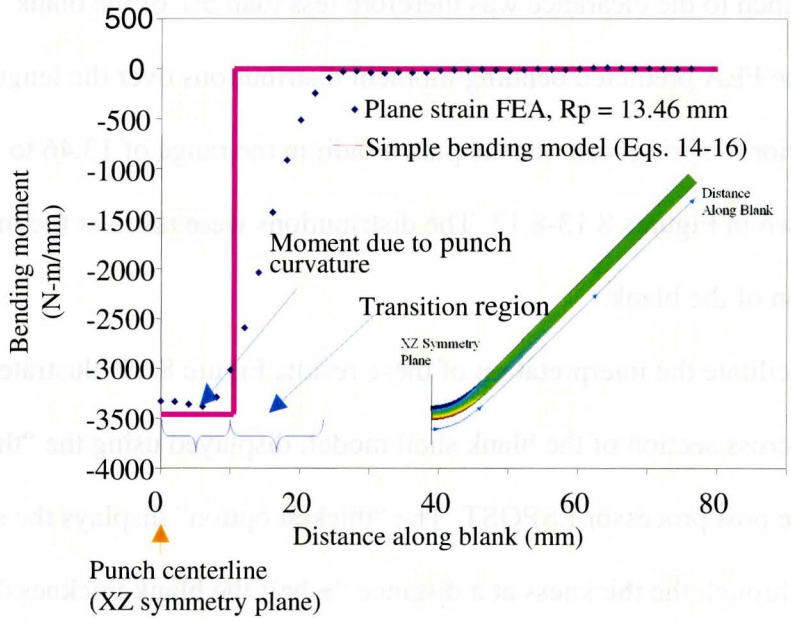

Figure 8.13 FEA predicted, stored bending moment at the bottom of the punch stroke compared to that predicted by simple bending theory for Rp = 13.46 mm.

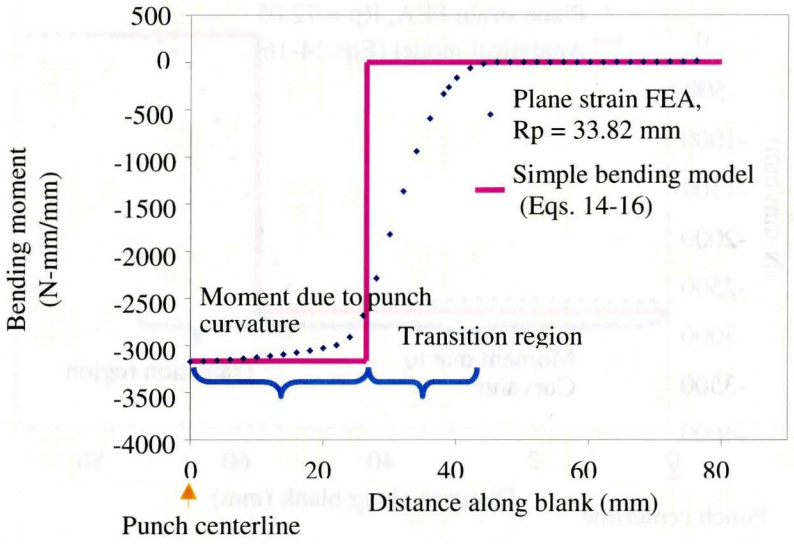

Figure 8.14 FEA predicted, stored bending moment at the bottom of the punch stroke compared to that predicted by simple bending theory for Rp = 33.82 mm.

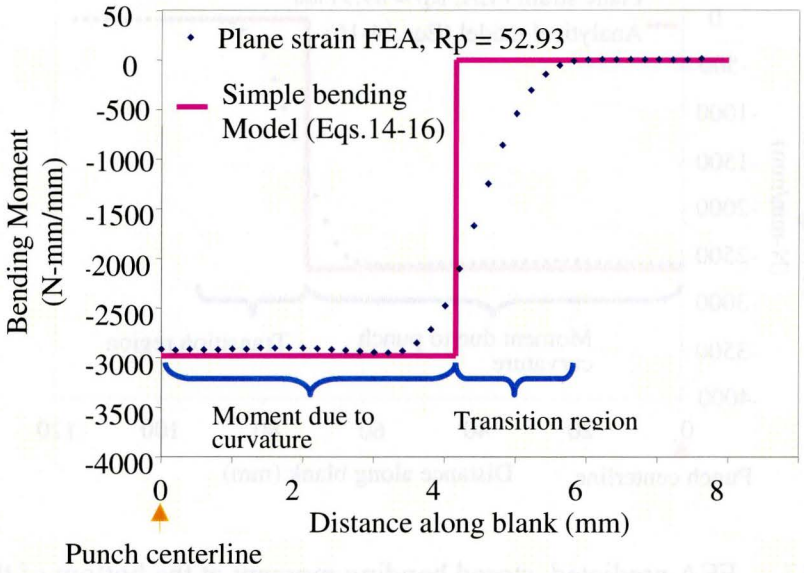

Figure 8.15 FEA predicted, stored bending moment at the bottom of the punch stroke compared to that predicted by simple bending theory for Rp = 52.93 mm.

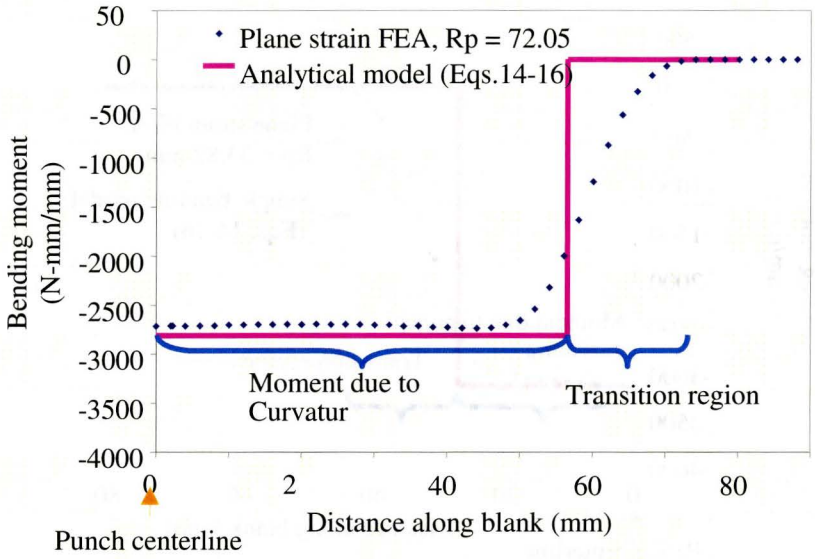

Figure 8.16 FEA predicted, stored bending moment at the bottom of the punch stroke compared to that predicted by simple bending theory for Rp = 72.05mm.

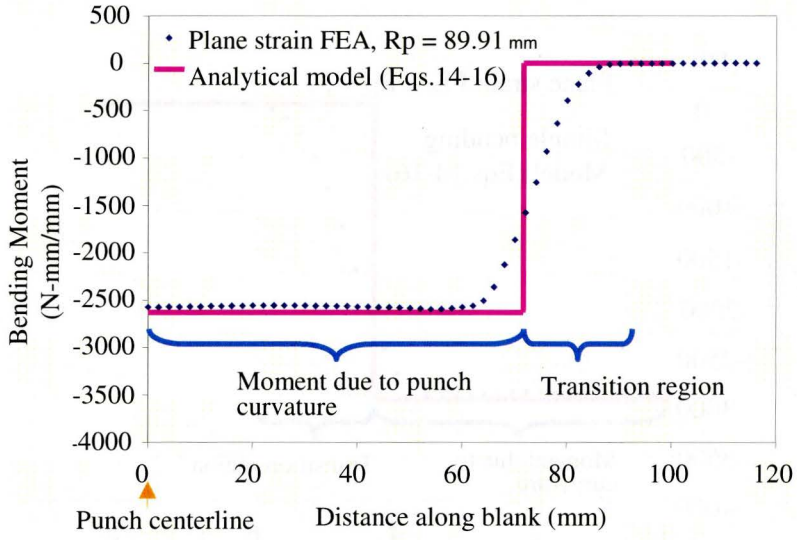

Figure 8.17 FEA predicted, stored bending moment at the bottom of the punch stroke compared to that predicted by simple bending theory for Rp = 89.91 mm.

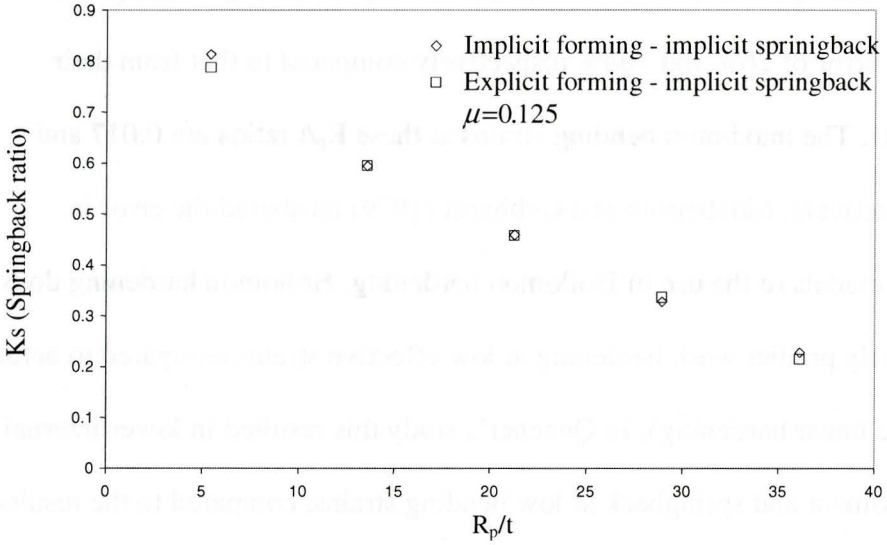

Figure 8.18 The effect of simulation method in predicted springback for the baseline simulations using Coulomb friction coefficient of 0.125.

8.2.6 Non-linear FEA solution procedure

The FEA results comparing the explicit forming-implicit springback method, to the implicit forming-implicit springback method, are shown in Figure 8.18. The results showed no significant difference in the predicted springback magnitude between the two methods.

8.2.7 Discussion

Queener and De Angelis (1968) developed an analytical model based on simple bending theory to predict bending stresses, bending moment, and springback in the V-die bending and springback of a AISI 1095 steel blank. Their results showed good agreement between the predicted springback ratio (Ks) and experiments, up to the R_p/t ratio of approximately 21. Their simple bending model underpredicted springback significantly (Figure 8.1) beyond this ratio. For

example, at the R_p of 72.04 and 89.91 mm, the simple bending model predicted Ks with an error of 26% and 166% respectively compared to that from their experiments. The maximum bending strains at these R_p/t ratios are 0.017 and 0.014 respectively. Sidebottom and Gebhardt (1979) attributed the error in Queener's models to the use of Hollomon hardening. Hollomon hardening does not accurately predict work hardening at low effective strains compared to actual (piece-wise linear hardening). In Queener's study this resulted in lower internal bending moment and springback at low bending strains, compared to the results presented by Sidebottom and Gebhardt using a piece-wise linear hardening approach.

In Queener's study, experimental stress strain data was not reported for the 1095 steel, and piece-wise linear work hardening was therefore not incorporated in the FEA. An exact comparison between the FEA and Queener's experimental results was, therefore, not possible. The baseline FEA of V-die bending and springback used Hollomon hardening as in Queener's work. From Sidebottom's work, the FEA would therefore be expected to underpredict the Queener's experimental springback, when the maximum bending strains are near the yield point of the material (i.e., large R_p/t ratios). However, springback from the FEA would be expected to show better agreement with that from Queener's analytical simple bending model (Eqs. 9,14-16,20).

The springback from the baseline FEA showed good agreement with that from Queener's simple bending model at R_p other than 13.46 and 89.91 mm. At

these R_p's, the Ks from the FEA was in error by approximately 20% compared to that from the analytical equations. The magnitude of the error from FEA was consistent with that expected using LSDYNA3D (Maker and Zhu, 2001). However, in this work, other factors are attributed to the error as explained further.

The FEA results were affected by anticlastic curvature formation. The effect of anticlastic curvature was demonstrated by comparing springback from the baseline FEA with that from the 3D shell FEA models using plane strain edge constraints (Figure 8.1). The edge constraints in the 3D shell plane strain models were used to simulate the bending of an infinitely wide plate. The edge constraints had two effects compared to the baseline models. The first is the complete suppression of anticlastic curvature, and the second is the promotion of a uniform bending stress across the blank width (Figures 8.3-8.6). Persistent anticlastic curvature suppresses springback by increasing the second moment of inertia of the blank at the end of bending, and this condition is more severe with a larger Searle parameter ($w^2/ (R_i t)$) (Horrocks and Johnson, 1967; Wang et al., 2005). Opposed to this is the promotion of uniform plane strain deformation with increasing Searle parameter. Uniform plane strain deformation across the blank width (as opposed to plane strain in the middle, and plane stress at the edges) conceptually increases (Wang et al., 2005). Visual inspection of the baseline FEA, showed more severe anticlastic curvature with smaller punch radii (Figure 8.2), which therefore acts to suppress springback. A comparison of the Ks from the baseline FEA with that

from Queener's analytical models did not provide an understanding of the discrepancies observed. Comparing the plane strain FEA to Queener's FEA models however, does provide insight as to the discrepancies between FEA and the analytical models. In this comparison, both FEA and the analytical models can be compared in the absence of the effect of anticlastic curvature.

Comparing the bending moment distributions along the blank length, between the plane strain FEA and from simple bending theory, provides insights into the difference between Ks from the FEA and from simple bending analytical models. Wang (1993) has argued that in V-die bending, springback is proportional to the integral of the moment distribution along the entire length of the blank. Simple bending theory assumes that springback is due solely to a constant bending moment directly under the punch (Queener and DeAngelis 1968). The predicted bending moment distribution, and therefore curvature from the analytical model, is essentially a step function that has a discontinuity at the tangent point at the punch and die. At the tangent point the analytical model assumes a bending moment of "0". This distribution is unrealistic. In real bending processes curvature is continuous over the blank length and therefore must transition from the punch to the die. From Marciniak et al., (2002), the blank shape under the punch in V-die bending does not necessarily conform perfectly to the punch curvature, as is assumed by simple bending theory.

From Wang's (1993) analysis of the effect of die clearance in V-die bending, the transition zone along the length of the blank between the tangent

points of the punch and die contributes to springback. This zone is apparent in the FEA results shown in Figures 8.13-8.17. The length of this zone increases with increasing punch to die clearance, resulting in greater springback. The effect of die clearance is consistent with that observed by others (for example, Levy, 1984). The deviation in the predicted springback ratio (Ks) between the 3D shell plane strain FEA and the simple bending model can therefore be seen in light of the differences in the bending moment distributions observed in Figures 8.13-8.17, in which one factor affecting the moment distribution is die clearance. Other factors to consider are the numerical parameters used in the FEA. The bending moment distribution along the blank is directly related to the curvature distribution (Wang, et al., 2005). FEA numerical parameters such as element stiffness, which is a function of element type (Schikorra et al., 2005), and contact penalty stiffness factor, which affects the degree of penetration of the blank into tooling (LSTC, 2006), directly affect the curvature distribution. Therefore these FEA numerical parameters should also affect springback vis a vie the moment distribution along the length of the blank.

There was good agreement when comparing the through-thickness bending and residual stress distributions (Figures 8.8-8.12) between the baseline FEA (in the middle width position of the blank), to that from the simple bending model assuming elastic-plastic bending (Eqs. 14-16 and Eq. 20 in Chapter 2). The bending stress distributions across the width of the blanks were, however, non-uniform with the lowest bending stresses at the free edges (Figures 8.3-8.6). This

was due to anticlastic curvature formation and uni-axial deformation at the blank edges as opposed to plane strain deformation at the center of the blank, as discussed previously. The Ks from the plane strain FEA differed from that for the simple bending model by a maximum of only 6.5%, demonstrating the effectiveness of the FEA method. These results, in conjunction with the agreement between the bending and residual stresses after springback, demonstrated that the shell element behaved in accordance to simple bending theory. Also demonstrated was the effectiveness of standard LSDYNA3D modeling methods, as described by Maker and Zhu (2001), to predict springback under the conditions of simple bending, described earlier in Chapter 2.

Overall, the factors not accounted for in simple bending theory such as the effect of the punch to die clearance, FEA numerical parameters, and actual blank curvature under the punch, contribute to the error in Ks between FEA and the simple bending analytical models from Chapter 2. This result was found, mindful that other parameters such as element size are also important as discussed earlier in Chapter 3. This study has demonstrated however that the 3D shell element behaves according to simple bending theory, as shown by the good agreement between the FEA and simple bending theory, in terms of bending and residual stress distributions, as well as the maximum bending moment under the punch.

Other FEA was performed investigating the effect of tooling friction and FEA solution procedure on Ks from FEA. The results show that varying Coulomb friction between 0.0 and 0.20 did not significantly affect the predicted springback

(Figure 8.7), which agrees with experimental and results from Nilsson et al. (1997). These results indicate that for V-die bending, friction within this range does not create tensile membrane stresses sufficient in magnitude to reduce the internal bending moment or affect the curvature of the blank under the punch (Marciniak et al., 2002).

The effect of FEA solution procedure is shown in Figure 8.18. These results show nearly equivalent results (predicted Ks value) when comparing the explicit forming-implicit springback procedure, to the implicit forming-implicit springback procedure. This is in agreement with results by Forcellese et al. (1996) for V-die bending. This is important for the general bending FEA, discussed later. These FE models used a number of 3D continuum elements through the blank thickness, resulting in small element sizes. If this FEA was performed using the explicit method, then the resulting time step as governed by the Courant condition, would also be small, resulting in prohibitive CPU times.

8.3 Simple bending theory applied to the bending and springback behavior of DP780 and DP980

In preparation for the V-die bending experiments, simple bending theory was used to investigate the bending and springback behavior of the two experimental steels, DP780 and DP980. The engineering properties of these materials are shown in Table 8-1 and Table 8-2 respectively.

Analytical equations from simple bending theory, discussed earlier in Chapter 2, were applied to the DP steels used in the experiments. Results are

shown for the predicted bending moment and springback using the various analytical equations. For example, pure plastic bending neglecting the elastic core (Eq. 9), an elastic–plastic assumption that includes the elastic core (Eqs. 14-16), and an elastic-plastic assumption in which the bending strains in terms of true strain (Eq. 17) are utilized. A principle assumption used in these equations is that the material obeys the Hollomon hardening law, and therefore the strength coefficient, "k", and the "n-value" are required inputs to the analytical equations. Experimental tensile curves of the DP steels from the longitudinal direction were used to determine "k" and the "n-value" by least squares curve fitting and the results are shown in Figures 8.19-8.20. Both DP steels were also assumed to be isotropic obeying Von Mises yield criterion by assuming $\bar{r}=1$ (see Table 8-1 and Table 8-2).

Table 8-1 DP780 cold rolled, engineering tensile properties. Note that each direction is an average of 3 tests according to the ASTM E8 standard

t (mm)	Direction	0.2% Offset yield strength (MPa)	Ultimate tensile strength (MPa)	Uniform elongation (%)	Total elongation (%)	n-value (4–6%)	r-value at 10%
2.00	0 deg. (L)	515.3	837.8	10.1	18.7	0.137	0.7882
2.00	45 deg.(D)	522.0	847.5	10.2	18.4	0.138	0.814
2.00	90 deg.(T)	522.6	848.7	10.0	17.6	0.140	1.063
			$\overline{R}$, average (L+2D+T)/4				0.870

Table 8-2 DP980 cold rolled, engineering tensile properties. Note that each direction is an average of 3 tests according to ASTM E8 standard

t (mm)	Direction	0.2% Offset yield strength (MPa)	Ultimate tensile strength (MPa)	Uniform elongation (%)	Total elongation (%)	n-value (4-6%)	r-value at 10%
1.457	0 deg. (L)	663.1	1053.4	7.8	12.1	0.099	0.781
1.457	45 deg.(D)	649.7	1059.2	7.2	10.5	0.096	0.786
1.457	90 deg.(T)	668.7	1063.5	8.0	12.1	0.098	1.081
			$\overline{R}$, average (L+2D+T)/4				0.858

A comparison between the "curve fitting" results, and actual tensile test data for DP780 and DP980 steels is shown in Figures 8.19-8-20. The results show that at low strains, Hollomon hardening overpredicts actual hardening. This behavior is also translated to the predicted bending stresses. The predicted bending stresses for two punch radii are shown for the DP980 material in Figures 8.21-8.22. Given the differences between the piece-wise linear hardening and Hollomon law hardening assumptions, results were generated to determine the effect of the hardening assumption on the predicted internal bending moment and springback for the different analytical equations described previously in Chapter 2.

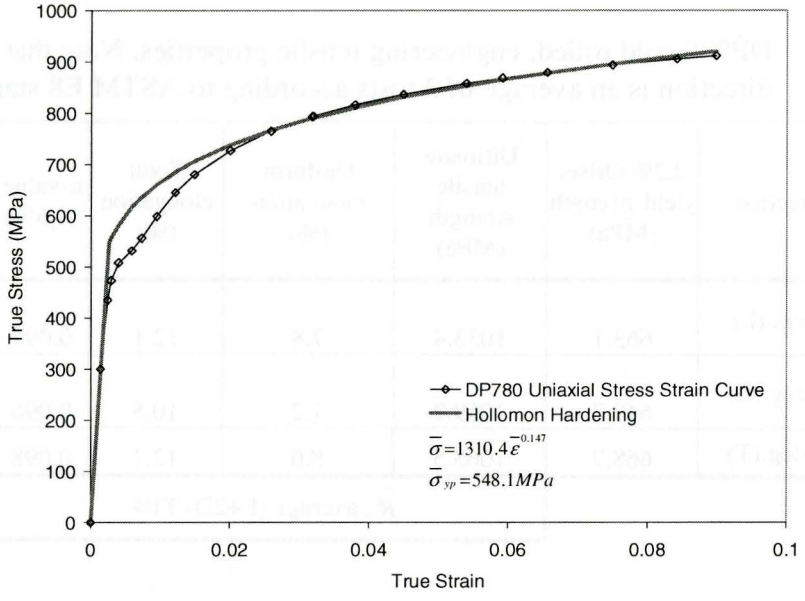

Figure 8.19 DP780 experimental true stress-true strain curve, compared to a Hollomon fit.

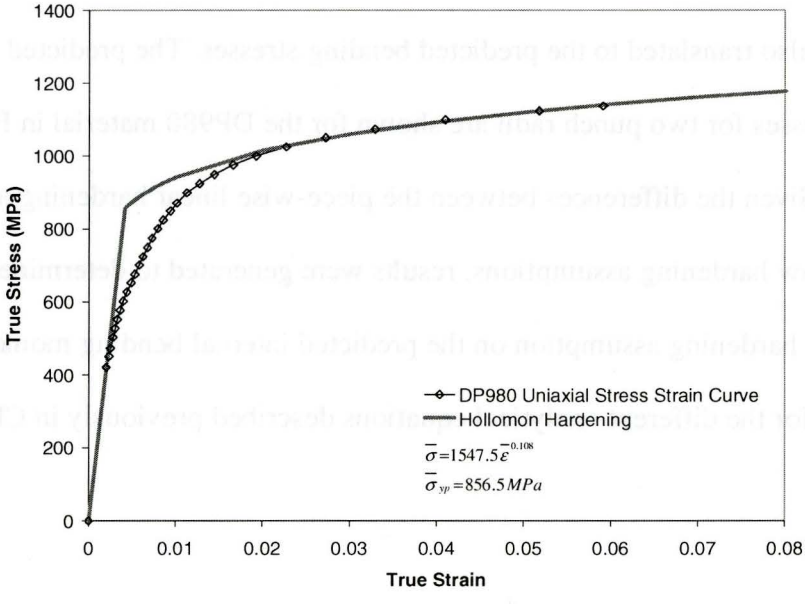

Figure 8.20 DP980 experimental true stress-true strain curve, compared to a Hollomon fit.

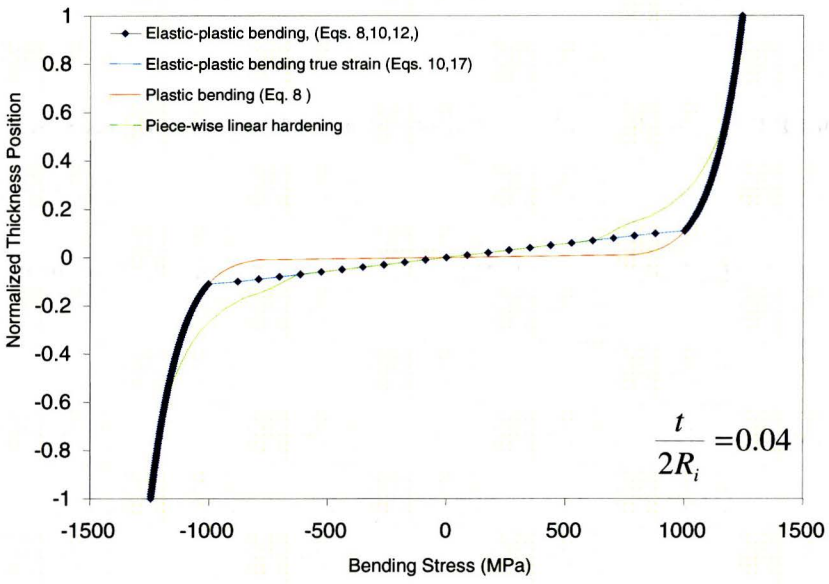

Figure 8.21 Predicted bending stresses for the DP980 steel, using the Hollomon hardening assumption, compared to piece-wise linear hardening at a maximum bending strain of 0.04.

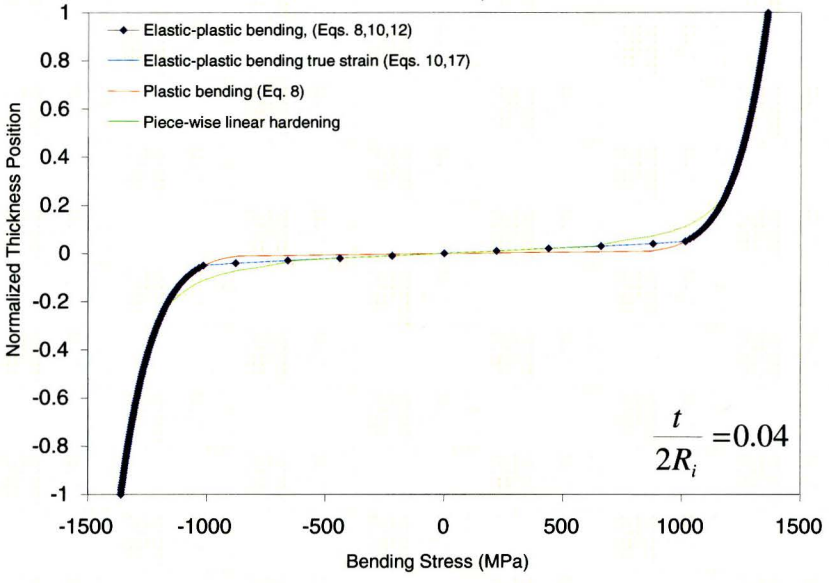

Figure 8.22 Predicted bending stresses for the DP980 steel, using the Hollomon hardening assumption, compared to piece-wise linear hardening at a maximum bending strain of 0.10.

The internal bending moment as a function of relative curvature for both DP steels is shown in Figures 8.23-8.24. The results show that, as bending curvature increases, the total internal bending moment also increases, and the elastic portion of the bending moment decreases to a magnitude of 0. The maximum elastic bending moment occurs at the curvature corresponding to the onset of yielding in the outermost fibers.

At low values of the relative bending curvature, the plastic bending equation using Hollomon hardening predicts larger internal bending moment compared to piecewise linear hardening. This trend agrees with the predicted bending stresses shown in Figures 8.21-8.22. A pure plastic assumption, which ignores elastic strains, predicts the largest internal bending moment compared to all other cases. The calculated bending moments using the elastic-plastic assumption, either with the true strain or engineering strain expressions, were not significantly different.

At larger bending curvatures, the calculated bending moments are essentially the same for the different cases including the different hardening assumptions. Also shown is the predicted bending moment for the bending curvature of the V-die experiments performed in this thesis. At this curvature, the calculated internal bending moment is essentially the same for the different cases including the different hardening assumptions.

The calculated springback as a function of the ratio R_m/t for the two DP steels is shown in Figure 8.25. The results show that for R_m/t of 5 to 20t, there is

no significant difference in springback for the different cases. Differences occur only at R_m/t greater than about 25. Piece-wise linear hardening predicts the largest Ks for R_m/t greater than 25, followed by solutions using elastic –plastic, and the plastic bending assumptions. The differences between Ks from the elastic-plastic assumption and from the elastic-plastic assumption using true strain, were insignificant. Also shown is greater springback (or lower springback ratio, Ks) for DP980 compared to DP780.

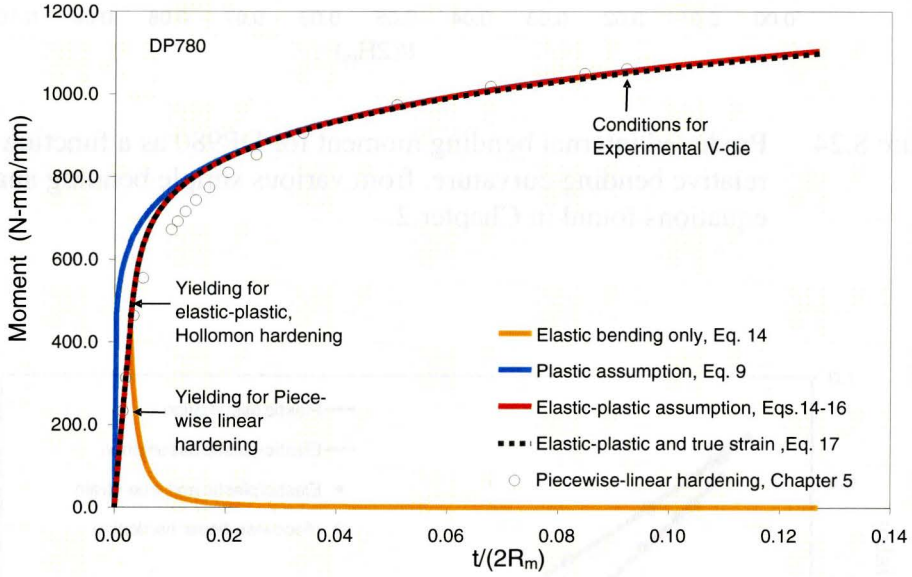

Figure 8.23 Predicted internal bending moment for DP780 as a function of relative bending curvature, from various simple bending analytical equations found in Chapter 2.

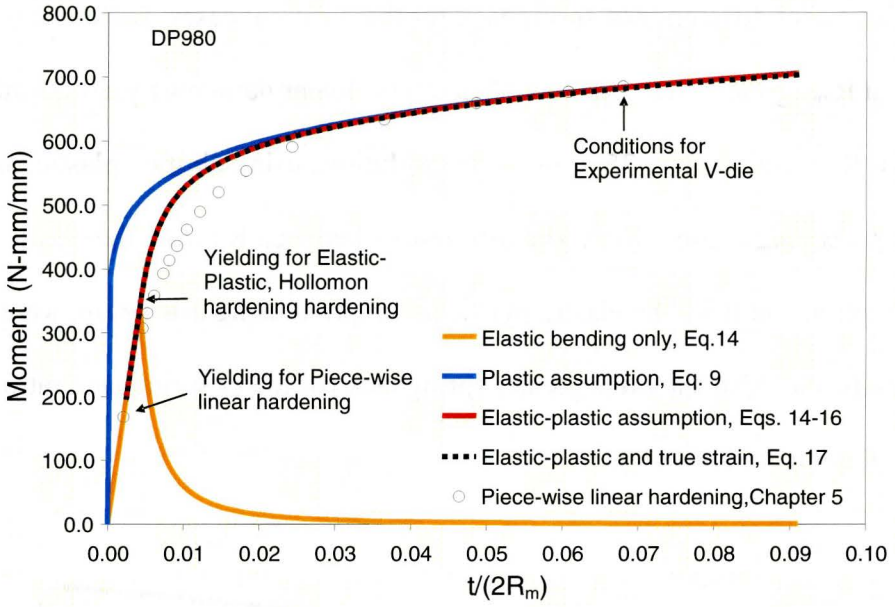

Figure 8.24 Predicted internal bending moment for DP980 as a function of relative bending curvature, from various simple bending analytical equations found in Chapter 2.

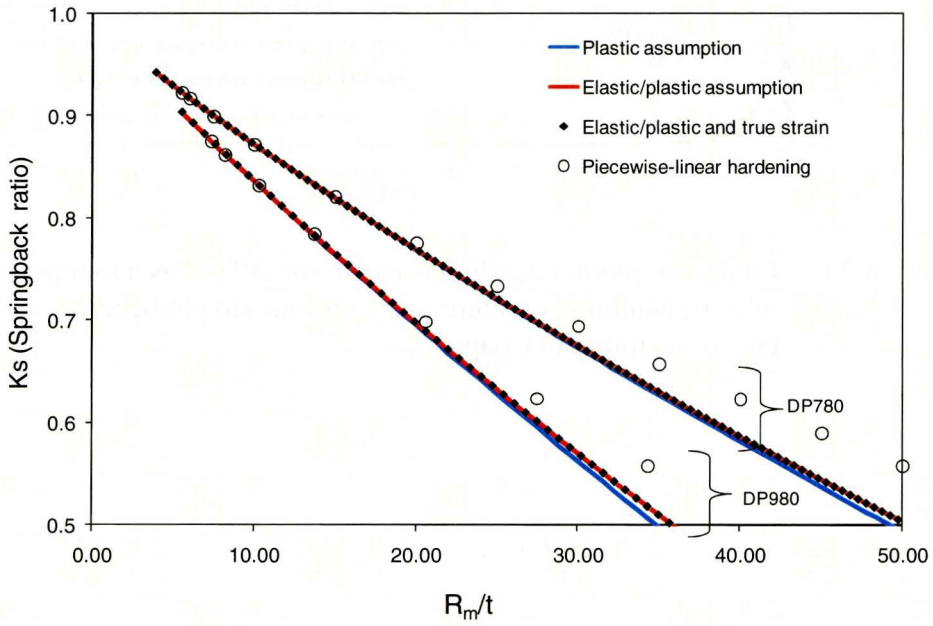

Figure 8.25 Various simple bending theory approaches used to predict springback for DP780 and DP980 as a function of the R_m/t ratio.

8.3.1 Discussion

Hollomon hardening for the DP780 and DP980 steel provides a good fit to the actual work hardening beyond the effective strain of 0.02. Below this, Hollomon hardening significantly overpredicts hardening. This results in a significant overprediction of the internal bending moment and springback at low bending strains (Figures 8.21-8.24), compared to that using piece-wise linear hardening.

The punch radius in the V-die experiments performed in this thesis was 10 mm. The corresponding principle bending strains for the steels therefore ranged from approximately 0.068 to 0.091, and the corresponding effective strains were approximately 0.078 to 0.105. At these strain levels, there is good agreement with respect to the bending moment and springback, between the various analytical equations presented earlier in Chapter 2 (Figures 8.23-8.25). It follows that a comparison of the analytical equations using the elastic-plastic approach (Eqs. 14-16, Eq. 20) to the FEA of the V-die bending experiments in this thesis, was sufficient.

8.4 FEA of V-Die bending experiments for DP780 and DP980 steels

Results are shown for the V-die bending and springback experiments for the DP steels having material properties described earlier in Table 8-1 and Table 8-2. The punch radius used was 10 mm and the punch to die clearance was on average 2.0 mm plus blank thickness, at the bottom of the punch stroke. The actual punch displacements used in the FEA were determined from in-situ CMM

measurements performed during the experiments. This activity was described earlier in Chapter 7.

The FEA incorporated kinematic, isotropic and mixed isotropic and kinematic hardening where appropriate. This required the calibration of the isotropic-kinematic hardening behavior to published values of Baushinger Effect Parameters (BEF) for similar DP steels, in the work by Sadagopan (2003).

8.4.1 Calibration of mixed hardening for the MAT103 material model in LSDYNA3D against similar DP780/980 steels

FEA uniaxial tension-compressions models of the DP780 and DP980 steels were calibrated against the published values of BEF for an effective prestrain of about 0.05 (Sadagopan, 2003). A portion of the FEA calibration results are shown in Figures 8.26-8.31. The FEA was used to determine the BEF parameter as a function of the mixed hardening parameter "α", and the results are plotted in Figures 8.32-8.33 for the DP780 and DP980 steels respectively. The results show that the DP780 steel best reproduces the published values of BEF when modeled as a pure kinematic hardening material. The DP980 steel shows mixed isotropic-kinematic hardening behavior, with a bias towards kinematic hardening. These results are also summarized in Table 8-3. Subsequent simulations of the V-die bending, and small radius bending experiments were therefore performed using MAT103 and the appropriate value of α from the calibration, in addition to pure isotropic and pure kinematic hardening assumptions.

Table 8-3 Published values for BEF for and calibrated hardening behavior of the DP780 and DP980 steels based on FEA (uni-axial) tension-compression simulations and using MAT103.

Material	BEF at a prestrain of 0.05 (as defined in Eq. 52, Chapter 3)	Mixed isotropic – kinematic hardening parameter, α, used in MAT103
DP780	0.38*	0.0 (Pure Kinematic Hardening)
DP980	0.34*	0.21 (Mixed Hardening)

* published tests for similar DP steels (Sadagopan, 2003)

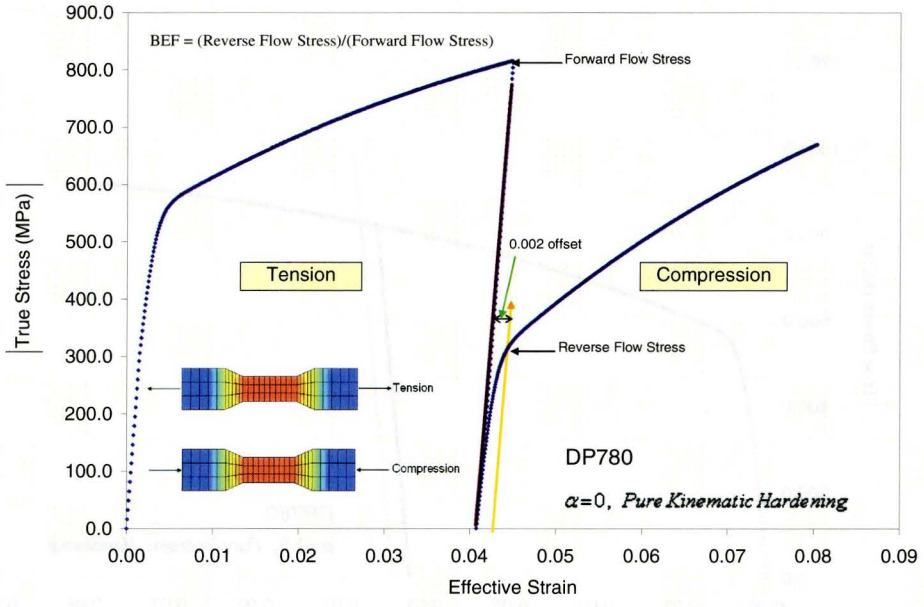

Figure 8.26 DP780 FEA uniaxial tension-compression test, stress-strain response and BEF calculation using LSDYNA3D material model MAT103 (α is set to 0 for pure kinematic hardening).

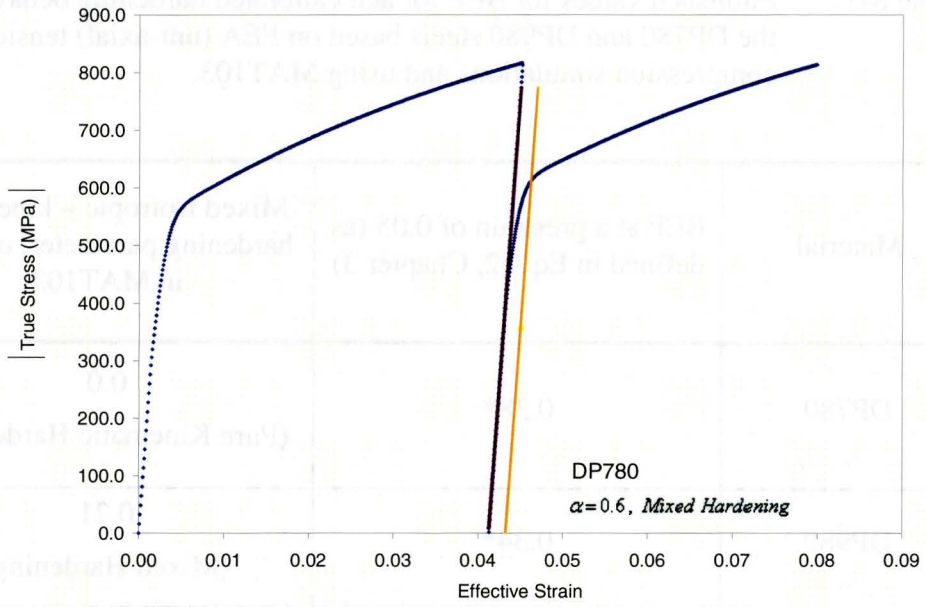

Figure 8.27 DP780 FEA uniaxial tension-compression test, stress-strain response and BEF calculation using LSDYNA3D material model MAT103 (α is set to 0.6 for mixed hardening).

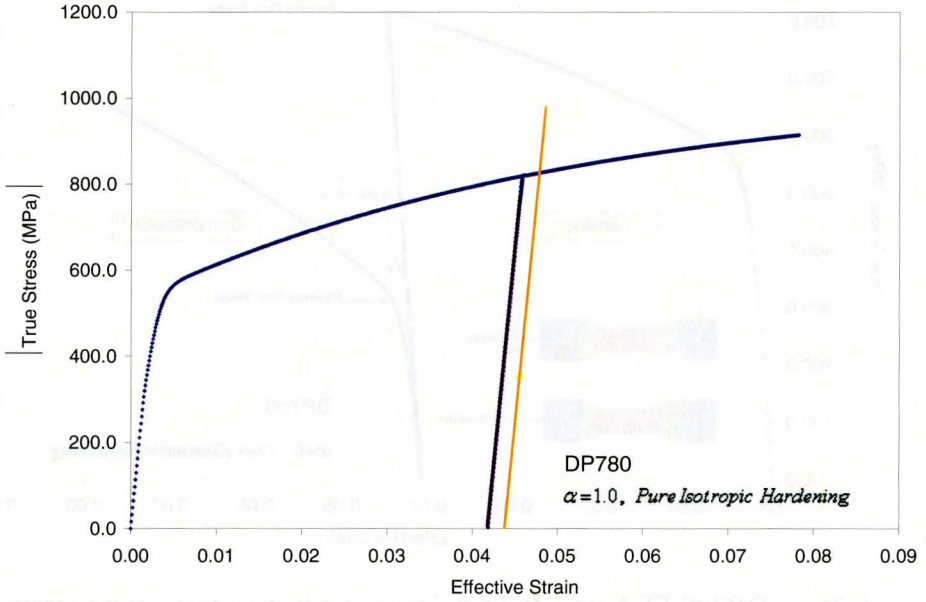

Figure 8.28 DP780 FEA uniaxial tension-compression test, stress-strain response and BEF calculation using LSDYNA3D material model MAT103 (α is set to 1 for pure isotropic hardening).

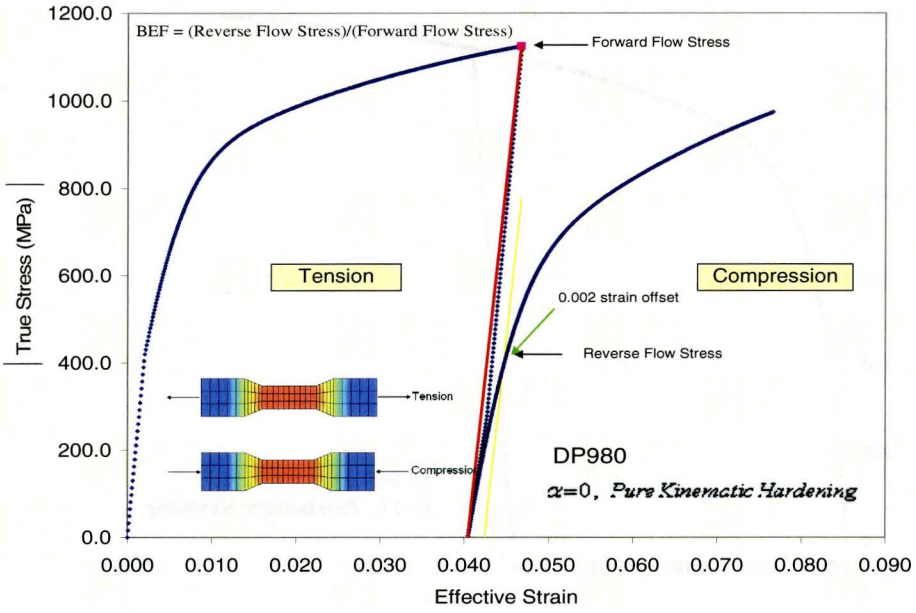

Figure 8.29 DP980 FEA uniaxial tension-compression test, stress-strain response and BEF calculation using LSDYNA3D material model MAT103 (α is set to 0 for pure kinematic hardening).

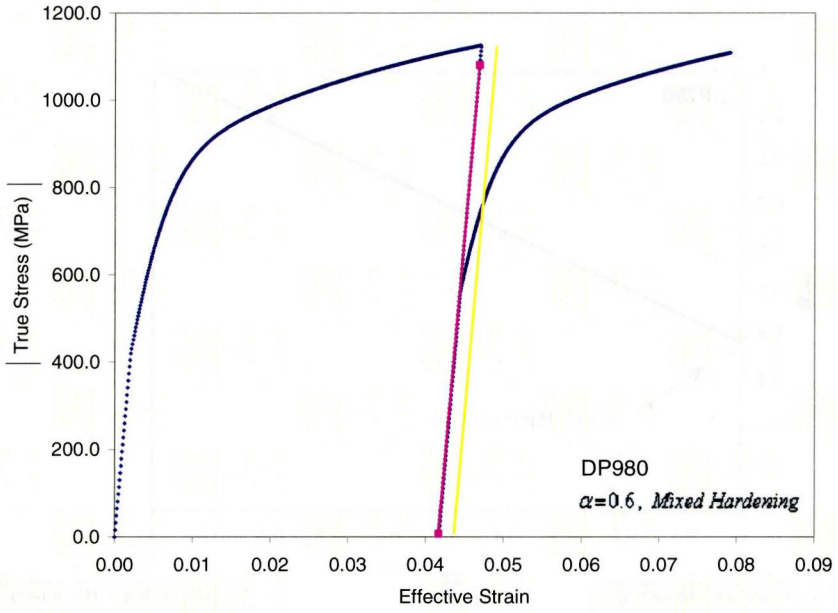

Figure 8.30 DP980 FEA uniaxial tension-compression test, stress-strain response and BEF calculation using LSDYNA3D material model MAT103 (α is set to 0.6 for mixed hardening).

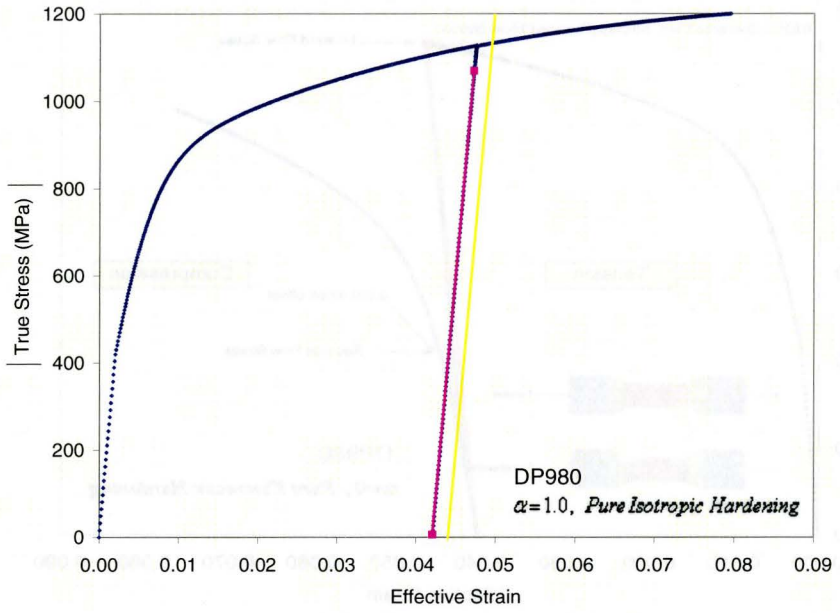

Figure 8.31 DP980 FEA uniaxial tension-compression test, stress-strain response and BEF calculation using LSDYNA3D material model MAT103 (α is set to 1 for pure isotropic hardening).

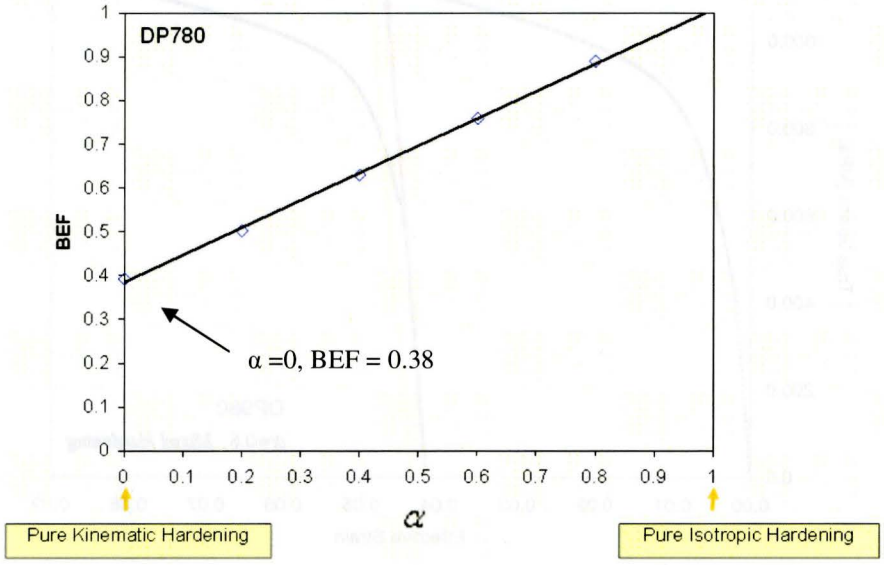

Figure 8.32 Predicted BEF as a function of α for the DP780 steel from FEA tension-compression simulations using LSDYNA3D material model MAT103.

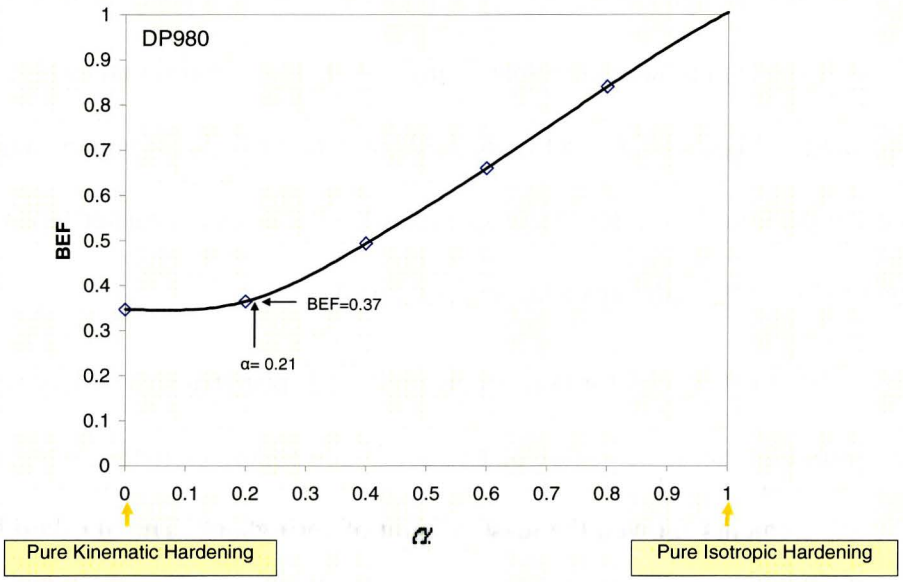

Figure 8.33 Predicted BEF as a function of α for the DP980 steel from FEA tension-compression simulations using LSDYNA3D material model MAT103.

8.4.2 FEA Simulations of the Experimental V-Die Bending Experiments

The FEA of the V-die bending experiments were performed in order to study the effect of element formulation (i.e., 3D shell, 2D and 3D continuum element) and material hardening assumptions (i.e., pure isotropic and kinematic hardening, and mixed isotropic – kinematic hardening) on the predicted bending and springback behaviors. Descriptions of the FEA models used are summarized in Table 8-4 and Table 8-5. All the FEA simulations were performed using the implicit forming-implicit springback technique and the results were compared to experimental springback measured in-situ using a portable CMM (described earlier in Chapter 6). The experimental springback measurements are summarized in Table 8-6 and compared to FEA in Table 8-7. These results are also plotted in

Figure 8.34 and Figure 8.35. The springback results are shown as the relative springback which relates the angle change relative to the original angle as illustrated in Figure 8.34 and Figure 8.35. In contrast to Ks, a higher magnitude of relative springback implies larger springback. As explained earlier in Chapter 2, a lower value of Ks indicates a larger springback.

The FEA results for both steels predicted springback to be largest for the 2D continuum elements, followed by the 3D continuum elements. The FEA using 3D shell elements showed the least amount of springback. The 3D shell FEA, however, showed the best agreement with experimental averages when using the appropriate mixed isotropic-kinematic model from the calibration results in Table 8-3. The FEA for all element formulations predicted increased springback as the hardening assumption was changed from pure isotropic to pure kinematic hardening. Simple bending theory predicted significantly less springback than the FEA models and the experimental springback. To contrast the differences in the predicted springback between simple bending theory and FEA, the bending moment distributions at the end of forming are shown in Figure 8.36 and Figure 8.37.

Table 8-4 Summary of FEA bending-springback runs for the DP780 steel (tooling friction, μ =0.125). The FEA was performed with the LSDYNA3D implicit code (version 971) using material model MAT103.

FEA Run	Element Type	Hardening Behavior
1	2D Continuum	Pure isotropic ($\alpha = 1$)
2	2D Continuum	Pure kinematic ($\alpha = 0$)
3	3D Continuum	Pure isotropic ($\alpha = 1$)
4	3D Continuum	Pure kinematic ($\alpha = 0$)
5	3D Shell	Pure isotropic ($\alpha = 1$)
6	3D Shell	Pure kinematic ($\alpha = 0$)

* implicit forming-implicit springback method used

Table 8-5 Summary of FEA bending-springback runs for the DP980 steel (tooling friction, μ =0.125). The FEA was performed with the LSDYNA3D implicit code (version 971) using material model MAT103.

FEA Run	Element Type	Hardening Behavior
1	2D Continuum	Pure isotropic ($\alpha = 1$)
2	2D Continuum	Mixed ($\alpha = 0.21$)
3	2D Continuum	Pure kinematic ($\alpha = 0$)
4	3D Continuum	Pure isotropic ($\alpha = 0$)
5	3D Continuum	Mixed ($\alpha = 0.21$)
6	3D Continuum	Pure kinematic ($\alpha = 0$)
7	3D Shell	Pure isotropic ($\alpha = 1$)
8	3D Shell	Mixed ($\alpha = 0.21$)
9	3D Shell	Pure kinematic ($\alpha = 0$)

* implicit forming-implicit springback method used

Table 8-6 Experimentally determined springback for V-die bending. Note that θ_i, θ_f, $\Delta\theta$, and the relative springback $\Delta\theta/(180°-\theta_i)$ are defined in Figure 2.4.

Grade	Direction	Sample No.	θ_i	θ_f	$\Delta\theta$	$\Delta\theta/(180°-\theta_i)$
DP780	Long	1	90.05°	98.68°	8.64°	0.096
		2	89.45	98.14	8.69	0.096
	Trans	1	87.74	97.41	9.67	0.105
		2	88.04	96.54	8.50	0.093
		3	87.95	96.38	8.42	0.092
				Avg.	8.78	0.096

Grade	Direction	Sample No.	θ_i	θ_f	$\Delta\theta$	$\Delta\theta/(180°-\theta_i)$
DP980	Long	1	88.58°	108.98°	20.39°	0.223
		2	89.51	112.04	22.53	0.249
	Trans	1	88.53	107.93	19.40	0.212
		2	88.12	106.85	18.74	0.204
		3	88.78	109.22	20.43	0.224
				Avg.	20.30	0.222

Table 8-7 Summary of FEA bending-springback results for DP980 and DP780 steels. Note that θ_i, θ_f, $\Delta\theta$, and the relative springback $\Delta\theta/(180°-\theta_i)$ are defined in Figure 2.4.

DP780		θ_i	θ_f	$\Delta\theta$	$\Delta\theta/(180°-\theta_i)$
2D Solids	α = 1 (Isotropic Hardening)	89.99°	98.24°	8.25°	0.092
	α = 0 (Kinematic Hardening)	89.94	100.23	10.28	0.114
3D Solids	α = 1 (Isotropic Hardening)	86.80	95.32	8.52	0.091
	α = 0 (Kinematic Hardening)	86.44	96.41	9.98	0.107
3D Shells	α = 1 (Isotropic Hardening)	85.79	93.72	7.93	0.084
	α = 0 (Kinematic Hardening)	86.32	95.04	8.72	0.093
DP980		θ_i	θ_f	$\Delta\theta$	$\Delta\theta/(180°-\theta_i)$
2D Solids	α = 1 (Isotropic Hardening)	89.81	110.60	20.79	0.231
	α = 0.21 (Mixed)	89.87	111.48	21.61	0.240
	α = 0 (Kinematic Hardening)	89.84	113.82	23.98	0.266
3D Solids	α = 1 (Isotropic Hardening)	88.89	109.80	20.91	0.229
	α = 0.21 (Mixed)	88.80	110.04	21.24	0.233
	α = 0 (Kinematic Hardening)	89.06	111.34	22.28	0.245
3D Shells	α = 1 (Isotropic Hardening)	87.50	107.04	19.54	0.211
	α = 0.21 (Mixed)	87.77	108.17	20.40	0.221
	α = 0 (Kinematic Hardening)	87.78	110.12	22.34	0.242

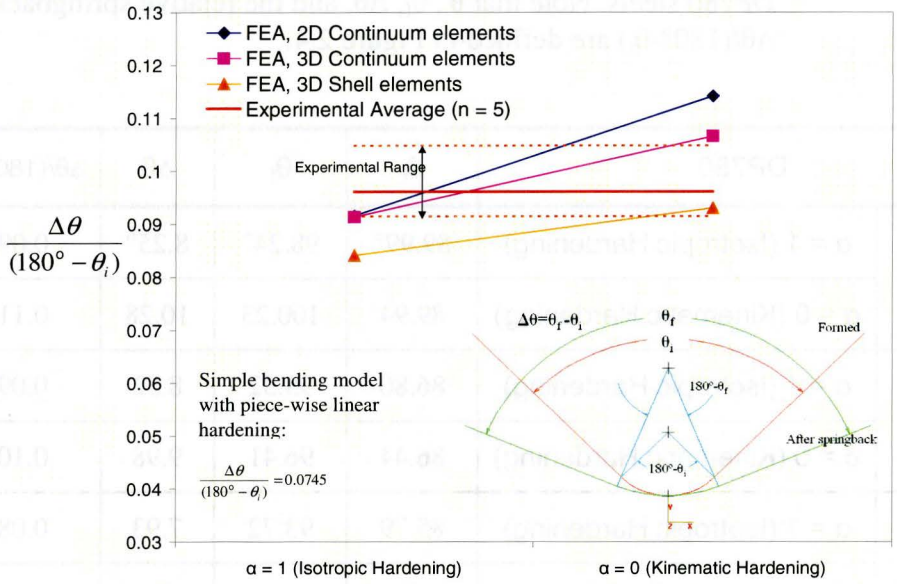

Figure 8.34 FEA predicted springback in V-die bending for the DP780 steel using various element types and material hardening assumptions, compared to experimentally measured springback.

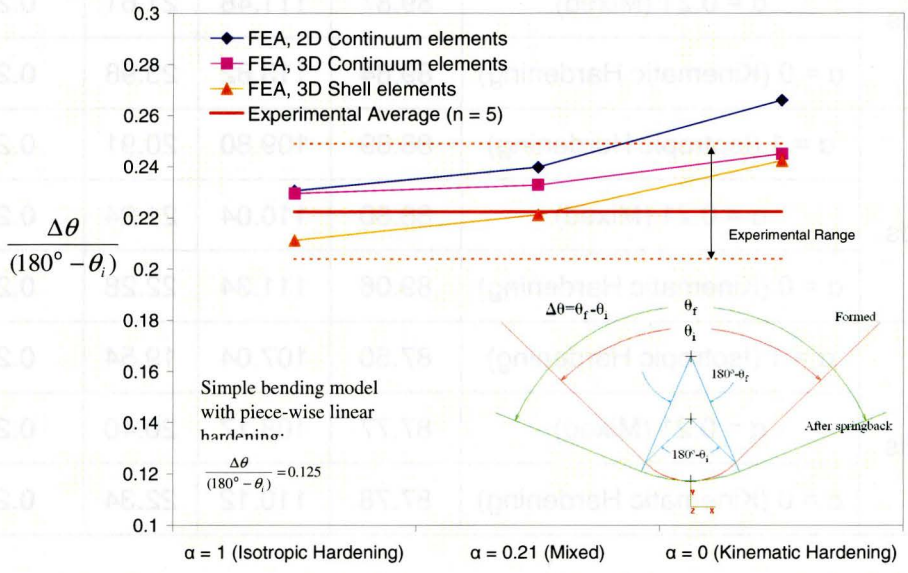

Figure 8.35 FEA predicted springback in V-die bending for the DP980 steel using various element types and material hardening assumptions, compared to experimentally measured springback.

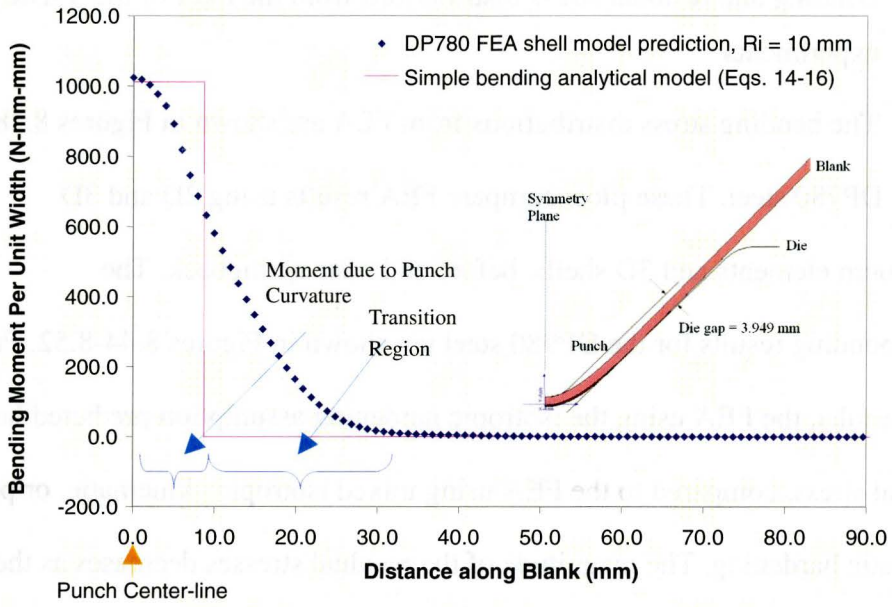

Figure 8.36 FEA predicted, stored bending moment at the bottom of the punch stroke in V-die bending compared to that predicted by simple bending theory for the DP780 steel.

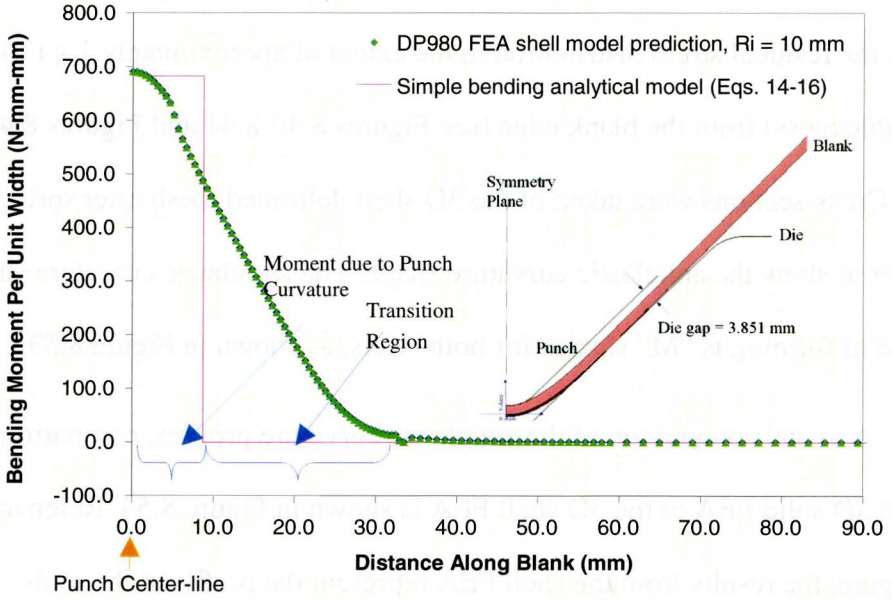

Figure 8.37 FEA predicted, stored bending moment at the bottom of the punch stroke in V-die bending compared to that predicted by simple bending theory for the DP980 steel.

8.4.3 Bending and residual stress distributions from the FEA of the V-Die experiments

The bending stress distributions from FEA are shown in Figures 8.38-8.43 for the DP780 steel. These plots compare FEA results using 2D and 3D continuum elements and 3D shells, before and after springback. The corresponding results for the DP980 steel are shown in Figures 8.44-8.52. From these results, the FEA using the isotropic hardening assumption predicted larger residual stress, compared to the FEA using mixed isotropic –kinematic, or pure kinematic hardening. The magnitude of the residual stresses decreases as the hardening assumption is changed from pure isotropic to pure kinematic hardening.

Permanent anticlastic curvature was also predicted for all 3D simulations. The results for the 3D continuum elements showed that anticlastic curvature affects the residual stress distribution to the extent of approximately 1 x t (one times thickness) from the blank edge (see Figures 8.40-8.41 and Figures 8.47-8.49). Cross-sections were taken of the 3D shell deformed mesh after springback in order to show the anticlastic curvature shape. The anticlastic curvature shape at the end of forming is "M" shaped for both steels, as shown in Figure 8.53.

A visual comparison of the anticlastic curvature profiles, comparing the DP780 3D solid FEA to the 3D shell FEA is shown in Figure 8.54. Referring to this figure, the results from the shell FEA represent the profile at the mid-thickness position. The 3D solid profile is plotted using the nodal coordinates only, and span the entire thickness of the blank.

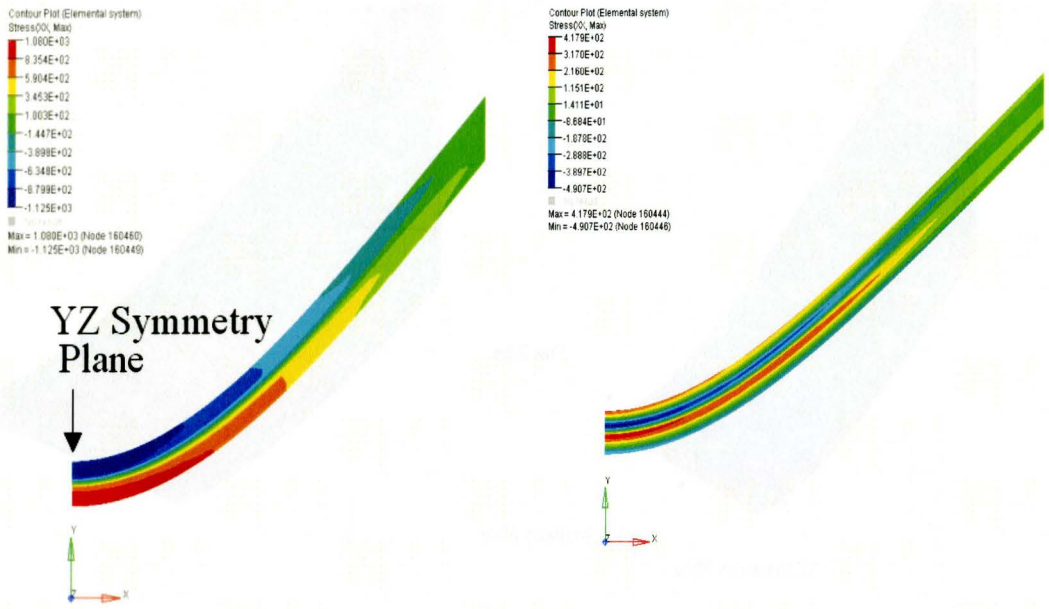

Figure 8.38 DP780, pure isotropic hardening assumption. 2D continuum FEA simulation of bending (left), followed by springback (right) showing bending stress distributions (in MPa).

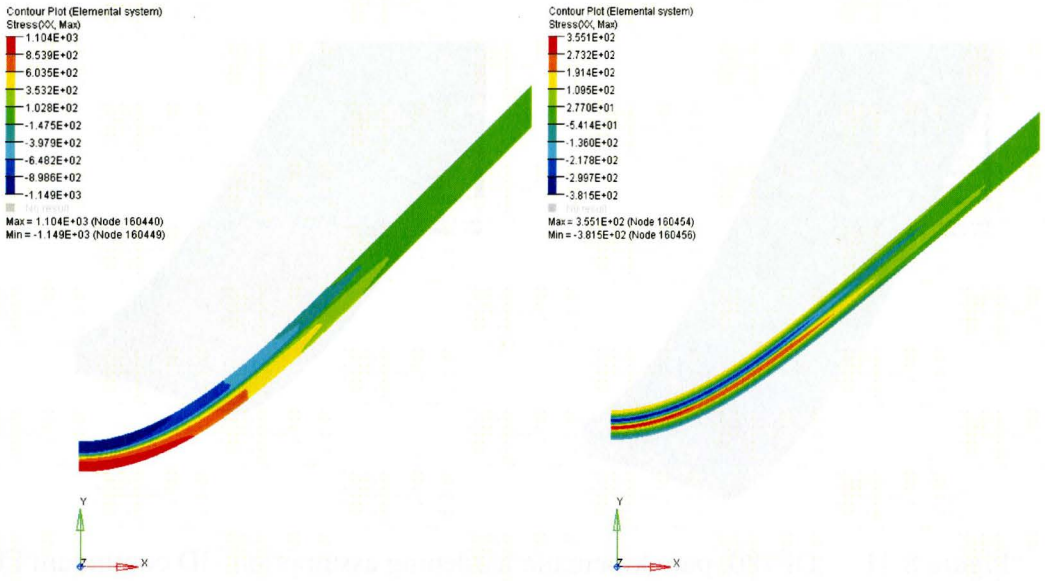

Figure 8.39 DP780, pure kinematic hardening assumption. 2D continuum FEA simulation of bending (left), followed by springback (right) showing bending stress distributions (in MPa).

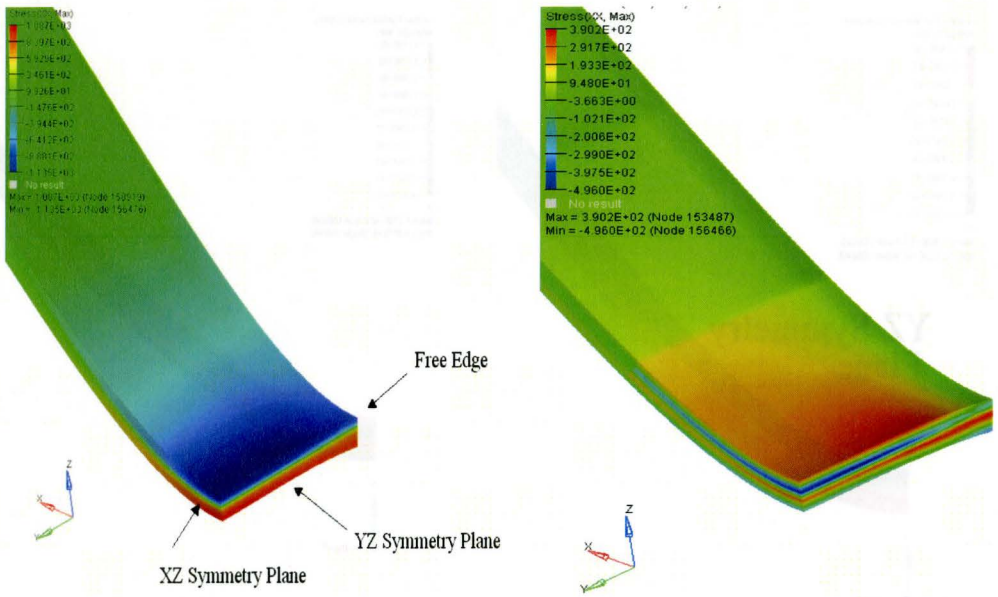

Figure 8.40 DP780, pure isotropic hardening assumption. 3D continuum FEA simulation of bending (left), followed by springback (right) showing bending stress distributions (in MPa, quarter symmetry is used).

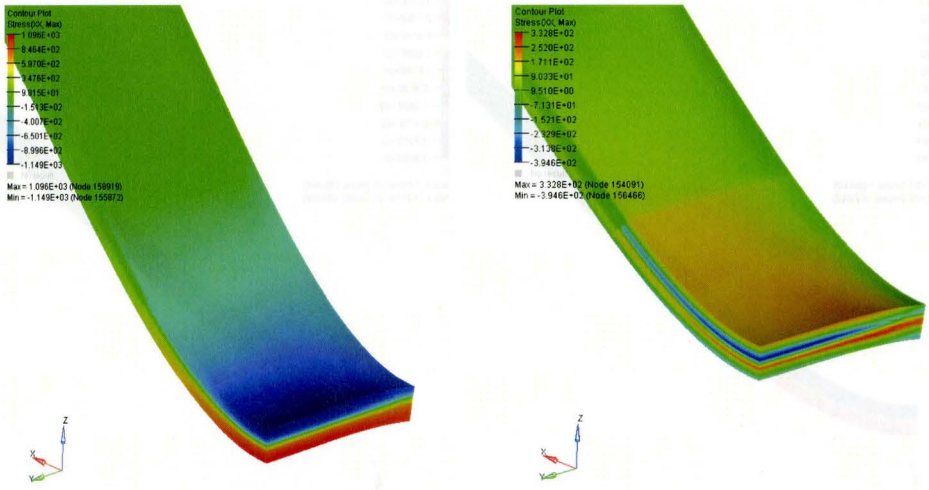

Figure 8.41 DP780, pure kinematic hardening assumption. 3D continuum FEA simulation of bending (left), followed by springback (right) showing bending stress distributions (in MPa, quarter symmetry is used).

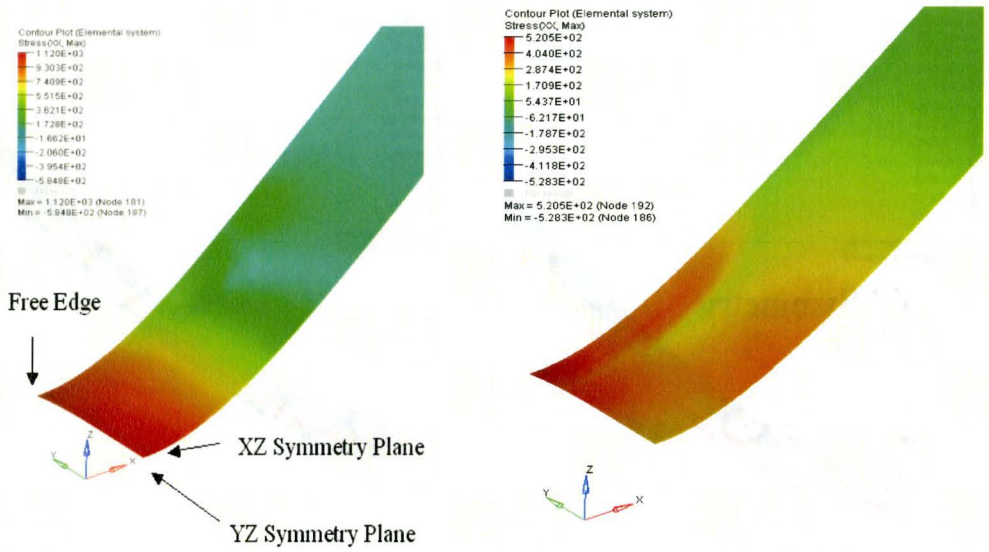

Figure 8.42 DP780, pure isotropic hardening assumption. 3D shell FEA simulation of bending (left), followed by springback (right) showing maximum bending stress distributions (in MPa, quarter symmetry is used).

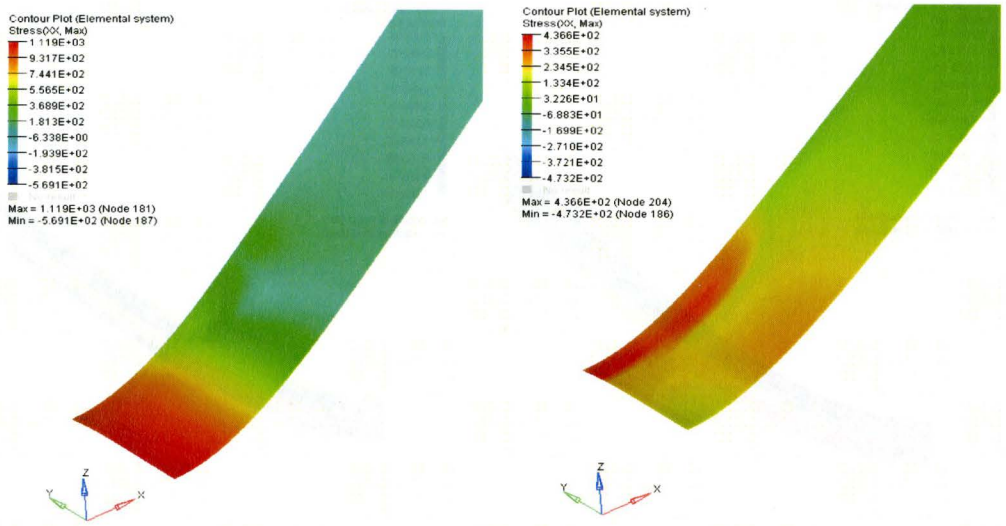

Figure 8.43 DP780, pure kinematic hardening assumption. 3D shell FEA simulation of bending (left), followed by springback (right) showing maximum bending stress distributions (in MPa, quarter symmetry is used).

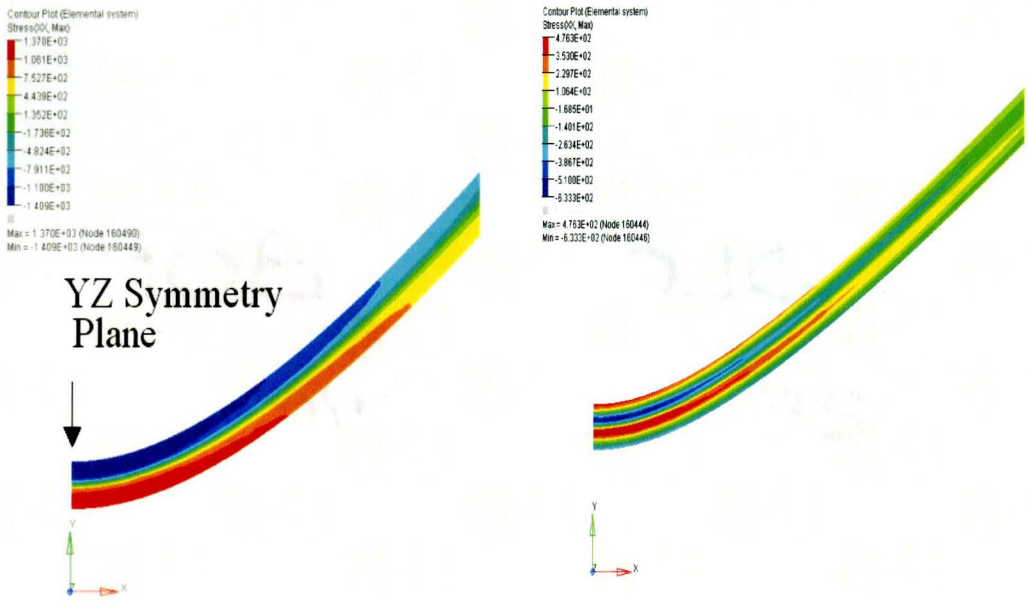

Figure 8.44 DP980, pure isotropic hardening assumption. 2D continuum FEA simulation of bending (left), followed by springback (right) showing bending stress distributions (in MPa).

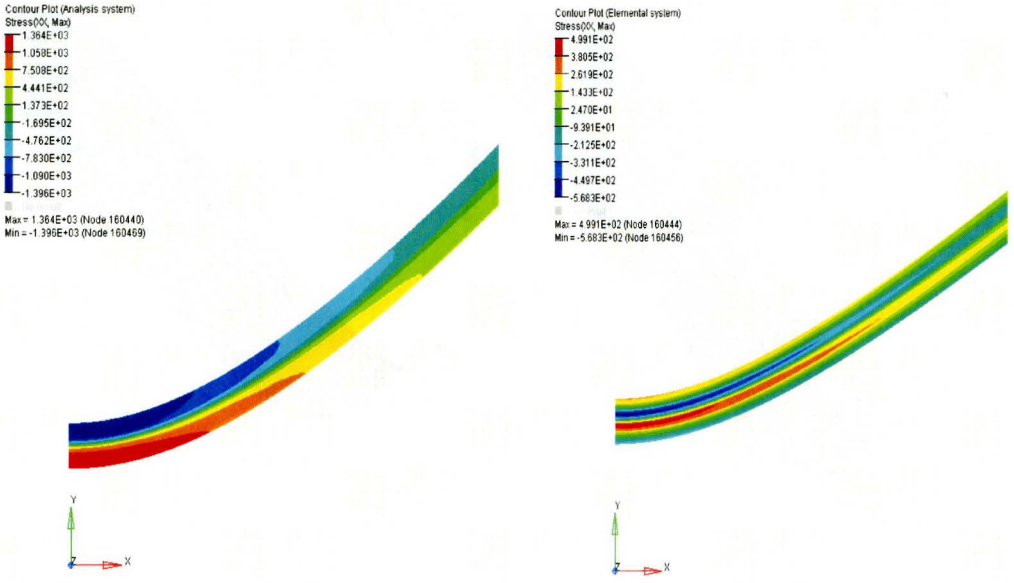

Figure 8.45 DP980, mixed hardening assumption ($\alpha = 0.21$). 2D continuum FEA simulation of bending (left), followed by springback (right) showing bending stress distributions (in MPa).

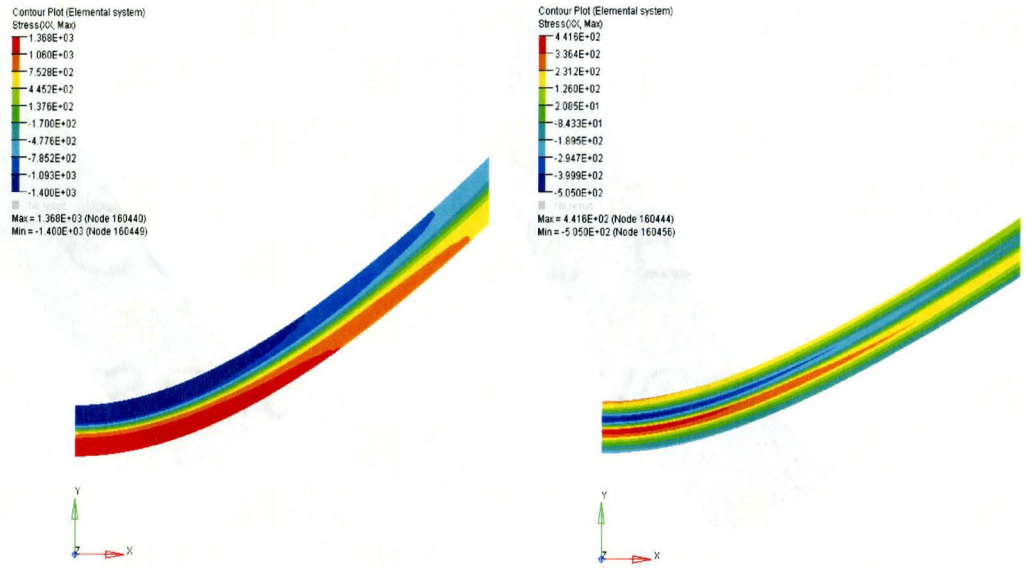

Figure 8.46 DP980, pure kinematic hardening assumption. 2D continuum FEA simulation of bending (left), followed by springback (right) showing bending stress distributions (in MPa).

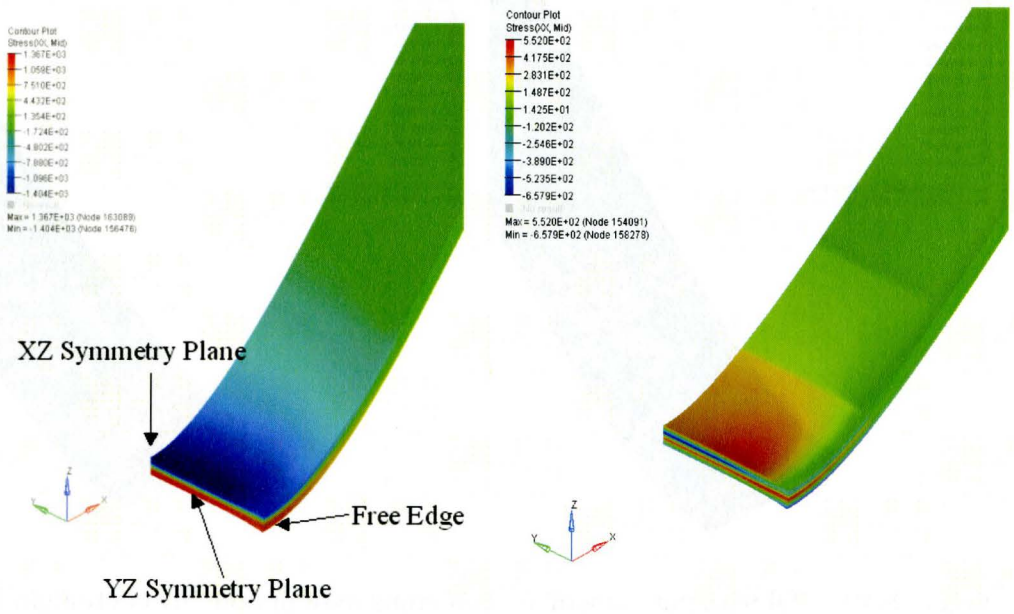

Figure 8.47 DP980, pure isotropic hardening assumption. 3D Continuum FEA simulation of bending (left), followed by springback (right) showing bending stress distributions (in MPa, quarter symmetry is used).

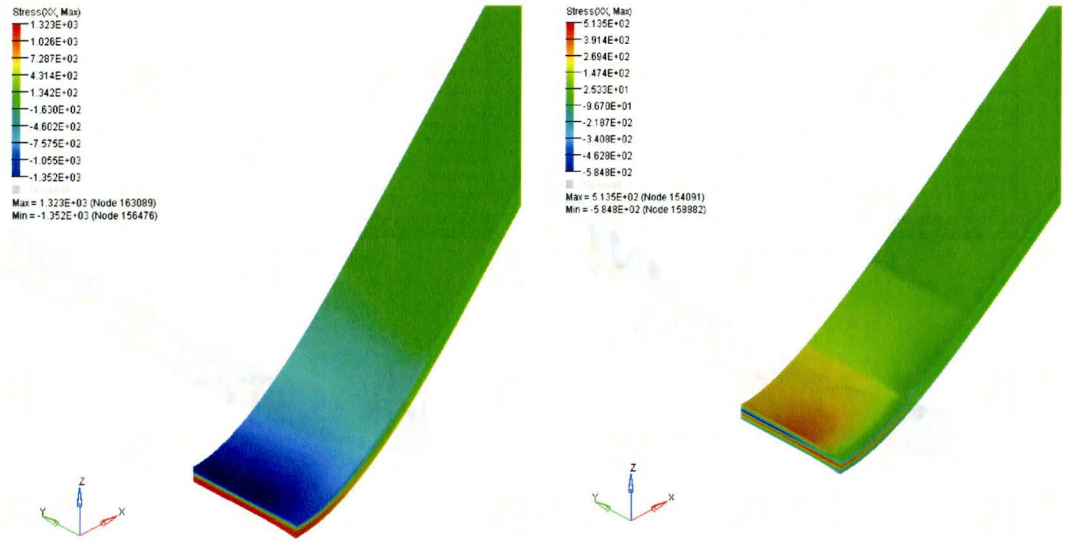

Figure 8.48 D980, mixed hardening assumption ($\alpha = 0.21$). 3D continuum FEA simulation of bending (left), followed by springback (right) showing bending stress distributions (in MPa, quarter symmetry is used).

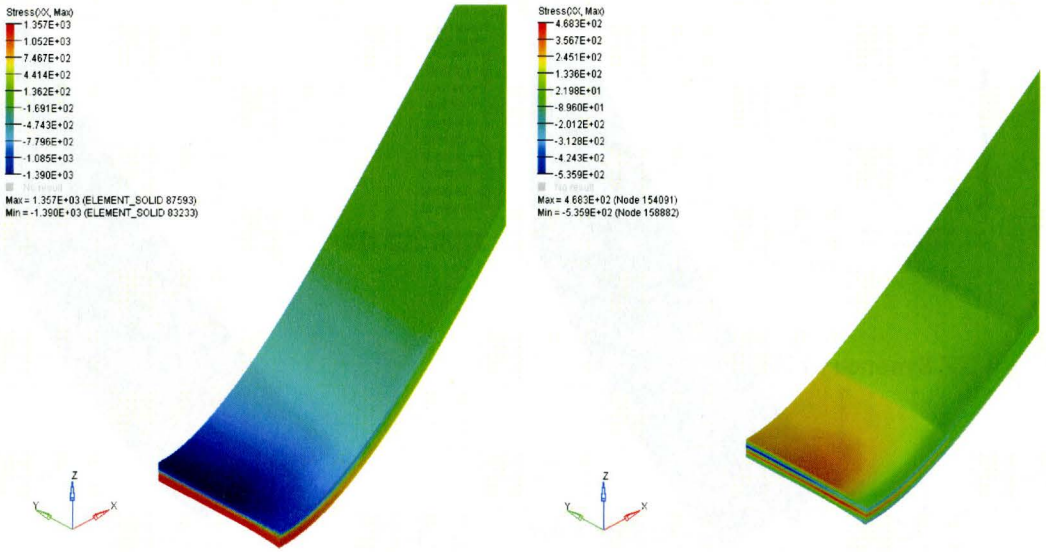

Figure 8.49 DP980, pure kinematic hardening assumption. 3D continuum FEA simulation of bending (left), followed by springback (right) showing maximum bending stress distributions (in MPa, quarter symmetry is used).

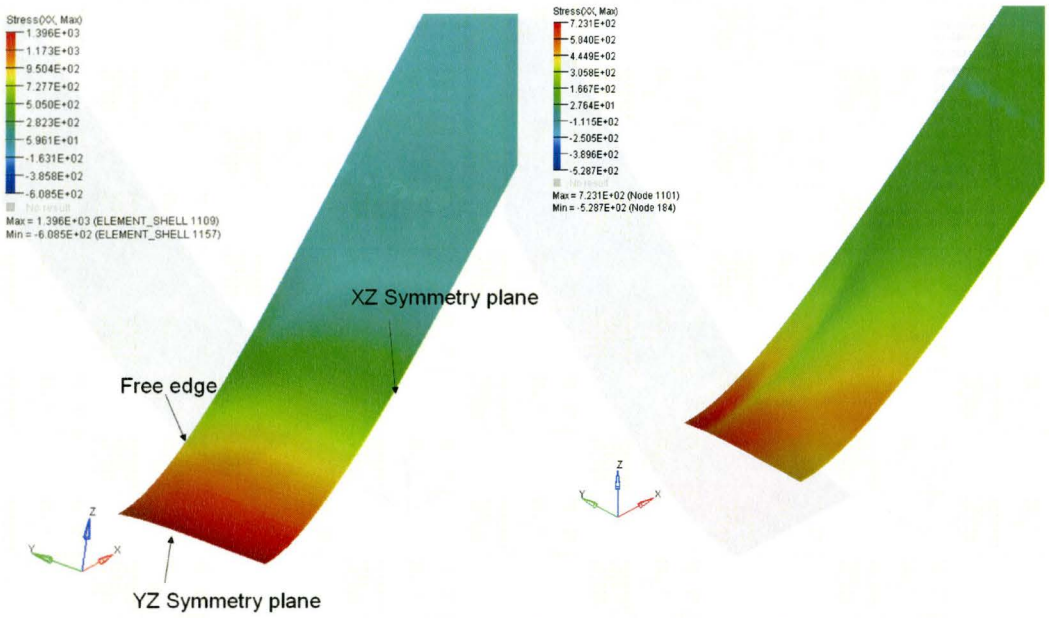

Figure 8.50 DP980, pure isotropic hardening assumption. 3D shell FEA simulation of bending (left) followed by springback (right) showing maximum bending stress distributions (in MPa, quarter symmetry is used).

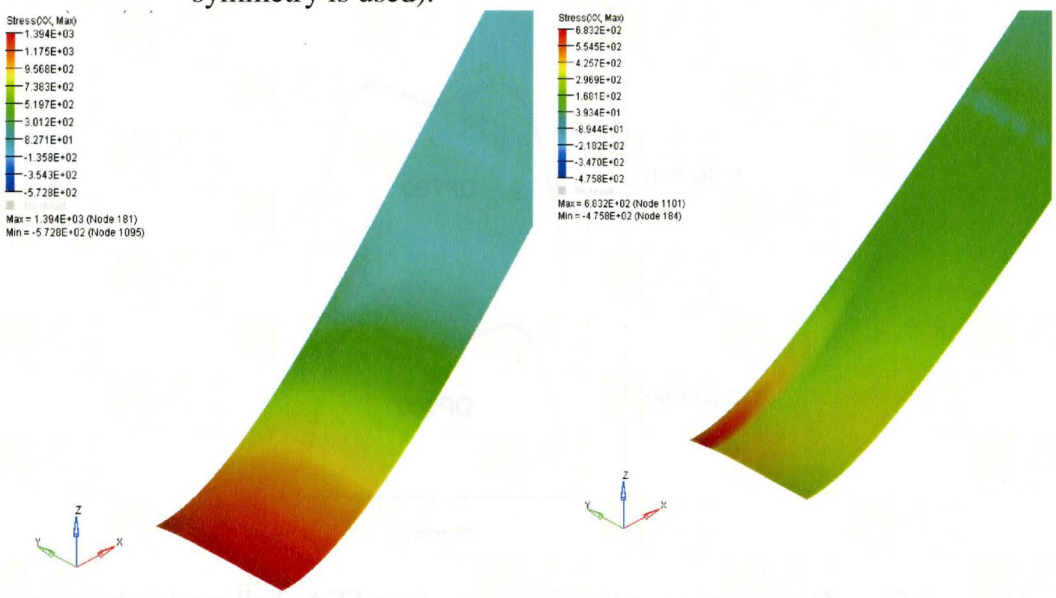

Figure 8.51 DP980, mixed hardening assumption ($\alpha = 0.21$). 3D shell FEA simulation of bending (left) followed by springback (right) showing maximum bending stress distributions (in MPa, quarter symmetry is used).

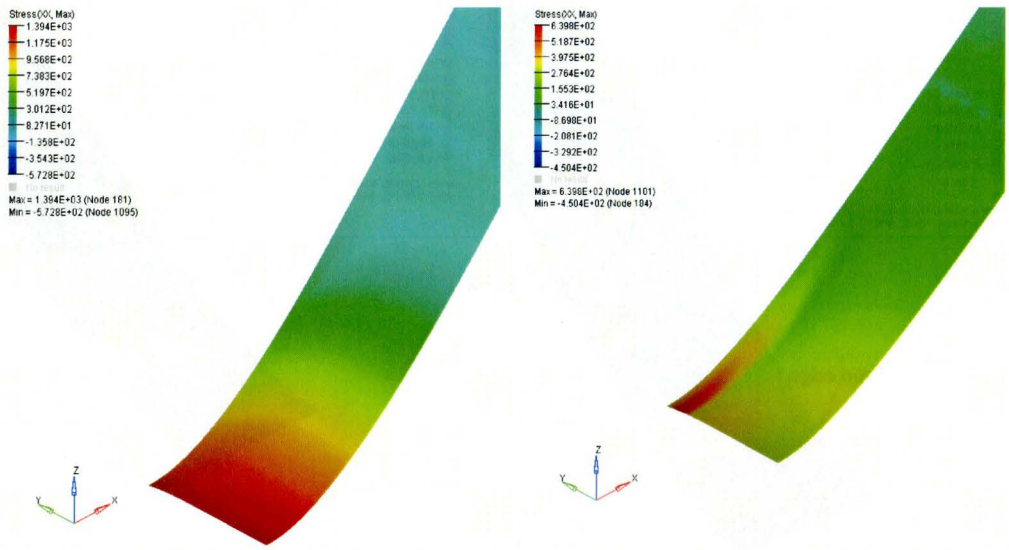

Figure 8.52 DP980, pure kinematic hardening assumption. 3D shell FEA simulation of bending (left) followed by springback (right) showing maximum bending stress distributions (in MPa, quarter symmetry is used).

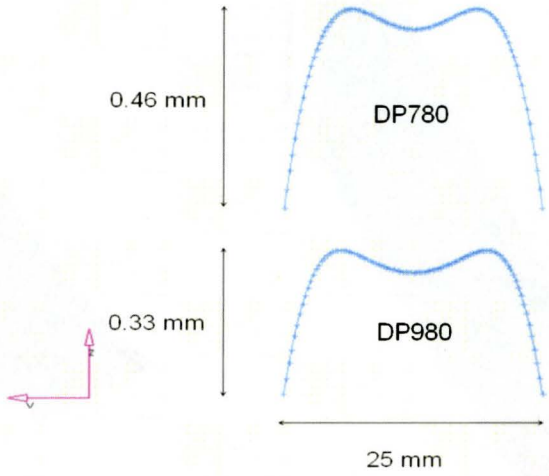

Figure 8.53 Cross section in the XZ plane of the FEA shell model showing anticlastic curvature shape and magnitude for both DP780 and DP980 steels.

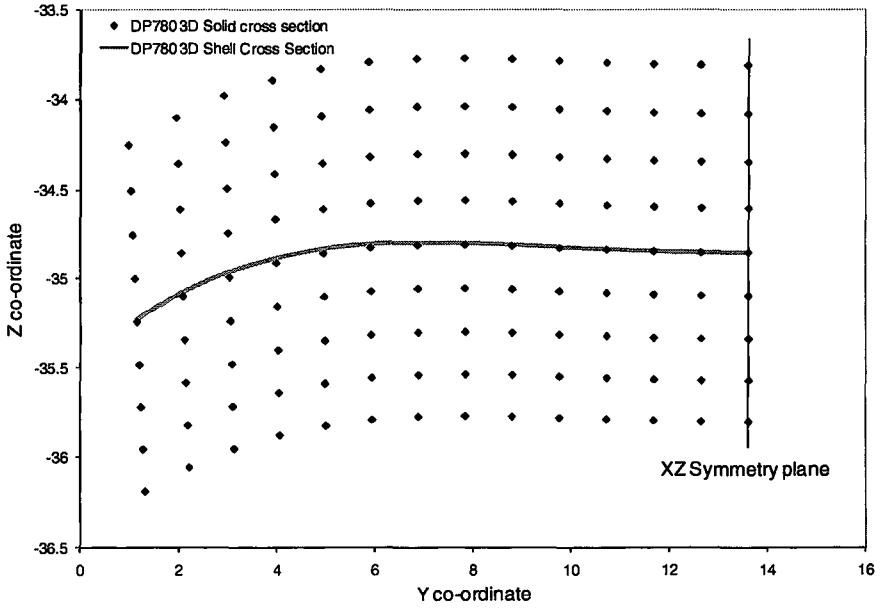

Figure 8.54. Cross-section at the DP780 3D solid and shell mesh taken at the apex of the bend, in the YZ plane, and after springback.

8.4.4 Through-thickness bending and residual stress distributions from the FEA of the V-die experiments

The through-thickness bending and residual stresses from the FEA at the end of forming and springback respectively, were compared to that from simple bending analytical models using the elastic-plastic approach (Eqs. 14-16 in Chapter 2). The results are shown in Figure 8.55. The stress distributions were obtained from the FEA models, at a position corresponding to the centerline (along the length direction) of the experimental blanks.

8.4.4.1 DP780 FEA results

For the DP780 steel, the R_p/t ratio was 5, which is at the limit of applicability for simple bending theory (Marciniak et al., 2002). The FEA showed

that the predicted bending stresses are consistently predicted, irrespective of the element formulation or the hardening assumption used. These stress distributions showed good to fair agreement with that from simple bending analytical models of the theory. The FEA models using 3D shell elements showed the best agreement. The 2D and 3D continuum element FEA however, predicted lower bending stresses in the tension fibers compared to simple bending theory and the 3D shell element FEA. Accordingly, the residual stresses due to springback in the tension region was less in magnitude for the 2D and 3D continuum elements compared to that in the 3D shells and using simple bending theory (Figures 8.56-8.58). This trend is similar to that from the FEA results observed for the small radius bending FEA to be shown later.

The results from FEA show a distinct pattern in which the outer bending fibers for the FEA models, using the pure kinematic hardening assumption, show lower magnitude of the residual stress, compared to models using pure isotropic hardening. This pattern was observed for the simulations across all element types used. A closer examination of the unloading behavior of the surface bending fibers showed that the unloading behavior, using the pure isotropic hardening assumption, was linear (Figures 8.59-8.61). For the pure kinematic hardening assumptions, unloading was non-linear accompanied by an increased magnitude of the unloading strain, and lower residual stresses.

8.4.4.2 DP980 FEA results

The predicted bending and residual stress distributions from the FEA for the DP980 steel using the isotropic hardening assumption (and for all element types), showed good agreement with that predicted by simple bending theory (Figures 8.62-8.63). The R_p/t ratio was 6.9, which is within the recommended range in which simple bending theory applies.

The FEA shows that the maximum/minimum predicted bending stresses are consistently predicted for all simulations, and in good agreement with that predicted using the simple bending analytical equations (Figure 8.62). This is in contrast to the DP780 2D and 3D continuum element FEA, in which the bending stresses in the tensile fibers were less than that predicted by simple bending theory (Figure 8.55 compared to Figure 8.62). Similar to the DP780 FEA, the residual stresses (magnitude) at the extreme fibers were lower as the material hardening assumption was changed from isotropic, to pure kinematic hardening. The unloading behaviors of the extreme tensile fibers are shown in Figures 8.66-8.68. The unloading behavior of the models using pure isotropic hardening was linear. For the mixed and pure kinematic hardening assumptions, unloading was non-linear with increasing unloading strain (magnitude) and lower residual stress, as the hardening assumption was changed from pure isotropic to pure kinematic hardening.

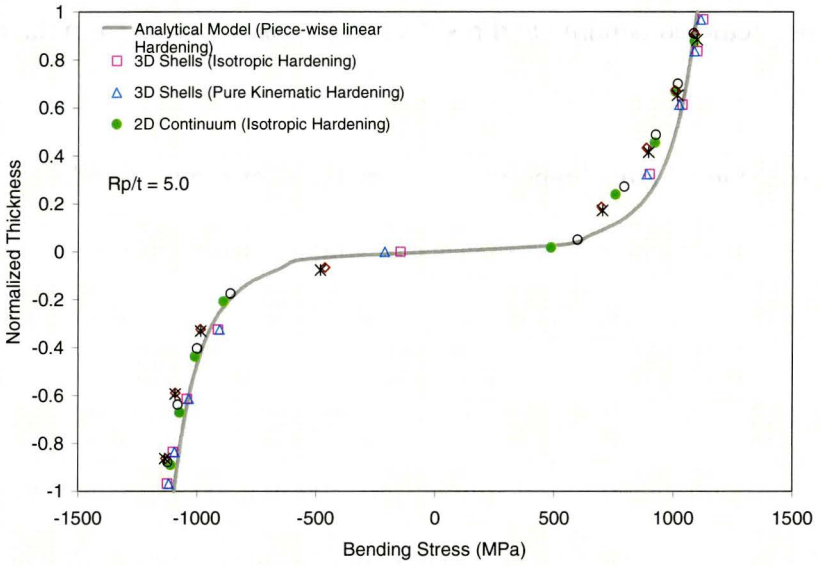

Figure 8.55 DP780 FEA predicted bending stress at the bottom of the punch stroke compared to that from simple bending theory using piece-wise linear hardening.

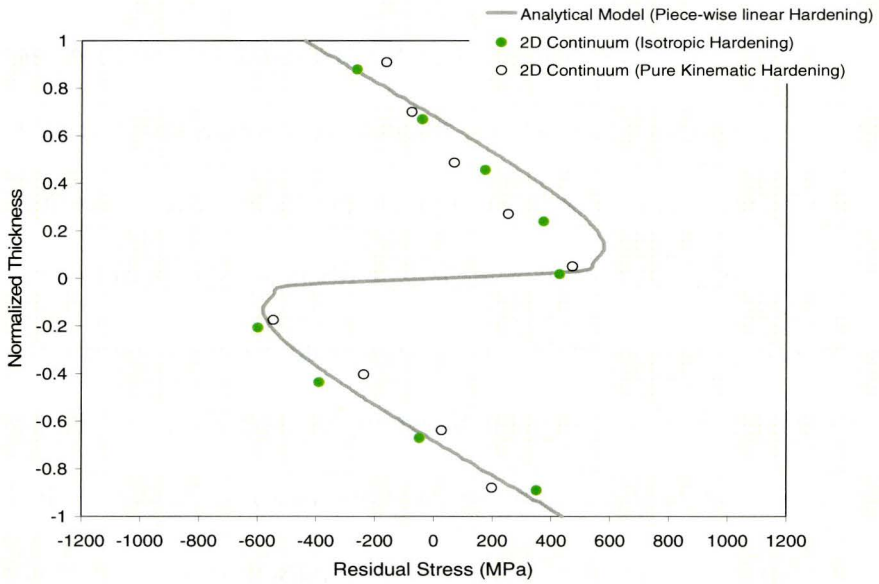

Figure 8.56 2D Continuum element FEA residual bending stress after springback for DP780. Compared are isotropic hardening and kinematic hardening assumptions to the analytical springback using simple bending theory (using piece-wise linear hardening and elastic unloading).

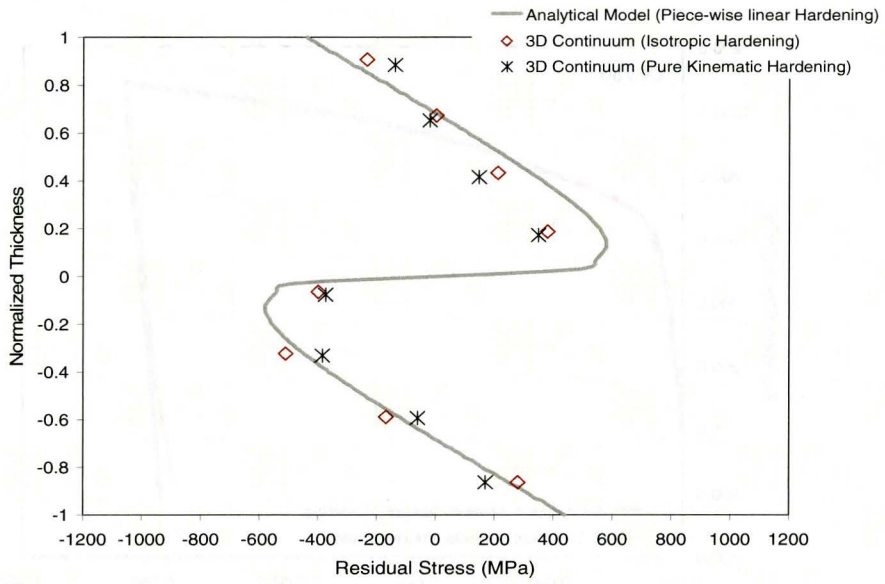

Figure 8.57 3D Continuum element FEA residual bending stress after springback for DP780. Compared are isotropic hardening and kinematic hardening assumptions to analytical springback using simple bending theory (using piece-wise linear hardening and elastic unloading).

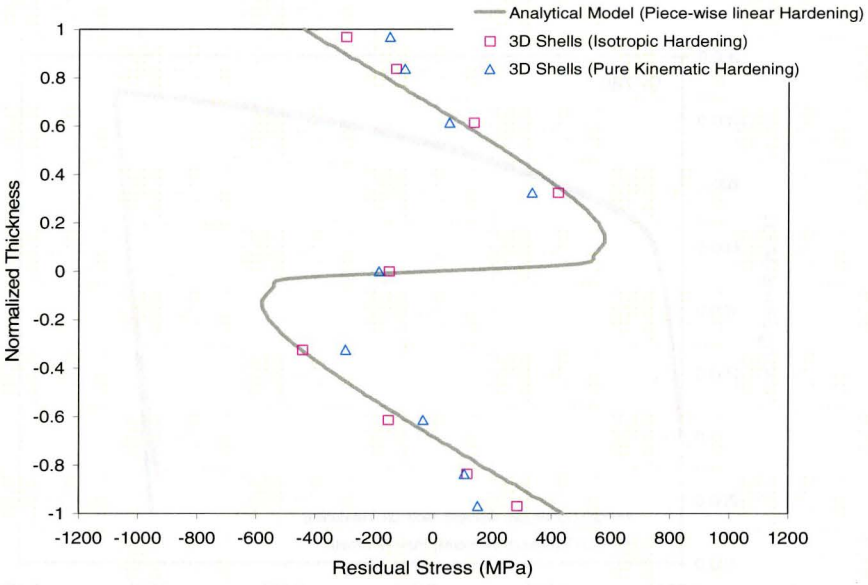

Figure 8.58 3D shell element FEA residual bending stress after springback for DP780. Compared are isotropic hardening and kinematic hardening assumptions to analytical springback using simple bending theory (using piece-wise linear hardening and elastic unloading).

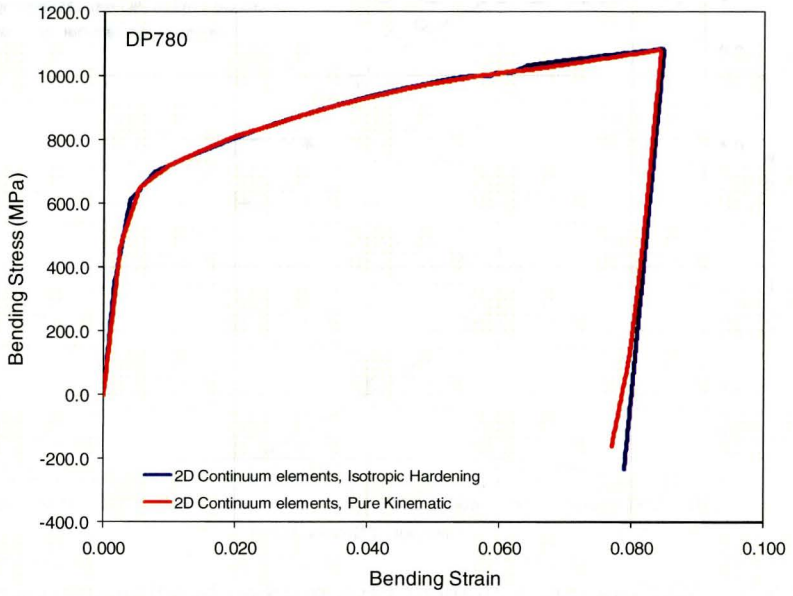

Figure 8.59 2D continuum element simulations for DP780. Loading and unloading of the extreme tensile fiber comparing pure isotropic and kinematic hardening assumptions in the FEA model.

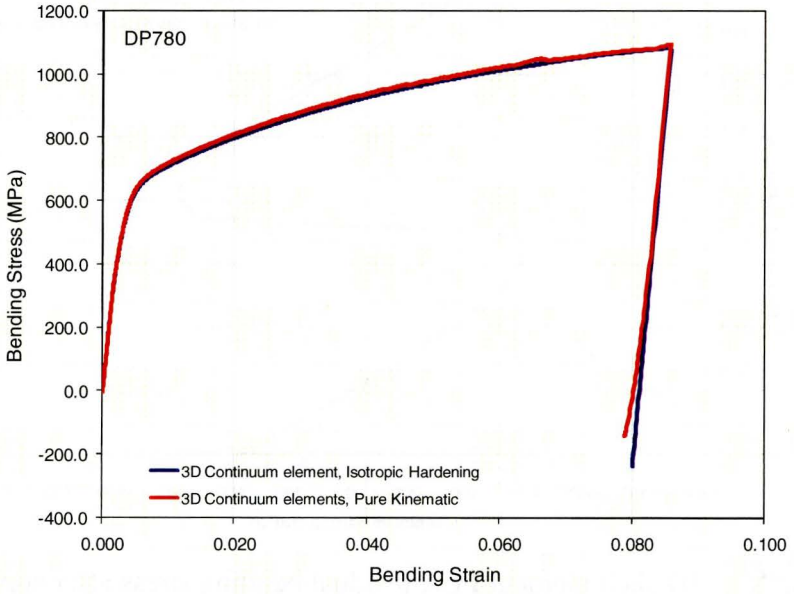

Figure 8.60 3D continuum element simulations for DP780. Loading and unloading of the extreme tensile fiber comparing pure isotropic and kinematic hardening assumptions in the FEA model.

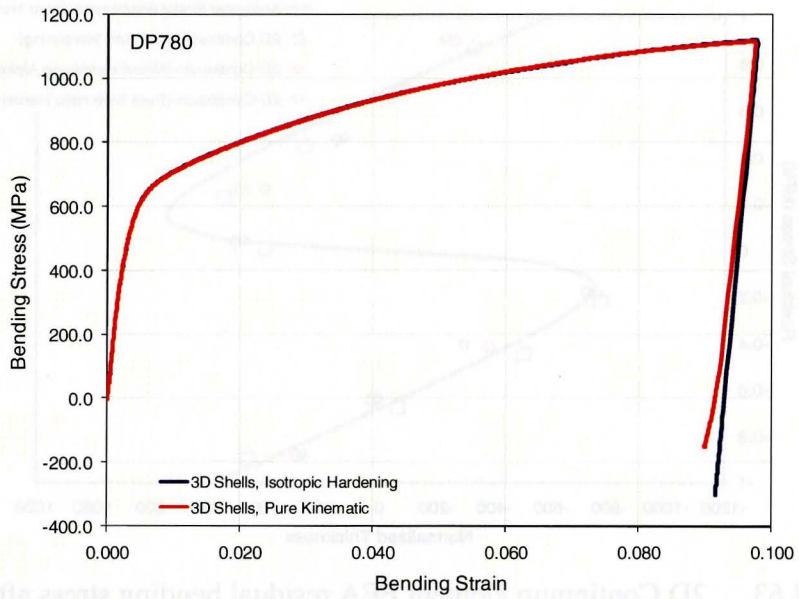

Figure 8.61 3D shell element simulations for DP780. Loading and unloading of the extreme tensile fiber comparing pure isotropic and kinematic hardening assumptions in the FEA model.

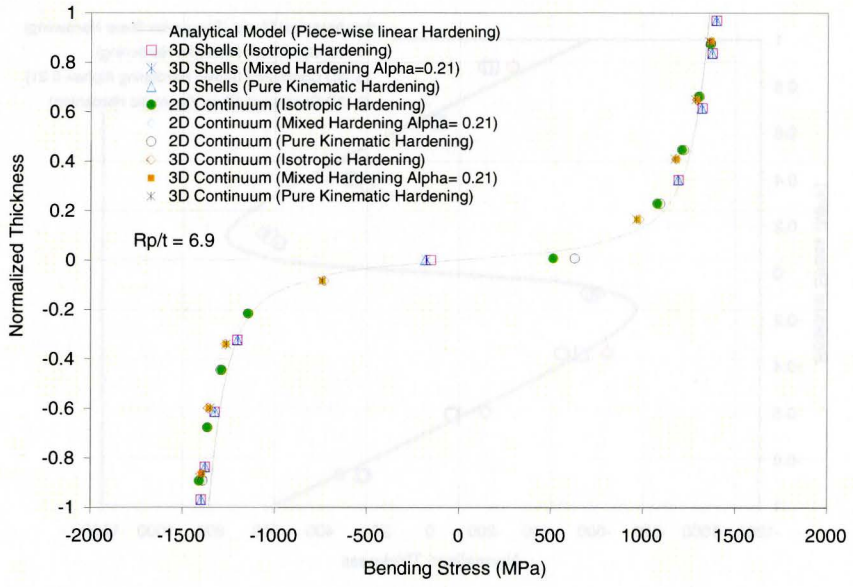

Figure 8.62 DP980 FEA predicted bending stress at the bottom of the punch stroke compared to that from simple bending theory using piece-wise linear hardening.

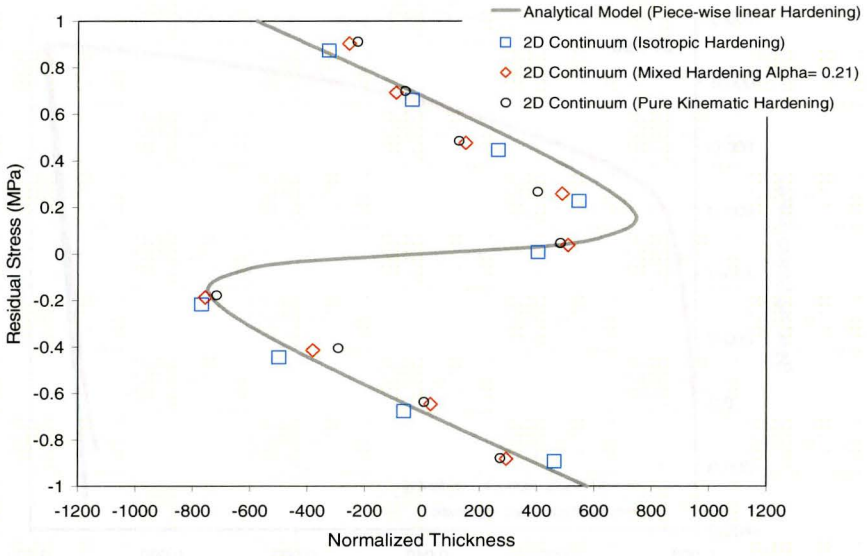

Figure 8.63 2D Continuum element FEA residual bending stress after springback for DP980. Compared are isotropic, mixed, and kinematic hardening assumptions to analytical springback using simple bending theory (using piece-wise linear hardening and elastic unloading).

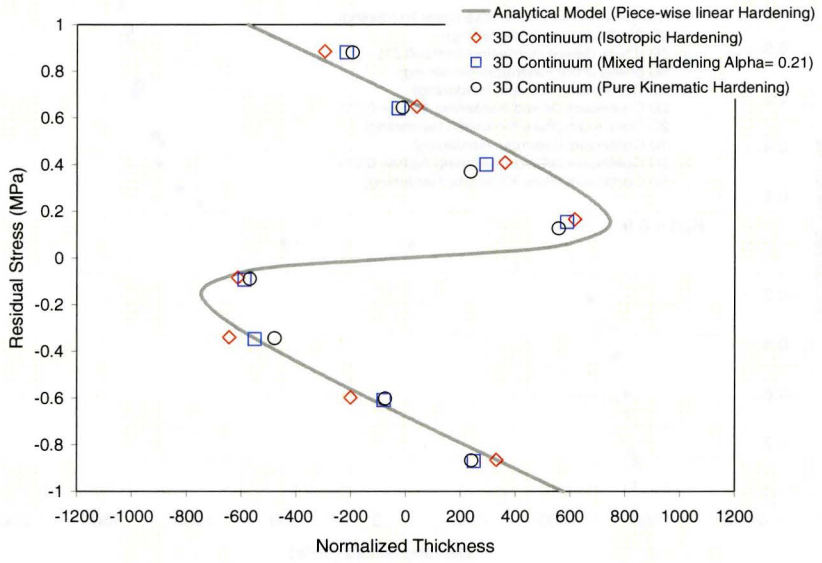

Figure 8.64 3D Continuum element FEA residual bending stress after springback for DP980. Compared are isotropic, mixed, and kinematic hardening assumptions to analytical springback using simple bending theory (using piece-wise linear hardening and elastic unloading).

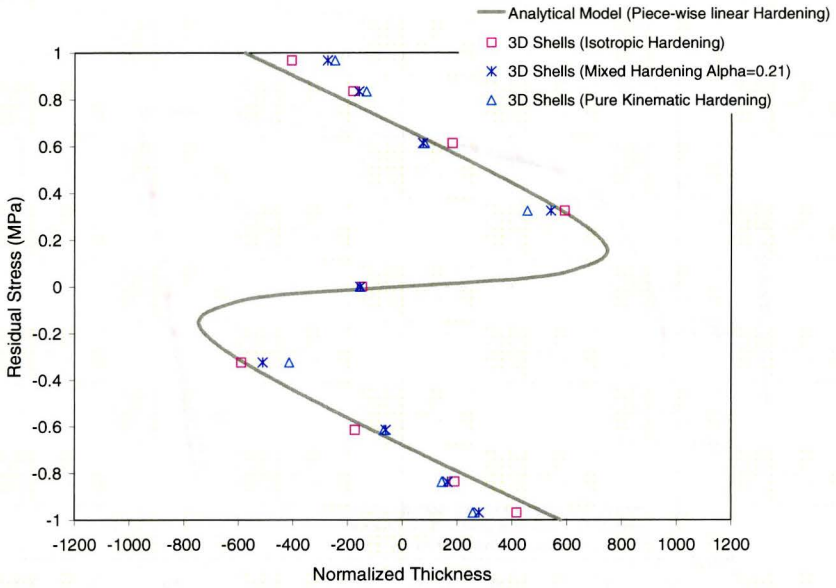

Figure 8.65 3D shell element FEA residual bending stress after springback for DP980. Compared are isotropic, mixed, and kinematic hardening assumptions to analytical springback using simple bending theory (using piece-wise linear hardening and elastic unloading).

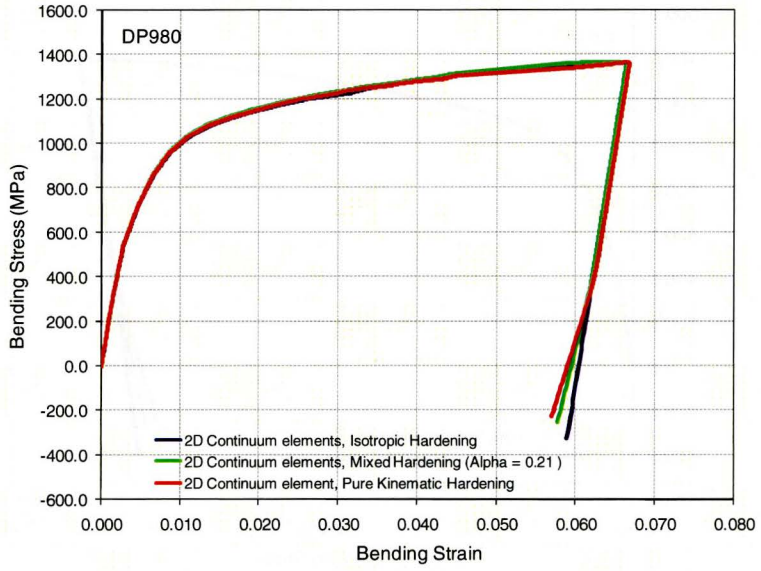

Figure 8.66 2D continuum element simulations for DP980. Loading and unloading of the extreme fiber comparing pure isotropic, mixed, and kinematic hardening assumptions in the FEA model.

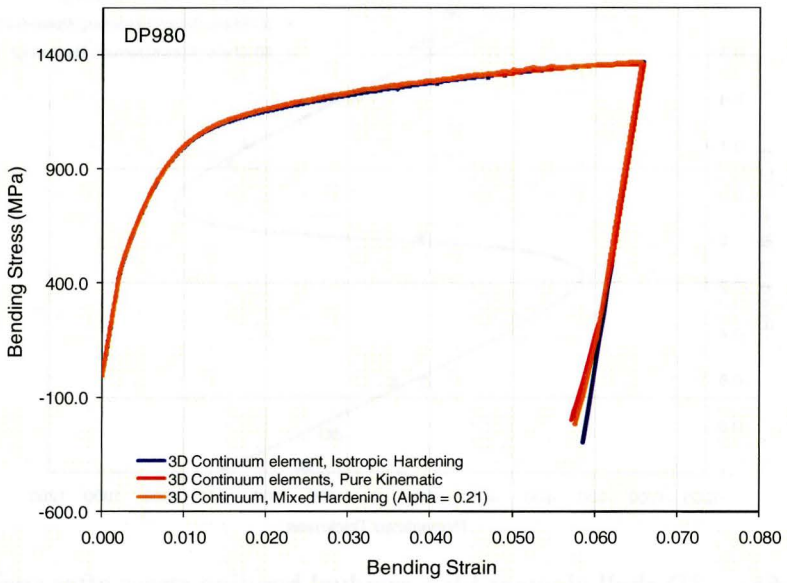

Figure 8.67 3D continuum element simulations for DP980. Loading and unloading of the extreme fiber comparing pure isotropic, mixed, and kinematic hardening assumptions in the FEA model.

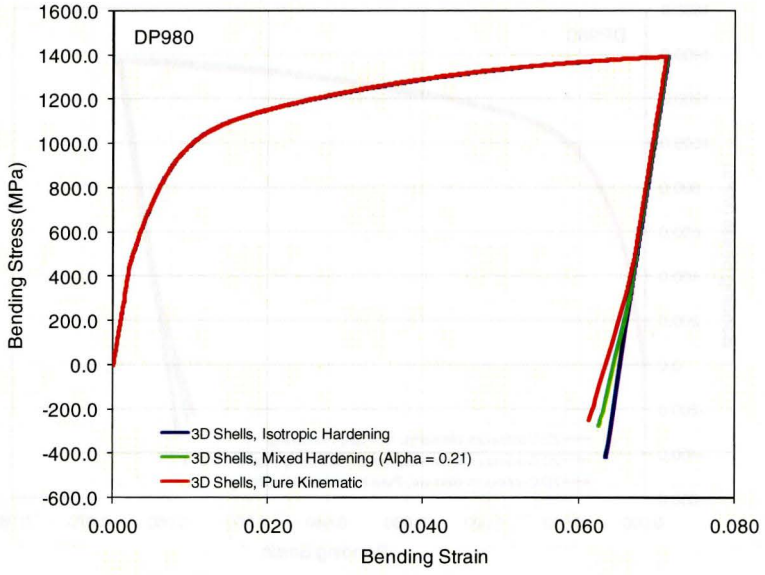

Figure 8.68 3D shell element simulations for DP980. Loading and unloading of the extreme fiber comparing pure isotropic, mixed, and kinematic hardening assumptions in the FEA model.

8.4.5 Discussion

In performing the FEA, work hardening was modeled using a piece-wise linear true stress-plastic strain curve, derived from actual tensile tests parallel to the rolling direction. Planar anisotropy was ignored and Von Mises criterion was assumed, due to it's general applicability to steels (Wang, 1993). A limitation in the FEA was therefore the lack of available experimental yield criterion for the DP steels, which has the potential to significantly affect the accuracy of springback from FEA (Kuwabara, 2004). Despite this, the springback from FEA showed good agreement with that from experiments, indicating that the use of Von Mises criterion in the FEA was a reasonable assumption.

In many FEA of sheet metal forming, regions of the formed blank can have effective strains that are beyond the true uniform strain from the tensile test. In these cases, work hardening beyond uniform true strain is estimated by a parabolic extrapolation of the work hardening curve (Zhu, 2001). Work hardening beyond the uniform true strain is therefore, estimated. The use of extrapolated or estimated work hardening in the V-die FEA was minimal. The nominal bending strain in the V-die experiments, prior to springback, was 0.068 to 0.091, or a Mises effective strain of .078 to 0.105 for the DP980 and DP780 steels respectively. From Table 8-1 and Table 8-2, the true uniform strain for the DP780 and DP980 steels was close to the effective strain in the bending tests for both steels.

In Section 8.2, springback from the FEA was reported in terms of the springback ratio (Ks) to be consistent with the work by Queener and DeAngelis (1968). It is more common to report the relative springback in terms of an angle (θ), or an absolute displacement relative to the baseline die geometry (Du et al., 2001; Yao et al., 2002; Xu et al., 2004; Ren et al., 2005; Wagoner et al., 2007;). To be more consistent with what has been reported by others over the last several years, springback results in this section, and the next (Section 8.5), are therefore reported in terms of the relative springback. The relative springback reported here is in terms of the included angle in the formed blank (prior to springback) as shown in Figure 2.4 in Chapter 2. Reporting springback in this way has the advantage of also being easily converted to the Ks value though Eq. 21 in Chapter 2. In the remaining discussion, springback is therefore interpreted as the relative springback.

8.4.5.1 Agreement between springback from FEA and Experiments

Overall, for all element types and for both DP steels, the FEA of V-die bending and springback using the pure isotropic hardening assumption resulted in a prediction error of 4.1 to 12.9% of the average experimental springback. Isotropic hardening is conventionally used for forming and springback simulations, and the FEA accuracy was acceptable by industry standards (Du et al., 2007). To improve the modeling of the material behavior, mixed isotropic-kinematic and pure kinematic hardening assumptions were utilized in the FEA models, using the appropriate hardening assumption for each DP steel. This was

determined by the calibration procedure described in Section 8.4.1. For the FEA models using shell elements, the use of the appropriate hardening assumption resulted in a springback prediction error (underprediction) from the FEA of 3.5 % and 0.4 % for the DP780 and DP980 steels respectively. The appropriate hardening applied to the 3D continuum element FEA resulted in a springback prediction error (overprediction) of 3.5% and 11% respectively for the DP780 and DP980 steels. The results for the 2D continuum models were worse as the springback error was 9% to 18.3% (overprediction) for DP980 and DP780 respectively. These results demonstrated that the FEA using 3D shells, and with the appropriate hardening model was the most suitable, for predicting springback in simple bending for the DP780 and DP980 steels. The 2D and 3D continuum models generally over predicted springback.

8.4.5.2 Accounting for springback differences between 2D, 3D continuum and 3D shell models

For the V-die bending FEA, It was demonstrated that the predicted springback was greatest for the 2D continuum models, followed by the 3D continuum, and the 3D shell models. V-die bending is a 3D problem, in which the non-uniform principle stress distribution across the blank width, as well as persistent anticlastic curvature affects springback, as shown earlier in Section 8.2. The 2D continuum models predict greater springback than the 3D continuum and shell models because in the 2D case, uniform plane strain bending is modeled, and persistent anticlastic curvature is suppressed. Under uniform plane strain bending,

the bending stresses at the center of the blank and edges, are assumed to be equivalent. The FEA demonstrated that 3D bending results in non-uniform bending stresses in which the center of the blank deforms under plane strain and the edges under uni-axial tension/compression. The results is lower bending stresses at the edges, and therefore lower bending moment compared to the case of uniform plane strain deformation. Persistent anticlastic curvature acts to decrease springback in the 3D continuum models compared to the 2D continuum models due to an increase in the cross section moment of inertia (Wang et al., 2004; Wang et al., 2005).

The 3D continuum models consistently showed more springback than the 3D shell models. For the purposes of this discussion, shell elements refer to 4 noded shells and 3D continuum element refer to 8 noded brick elements. The difference in springback between the element types can be attributed to differences in the stiffness of the elements themselves. The shell elements in this case resist displacements and rotations from deformation. The 3D continuum element, as well as the similar 2D continuum element, resists displacements only, therefore should be less stiff in structural simulations. Stühmeyer (2005) demonstrated this stiffness difference using an FEA model of a short cantilever beam, and Schikorra et al. (2005) demonstrated that shells are stiffer in bending using the FEA of DP600 in air bending. Shell elements should therefore show less springback than 3D continuum elements, under equivalent bending moment load. The FEA in Figure 8.55 and Figure 8.62 demonstrated that the bending stresses

and therefore bending moment were approximately equivalent for all element formulations, at the end of bending. There is some evidence showing that the 3D shell behaves in this way, when comparing the 3D continuum to the 3D shell FEA for the DP780 steel (assuming isotropic hardening). In this case, the 3D continuum element FEA predicted more springback than the corresponding 3D shell FEA (Figure 8.34). This was in spite of a slightly higher internal bending stresses at the end of forming (Figure 8.55), and very similar anticlastic curvature profiles (Figure 8.54).

8.4.5.3 Through thickness bending and residual stress distribution from FEA, for DP780 and DP790

The FEA though-thickness bending stress distributions for DP780 for both kinematic and isotropic hardening assumptions showed fair to good agreement with that of the analytical model from simple bending theory, with the shell element models showing the best agreement (Figure 8.55 and Figure 8.62). This was reasonable since the shell elements have kinematics similar to that of simple bending theory (LSTC, 2006).

In the FEA of DP780, differences in the bending stress distribution were observed between the shell and continuum elements. The 2D and 3D continuum elements models predicted less tensile stress than that from the shells (and simple bending theory) at tensile bending fibers intermediate to the outer surface and the neutral axis. On the compression side, differences in bending stresses were not significant. The distribution of bending stresses for the continuum element models

is consistent with that from general bending theory shown later in Figures 8.83-8.84. These results reaffirm the simple bending theory limit for R_p/t ratios at approximately 4-5 (. The results also demonstrate the effect of the differences in 3D shell and continuum element kinematics near the limits of simple bending. For the 3D shell elements, plane sections essentially remained plane resulting in agreement with the through thickness bending stresses from simple bending theory. This restriction does not apply to the continuum elements used.

Again, referring to the DP780 FEA, the residual bending stresses after springback, considering the FEA using pure isotropic hardening only, showed good agreement between the shell element models and that from simple bending theory. In the continuum element FEA, the agreement was poor to fair, due to the differences in bending stresses discussed previously.

Referring to the DP980 FEA, for all element formulations and both isotropic and kinematic hardening assumptions, the predicted though-thickness bending stress distribution generally showed good agreement with that from simple bending theory. This was consistent with the experimental bending condition, as bending was within the limit of simple bending theory, with R_p/t of 6.9. The results therefore demonstrated that the under these conditions, FEA models for all the element formulations deformed according to simple bending theory (i.e. plane sections remained plane). Considering only pure isotropic hardening, the residual stress distribution after springback from the FEA also showed fair agreement with that from simple bending theory. Springback from the

FEA was greater in the 3D continuum models compared to the 3D shell models for the same reasons discussed for the DP780 case.

In the FEA, the material behavior for loading-unloading deformation was approximated vis a vie the calibration shown earlier in Section 8.4.1. The results indicated that numerically, the DP780 steel behavior was that of pure kinematic hardening, and the DP980 steel showed mixed isotropic-kinematic behavior. Differences between the pure isotropic and pure kinematic hardening FEA were observed in the residual stress distributions. Unloading in the pure isotropic hardening FEA was linear. In the pure kinematic hardening case, there was softening of extreme bending fibers on unloading. This indicated non-linear unloading during springback, and increased recovery strain and springback, compared to the FEA using pure isotropic hardening. This behavior was observed for all element types used (Figures 8.56-8.61 and Figures 8.63-8.68). The agreement between springback from the FEA models, with the appropriate hardening assumption, and experiments suggests that non-linear unloading of extreme bending fibers is a mechanism for springback in DP780 and DP980 steels under simple bending conditions.

Other researchers have identified greater springback in the FEA of 3D pure bending problems, assuming mixed or pure kinematic hardening (for example, Schikorra et al. 2005). None have, however, identified potential mechanisms for this phenomenon.

8.4.5.4 Bending stress and moment distribution effect on springback

As discussed earlier, V-die bending is a 3D problem due to anticlastic curvature and non-uniform bending stresses across the width of the blank. Deformation occurs under the conditions of plane strain at the center of the blank to plane stress at the edges. FEA models using 2D continuum elements do not model these phenomena and therefore the predicted springback is an approximation of 3D bending-springback. The predicted springback from the 2D FEA models, using the pure isotropic assumption should however compare well with that from simple bending theory. This is because simple bending theory also assumes uniform plane strain bending, and neglects the effects of anticlastic curvature. The results however, show that this is not the case. Springback predicted from simple bending theory significantly underpredicted that from the 2D FEA models using the pure isotropic hardening assumption. The reason for this is the effect of punch to die clearance on the bending moment and curvature distribution along the sample length (Wang, 1993). This effect of this was demonstrated in Section 8.2. In the V-die FEA and experiments, the punch to die clearance was approximately 2 mm plus the blank thickness. Figures 8.36-8.37 show the bending moment distribution from the 3D shell FEA (pure isotropic hardening assumption) taken at the center, and along the length of the blank. Post-processing of the moment distribution along the length of the blank is convenient in shell elements since the nodes include a rotational degree of freedom. Also the through-thickness stress distribution in the shell elements at the center of the

blank is comparable to that from the 2D continuum FEA (Figure 8.55 and Figure 8.62). The peak bending moments from FEA show good agreement with simple bending theory, and show an additional bending moment in the blank that accounts for the transition from the punch to the die. Total springback is proportional to the area under the curves (Wang, 1993), and from these figures, springback from FEA is shown to be greater than that from simple bending theory. Simple bending theory for V-die bending therefore does not account for the moment distribution resulting from die clearance, and this is responsible for the underprediction compared to the experiments and FEA.

8.5 Small Radius Bending Experiment on a Commercial Bending Machine Using DP780

Small radius bending experiment were performed on a commercial bending machine in which a 25 mm wide blank was bent around a bending block having a radius of 1 mm, and an inclination of 40°. It was assumed that the blank had an inclination angle of 40° just prior to springback. As expected, the blank undergoes springback after removal from tooling. A portable CMM was then used to digitize the bottom surface (outside radius side) of blanks after removal from the die. The CMM data was used to measure the final bending angle after springback as explained in Chapter 6. Only the DP780 steel was studied. The DP980 steels fractured in the bending machines, despite the edge preparation in which the blank edges were polished (Figure 6.20 in Chapter 6).

8.5.1 General bending model applied to the small radius bending experiments for DP780

A modified form of the general bending model by Tan and Magnusson (1995) was used to analyze the evolution of principle bending stresses and material thinning as a function of bending curvature. This model was used to contrast the differences in bending stresses for the pure isotropic and kinematic hardening assumptions. The derivation of this model is outlined in Appendix A. The numerical procedure to solve the governing differential equation was presented earlier in Chapter 5, and the corresponding MATLAB® program is shown in Appendix B.

The general bending model uses Ludwig hardening to model work hardening. Plastic bending is assumed and elastic strains are ignored. The true stress-plastic strain data incorporated the experimental tensile data up to a true plastic strain of 0.10, which was close to, but before the uniform plastic strain. Beyond this point, a power law fit was used to extrapolate the curve to a plastic strain of 0.52. The results are shown in Figure 8.69.

The results for the solution to the general bending equation (Eq. 24 in Chapter 2) are shown in Figure 8.70. Consistent with the nomenclature used by Tan and Magnusson (1995), there are two analytical solutions designated as Model I and Model II, for the cases of pure isotropic and pure kinematic hardening, respectively. The analytical results for Model I and Model II therefore compare plastic bending using pure isotropic and kinematic hardening

assumptions, consistent with the material calibration performed in Section 8.4.1 and shown in Figure 8.32. The results show that for the pure kinematic hardening assumption, with increasing bending curvature (κ), there is greater neutral axis shifting (ρ), and material thinning (η), compared to the case of pure isotropic hardening. The results for the pure isotropic hardening assumption show negligible thinning. For example, at the bending curvature of 1.8, η has a value of 0.9946, implying 0.54% thinning. The experimental bending conditions as defined in terms of the geometric parameters of bending, κ, ρ, and η, are also shown in Table 8-8, and plotted in Figure 8.70. These values were determined by the solution to the general bending equation.

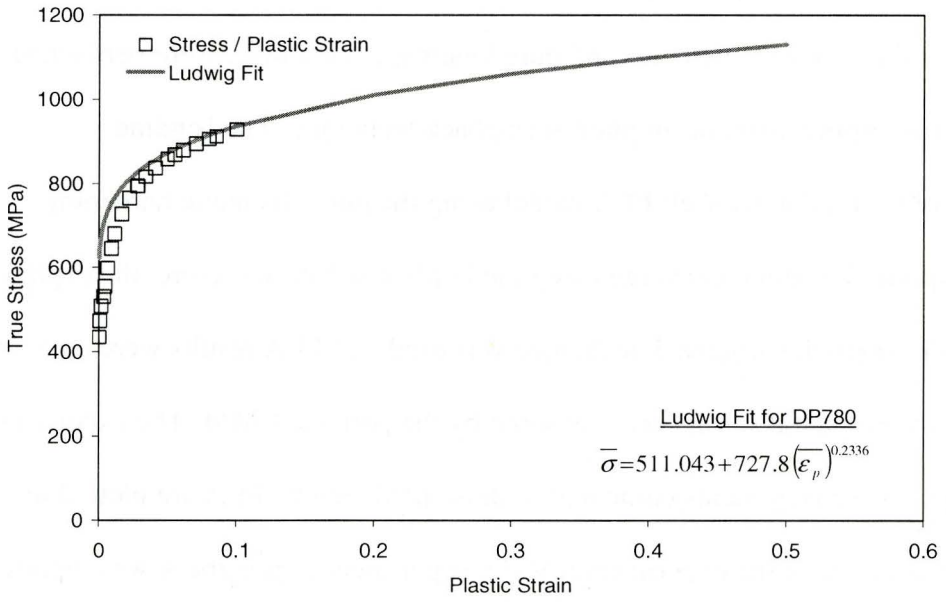

Figure 8.69 Ludwig fit for the DP780 steel compared to the actual true stress-plastic strain curve from the longitudinal direction tensile test.

8.5.2 FEA Analysis compared to experimental results for the small radius bending experiments

FEA models of the small radius bending experiments used piece-wise linear hardening consisting of true stress–plastic strain data, from tensile tests for the DP780 steel in the rolling direction. Consistent with the bending experiments, the FEA models used a bending block radius of 1 mm, and a bending block inclination of 40°.

Similar to the V-die FEA results, the FEA results for small radius bending were performed with the intention of examining the effects of element formulation (i.e., 3D shell and 2D/3D continuum element) and material modeling assumptions (i.e., pure isotropic hardening compared to pure kinematic hardening) on bending and springback. All the FEA simulations, except for the model using 3D shell elements and pure kinematic hardening, were performed using the implicit forming-implicit springback technique. The bending simulations for the 3D shell FEA model using the pure kinematic hardening assumption would not converge using the implicit solver; therefore, the explicit forming- implicit springback technique was used. All FEA results were compared to the experimental springback measured by the portable CMM. The experimental springback measurements compared to those predicted by FEA are plotted in Figure 8.71. As in the experimental V-die experiments, springback was reported as the relative springback. The data results are summarized in Table 8-9.

Table 8-8 Experimental bending conditions for DP780 in terms of the geometric parameters of bending, as determined by the solution to the general bending model (Eq. 24 in Chapter 2).

Analytical solution to the general bending model (Chapter 5)	Ri (mm)	κ	η	ρ
Model I (pure isotropic hardening)	1.00	0.9995	0.9991	0.8392
Model II (pure kinematic hardening)	1.00	0.9753	0.9514	0.8221

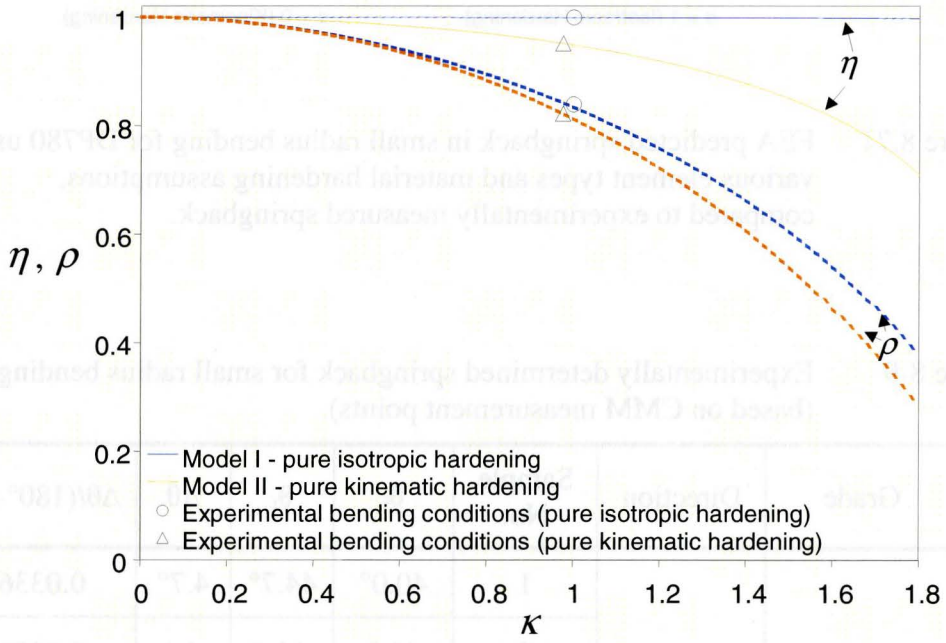

Figure 8.70 Solution to the general bending equation for cases of pure isotropic and pure kinematic hardening, based on the Ludwig fit of the DP780 experimental stress strain curve. Bending parameters for κ, η, and ρ are shown for the experimental bending conditions (R_i = 1.0 mm).

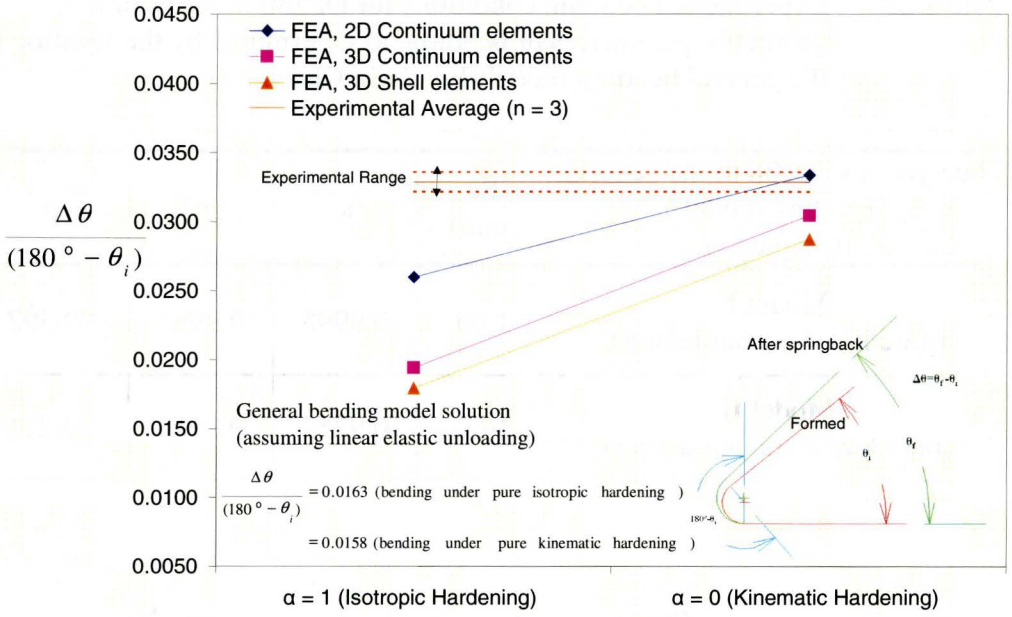

Figure 8.71 FEA predicted springback in small radius bending for DP780 using various element types and material hardening assumptions, compared to experimentally measured springback.

Table 8-9 Experimentally determined springback for small radius bending (based on CMM measurement points).

Grade	Direction	Sample No.	θ_i	θ_f	$\Delta\theta$	$\Delta\theta/(180°-\theta_i)$
DP780	Long	1	40.0°	44.7°	4.7°	0.0336
		2	40.0	44.6	4.6	0.0329
		3	40.0	44.5	4.6	0.0321
				Avg.	4.6	0.0329

Table 8-10 Summary of predicted (FEA) bending-springback results for the small radius bending experiments using DP780 steel.

DP780		θ_i	θ_f	$\Delta\theta$	$\Delta\theta/(180°-\theta i)$
2D Solids	$\alpha = 1$ (Isotropic Hardening)	40.8°	44.4°	3.62°	0.0260
	$\alpha = 0$ (Kinematic Hardening,)	41	45.6	4.64	0.0334
3D Solids	$\alpha = 1$ (Isotropic Hardening)	42.9	45.6	2.66	0.0194
	$\alpha = 0$ (Kinematic Hardening,)	38.6	42.9	4.33	0.0304
3D Shells	$\alpha = 1$ (Isotropic Hardening)	40.9	43.4	2.50	0.0179
	$\alpha = 0$ (Kinematic Hardening,)	39.9	43.9	4.03	0.0287

Overall, the FEA predicted springback ranged, from 54% to 101% of the average experimental springback. The predicted springback was greatest for the 2D continuum element followed by the 3D continuum, and then the 3D shell elements. The predicted springback was highest in the FEA models using pure kinematic hardening as opposed to pure isotropic hardening. Springback was also predicted using the analytical bending moment from Model I and Model II, considering elastic unloading only. These results significantly underpredicted springback, but showed reasonable agreement with the shell element FEA using the pure isotropic hardening assumption.

The least amount of springback was predicted using shell elements for the pure isotropic hardening assumption, which is the conventional method used in sheet metal forming. This case predicted only 54% of the experimental springback. All 3D models predicted springback that was outside of the experimental range; however, the 2D and 3D continuum FEA, using the pure kinematic hardening assumption, showed the best agreement with the experimental average, predicting 101 and 92% of the experimental springback respectively.

The FEA models using the continuum elements and pure kinematic hardening assumption predicted 6.3% material thinning at the apex of the bend (Figure 8.72). This was consistent with the analytical general bending Model II, which predicts 5% thinning, and the experimentally measured (using a point micrometer) result of 6% thinning. The 2D and 3D continuum element FEA predicted even less thinning, 4.2 and 4.1 % respectively. The FEA using shell element did not predict significant material thinning (Figure 8.73).

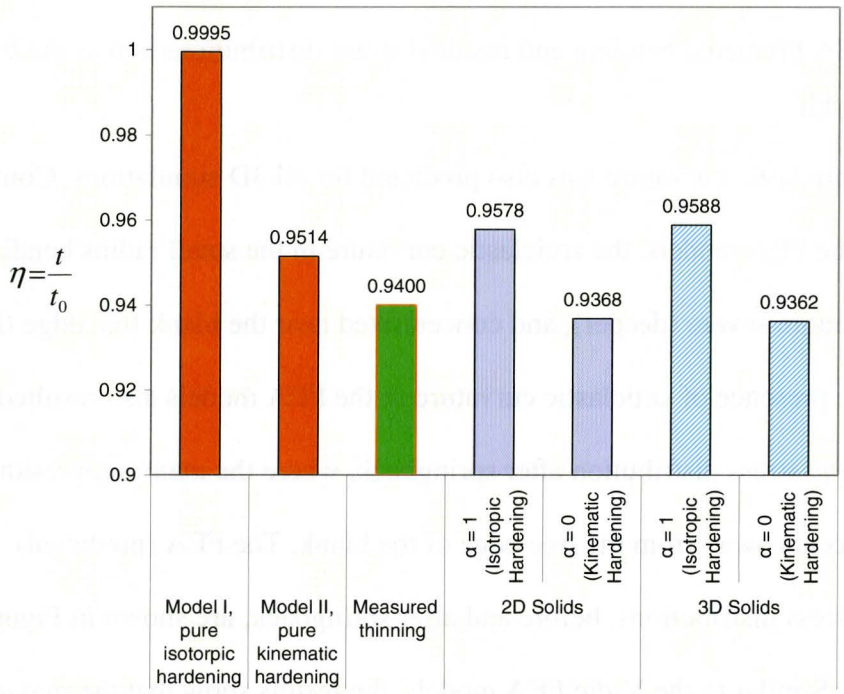

Figure 8.72 FEA (predicted) thinning at the apex of the bend using various element types for both pure isotropic and kinematic hardening, compared to that measured experimentally (average of 3 specimens) and that predicted by the general bending model.

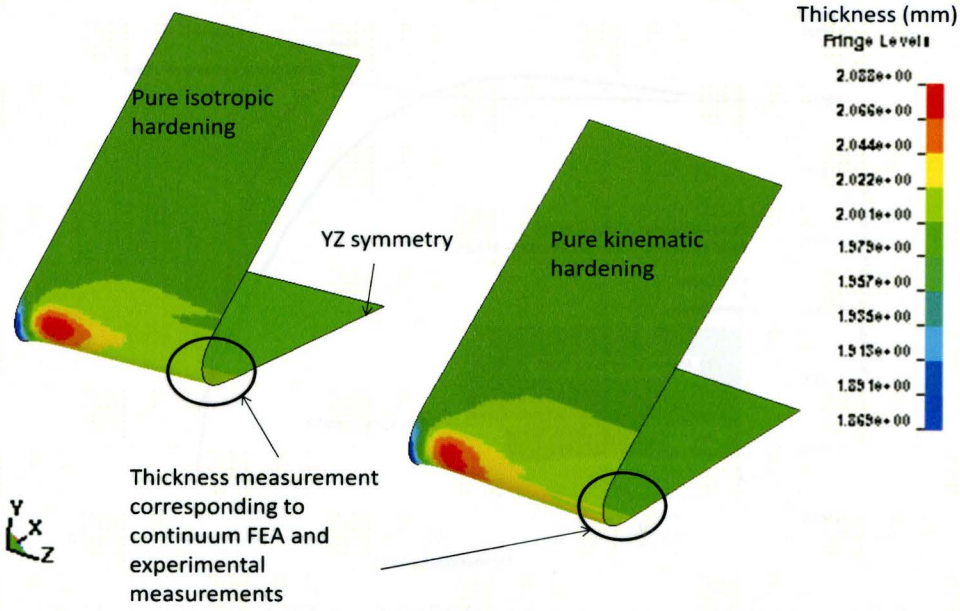

Figure 8.73 3D shell FEA thickness after bending and springback for DP780, showing insignificant thinning at the centerline of the blank.

8.5.3 FEA Predicted bending and residual stress distributions across the blank width

Anticlastic curvature was also predicted for all 3D simulations. Compared to the V-die FEA models, the anticlastic curvature in the small radius bending FEA was more severe (deeper), and concentrated near the blank free edge (Figure 8.74). The presence of anticlastic curvature in the FEA models also resulted in a non-uniform stress distribution after springback, where the maximum residuals stresses occurs away from the free edge of the blank. The FEA (predicted) bending stress distributions, before and after springback, are shown in Figures 8.75-8.82. Similar to the V-die FEA models, the results show that the maximum predicted residual stress after springback was largest for the models using isotropic hardening.

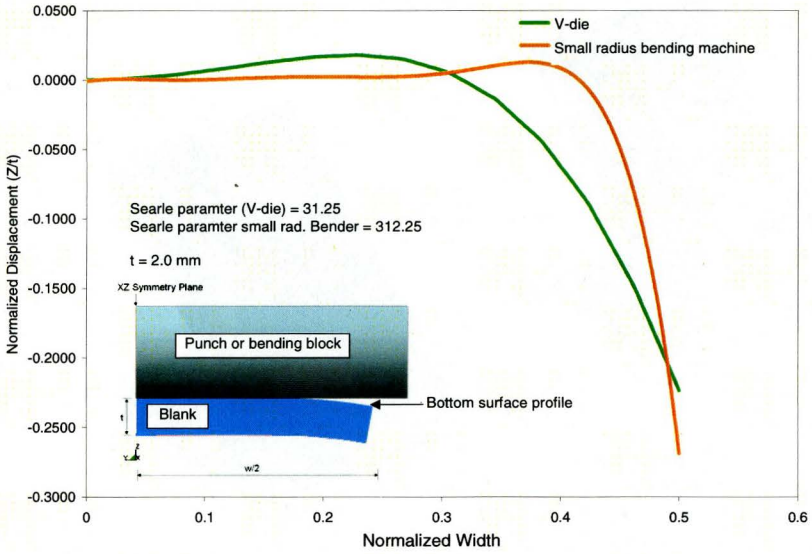

Figure 8.74 Anticlastic curvature for DP780 from FEA comparing V-die bending and small radius bending.

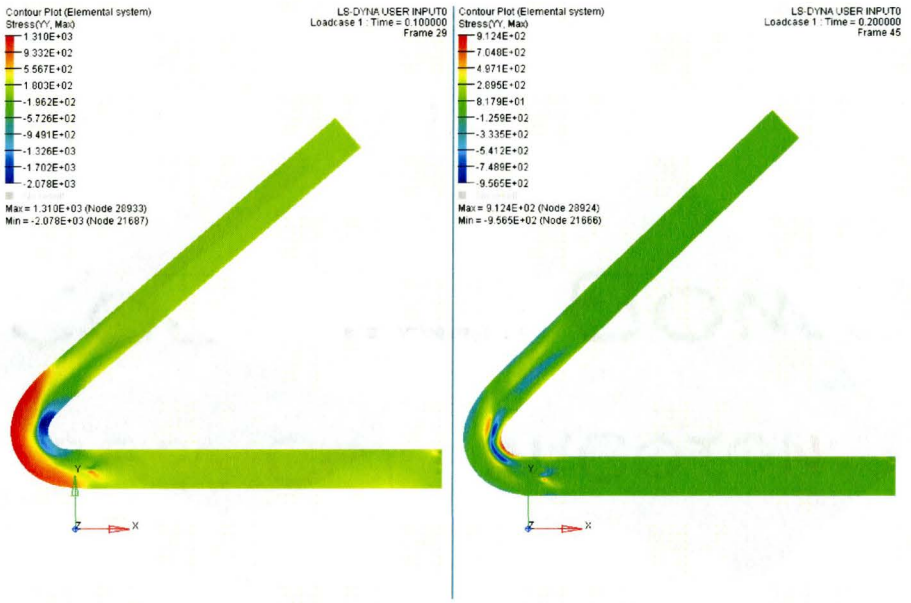

Figure 8.75 2D continuum FEA of DP780 in small radius bending. Shown are bending (left), followed by springback (right) and the associated stress distribution (in MPa). Analysis assumed pure isotropic hardening.

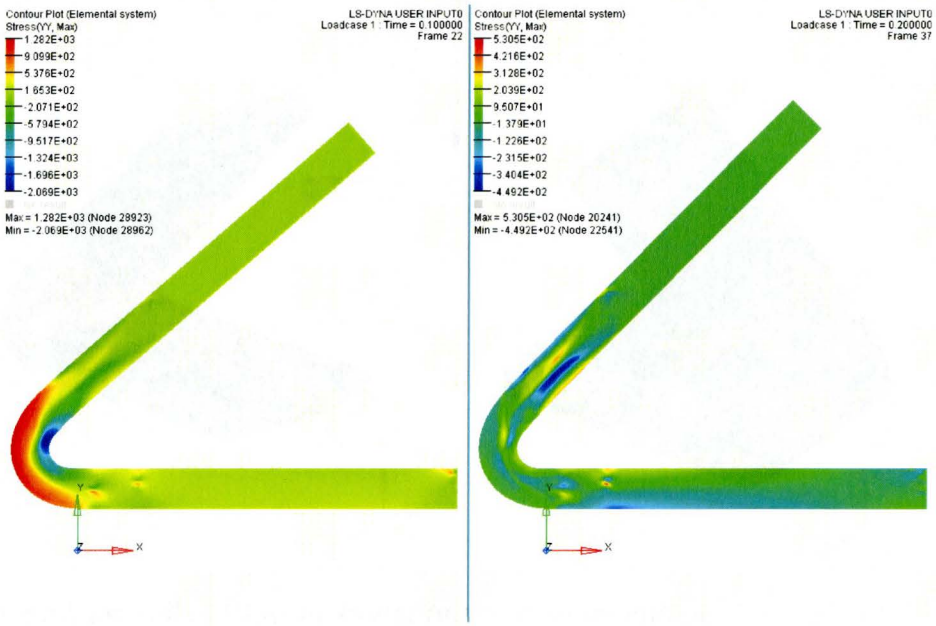

Figure 8.76 2D continuum FEA of DP780 in small radius bending. Shown are bending (left), followed by springback (right) and the associated stress distribution (in MPa). Analysis assumed pure kinematic hardening.

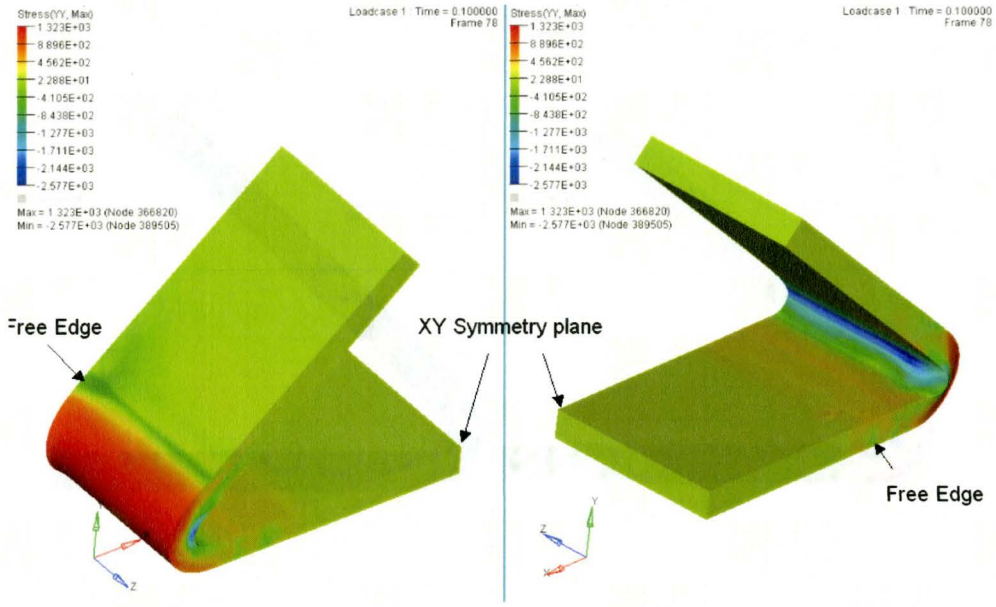

Figure 8.77 3D continuum FEA of small radius bending of DP780 steel showing the resulting bending stress distribution (in MPa, quarter symmetry is used in the FEA model). Analysis assumed pure isotropic hardening.

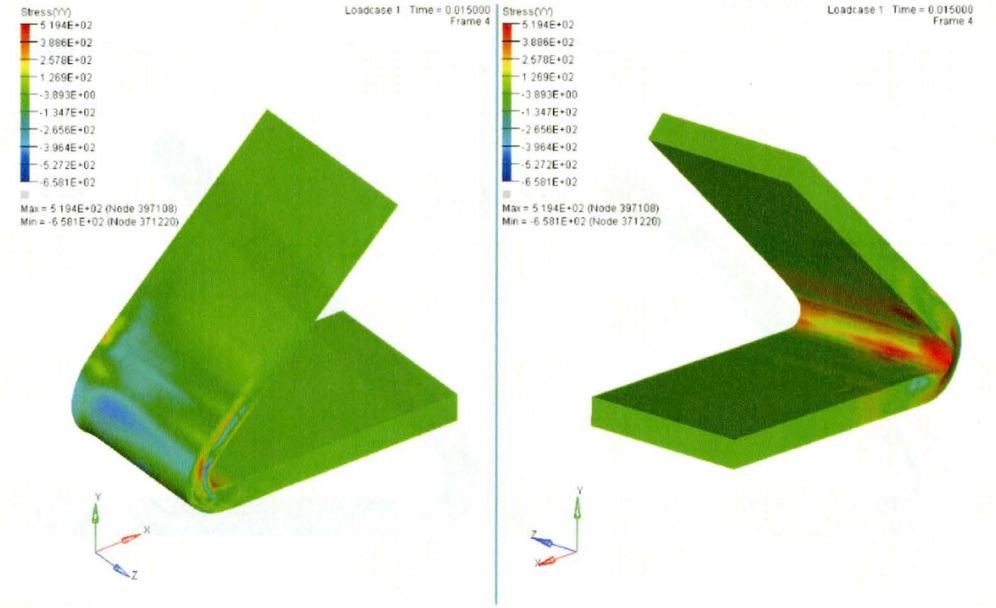

Figure 8.78 3D continuum FEA of springback in small radius bending of DP780 steel showing the resulting bending stress distribution (in MPa, quarter symmetry is used in the FEA model). Analysis assumed pure kinematic hardening.

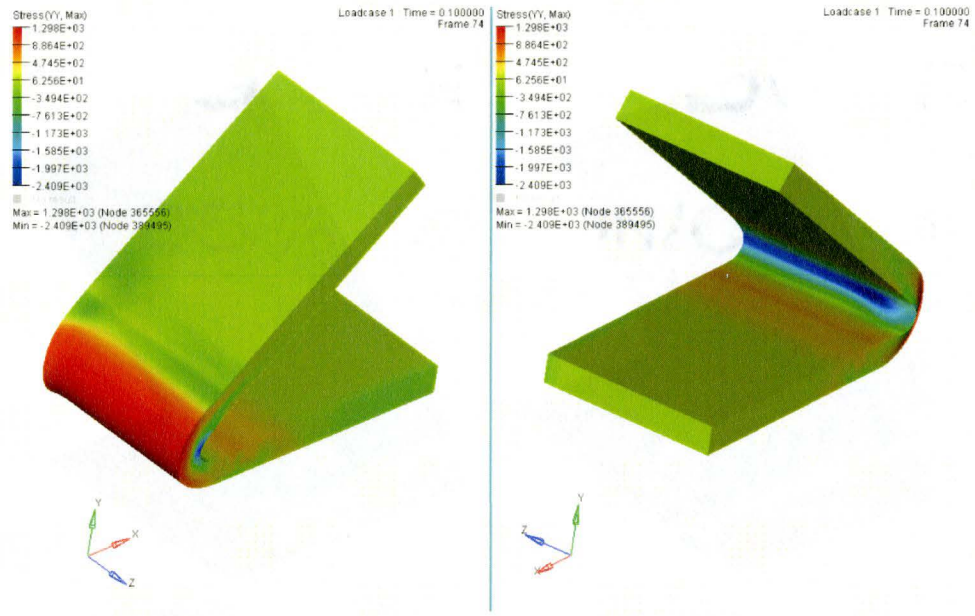

Figure 8.79 3D continuum FEA of small radius bending of DP780 steel showing the resulting bending stress distribution (in MPa, quarter symmetry is used in the FEA model). Analysis assumed pure isotropic hardening.

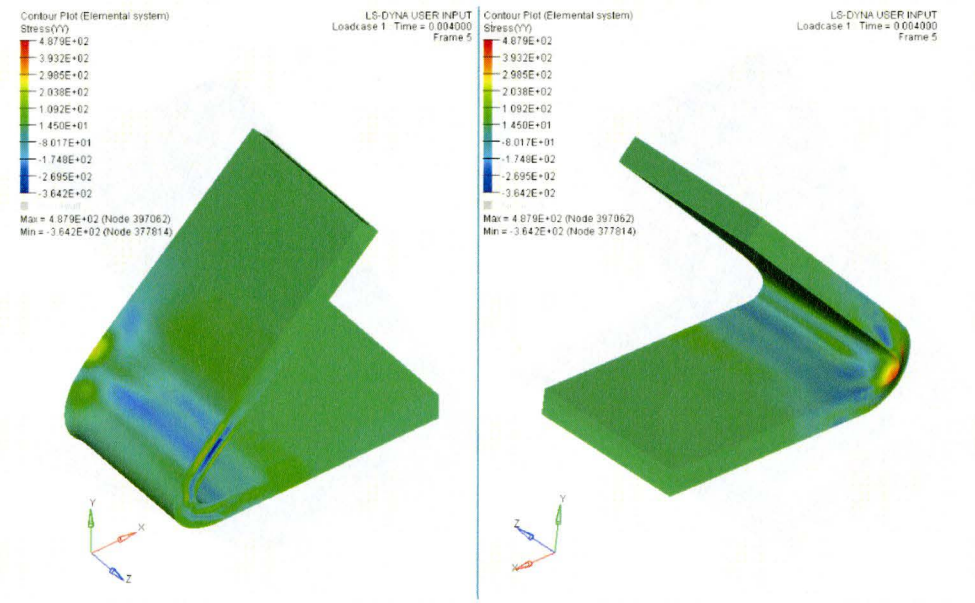

Figure 8.80 3D continuum FEA of springback in small radius bending of DP780 steel showing the resulting bending stress distribution (in MPa, quarter symmetry is used in the FEA model). Analysis assumed pure kinematic hardening.

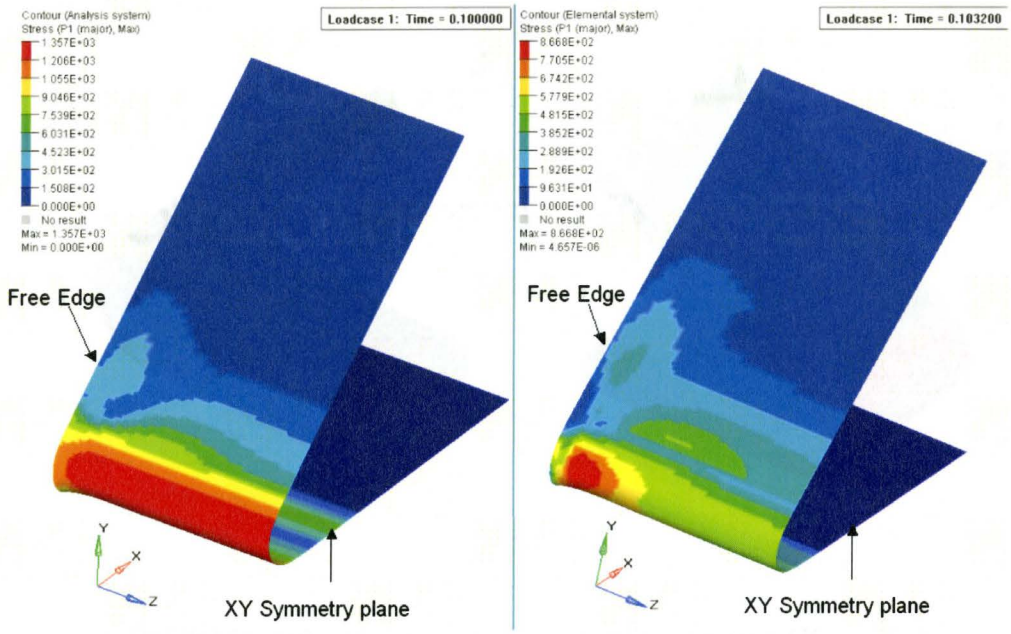

Figure 8.81 3D shell FEA of DP780 in small radius bending. Shown are bending (left), followed by springback (right) and the associated stress distribution (Maximum stress in MPa). Analysis assumed pure isotropic hardening.

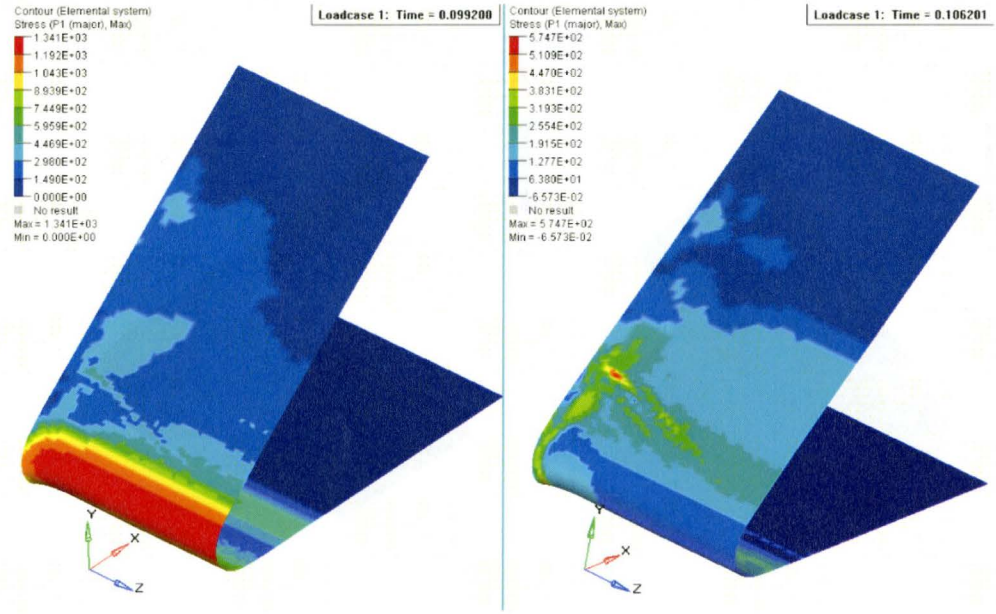

Figure 8.82 3D shell FEA of DP780 in small radius bending. Shown are bending (left), followed by springback (right) and the associated stress distribution (Maximum stress in MPa). Analysis assumed pure kinematic hardening.

8.5.4 FEA predicted through-thickness bending stress distributions.

The predicted (FEA) bending stress distributions, through the thickness, for loading (bending) are compared for all simulations in Figures 8.83-8.84. The FEA stress distributions were measured along a cross-section at the apex of the bend and parallel to the XY symmetry plane shown in Figures 8.77-8.78. The through-thickness stress distributions for the shell elements were determined at the though-thickness integration points (21 in this case). Also shown for reference is the predicted bending distribution using piece-wise linear hardening for simple bending theory. This was calculated using the numerical procedure presented earlier in Chapter 5. The R_i/t ratio for the small radius bending experiments is 0.5. The continuum element FEA predicts that the bending stresses develop differently depending on the material hardening assumption. Figure 8.83 and Figure 8.84 show predicted bending stresses for the 2D and 3D continuum and 3D shell element FEA, as well as for the analytical bending Models I and II, and that from simple bending theory. Both general bending Models I and II predict neutral axis shifting in the direction towards the bending block. Under the isotropic hardening assumption, neutral axis shifting results in re-hardening of fibers that were previously in compression, that are then re-loaded in tension. In contrast, for the pure kinematic hardening assumption, neutral axis shifting results in softening of these fibers. The FEA results using the continuum elements also predict this trend. However, the phenomenon is not as distinct as that predicted by the general

bending models. The shell models do not predict any differences in the bending stress distribution for the kinematic and isotropic hardening assumptions, and show good agreement with that from simple bending theory.

In the continuum element FEA, the predicted bending stresses in the tensile fibers showed agreement with that predicted using the general bending models. The agreement was not as good for the compression bending fibers that were near the surface of the blank. However, both FEA and analytical results predict that the minimum compressive stress (i.e., highest magnitude) occurs below the surface of the blank. The FEA using 3D shells predicted bending stresses in the tensile fibers, that were higher in magnitude to that from the continuum element FEA, as well as from the general bending models. On the other hand, the 3D shell element FEA predicted compressive bending stresses that were lower in magnitude to that from continuum element FEA and the general bending models. There was good agreement between the predicted bending stresses at the outer surface fibers, when comparing general and simple bending models.

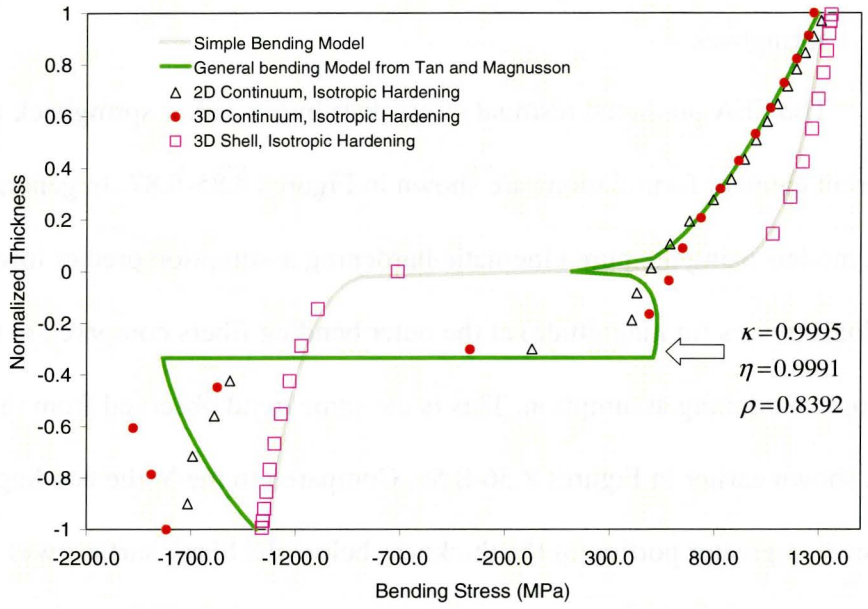

Figure 8.83 DP780 FEA predicted bending stress at the apex of the bend (pure isotropic hardening assumption), compared to that predicted by simple and general bending theory (Model I).

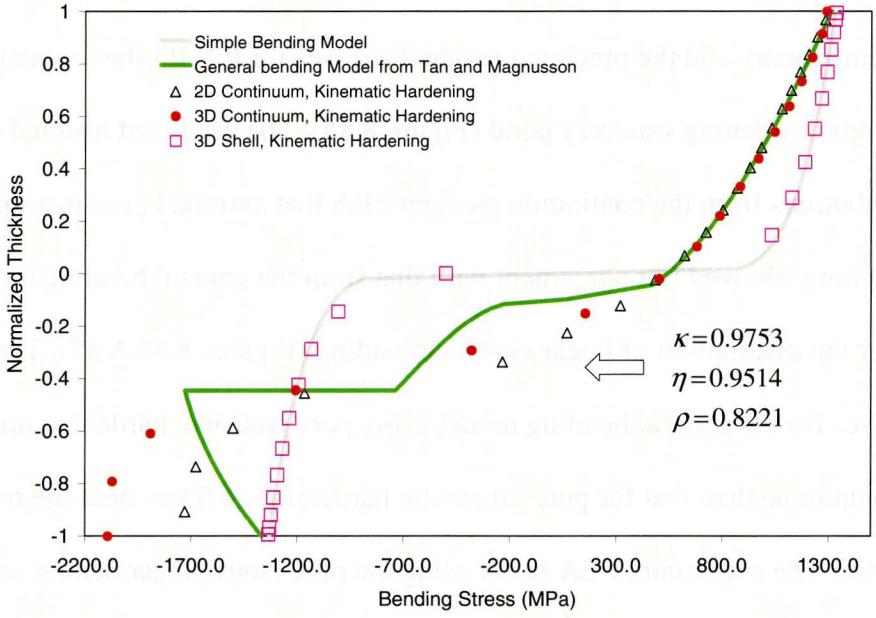

Figure 8.84 DP780 FEA predicted bending stress at the apex of the bend (pure kinematic hardening assumption), compared to that predicted by simple and general bending theory (Model II).

8.5.5 FEA Predicted through thickness residual stress distributions after springback

The FEA predicted residual stress distributions after springback for the different element formulations are shown in Figures 8.85-8.87. In general, the FEA models using the pure kinematic hardening assumption predict lower residual stresses (in magnitude) at the outer bending fibers compared to the pure isotropic hardening assumption. This is the same trend observed from the V-die FEA shown earlier in Figures 8.56-8.58. Compared to the V-die bending FEA, however, a greater portion of the thickness below the blank surface was affected.

Figures 8.85-8.87 also show the predicted residual stress distribution from simple bending theory and from the general bending models (Model I and II), both of which assumed linear (elastic) unloading. Agreement between simple bending theory and the predicted residual stresses for the 3D shell models using isotropic hardening was very good (Figure 8.85). The predicted residual stress distributions from the continuum element FEA that assumed pure isotropic hardening, showed fair agreement with that from the general bending models under the assumption of linear elastic unloading (Figures 8.86-8.87). The residual stresses for the general bending model using pure isotropic hardening are greater in magnitude than that for pure kinematic hardening, at fibers near the mid-surface. The continuum FEA result using the pure isotropic hardening assumption showed the same trend.

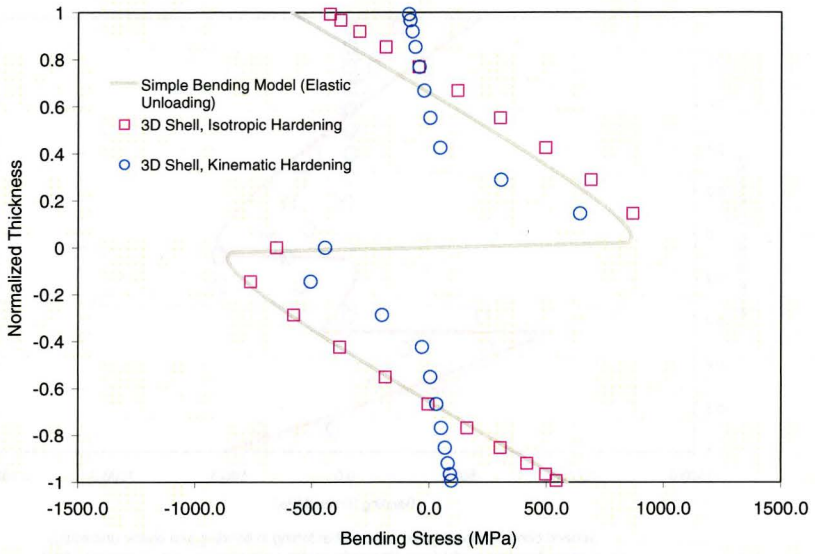

Figure 8.85 FEA predicted residual bending stress after springback for DP780 using 3D shell elements (at the apex of the bend). Compared are the isotropic and kinematic hardening assumptions to simple bending theory (using piece-wise linear hardening and elastic unloading).

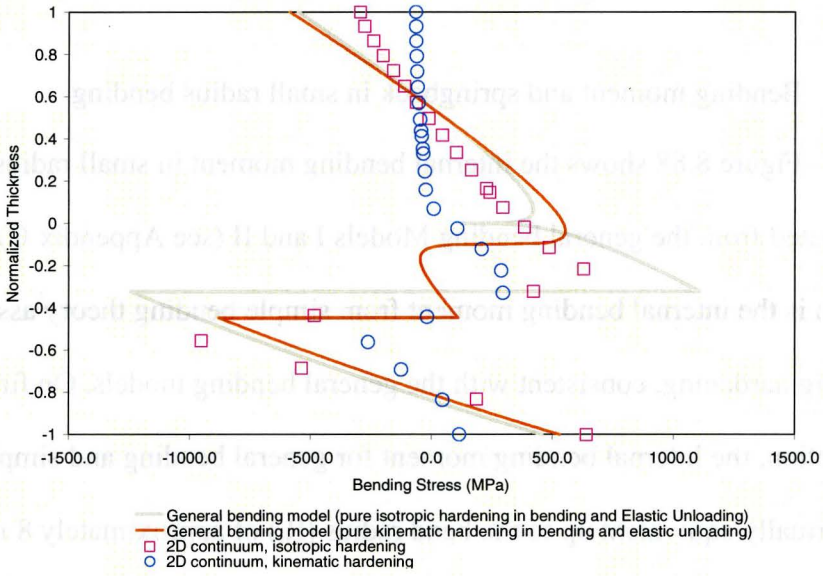

Figure 8.86 FEA predicted residual bending stress after springback for DP780 using 2D continuum elements (at the apex of the bend). The residual stress from the analytical general bending model is also shown, assuming isotropic hardening and linear (elastic) unloading.

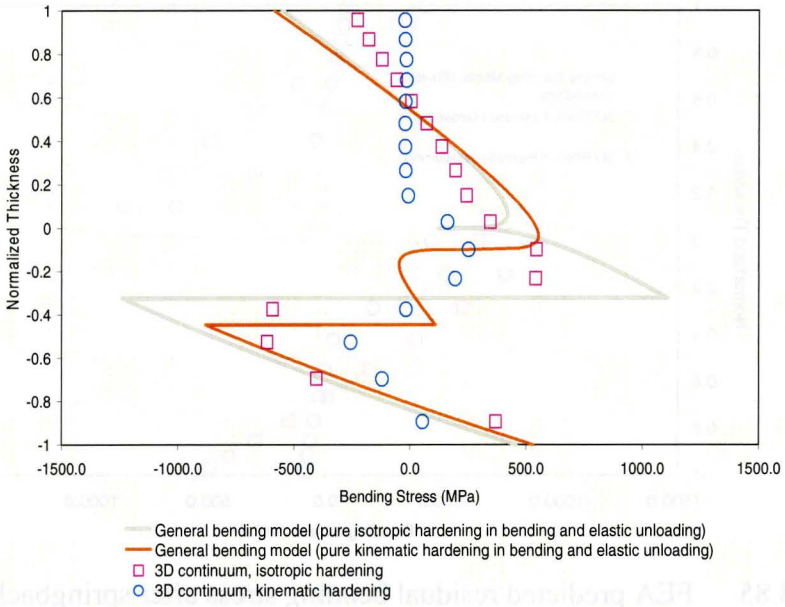

Figure 8.87 FEA predicted residual bending stress after springback for DP780 using 3D continuum elements (at the apex of the bend). The residual stress from the analytical general bending model is also shown, assuming isotropic hardening and linear (elastic) unloading.

8.5.6 Bending moment and springback in small radius bending

Figure 8.88 shows the internal bending moment in small radius bending calculated from the general bending Models I and II (see Appendix C). Also shown is the internal bending moment from simple bending theory assuming Ludwig hardening, consistent with the general bending models. On first inspection, the internal bending moment for general bending and simple bending are virtually equivalent up to the bend radius (R_i) of approximately 8 mm. Beyond this, the bending moment in the general bending Model II rapidly decreases, in parallel with the decrease in thinning shown in Figure 8.70. The bending moment

for general bending Model I is virtually identical to that for simple bending, up to an inside bending radius of 0.5 mm.

Springback for the general bending Models I and II as a function of inside bend radius (R_i) and assuming linear elastic unloading, is shown in Figure 8.89. For models I and II, springback is essentially the same as that from simple bending theory up to a bending radius of approximately 6 mm-7 mm. Beyond this point, springback decreases for Model II. For the experimental bending conditions using R_i=1.0 mm, Model I predicts approximately 3% more springback than Model II. The simple bending model predicts nearly identical springback to that from Model I (assuming linear elastic unloading).

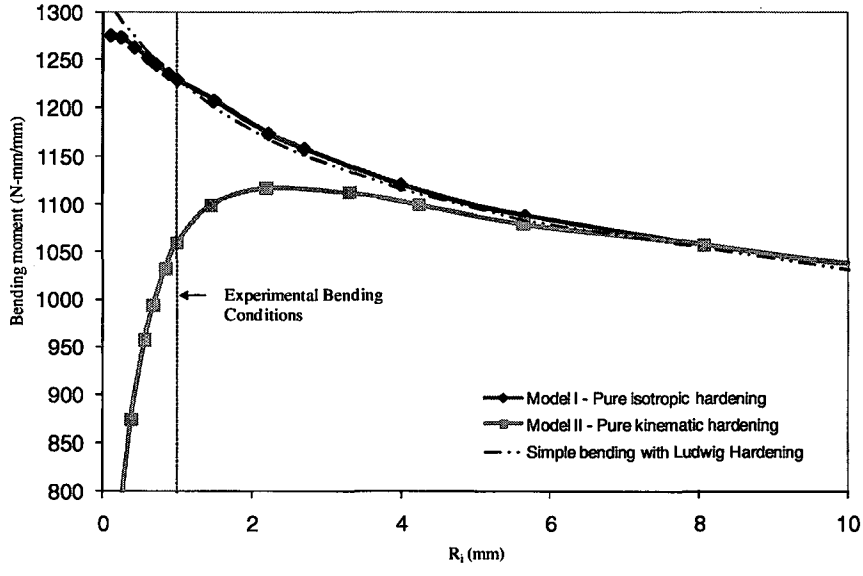

Figure 8.88 Predicted bending moment for the DP780 steel (initial thickness of 2.0 mm), from the general bending model compared to simple bending theory using Ludwig hardening (same as in the general bending model) as a function of inside (R_i) or bending block radius.

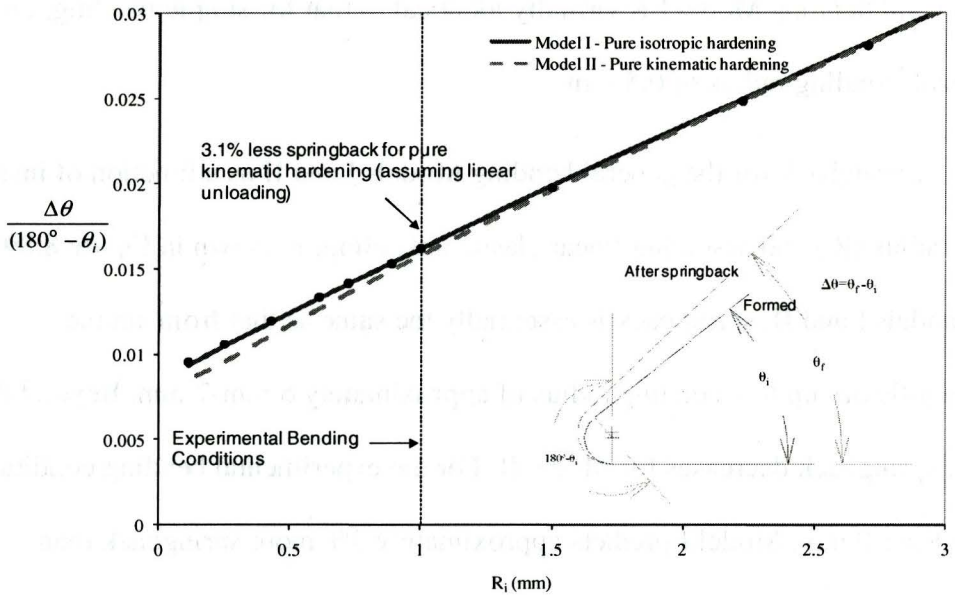

Figure 8.89 Predicted bending springback for the DP780 steel (initial thickness of 2.0 mm), from the general bending model as a function of inside (R_i) or bending block radius. Elastic unloading is assumed.

8.5.7 Discussion

Von Mises criterion was assumed in the FEA of the small radius bending experiments and the limitations of this assumption are the same as those discussed for the FEA of the V-die experiments.

The work hardening behavior at the strain levels in the small radius bending tests was largely unknown and therefore parabolic extrapolation of the hardening curve was required as recommended by the FEA code developers (Zhu, 2001). This was a limitation of the FEA. The maximum bending strains in the small radius experiments were approximately 0.5, or a Mises effective strain of 0.58.

8.5.7.1 Experimental springback compared to FEA

As in the V-die results, the FEA and experimental results for bending to a small radius (R_i =1.0 mm) were reported using the relative springback as described in Figure 2.4 in Chapter 2. Springback from the FEA using the pure isotropic hardening assumption underpredicted the experimental springback to a large degree. In this case, the springback prediction error was 20.9%, 40.9% and 45.4% for the 2D continuum, 3D continuum, and 3D shell models respectively. This is in contrast to the DP780 FEA models for V-die bending, in which the error in the predicted springback was small (i.e. less than 13%). The FEA using the pure kinematic hardening assumption, which was appropriate as indicated by the calibration study from Section 8.4, resulted in significant improvement in the predicted springback. The springback error using pure kinematic hardening was, 1.6% (overprediction), 7.4% (underprediction), and 12.5% (underprediction) for the 2D continuum, 3D continuum, and 3D shell models respectively.

As was the case for the V-die FEA, springback from the FEA of small radius bending was greatest for the 2D continuum models, followed by the 3D continuum, and the 3D shell models. The explanation for this trend is the same as that explained for the case of V-die bending. In contrast to the V-die FEA, the differences in springback between the 2D continuum and 3D continuum FEA were larger. Supporting this result is more severe anticlastic curvature and therefore larger bending resistance in the 3D models of the small radius bending FEA, compared to that in V-die bending (Figure 8.74). Compared to the V-die

FEA, in small radius bending, anticlastic curvature is concentrated towards the edge of the blank, with greater deflection away from the punch, a trend that is consistent with increasing Searle parameter (Wang et al., 2004). Although the 2D continuum element FEA provides the most accurate springback prediction under pure kinematic hardening, it does not model the physics of bending associated with the deformation of the free edges (i.e., anticlastic curvature). The 2D elements are therefore not necessarily the correct elements to use for this problem.

8.5.7.2 Through thickness bending stresses and thinning deformation

An analytical model for general bending using the method by Tan et al. (1995) provides insights into the kinematics of bending for the cases of pure isotropic and pure kinematic hardening. A modified version of their model (Chapter 5) was applied to the DP780 steel used in this thesis, and the hardening of the DP780 steel was approximated using Ludwig hardening (Figure 8.69). By applying Ludwig hardening, plastic bending is assumed and elastic strains are ignored. The analysis from Section 8.3 showed that inclusion of the elastic bending strains, in terms of affecting springback, is only important when the surface bending strains are less than 0.04.

The solutions to the general bending Models I and II are shown in Figure 8.70. These results show the trend of greater neutral axis shifting (κ) and material thinning (η) with increasing bending curvature. The thinning trend is reproduced in the FEA models. Figure 8.72 shows predicted thinning for FEA models compared to experimentally measured thinning, at the values κ, η and ρ,

describing the experimental bending conditions (Table 8-9, determined from Figure 8.70). The 3D shell FEA did not show significant thinning deformation at the apex of the bend, because they do not produce thinning (Figure 8.73) in the absence of membrane strains (LSDYNA3D, 2006). The 2D and 3D continuum FEA predicted more thinning for the kinematic hardening assumption compared to isotropic hardening assumption. The experimentally measured thinning was closest to that from 2D and 3D continuum FEA using the pure kinematic hardening assumption. This result also showed good agreement with that predicted using the general bending Model II as well as from the experiments. These result further support the use of pure kinematic hardening in the FEA models using continuum elements, and that the 3D shell does not capture this bending behavior.

Under the experimental bending conditions, the general bending model shows that bending stresses develop differently depending on the material model used. Figures 8.83-8.84 show the predicted principle bending stresses for the 2D and 3D continuum, and 3D shell FEA models compared to the analytical models for general bending (for isotropic and kinematic hardening). In the general bending model, neutral axis shifting results in hardening for Model I, and softening for Model II. The continuum FEA models also predict this trend, and the shell models do not due to the limitation of the shell element kinematics (i.e. absence of neutral axis shifting). These results also demonstrate that the 3D shell

element may not be appropriate for the modeling of general bending and the associated springback.

8.5.7.3 Through thickness residual stresses

The predicted (FEA) residual stresses for the shell and continuum models are shown in Figures 8.85-8.87. The FEA results show that the residual stresses in the surface and sub-surface fibers are lower for the kinematic hardening assumption compared to isotropic hardening assumption. However, the extent of fibers affected by this phenomenon is greater than in the V-die bending FEA (Figures 8.56-8.58). Similar to the V-die FEA results, the lower residual stresses in the surface fibers indicate non-linear unloading and therefore more recovery strain and springback. The greater extent of surface fibers affected in the small radius bending FEA indicates a larger springback effect using the kinematic hardening assumption, compared to the corresponding case in the V-die bending FEA.

There was marginal agreement between the residual stresses from the 2D and 3D continuum FEA compared to that from the general bending models (Model I and Model II), assuming linear unloading (Figure 8.86 and Figure 8.87). The areas of largest discrepancies were at or near the mid-surface fibers. The lack of agreement for peak stresses near the neutral surface may be the result of differences in work hardening as modeled in the FEA compared to the general bending model. In the FEA, work hardening is modeled using a piece-wise linear representation of the actual true stress-plastic strain curve. In the general bending

model, Ludwig hardening is used. At low values of effective strain, Ludwig hardening significantly over-predicts work hardening, compared to the corresponding piece-wise linear hardening curve, as shown in Figure 8.69.

8.5.7.4 Bending moment and springback assuming linear elastic unloading for Models I and II, compared to simple bending theory

Springback is a direct function of the internal bending moment at the end of forming (Wang et al., 2005). The analytical and FEA results for small radius bending have demonstrated a complex interaction between the developed bending stresses and thinning deformation at the apex of the bend, in relation to the hardening assumption. In Figure 8.88 and Figure 8.89 this relationship is explained, as well as the impact on springback. Figure 8.88, shows the effect on the internal bending moment from thinning deformation and bending stress evolution, as a function of the bending block radius (R_i). Compared are the results from the general bending model and a corresponding simple bending model using the same Ludwig work hardening equation, as in the general bending model.

Referring to Figure 8.88, in comparing Model II in relation to Model I, as the bending block radius decreases there is increased thinning deformation and a reduction of the internal bending stresses due to neutral axis shifting. This trend has been explained in the previous sections (Figure 8.70). Both thinning and lower internal bending stresses act to reduce the internal bending moment below that in Model I and the simple bending model, at the experimental bending conditions. Note that for the simple bending model and the general bending

Model I, thinning deformation is negligible. The effect of thinning deformation is to reduce the moment carrying capacity of the cross section, with the expected effect on springback (i.e. decreasing springback). At the same time, thinning deformation reduces the bending resistance of the cross section vis a vie, a lower second moment of inertia. This effect acts to increase springback (see Eq. 21 in Chapter 2).

Again, referring to Figure 8.88, the predicted internal bending moment for Model I is nearly identical to that from the simple bending model over the range of R_i shown, despite the differences in the through-thickness stress distributions shown in Figure 8.83. This is in agreement with the work by Zhang et al. (1998) in which a general bending model was developed assuming isotropic hardening. These researchers showed that thinning was insignificant and can be ignored in calculating springback. Indirectly, the results in this thesis show that the differences in the bending stress distribution, comparing the general bending Model I, and simple bending, have little impact on the resulting bending moment and therefore springback. The converse is not true for pure kinematic hardening.

Figure 8.89 shows the predicted springback assuming linear unloading and using Eq. 21 from Chapter 2. From this equation, springback increases with increasing internal bending moment and bending radius, and decreasing thickness of the cross section. In Model I thinning deformation is negligible, and in the simple bending model, it is assumed that there is no thinning deformation. Springback for these models is therefore a direct function of the internal bending

moment and bending radius. The predicted springback for Model I and that from the simple bending model are therefore fortuitously nearly identical, being a linear decreasing function of the bending block radius.

In contrast, Model II predicts both lower internal bending moment and greater thinning with decreasing R_i. The net result of these opposing effects is shown in Figure 8.89. At large values of R_i the predicted springback is close to that from Model I and from the simple bending model. At the experimental bending radius R_i of 1 mm, Model II predicts approximately 3% less springback than model I and the simple bending model. This result is in direct contradiction to the FEA which showed greater springback under the pure kinematic assumption, compared to that using the pure isotropic assumption. Further, the 3D continuum element FEA using the pure kinematic hardening assumption showed the best agreement with the experimental springback (Figure 8.71). This contradiction can be explained in terms of the assumption of linear-elastic unloading used to obtain the results in Figure 8.89. Previously for the V-die bending FEA, it was identified that non-linear unloading of surface fibers was an important mechanism resulting in increased springback (Figures 8.56-8.61). These results in conjunction with those shown in Figures 8.88-8.89, imply that non-linear unloading of surface fibers is an important mechanism for increased springback in the small radius bending of the DP780 steel sheet.

CHAPTER 9
CONCLUSIONS AND RECOMMENDATIONS

9.1 Conclusions

In this thesis, the bending and springback behavior of DP780 and DP980 steel sheet was studied under simple and general bending conditions using FEA (LSDYNA3D), analytical models, and experiments. The FEA examined the interaction between the element formulation, and the material hardening assumption, in terms of the effect on the resulting bending and residual stresses after springback, and the predicted springback itself. The analytical models and experimental results were then analyzed in conjunction with the FEA results.

The FEA of sheet metal forming and springback, was performed using the parameters of the analytical simple bending model by Queener and DeAngelis (1968). Simple bending and springback for an AISI 1095 sheet was the focus of study. The FEA for this study assumed pure isotropic hardening; Von Mises yield criterion and Hollomon work hardening. It was demonstrated that under simple bending conditions, the 3D shell element behaved in accordance with simple bending theory showing good agreement with Queener's simple bending analytical model, in terms of the predicted springback, bending stresses, and residual bending stresses after springback. Also demonstrated was the effectiveness of standard FEA modeling methods using LSDYNA3D (Maker and Zhu, 2001), to model bending and springback under the conditions of simple bending. The springback error comparing FEA to the analytical simple bending

model (in terms of Ks) was 6% and was attributed to a small amount of die clearance in the FEA as explained by Wang (1993). Error was also possibly due to the FEA numerical parameters, such as the contact algorithm, that affected the bending curvature of the blank.

Subsequently, V-die bending experiments were performed for DP780 and DP980 steel sheet. The experiments were modeled using FEA (LSDYNA3D) and the analytical elastic-plastic simple bending equation from the work of Queener and DeAngelis. In the FEA, the effect of element formulation (i.e., 2D and 3D continuum element as well as 3D shell element) and hardening assumption (i.e. pure isotropic, mixed isotropic-kinematic and pure kinematic hardening) were studied assuming Von Mises yield criterion. Work hardening was modeled using piece-wise linear work hardening obtained from experimental tensile tests. The material model used in LSDYNA3D was MAT103 and the bending and springback behavior was modeled accounting for pure isotropic, mixed isotropic-kinematic and pure kinematic hardening. The appropriate mixed isotropic-kinematic hardening behavior for the experimental DP steels was estimated by calibrating the material model (MAT103) vis a vie FEA of uniaxial tension-compression tests in which the hardening assumption was varied from pure isotropic to pure kinematic hardening. From each FEA, the Baushinger effect parameter (BEF) as defined by Sadagopan (2003) was calculated. The variation in BEF from the FEA, as a function of mixed hardening, was compared to published values of BEF (Sadagopan, 2004). It was found that the FEA using 3D shells, and

with the appropriate hardening assumption, from the calibration procedure, was most suitable for predicting springback in simple bending for the DP780 and DP980 steels, whereas the 2D and 3D continuum FEA models generally overpredicted springback.

The FEA using the appropriate mixed hardening assumption suggested that non-linear unloading of extreme bending fibers is a possible mechanism for springback in DP780 and DP980 steels under simple bending conditions. Non-linear unloading results in greater springback compared to that assuming linear unloading. Accordingly, the bending model from Queener and DeAngelis (1968) significantly underpredicted the experimental springback, primarily due to the inability to account for non-linear unloading, as well as the effect of die clearance as described by Wang (1993).

Lastly, the bending and springback behavior of DP780 was investigated under general bending conditions. Bending and springback experiments were performed on a commercial bending machine such that the R_p/t ratio was 0.5. The experiments were modeled using the analytical general bending model by Tan and Magnusson (1995). This model investigated the kinematics of general bending as a function of the hardening assumption. FEA of the bending experiments was also performed using LSDYNA3D. The FEA investigated the effect of element formulation (i.e., 2D and 3D continuum element as well as 3D shell element) and hardening assumption (i.e. pure isotropic and pure kinematic hardening) on the evolution of bending stresses and the kinematics of general bending, as well as the

predicted springback. Similar to the V-die study, the FEA assumed Von Mises yield criterion, and piece-wise linear work hardening obtained from experimental tensile tests. The material model used was MAT103. The results from the previous hardening calibration procedure showed that the appropriate hardening assumption for the FEA was that of pure kinematic hardening. The FEA showed that the 3D continuum model using the pure kinematic hardening assumption resulted in the smallest springback error (i.e. 7% error compared to the experiments). This FEA also showed that non-linear unloading of surface fibers during springback is a possible mechanism causing increased springback in the general bending of DP780, compared to the FEA using the pure isotropic hardening assumption in which unloading was linear. The 3D shell FEA using the pure isotropic hardening assumption, which is the conventional technique in sheet metal forming, predicted only 54% of the experimental springback. The results also showed that the 3D shell element may not be appropriate for the FEA of general bending and the associated springback. The 3D shell FEA does not model the interaction of the hardening assumption with the kinematics of general bending. The 3D shell does not model neutral axis shifting and the associated change in the bending stress distribution as a function of the hardening assumption. It also does not account for thinning deformation in bending, as predicted by the general bending model and continuum element FEA for the pure kinematic hardening assumption. Both of these models showed good agreement with the experimentally measured thinning.

For all the FEA performed, predicted the springback magnitude was generally in the order; 2D continuum >3D continuum > 3D shells, and kinematic hardening > mixed hardening> isotropic hardening. It was shown that the 2D continuum element may not be appropriate to model springback in general bending, as the effect of anticlastic curvature, which significantly suppresses springback under these conditions, is not modeled.

9.2 Recommendations for future work

In Chapter 8, the 3D continuum FEA and the analytical general bending model results predicted 5-6% thinning deformation for general bending of DP780 under the pure kinematic hardening assumption. These results were supported by the experimentally measured thinning deformation. Recently, industry awareness of premature fracture in the stampings of DP steels has grown. This phenomenon poses a challenging barrier to the manufacturability of many stampings utilizing the higher strength DP steels (Fekete, 2008). Fracture has been observed in areas of the stamping that experienced plane strain bending – unbending, with superimposed tension. It is therefore recommended to extend this research with the goal of incorporating the effect of the hardening assumption into an FEA material model that accounts for failure and thinning deformation in plane strain bending-unbending with tension deformation.

REFERENCES

Alves, J. L., Olivera, M. C., and Menezes, L. F., (2004). Springback evaluation with several phenomenological yield criteria. *Materials Science Forum, 455-456,* 723-737.

American Iron and Steel Institute (AISI)., (2002). *Automotive Steel Design Manual* (Rev. 2nd ed.). Detroit, American Iron and Steel Institute (AISI). Retrieved May 5, 2006, from The Auto-Steel partnership web site, http//www.a-sp.org

American Iron and Steel Institute (AISI)., (2006). *The steel industry technology roadmap for automotive.* Detroit, American Iron and Steel Institute (AISI). Retrieved May 5, 2006, from http:\\www.autosteel.org-AM

Ashwell, D. G. (1950). The pure bending of beams and plates. Journal of the Royal Aeronautical Society, 170, 708-715.

Asnafi, N. (2000). Springback and fracture in v-die air bending of thick stainless steel sheets. *Materials and Design, 21,* 217-236.

Berstad, O., Hopperstad, S., and Langseth, M., (1994). Elasto-viscoplastic constitutive models in the explicit finite element code LS-DYNA3D. 2nd International LS-DYNA3D Conference, San Francisco.

Blumel, K. W., Ufermann, P., Graham, J., (1999), Numerical modeling of tailored blank applications for autobody components, SAE International Congress and Exposition, Detroit, Michigan, USA, paper No. 1999-01-0679

Brown, C. M., Binder, W. O., and Franks, R., (1944). Methods for computing springback when bending stainless steel. Metal Progress, 1077-1080.

Carden, W. D., Geng, L. M., Matlock, D. K., and Wagoner, R. H., (2002). Measurement of springback. International Journal of Mechanical Sciences, 44 (1), 79-101.

Chapman, F. B., Hazlet, T. H., and Schroder, W., (1942). Springback in flanging. Product Engineering, 382-383.

Cleveland, R. M., and Ghosh, A. K., (2002). Inelastic effects on springback in metals. International Journal of Plasticity, *18 (5-6),* 769-785.

Cook, R. D, Malcus, D. S., Flema, M. E., Witt, R. J., (2001), *Concepts and Applications of Finite Element Analysis 4th ed,* New York, New York, Wiley, 2001

Davies, R. G. (1981). Springback in high-strength steels. Journal of Applied Metalworking, 1(4), 45-52.

Demeri, M. (2002). Residual stresses in cup drawing of automotive alloys. SAE International Congress and Exposition, Detroit, Michigan,USA, paper No. 2002-01-0135.

Du, C., Chen, X. M., Lim, T., Chang, T., Xiao, P., and S, D. Liu (2007). Correlation of FEA prediction and experiments on Dual Phase steel automotive rails. AIP Conf. Proc. / Volume 908 / Issue 1. NUMIFORM '07; Proceedings of the 9th International Conference on Numerical Methods in Industrial Forming Processes.

Du, C., Shi, M. F., Chen, X. M., Liu, S. D., and Yao, H. (2001). Rail type stamping springback/experiment vs. simulation. Sixth US Conference on Computational Mechanics (USNCCM VI). Detroit, Michigan, USA.

Du, C., Wu, J., Militisky, M., Principle, J., Garnett, M., and Zhang, L. (2004). Springback control with variable binder force-experiments and FEA simulation. Proceedings of the 8th International Symposium on Numerical Methods in Industrial Forming Processes (2004). American Institute of Physics: College Park, MD.

Dutton, T., (2005), Review of sheet metal forming simulation progress to date, future developments, 8th International LS-DYNA Users Conference , downloaded April 12, 2008, from *http --www.dynalook.com-documents-8th_International_ls-dyna-09-1.pdf*

Eary, D. F., and Reid, E. A. (1974). *Techniques of Pressworking Sheet Metal* (2nd Ed.). Englewood Cliffs New Jersey Prentice-Hall.

Fei, D., and Hodgson, P. (2006). Experimental and numerical studies of springback in air V-bending process for cold rolled TRIP steels. Nuclear Engineering and Design, 236, 1847-1851.

Fekete, J. R. (2003). Measurement and analysis of flange springback for HSLA and Dual Phase steels. The American Iron and Steel Institute (AISI), Automotive Applications Committee (AAC), Designs in Steel Seminar. February 19, 2003. Livonia, MI.

Finn, M. J., Galbraith, P. C., Wu, L., Hollquist, J. O., Lum, L., and Lin, T. L. (1995). Use of coupled explicit-implicit solver for calculating spring-back in automotive body panels. Materials Processing Technology, *50,* 359-409.

Forcellese, A., Fratini, L., Gabrielli, F., and Micari, F. (1996). Computer aided engineering of sheet metal bending process. Journal of Materials Processing Technology, 60, 225-232.

Frank, W. W., Philip, D. H., Charles, B., and Grump, J. R. (1985). *Die Design Handbook, National Technical Committee Society of Manufacturing Engineers*. New York McGraw-Hill.

Galbraith, C. (1998). Sheet Metal Forming Simulation using LSDYNA (Training Course Materials). LSTC, Livermore, California.

Gardiner, F. J. (1957). The springback of metals. *ASME Transactions, 79*(1), 1-9.

Geng, L., and Wagnoner, R. H. (2001). Role of plastic instability and its evolution on springback. International of Mechanical Sciences, 44, 123-148.

Gomes, C., Onipede, O., and Lovell, M. (2005). Investigation of springback in high strength anisotropic steels. Journal of Materials Processing Technology, 159, 91-98.

Hill, R., (1950) *The Mathematical Theory of Plasticity*, Oxford University Press, Oxford.

Horrocks, D., and Johnson, W., (1967). On the anticlastic curvature with special reference to plastic bending. International Journal of Mechanical Sciences, *9*, 835-861.

Hosford, W. F., and Caddel, R. M. (1993). *Metal forming, Mechanics and Metallurgy* (2nd ed., Rev.). New Jersey PTR Prentice Hall.

International Iron and Steel Institute (IISI), 2003, Advanced high strength steel guidelines, downloaded March 3, 2004, from www.worldautosteel.org-.

Inamadar, M. V., Date, P. P., and Subnis, S. V., (2002). On the effects of geometric parameters on springback in sheets of five materials subject to air vee bending. Journal of Materials Processing Technology, *123*, 459-463.

Johnson, W., and Yu, X. T. (1981). On springback after the pure bending of beams and plates of elastic work-hardening materials.--III. International Journal of Mechanical Sciences, *23,* 687-695.

Lee, S. W., and Yang, D. Y. (1998). An assessment of numerical parameters influencing springback in explicit finite element analysis of sheet metal forming processes. Journal of Materials Processing Technology, *80-81,* 60-67.

Lemaitre, J., and Chaboche, J. L. (2002). *Mechanics of Solid Materials.* Cambridge: Cambridge University Press.

Leu, D. K. (1997). A simplified approach for evaluating bendability and springback in plastic bending anisotropic sheet metals. Journal of Materials Processing Technology, *66,* 9-17.

Levy , B. S, Van Tyne , C. J, Moon, Y. H., and Mikalsen, C. (2006). The Effective Unloading Modulus for Automotive Sheet Steels. SAE International Congress and Exposition, Detroit, Michigan, USA, paper No. *2006-01-0146.*

Levy, B.(1984). Empirically derived equations for predicting springback in bending. Journal of Applied Metalworking. 3 (2), 135-141.

Li, K.P., Carden, W. P., Wagoner. (2002). Simulation of springback. International Journal of Mechanical Sciences, *44,* 103-122.

Lim, T., and Dietrick, T. (2006, June). Springback simulation of the Numisheet Benchmark II using DP600. Paper presented at the meeting of the 9th international LS-DYNA Users Conference. Detroit, Michigan.

Ling, Y. E., Lee, H. P., and Cheok, B. T. (2005). Finite element analysis of springback in L-bending of sheet metal. Journal of Materials Processing Technology, 168, 296-301.

Luzin, V., Banovic, S., Gnaupel-Herold, T., Prask, H. J., and Ricker, R. E. (2005). Measrement and calculation of elastic properties in low carbon steel sheet. Material Science Forum, 495-497, 1591-1596.

LSTC, (2006), LSDYNA3D Theoretical Manual, Livermore Software Technology Corporation.

LSTC, (2003) Implicit notes, downloaded from ftp.lstc.com

Magnusson, C., and Tan, Z. (1994). Mathematical modeling of V-die bending process. Paper presented at the meeting of the 16th Biennial IDDRG Congress, Borlange and Goteborg, Sweden.

Maker, B. N., and Zhu, X. (2001). Input parameters for springback simulation using LS-DYNA. , Retrieved from http:--www.dynalook.com www.dynalook.com

Maker, B., and Zhu , X. (2000). Input parameters for metal forming simulation using LSDYNA. 6th International LSDYNA Users Conference, Detroit MI, April 2000, Session 12-1., Retrieved from http://www.dynalook.com

L, *Mechanics of Sheet Metal Forming* (2nd Ed. 2002, Revised). Oxford Butterworth Heinemann.

Mendelson, A. (1968). *Plasticity-Theory and Application.* New York, Macmillan.

Mori, K., Akita, K., and Abe, Y. (2007). Springback behavior in bending of ultra-high-strength steel sheets using CNC servo press. International Journal of Machine Tools and Manufacturing, 47, 321-325.

Nilsson, A., Melin, L., and Magnusson, C. (1997). Finite-element simulation of V-die bending, a comparison with experimental results. Journal of Materials Processing, *65*, 52-58.

Oliveira, M. C., Alves, J. L., Chapparo, B. M., and Menzes, L. F., (2007). Study on the influence of work- hardening in modeling springback prediction. International Journal of Plasticity, *23*, 516-543.

Papeleux, L., and Ponthot, J. P. (2002). Finite element simulation of springback in sheet metal forming. Journal of Materials Processing Technology, *125-126*(9), 785-791.

Proska, F. (1959). Der Stahlbau., 28(59), 29-36.

Queener, C. A., and De Angelis, R. J. (1968). Elastic springback and residual stresses in sheet metal formed by bending. Transactions of the ASM, 61, 757-768.

Rolf, R. L., and Patrick, E. P. (1978). Bending and springback of aluminum sheet and plate. A.S.T.M, STP 647, 65-85.

Sachs, G. (1950). *Principles and Methods of Sheet -Metal Fabricating*. New York Reinhold Publishing Corp. .

Sachs, G., and Voegeli, H. E.,(1966). *Principal and Practice of Sheet Metal Fabricating*. Stamford Reinhold Publishing Co.

Schikorra, M., Govindarajan, Brosius, A., and Kleiner, M., (2005). Springback analysis of sheet metals regarding material hardening. Advanced Materials Research Volumes, 6-8(2005), 721-729.

Shanley, F. R. (1942). Elastic theory in sheet metal forming problems. Journal of Aeronautical Science, 9, 313-333.

Sidebottom, O. M., and Gebhardt, C. F., (1979). Elastic springback in plates and beams formed by bending. Experimental Mechanics, 19, 371-377.

Sadagopan, S., (2003). Formability characterization of a new generation of high strength steels. American Iron and Steel Institute, Pittsburg, PA, Retrieved May 5, 2006, from http//www.autosteel.org

Simo, J. C., Aremo, F., (1992). Geometrically non-linear enhanced strain mixed methods and the method of incompatible modes, International Journal of Numerical Methods in Engineering, 33, 1413-1449.

Smith, L. M., Ganeshmurthy, S., Chen, C. C.,Lim, T., Murty, P.,(2004), Finite element modeling of the tubular hydroforming process, part 1: strain rate-independent material model assumption, International Journal of Materials Processing Technology, 147 (1)

Soldaat, R. J., (1985). *Bending and Denting Performance of Strain Aged Sheet Steel* (Master Thesis, McMaster University, 1985).

Tan, Z., Persson, B., and Magnusson, C., (1995), Plastic bending of anisotropic sheets. International Journal of Mechanical Sciences, 37(4), 405-421

Tseng, A. A., Chen, T., Jen, K. P., and Ochial, T. (1994). Forming and fractographical characteristics of copper-nickel-beryllium sheets. Journal of Materials Engineering and Performance, 3(5), 619-634.

Tseng, A., Muller, J., and Hahn, Y. H. (1996). Mechanical and bending characteristics of invar sheets. Materials and Design, 17(2), 89-96.

Van Riemsdijk, I, Internal Dofasco Research Test Report# 931939-0067-RS-05

Wagoner, R. H., and Chenot, J. L. (1996). *Fundementals of Metal Forming*. New York John Wiley and Sons, Inc.

Wagoner, R. H., and Li, M. (2007). Simulation of springback -Through thickness integration. International Journal of Plasticity, 23, 345-360.

Wang, C. (1993). *Mechanics Of Bending, Flanging, And Deep Drawing And A Computer-Aided Modeling System For Predictions Of Strain, Fracture, Wrinkling And Springback In Sheet Metal Forming* (Doctoral dissertation, Ohio State University, 1993).

Wang, C., Kinzel, G., and Alton, T. (1993). Mathematical modeling of plane-strain bending of sheet and plate. Journal of Materials Processing Technology, 39, 279-304.

Wang, J. F., Wagoner, R. H., Matlock, D. K., and Barlat, F. (2005). Anticlastic curvature in draw-bend springback. International Journal of Solids and Structures, 42, 1287-1307.

Weimer, K., (2001), LS-DYNA Users Guide, Revision 1.19, CAD-FEM GmbH, downloaded January 10, 2002 from www.dynamore.de

Yao, H., Liu, S. D., Du, C., and Hu, Y. (2002). Techniques to improve spring back prediction accuracy using dynamic explicit FEA codes SAE International Congress and Exposition, Detroit, Michigan, Paper No. *2002-01-0159*

Xu, W. L., Ma, C. H., and Feng, W. J. (2004). Sensitive factors in springback simulation for sheet metal forming. Journal of Materials Processing Technology, 151, 217-222.

Zhang, Z. T., and Hu, S. J. (1998). Stress and residual stress distribution in plane strain bending. International Journal of Mechanical Sciences, *40*(6), 533-543.

Zeng, D., Xia, C. X.,(2006). Understanding through-thickness integration in springback simulation. SAE International Congress and Exposition, Detroit, Michigan, oral presentation only.

Zienkiewicz, O. C., Taylor, R. L., *The Finite Element Method, Volumes I,II,III*, Oxford, England, Butterwoth-Heinmann, 2000

Zhu, X., (2001), Simulation and metal forming notes I, FEA Information International News, 2002-02,10-11, downloaded from www.feainformation.com

APPENDIX A-DERIVATION OF THE GENERAL BENDING MODEL

In the work by Tan et al. (1995), a general bending model was developed for planar anisotropic sheets. In Tan's model, Voce hardening was assumed for isotropic hardening, and Ludwig hardening was assumed for pure kinematic hardening. In this thesis, Tan's general bending model using a pure isotropic hardening assumption was modified, instead incorporating Ludwig working hardening. This ensured a consistent work hardening assumption in the modeling of general bending for both pure isotropic and kinematic hardening.

The following derivations for Tan's general bending model are shown assuming planar isotropy, Ludwig work hardening, and pure isotropic hardening. These derivations following the general technique by Tan and Magnusson, with intermediate steps added in this thesis for clarity.

Given the yield function where $\overline{\sigma}$ is Von Mises effective stress given by equation

$$F(\sigma_{ij},\sigma_0)=\left(\frac{3}{2}S_{ij}S_{ij}\right)^{1/2}-\sigma_0=0 \qquad \text{A. 1}$$

$$S_{ij}=\sigma_{ij}-\delta_{ij}\frac{\sigma_{kk}}{3} \qquad \text{A. 2}$$

The effective plastic strain is given by

$$d\overline{\varepsilon^p}=\sqrt{\frac{2}{3}\left(d\varepsilon_{ij}^p\right)\left(d\varepsilon_{ij}^p\right)} \qquad \text{A. 3}$$

From the flow rule;

$$d\varepsilon_{ij}^{p} = d\lambda \frac{\partial F}{\partial \sigma_{ij}} \qquad \text{A. 4}$$

$$\frac{\partial F}{\partial \sigma_{ij}} = \frac{1}{2} \frac{\dfrac{\partial}{\partial \sigma_{ij}}\left[\dfrac{3}{2} S_{ij} S_{ij}\right]}{\sqrt{\dfrac{3}{2} S_{ij} S_{ij}}} = \left(\frac{3}{2\sigma_0}\right) S_{ij} \qquad \text{A. 5}$$

$$d\varepsilon_{ij}^{p} = d\lambda \left(\frac{3}{2\sigma_0}\right)\left(S_{ij}\right) \qquad \text{A. 6}$$

Re-arranging

$$S_{ij} = \frac{2\sigma_o}{3} \frac{d\varepsilon_{ij}^{p}}{d\lambda} \qquad \text{A. 7}$$

Substitution into the yield function F

$$F(\sigma_{ij}, \sigma_0) = \left(\frac{3}{2}\left[\frac{2\sigma_o}{3}\frac{d\varepsilon_{ij}^{p}}{d\lambda}\right]\left[\frac{2\sigma_o}{3}\frac{d\varepsilon_{ij}^{p}}{d\lambda}\right]\right)^{1/2} - \sigma_0 = 0 \qquad \text{A. 8}$$

Simplifying gives the solution for dλ.

$$F(\sigma_{ij}, \sigma_0) = \frac{\sigma_0}{d\lambda}\left(\frac{2}{3} d\varepsilon_{ij}^{p} d\varepsilon_{ij}^{p}\right)^{1/2} - \sigma_0 = 0 \qquad \text{A. 9}$$

$$F(\sigma_{ij}, \sigma_0) = \frac{\sigma_0}{d\lambda}\left(\frac{2}{3} d\varepsilon_{ij}^{p} d\varepsilon_{ij}^{p}\right)^{1/2} - \sigma_0 = 0 \qquad \text{A. 10}$$

$$F(\sigma_{ij}, \sigma_0) = \frac{\sigma_0}{d\lambda} \bar{\varepsilon}^{p} - \sigma_0 = 0 \qquad \text{A. 11}$$

$$d\lambda = d\bar{\varepsilon}^p \qquad \text{A. 12}$$

Therefore the flow rule gives the familiar expression,

$$d\varepsilon_{ij}^p = \left(\frac{3d\bar{\varepsilon}^p}{2\sigma_0}\right)(S_{ij}) \qquad \text{A. 13}$$

In terms of principle directions only,

$$d\varepsilon_1^p = \frac{d\bar{\varepsilon}^p}{\sigma_0}\left(\sigma_1 - \frac{\sigma_2+\sigma_3}{2}\right) \qquad \text{A. 14}$$

$$d\varepsilon_1^p = \frac{d\bar{\varepsilon}^p}{\sigma_0}\left(\sigma_1 - \frac{\sigma_2+\sigma_3}{2}\right) \qquad \text{A. 15}$$

$$d\varepsilon_3^p = \frac{d\bar{\varepsilon}^p}{\sigma_0}\left(\sigma_3 - \frac{\sigma_1+\sigma_2}{2}\right) \qquad \text{A. 16}$$

Assuming Von Mises criterion, uni-axial tension, and proportional deformation $(\sigma_2 = \sigma_3 = 0)$,

$$\bar{\sigma} = \sqrt{\frac{1}{2}\left[(\sigma_1-\sigma_2)^2 + (\sigma_1-\sigma_3)^2 + (\sigma_2-\sigma_3)^2\right]} \qquad \text{A. 17}$$

$$\bar{\sigma} = \sigma_1 \qquad \text{A. 18}$$

For the effective strain in uni-axial tension, the relationship between the stress ratio and the strain ratio is used, assuming proportional deformation, the stress and strain ratios are defined by equations A. 19 and A. 20 respectively.

$$\alpha_s = \frac{\sigma_2}{\sigma_1} \qquad \text{A. 19}$$

$$\beta = \frac{d\varepsilon_2^p}{d\varepsilon_1^p} \qquad \text{A. 20}$$

From the flow rule,

$$\beta = \frac{\frac{d\bar{\varepsilon}^p}{\sigma_0}\left(\sigma_2 - \frac{\sigma_1}{2}\right)}{\frac{d\bar{\varepsilon}^p}{\sigma_0}\left(\sigma_1 - \frac{\sigma_2}{2}\right)} \qquad \text{A. 21}$$

Using the definition of the stress ratio,

$$\beta = \frac{\frac{\sigma_1}{2}\left(\frac{2\sigma_2}{\sigma_1} - 1\right)}{\frac{\sigma_1}{2}\left(2 - \frac{\sigma_2}{\sigma_1}\right)} = \frac{2\alpha_s - 1}{2 - \alpha_s} \qquad \text{A. 22}$$

From equation A. 22, α_s can be determined in terms of β;

$$\alpha_s = \frac{2\beta + 1}{2 + \beta} \qquad \text{A. 23}$$

For uni-axial deformation, $\alpha=0$ which therefore results in $\beta=1/2$.

Applying the constant volume criterion, the ratio of plastic strains is therefore,

$$d\varepsilon_1^p : d\varepsilon_2^p : d\varepsilon_3^p = 1 : \frac{1}{2} : -\frac{1}{2} \qquad \text{A. 24}$$

Using the Von Mises effective strain definition, and assuming proportional loading, the effective plastic strain is given by equation A. 25, and for the case of

uni-axial tension, the effective plastic strain is equivalent to the principle plastic strain (equation A. 26).

$$\bar{\varepsilon}^p = \sqrt{\frac{2}{3}\left[\left(\varepsilon_1^P\right)^2 + \left(\varepsilon_2^P\right)^2 + \left(\varepsilon_3^P\right)^2\right]} \qquad \text{A. 25}$$

$$\bar{\varepsilon}^p = \varepsilon_1^P \qquad \text{A. 26}$$

In summary, under uni-axial tension, $\bar{\sigma} = \sigma_1$, $\bar{\varepsilon}^p = \varepsilon_1^p$.

Referring to Figure 2.6, For plane strain general bending, let 1 be the direction of principle bending strains and stresses, 2 the direction across the width (z direction), 3 the direction through the sheet thickness (radial direction, r)
Under plain strain deformation,

$$d\varepsilon_2^p = 0,\ d\varepsilon_3^P = -d\varepsilon_1^P \qquad \text{A. 27}$$

From the flow rule, using Von Mises criterion;

$$d\varepsilon_2^p = \frac{d\bar{\varepsilon}^p}{\sigma_0}\left(\sigma_2 - \frac{(\sigma_1 + \sigma_3)}{2}\right) = 0 \qquad \text{A. 28}$$

And it follows that,

$$\sigma_2 = \frac{(\sigma_1 + \sigma_3)}{2} \qquad \text{A. 29}$$

Substituting equation this into Von Mises criterion Yields

$$\bar{\sigma} = \sqrt{\frac{1}{2}\left[\left(\sigma_1 - \frac{\sigma_1 + \sigma_3}{2}\right)^2 + \left(\frac{\sigma_1 + \sigma_3}{2} - \sigma_3\right)^2 + (\sigma_1 - \sigma_3)^2\right]} \qquad \text{A. 30}$$

$$\bar{\sigma} = \frac{\sqrt{3}}{2}(\sigma_1 - \sigma_3) \qquad \text{A. 31}$$

Reverting to the notation in the work by Tan and Magnusson, and noting that $\sigma_\theta = \sigma_1$, $\sigma_r = \sigma_3$, the general bending equation is therefore given in equation A. 32

$$r\frac{d\sigma_r}{dr} = \sigma_\theta - \sigma_r = C\bar{\sigma}, \text{ where } C = \frac{2}{\sqrt{3}} \qquad \text{A. 32}$$

The Ludwig hardening law is shown in equation A. 33.

$$\bar{\sigma} = \sigma_0 + k_L\left(\bar{\varepsilon}^p\right)^{n_L} \qquad \text{A. 33}$$

And under plain strain deformation, the principle plastic bending strain is related to the effective plastic strain as follows,

$$\bar{\varepsilon}^p = \sqrt{\frac{2}{3}\left[\left(\varepsilon_1^p\right)^2 + 0 + \left(-\varepsilon_1^p\right)^2\right]} = C\varepsilon_1^p \qquad \text{A. 34}$$

Substituting of equation A. 34 into equations A. 32-33 gives the form of the general bending equation used by Tan and Magnusson (equation A. 35). In this equation, the ± signs are dependant on the bending zone as well as the hardening assumption used, as will be shown shortly.

$$r\frac{d\sigma_r}{dr} = \overset{\text{depends on Zone}}{\overset{\frown}{\pm}} C\left[\sigma_0 \overset{\text{depends on hardening assumption}}{\overset{\frown}{\pm}} k_L\left(C\varepsilon_1^p\right)^{n_L}\right] \qquad \text{A. 35}$$

Tan and Magnusson examined two cases. The first was general bending under pure isotropic hardening, and the second, general bending under pure kinematic hardening.

They argued that the form of the differential equation varied according to the definition of three bending zones (Figure 2.6 in Chapter 2). In their work, the differential equation A. 35 is applied parametrically, across the three bending zones, depending if deformation is tensile (Zone I), compressive (Zone II) or tensile with a compressive pre-strain using either pure isotropic or pure kinematic hardening (Zone III).

Mode I assuming pure Isotropic hardening

The following derivations essentially use the solution methods by Tan et al. (1995), however, the resulting equations have not been reported in the literature. These equations describe general bending use Ludwig hardening and the pure isotropic hardening assumption. As in Tan's work, the differential equations in the three bending Zones describing the radial stresses are given by equations A. 36-A. 38.

Zone I (tensile)
$$r\frac{d\sigma_r}{dr} = C\left[\sigma_0 + k_L\left(C\ln\frac{r}{R_u}\right)^{n_L}\right] \qquad \text{A. 36}$$

Zone II (compressive)
$$r\frac{d\sigma_r}{dr} = -C\left[\sigma_0 + k_L\left(C\ln\frac{R_u}{r}\right)^{n_L}\right] \qquad \text{A. 37}$$

Zone III for pure isotropic hardening (fibres pre-strain in compression, then tension)

$$r\frac{d\sigma_r}{dr} = C\left[\sigma_0 + k_L\left(C\ln\frac{r}{R_u}\right)^{n_L}\right] \quad \text{A. 38}$$

Note that $\varepsilon_\theta = \ln\frac{r}{R_u}$, is the bending strain in the tangential direction, where R_u is the radial position at which there is 0 net strain (i.e. the un-stretched bending radius as define by Tan et al. (2005)).

Integration of equations A. 36-38 subject to the boundary conditions in equations A. 39-41, yields the radial stress distribution through the sheet thickness.

$$\sigma_r(ZoneI)\big|_{R=Ry} = \sigma_r(ZoneII)\big|_{R=Ri} = 0 \quad \text{A. 39}$$

$$\sigma_r(ZoneI)\big|_{R=Ru} = \sigma_r(ZoneIII)\big|_{R=Ru} \quad \text{A. 40}$$

$$\sigma_r(ZoneII)\big|_{R=Rn} = \sigma_r(ZoneIII)\big|_{R=Rn} \quad \text{A. 41}$$

For example, to solve for the radial stresses in bending Zone I, equation A.36 is integrated with respect to the radius "r".

$$\int d\sigma_r = \int\frac{C}{r}\left[\sigma_0 + k_L\left(C\ln\frac{r}{R_u}\right)^{n_L}\right] \quad \text{A. 42}$$

$$\sigma_r = C\ln\left(\frac{r}{R_u}\right)\sigma_0 + \frac{k_L C^{n_L+1}}{n+1}\left(\ln\frac{r}{R_u}\right)^{n_L+1} + X \quad \text{A. 43}$$

Where, X is the integration constant in equation A.43.

Tan and Magnusson grouped the constants in equation A. 43, as shown in equations A. 44-45, resulting in equation A. 46.

$$k1 = C\sigma_0 \qquad \text{A. 44}$$

$$k2 = \frac{k_L C^{n_L+1}}{n_L+1} \qquad \text{A. 45}$$

Applying the boundary condition of 0 radial stress at the outside bend surface, at r = R_y, gives the integration constant X.

$$X = -k1 \ln\left(\frac{R_y}{R_u}\right) - k2\left(\ln\frac{R_y}{R_u}\right)^{n_L+1} \qquad \text{A. 46}$$

Therefore the radial stress distribution in Zone I is given by equation A. 47.

$$\text{Zone I} \qquad \sigma_r = -k1\left[\ln\left(\frac{R_y}{R_u}\right) - \ln\left(\frac{r}{R_u}\right)\right] - k2\left[\left(\ln\frac{R_y}{R_u}\right)^{n_L+1} - \left(\ln\frac{r}{R_u}\right)^{n_L+1}\right] \qquad \text{A. 47}$$

For Zone II, equation A. 37 is integrated and the boundary condition of 0 radial stress at the inside of the bend (i.e., r=R_i) is applied. The solution for the radial stress distribution is then given by equation A. 48.

$$\text{Zone II} \qquad \sigma_r = k1\left(\ln\frac{R_u}{r} - \ln\frac{R_u}{R_i}\right) - k2\left[\left(\ln\frac{R_u}{R_i}\right)^{n_L+1} - \left(\ln\frac{R_u}{r}\right)^{n_L+1}\right] \qquad \text{A. 48}$$

For the radial stresses in Zone III, the boundary condition of continuity of radial stresses at the interface of Zones I and III, at the position r = R_u, is applied (equation A.41).

Again assuming isotropic hardening and integrating equation A.38 with respect to r, results in equation A.49, where X is the integration constant. Applying the boundary condition of continuity of radial stresses at r= R_u (equation A. 50), yields equation A. 51.

Zone III
$$\sigma_r = -k1\ln\left(\frac{R_u}{r}\right) - k2\left(\ln\frac{R_u}{r}\right)^{n_L+1} + X \qquad \text{A. 49}$$

$$\overbrace{-k1\left[\ln\left(\frac{R_y}{R_u}\right)-\ln\left(\frac{R_u}{R_u}\right)\right]-k2\left[\left(\ln\frac{R_y}{R_u}\right)^{n_L+1}-\left(\ln\frac{R_u}{R_u}\right)^{n_L+1}\right]}^{\sigma_r(Zone\,I)|_{r=Ru}} = \underbrace{-k1\ln\left(\frac{R_u}{R_u}\right)-k2\left(\ln\frac{R_u}{R_u}\right)^{n_L+1}+X}_{\sigma_r(Zone\,III)|_{r=Ru}} \qquad \text{A. 50}$$

Solving for X and inserting this into back into equation A. 49 gives the equation for the radial stresses in Zone III (equation A.52).

$$\text{Zone III} \quad \sigma_r = k2\left[-\ln\left(\frac{R_u}{r}\right)^{n_L+1}-\left(\ln\frac{R_y}{R_u}\right)^{n_L+1}\right]+k1\left[-\ln\left(\frac{R_u}{r}\right)-\left(\ln\frac{R_y}{R_u}\right)\right] \qquad \text{A. 51}$$

Once the equations for the radial stresses have been derived, then the last boundary condition (equation A. 41) is used to derive a form of the general bending differential equation in terms of the geometric parameters η, ρ, and κ.

Appling continuity of radial stresses at the interface between Zones II and III (at r = R_n) yields equation A. 52.

$$\overbrace{k1\left(\ln\frac{R_u}{R_n}-\ln\frac{R_u}{R_i}\right)-k2\left[\left(\ln\frac{R_u}{R_i}\right)^{n_L+1}-\left(\ln\frac{R_u}{R_n}\right)^{n_L+1}\right]}^{\sigma_r(Zone\ II)|_{r=Rn}} = \underbrace{k2\left[-\ln\left(\frac{R_u}{R_n}\right)^{n_L+1}-\left(\ln\frac{R_y}{R_u}\right)^{n_L+1}\right]+k1\left[-\ln\left(\frac{R_u}{R_n}\right)-\left(\ln\frac{R_y}{R_u}\right)\right]}_{\sigma_r(Zone\ III)|_{r=Rn}} \quad \text{A. 52}$$

Equation A. 52 is simplified in the following equations.

$$k1\left(\ln\frac{R_u}{R_n}-\ln\frac{R_u}{R_i}\right)-k2\left[\left(\ln\frac{R_u}{R_i}\right)^{n_L+1}-\left(\ln\frac{R_u}{R_n}\right)^{n_L+1}\right] -\left[k2\left[-\ln\left(\frac{R_u}{R_n}\right)^{n_L+1}-\left(\ln\frac{R_y}{R_u}\right)^{n_L+1}\right]+k1\left[-\ln\left(\frac{R_u}{R_n}\right)-\left(\ln\frac{R_y}{R_u}\right)\right]\right]=0 \quad \text{A. 53}$$

$$k1\left(2\ln\frac{R_u}{R_n}-\ln\frac{R_u}{R_i}+\ln\frac{R_y}{R_u}\right)-k2\left[\left(\ln\frac{R_u}{R_i}\right)^{n_L+1}-\left(\ln\frac{R_u}{R_n}\right)^{n_L+1}\right] -k2\left[-\ln\left(\frac{R_u}{R_n}\right)^{n_L+1}-\left(\ln\frac{R_y}{R_u}\right)^{n_L+1}\right]=0 \quad \text{A. 54}$$

$$k1\left(2\ln\frac{R_u}{R_n}-\ln\frac{R_u}{R_i}+\ln\frac{R_y}{R_u}\right)=-k2\left[-\left(\ln\frac{R_u}{R_i}\right)^{n_L+1}+2\left(\ln\frac{R_u}{R_n}\right)^{n_L+1}+\left(\ln\frac{R_y}{R_u}\right)^{n_L+1}\right] \quad \text{A. 55}$$

$$\ln\frac{R_iR_y}{R_n^2}=-\frac{k2}{k1}\left[-\left(\ln\frac{R_u}{R_i}\right)^{n_L+1}+2\left(\ln\frac{R_u}{R_n}\right)^{n_L+1}+\left(\ln\frac{R_y}{R_u}\right)^{n_L+1}\right] \quad \text{A. 56}$$

By applying the definitions used in the geometry of bending (equations A.57-62), also described in Chapter 2, results in equation A. 63.

Relative neutral axis shift

$$\rho=\frac{R_n}{R_u} \quad \text{A. 57}$$

Relative thickness

$$\eta=\frac{t}{t_o} \quad \text{A. 58}$$

Relative bending curvature

$$\kappa = \frac{t}{R_m} \qquad \text{A. 59}$$

Outside bend radius

$$R_y = \left(1 + \frac{\kappa}{2}\right) R_m \qquad \text{A. 60}$$

Inside bend radius

$$R_i = \left(1 - \frac{\kappa}{2}\right) R_m \qquad \text{A. 61}$$

Radius of the un-stretched fibre

$$R_u = \eta R_m \qquad \text{A. 62}$$

Equations A. 57-62 describe the bending geometry in general bending (From Tan and Magnusson, 1995). Substituting equations A. 57 and A. 61 into equation A. 56 yields equation A. 63.

$$\ln\left(\frac{Ri \cdot Ry}{Rn^2}\right) = \frac{k2}{k1} \cdot \left[-2 \cdot \ln\left(\frac{1}{\rho}\right)^{(n+1)} - \ln\left(\frac{1 + \frac{\kappa}{2}}{\eta}\right)^{(n+1)} + \ln\left(\frac{\eta}{1 - \frac{\kappa}{2}}\right)^{(n+1)} \right] \qquad \text{A. 63}$$

The differential equation describing the geometry of bending as a function of the relative bending curvature is given in A. 64. This equation in conjunction with equation A. 63 is used to solve for ρ and η as a function of κ. Equation A. 64 is integrated using the Runge Kutta method using the methodology described by Tan and Magnusson (1995). This method is explained in Chapter 5. The corresponding MATLAB® program is in Appendix B.

$$\frac{d\eta}{d\kappa} = -\frac{\eta}{2\kappa}\left(\frac{1 - \kappa^2/4}{\eta^2 \rho^2} - 1\right) = -\frac{\eta}{2\kappa}\left(\frac{R_y R_i}{R_n^2} - 1\right) \qquad \text{A. 64}$$

Mode II assuming pure Kinematic hardening

For general bending assuming pure kinematic hardening and using Ludwig work hardening, the radial stresses are parameterized in the bending Zones I and II using equations A. 36-A. 37. The radial stresses in Zone III are given by equation A. 65, as described in Chapter 2. The procedure for obtaining the equations for the radial stresses and the solution to the differential equation A. 64 is essentially the same as that presented for the case of pure isotropic hardening. The solution is presented in Tan's paper and not reproduced here. The corresponding MATLAB® program however, is shown in Appendix B.

Zone III for pure kinematic hardening (fibres pre-strain in compression, then tension)

$$r\frac{d\sigma_r}{dr} = C\left[\sigma_0 - k_L\left(C\ln\frac{r}{R_u}\right)^{n_L}\right] \qquad \text{A. 65}$$

Determination of bending stresses from the radial stresses

The bending stress distribution can be obtained from the radial stress distribution using equation A. 31, as shown in A. 66. With the bending stress distribution known, the bending moment can be found using Eq.50 as described in Chapter 2.

$$\sigma_\theta = \frac{2}{\sqrt{3}}\bar{\sigma} + \sigma_r \qquad \text{A. 66}$$

APPENDIX B-MATLAB® PROGRAMS

1.0 General Bending Model I MATLAB® program used to integrate Eq. 24 for DP780, assuming pure isotropic hardening

A full description of this program including a flowchart is shown in Chapter 5.

MAIN PROGRAM MODEL I

```
%initial bending conditions
global rho
to=2.00;
%
number_of_increments=200
dk=(k_max-k_min)-number_of_increments;
%start of calculations
%
% inital calculation
rho=1;
k=.00
N=.99999
count=1
eta(1 90)=1.0
for k=0.02 .02 1.8
      %
    options=odeset('RelTol',1e-5,'AbsTol',[1e-6],'Stats','on');
    [x,y]=ode45('eq22a',[k-(.02-0.0000001),k],eta(count),options);
    A=size(x);
    %get the last values in the returned vectors
    N=y(A( ,1));
    eta(count)=N;
    t=N*to
    Rm=t-k
    Ru=N*Rm
    Ri=(1-k-2)*Rm
    Ry=(1+k-2)*Rm
    %stress equivalence at nuetral surface
    %start-find R_nuetral with a tolerance of .001
    R=Ri;
    while ( (sII(Ri,Ru,R)-sIII(Ry,Ru,R))>0);
        R=R+.001;
        if (R>Ry)
            pause
        end
    end
    %output Rn
    %
    Rn=R-.001
    rho=Rn-Ru
```

```
    kappa(count)=k
    relative_curvature(count)=rho;
    %
    count=count+1
    eta%
end
rho_I=relative_curvature'
kappa_I=kappa'
etta_I=eta'
csvwrite('rho',rho_I)
csvwrite('k',kappa_I)
csvwrite('N',etta_I)
```

%Function call evaluation of differential equation for general bending

```
function dNdk=eq22(k,N)
% x is the same as k
% y is the same as global etta
global term1 term2 rho
to=2.00;
K=727.78;
sigma_0=511.043;
R0=1;
R90=1;
n=0.2336;
%
C0=(((1+R0)*(R90-R0+R90))-(1+R0+R90))^0.5;
C90=(((1+R0)*(1+R90))-(1+R0+R90))^0.5;
%for planar isotropy
C=C90;
%
%
k1=C*sigma_0;
k2=K*(C^(n+1))-(n+1);
term1=2*(log(1-rho))^(n+1);
term2=(log((1+k-2)-N))^(n+1);
term3=(log((N-(1-k-2))))^(n+1);
%
delta=(k2-k1)*(-term1-term2+term3);
dNdk=-(N)-(2*k)*(exp(delta)-1);
%
%
%eof-dNdk
```

Function call to determine radial stress in bending zone II at position "R"

```
function sigmaII=sII(Ri,Ru,R)
to=2.00;
K=727.78;
sigma_0=511.043;
R0=1;
R90=1;
n=0.2336;
C0=(((1+R0)*(R90-R0+R90))-(1+R0+R90))^0.5;
```

```
C90=(((1+R0)*(1+R90))-(1+R0+R90))^0.5;
%for planar isotropic case, else planar isotropy calculate c
according to Tans paper
C=C90;
%
%
k1=C*sigma_0;
k2=K*(C^(n+1))-(n+1);
sigmaII=k1*(log(Ru-R)-log(Ru-Ri))-k2*((log(Ru-Ri))^(n+1)-(log(Ru-
R))^(n+1))
%eof - sigmaII
```

Function call to determine radial stress in bending zone III at position "R"

```
function sigmaIII=sIII(Ry,Ru,R)
to=2.00;
K=727.78;
sigma_0=511.043;
R0=1;
R90=1;
n=0.2336;
C0=(((1+R0)*(R90-R0+R90))-(1+R0+R90))^0.5;
C90=(((1+R0)*(1+R90))-(1+R0+R90))^0.5;
%isotropic case else set c to equation in tans paper
C=C90;
k1=C*sigma_0;
k2=K*(C^(n+1))-(n+1);
%
%
sigmaIII=-k1*(log(Ry-Ru)+log(Ru-R))-k2*((log(Ry-
Ru))^(n+1)+(log(Ru-R))^(n+1))
%eof - sigmaIII
```

2. General Bending Mode II MATLAB® program usied to integrate Eq. 24 for DP780 assuming pure kinematic hardening

MAIN PROGRAM MODEL II

```
%initial bending conditions
to=2.00;
%
%start of calculations
rho=1;
k=.00
N=1
count=1
eta(count)=1
options=odeset('RelTol',1e-4,'AbsTol',[1e-5],'Stats','on');
for k=0.02 .02 1.8
      %
```

```
    [x,y]=ode45('eq22',[k-(.02-
0.000000001),k],eta(count),options);
      %end
    A=size(x);
    %get the last values in the returned vectors
    N=y(A( ,1));
    t=N*to
    Rm=t-k
    Ru=N*Rm
    Ri=(1-k-2)*Rm
    Ry=(1+k-2)*Rm
    %stress equivalence at nuetral surface
    %start - find R neutral with a tolerance of .001
    R=Ri;
    while ( (sII(Ri,Ru,R)-sIII(Ry,Ru,R))>0);
        R=R+.001;
        if (R>Ry)
            pause
        end
    end
    %output Rn
    count=count+1
    Rn=R-.001
    rho=Rn-Ru
    kappa(count)=k
    relative_curvature(count)=rho
    eta(count)=N
    %
end
rho_II=relative_curvature'
Kappa_II=kappa'
etta_II=eta'
csvwrite('rho',rho_II)
csvwrite('k',Kappa_II)
csvwrite('N',etta_II)
```

Function call to determine radial stress in bending zone II at position "R"

```
function sigmaII=sII(Ri,Ru,R)
to=2;
K=727.78;
sigma_0=511.043;
R0=1;
R90=1;
n=0.2336;
to=2;
C0=(((1+R0)*(R90-R0+R90))-(1+R0+R90))^0.5;
C90=(((1+R0)*(1+R90))-(1+R0+R90))^0.5;
C=C90;
%
%
k1=C*sigma_0;
k2=K*(C^(n+1))-(n+1);
sigmaII=k1*(log(Ru-R)-log(Ru-Ri))-k2*((log(Ru-Ri))^(n+1)-(log(Ru-
R))^(n+1))
```

```
%eof - sigmaII
```

Function call to determine radial stress in bending zone III at position "R"

```
function sigmaIII=sIII(Ry,Ru,R)
to=2.00;
K=727.78;
sigma_0=511.043;
R0=1;
R90=1;
n=0.2336;
to=2;
C0=(((1+R0)*(R90-R0+R90))-(1+R0+R90))^0.5;
C90=(((1+R0)*(1+R90))-(1+R0+R90))^0.5;
C=C90;
k1=C*sigma_0;
k2=K*(C^(n+1))-(n+1);
%
%
sigmaIII=-k1*(log(Ry-Ru)+log(Ru-R))-k2*((log(Ry-Ru))^(n+1)-
(log(Ru-R))^(n+1))
%eof - sigmaIII
```

MATLAB® program for incremental (simple) bending incorporating piece-wise linear hardening

A full description of this program including a flowchart is shown in Chapter 5.

```
%incremental bending, using simple bending assumptions
E=2.07E+05;
v=0.30;
t=1.457;
Rp=10
rho=Rp+t-2;
Eprime=E-(1-v^2);
StressStrainCurve=dlmread('980.csv',',');
TrueStress=StressStrainCurve( ,2);
effStrain=StressStrainCurve( ,1);
ep=effStrain-TrueStress-E;
e1_yield=((1-v^2)-sqrt(1+v^2-v))*effStrain(1);
Sigma1_yield=2-sqrt(3)*TrueStress(1);
i=2 (length(StressStrainCurve));
Hp(i)=(TrueStress(i)-TrueStress(i-1)).-(ep(i)-ep(i-1));
rhoFullyElastic=(t-2)-e1_yield;
%
div=200
dt=(t-2)-div
j=1 div
t_half=dt*j
e1_max=(t_half)-rho
```

```
% Initialize bending at just prior to platic deformation, fully
elastic
% bending
steps=10;
Delta_Rm=(rho-rhoFullyElastic)-steps
Rm = rhoFullyElastic
e1_start=t_half-Rm;
% Increment Bending curvature, or decrement bending radius until
target
e1=e1_start;
Sigma1=Sigma1_yield;
for k=1 steps;
    Rm=Rm+Delta_Rm
    e1_increment=(t_half-Rm)-e1;
    e1=e1+e1_increment;
    Pfiber=find(e1>e1_yield);
    Delta_e1(Pfiber)=e1_increment(Pfiber);
    e1p(Pfiber)=e1(Pfiber)-Sigma1(Pfiber)-Eprime;
    ep_eff(Pfiber)=2-sqrt(3)*e1p(Pfiber);
    %Assigns hardening modulus associated with each plastic
     bending fiber.
     for k=Pfiber(1) Pfiber(length(Pfiber))
          for m=1 (length(StressStrainCurve)-1);
              if(ep_eff(k)>=ep(m) and ep_eff<=ep(m+1))
                    dSdep(k)=Hp(m+1);
              end
          end
    end
    %stop
    Delta_Sigma1(Pfiber)=Delta_e1(Pfiber).*((1-v^2)-E+(3-4)*(1.-
                              dSdep(Pfiber))).^-1;
    Sigma1(Pfiber)=Sigma1(Pfiber)+Delta_Sigma1(Pfiber);
    Ecore=find(e1<=e1_yield);
    Sigma1(Ecore)=e1(Ecore)*E-(1-v^2);
end
plot(Sigma1,e1);
%moment calculation
M1=Sigma1.*dt;
M2=M1.*(t_half-dt-2);
Moment=2*sum(M2)
rhoFullyElastic
```

APPENDIX C-MATHCAD SHEETS

1. Example MATHCAD2000 sheet used to calculate bending stresses in general bending for pure isotropic hardening using as input κ, η, and ρ from the solution to the general bending equation Eq. 24 in Chapter 2.

DP780

Model I results $\kappa := 0.9995 \quad \eta := 0.9991 \quad \rho := 0.8392$

TEST

$\sigma o := 511.043$

$k := 727.78$

$n := 0.2336$

$to := 2.0$

$t := \eta \cdot to$

$Rm := \frac{t}{\kappa}$

$Ri := \left(1 - \frac{\kappa}{2}\right) \cdot Rm$

$Ry := \left(1 + \frac{\kappa}{2}\right) \cdot Rm$

$Ru := \eta \cdot Rm$

$Rn := \rho \cdot Ru$

$C := \frac{2}{\sqrt{3}}$

$k1 := C \cdot \sigma o$

$k2 := k \cdot \frac{C^{n+1}}{n+1}$

Number of intervals per zone (just for plotting purposes)

$interval := 20$

$i := 0..interval$

$Ri = 1 \qquad Ru = 1.997$

$Ry = 2.998 \qquad Rn = 1.676$

$Rm = 1.999 \qquad t = 1.998$

Zone I Ru<=R1<=Ry

$R1_i := Ru + \frac{Ry - Ru}{interval} \cdot i$

$\sigma r\_I_i := -k1 \cdot \left(\ln\left(\frac{Ry}{Ru}\right) - \ln\left(\frac{R1_i}{Ru}\right)\right) - k2 \cdot \left[\left(\ln\left(\frac{Ry}{Ru}\right)\right)^{n+1} - \left(\ln\left(\frac{R1_i}{Ru}\right)\right)^{n+1}\right]$

$$\sigma\_\theta 1_i := \sigma r\_I_i + C\cdot\left[\sigma o + k\cdot\left(C\cdot\ln\left(\frac{R1_i}{Ru}\right)\right)^n\right]$$

zone II, Ri<R2<Rn

$$R2_i := Ri + \frac{Rn - Ri}{interval}\cdot i \qquad Rn = 1.676 \qquad Ri = 1$$

$$\sigma r\_II_i := k1\cdot\left(\ln\left(\frac{Ru}{R2_i}\right) - \ln\left(\frac{Ru}{Ri}\right)\right) - k2\cdot\left[\left(\ln\left(\frac{Ru}{Ri}\right)\right)^{n+1} - \left(\ln\left(\frac{Ru}{R2_i}\right)\right)^{n+1}\right]$$

$$\sigma\_\theta 2_i := -C\cdot\left[\sigma o + k\cdot\left(C\cdot\ln\left(\frac{Ru}{R2_i}\right)\right)^n\right] + \left[k1\cdot\left(\ln\left(\frac{Ru}{R2_i}\right) - \ln\left(\frac{Ru}{Ri}\right)\right) - k2\cdot\left[\left(\ln\left(\frac{Ru}{Ri}\right)\right)^{n+1} - \left(\ln\left(\frac{Ru}{R2_i}\right)\right)^{n+1}\right]\right]$$

zone III, Rn<R<Ru

Rn = 1.676

Ru = 1.997

$$R3_i := Rn + \frac{Ru - Rn}{interval}\cdot i$$

$$\sigma r\_III_i := \left[-\ln\left(\frac{Ru}{R3_i}\right)^{(n+1)} - \ln\left(\frac{Ry}{Ru}\right)^{(n+1)}\right]\cdot k2 + \left(-\ln\left(\frac{Ru}{R3_i}\right) - \ln\left(\frac{Ry}{Ru}\right)\right)\cdot k1$$

$$\sigma\_\theta 3_i := C\cdot\left[\sigma o + k\cdot\left(C\cdot\ln\left(\frac{Ru}{R3_i}\right)\right)^n\right] + \left[\left[-\ln\left(\frac{Ru}{R3_i}\right)^{(n+1)} - \ln\left(\frac{Ry}{Ru}\right)^{(n+1)}\right]\cdot k2 + \left(-\ln\left(\frac{Ru}{R3_i}\right) - \ln\left(\frac{Ry}{Ru}\right)\right)\cdot k1\right]$$

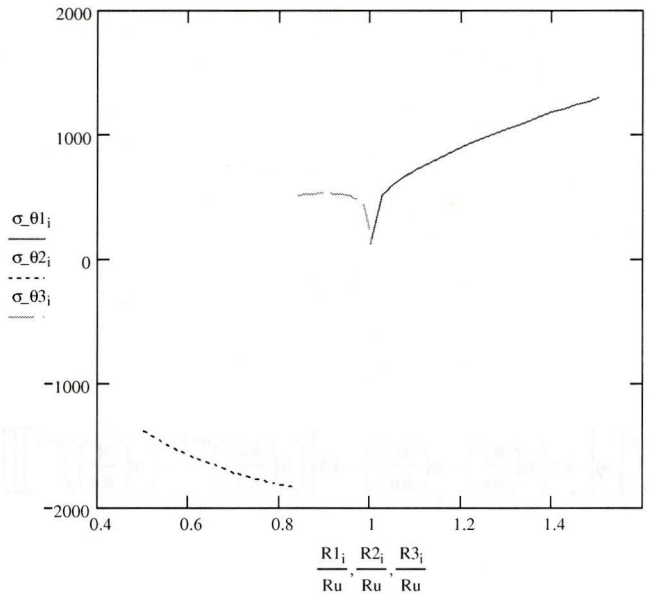

2. MATHCAD 2000 sheet to calculate the internal bending moment for the general and simple bending models assuming Ludwig work hardening and pure isotropic hardening

Model 1 results

DP780

$\sigma o := 511.043$ $\kappa := .4$

$k := 727.78$

$n := 0.2336$ $\eta := .99963$

$to := 2.0$ $\rho := 0.97363$

$t := \eta \cdot to$

$Rm := \frac{t}{\kappa}$

$Ri := \left(1 - \frac{\kappa}{2}\right) \cdot Rm$

$Ry := \left(1 + \frac{\kappa}{2}\right) \cdot Rm$

$Ru := \eta \cdot Rm$

$Rn := \rho \cdot Ru$

$C := \frac{2}{\sqrt{3}}$

$k1 := C \cdot \sigma o$

$k2 := k \cdot \frac{C^{n+1}}{n+1}$

Zone I Ru<=R1<=Ry

$$M1 := \int_{Ru}^{Ry} \left[C \cdot \left[\sigma o + k \cdot \left(C \cdot \ln\left(\frac{R}{Ru}\right) \right)^n \right] + \left[-k1 \cdot \left(\ln\left(\frac{Ry}{Ru}\right) - \ln\left(\frac{R}{Ru}\right) \right) - k2 \cdot \left[\left(\ln\left(\frac{Ry}{Ru}\right) \right)^{n+1} - \left(\ln\left(\frac{R}{Ru}\right) \right)^{n+1} \right] \right] \right] \cdot (R)\, dR$$

M1 = 5378.033

zone II, Ri<R2<Rn

Rn = 4.8645 Ri = 3.9985

$$M2 := \int_{Ri}^{Rn} \left[-C \cdot \left[\sigma o + k \cdot \left(C \cdot \ln\left(\frac{Ru}{R}\right)\right)^{n} \right] + \left[k1 \cdot \left(\ln\left(\frac{Ru}{R}\right) - \ln\left(\frac{Ru}{Ri}\right)\right) - k2 \cdot \left[\left(\ln\left(\frac{Ru}{Ri}\right)\right)^{n+1} - \left(\ln\left(\frac{Ru}{R}\right)\right)^{n+1} \right] \right] \right] \cdot (R)\, dR$$

M2 = –4702.0167

zone III, Rn<R<Ru

Rn = 4.8645

Ru = 4.9963

$$M3 := \int_{Rn}^{Ru} \left[C \cdot \left[\sigma o + k \cdot \left(C \cdot \ln\left(\frac{Ru}{R}\right)\right)^{n} \right] + \left[\left[-\ln\left(\frac{Ru}{R}\right)^{(n+1)} - \ln\left(\frac{Ry}{Ru}\right)^{(n+1)} \right] \cdot k2 + \left(-\ln\left(\frac{Ru}{R}\right) - \ln\left(\frac{Ry}{Ru}\right)\right) \cdot k1 \right] \right] \cdot (R)\, dR$$

M3 = 445.4994

Mt := M1 + M2 + M3

Mt = 1121.5156

Ludwig Simple Bending

$$Msimple := 2 \cdot \int_{0}^{1} C \cdot \left[\sigma o + k \cdot \left(C \cdot \ln\left(1 + \frac{z}{Ri + 1}\right)\right)^{n} \right] \cdot (z)\, dz$$

Msimple = 1116.4099

3. MATHCAD 2000 sheet to calculate internal bending moment and tangential stresses for the general bending models assuming Ludwig work hardening and pure kinematic hardening

DP780

Model II results

TEST $(\kappa \ \eta \ \rho) := (0.9753\ 0.9514\ 0.8221)$

$\sigma o := 511.043$

$k := 727.78$

$n := 0.2336$

$to := 2.0$

$t := \eta \cdot to$

$Rm := \frac{t}{\kappa}$

$Ri := \left(1 - \frac{\kappa}{2}\right) \cdot Rm$

$Ry := \left(1 + \frac{\kappa}{2}\right) \cdot Rm$

$Ru := \eta \cdot Rm$

$Rn := \rho \cdot Ru$

$C := \frac{2}{\sqrt{3}}$

$k1 := C \cdot \sigma o$

$k2 := k \cdot \frac{C^{n+1}}{n+1}$

Number of intervals per zone (just for plotting purposes)

$interval := 200$

$i := 0..interval$

Ri = 0.9996 Ru = 1.8562

Ry = 2.9024 Rn = 1.526

Rm = 1.951

t = 1.9028

Zone I Ru<=R1<=Ry

$R1_i := Ru + \frac{Ry - Ru}{interval} \cdot i$

Ru = 1.8562

Ry = 2.9024

$$\sigma r\_I_i := -k1\cdot\left(\ln\left(\frac{Ry}{Ru}\right) - \ln\left(\frac{R1_i}{Ru}\right)\right) - k2\cdot\left[\left(\ln\left(\frac{Ry}{Ru}\right)\right)^{n+1} - \left(\ln\left(\frac{R1_i}{Ru}\right)\right)^{n+1}\right]$$

$$\sigma\_\theta 1_i := \sigma r\_I_i + C\cdot\left[\sigma o + k\cdot\left(C\cdot\ln\left(\frac{R1_i}{Ru}\right)\right)^n\right]$$

$$M1 := \int_{Ru}^{Ry}\left[C\cdot\left[\sigma o + k\cdot\left(C\cdot\ln\left(\frac{R}{Ru}\right)\right)^n\right] + \left[-k1\cdot\left(\ln\left(\frac{Ry}{Ru}\right) - \ln\left(\frac{R}{Ru}\right)\right) - k2\cdot\left[\left(\ln\left(\frac{Ry}{Ru}\right)\right)^{n+1} - \left(\ln\left(\frac{R}{Ru}\right)\right)^{n+1}\right]\right]\cdot(R)\,dR$$

$M1 = 2397.2791$

zone II, Ri<R2<Rn

$$R2_i := Ri + \frac{Rn - Ri}{interval}\cdot i \qquad Rn = 1.526 \qquad Ri = 0.9996$$

$$\sigma r\_II_i := k1\cdot\left(\ln\left(\frac{Ru}{R2_i}\right) - \ln\left(\frac{Ru}{Ri}\right)\right) - k2\cdot\left[\left(\ln\left(\frac{Ru}{Ri}\right)\right)^{n+1} - \left(\ln\left(\frac{Ru}{R2_i}\right)\right)^{n+1}\right]$$

$$\sigma\_\theta 2_i := -C\cdot\left[\sigma o + k\cdot\left(C\cdot\ln\left(\frac{Ru}{R2_i}\right)\right)^n\right] + \left[k1\cdot\left(\ln\left(\frac{Ru}{R2_i}\right) - \ln\left(\frac{Ru}{Ri}\right)\right) - k2\cdot\left[\left(\ln\left(\frac{Ru}{Ri}\right)\right)^{n+1} - \left(\ln\left(\frac{Ru}{R2_i}\right)\right)^{n+1}\right]\right]$$

$$M2 := \int_{Ri}^{Rn}\left[-C\cdot\left[\sigma o + k\cdot\left(C\cdot\ln\left(\frac{Ru}{R}\right)\right)^n\right] + \left[k1\cdot\left(\ln\left(\frac{Ru}{R}\right) - \ln\left(\frac{Ru}{Ri}\right)\right) - k2\cdot\left[\left(\ln\left(\frac{Ru}{Ri}\right)\right)^{n+1} - \left(\ln\left(\frac{Ru}{R}\right)\right)^{n+1}\right]\right]\cdot(R)\,dR$$

zone III, Rn<R<Ru

$Rn = 1.526$

$Ru = 1.8562$

$$R3_i := Rn + \frac{Ru - Rn}{interval}\cdot i$$

$$\sigma r\_III_i := \left[-\ln\left(\frac{Ru}{R3_i}\right)^{(n+1)} - \ln\left(\frac{Ry}{Ru}\right)^{(n+1)}\right]\cdot k2 + \left(-\ln\left(\frac{Ru}{R3_i}\right) - \ln\left(\frac{Ry}{Ru}\right)\right)\cdot k1$$

$$\sigma\_\theta 3_i := C\cdot\left[\sigma o - k\cdot\left(C\cdot\ln\left(\frac{Ru}{R3_i}\right)\right)^n\right] + \left[\left[-\ln\left(\frac{Ru}{R3_i}\right)^{(n+1)} - \ln\left(\frac{Ry}{Ru}\right)^{(n+1)}\right]\cdot k2 + \left(-\ln\left(\frac{Ru}{R3_i}\right) - \ln\left(\frac{Ry}{Ru}\right)\right)\cdot k1\right]$$

$$M3 := \int_{Rn}^{Ru}\left[C\cdot\left[\sigma o - k\cdot\left(C\cdot\ln\left(\frac{Ru}{R}\right)\right)^n\right] + \left[\left[-\ln\left(\frac{Ru}{R}\right)^{(n+1)} - \ln\left(\frac{Ry}{Ru}\right)^{(n+1)}\right]\cdot k2 + \left(-\ln\left(\frac{Ru}{R}\right) - \ln\left(\frac{Ry}{Ru}\right)\right)\cdot k1\right]\right]\cdot(R)\,dR$$

$M1 = 2397.2791$

$M2 = -1058.7978$

$M3 = -278.7264$

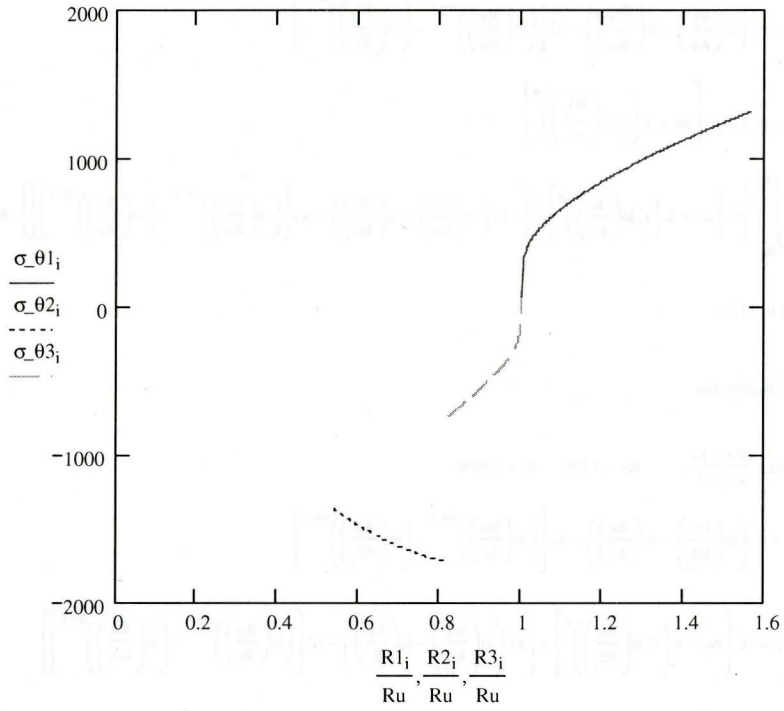

(Mt Ri t) = (1059.755 0.9996 1.9028)

APPENDIX D-INCREMENTAL STRESS STRAIN EQUATIONS

(Derivation of incremental stress strain relationships for the incremental bending program using piece-wise linear hardening)

In the following derivation, simple bending theory is assumed (see Chapter 2) as well as plane stress deformation. The yield function using Von Mises criterion was given in Appendix A (equation A. 1). For case of plane stress, Von Mises criterion is given by equation D. 1, where the direction of the principle bending stress corresponds to the direction 1.

$$2\bar{\sigma}^2 = \sigma_1^2 + \sigma_2^2 - \sigma_1\sigma_2 \qquad \text{D. 1}$$

In Appendix A, the strain and stress ratios were defined in equations A. 20 and A. 23, respectively. For plane strain deformation, the strain ratio β, is 0. The stress ratio α_s, is therefore 1/2. Using the ratio between σ_2 and σ_1, in equation D. 1 results in Von Mises criterion for plane stress and plane strain deformation, shown in equation D. 2.

$$\bar{\sigma} = \frac{\sqrt{3}}{2}\sigma_1 \qquad \text{D. 2}$$

The incremental stress strain relationship for elastic – plastic deformation was developed in Chapter 4 (Section 4.6). Consider a single bending fiber in plane strain, with deformation in the principle (1) direction. Pure elastic deformation is determined by the component of the elastic constitutive matrix given by equation D. 3

$$E' = \frac{E}{1-\nu^2} \qquad \text{D. 3}$$

From equation D. 2, the derivative of the yield function with respect to the stress component σ_1 is given by equation D. 4.

$$\frac{\partial F}{\partial \sigma_1} = \frac{\sqrt{3}}{2} \qquad \text{D. 4}$$

The substitution of equations D. 3 and D. 4, into the elastic-plastic constitutive matrix (Eq. 114 in Chapter 4) yield the incremental stress strain relationship shown in equation D. 5. This equation was then used to develop an incremental bending program in MATLAB®, that incorporated piece-wise linear hardening as described in Chapter 5. The computer program is also shown in Appendix B

$$d\sigma_1 = \left(E' - \frac{E'\frac{\sqrt{3}}{2}\frac{\sqrt{3}}{2}E'}{\frac{\sqrt{3}}{2}E'\frac{\sqrt{3}}{2} + H_p} \right) d\varepsilon_1$$

$$= \left(\frac{H_p E'}{\frac{3}{4}E' + H_p} \right) d\varepsilon_1 \qquad \text{D. 5}$$

$$= \left(\frac{\frac{3}{4}E' + H_p}{H_p E'} \right)^{-1} d\varepsilon_1$$

$$= \left(\frac{3}{4H_p} + \frac{1}{E'} \right)^{-1} d\varepsilon_1$$